

*Viscous-inviscid interaction in a transonic flow
caused by a discontinuity in wall curvature*

Yumashev, Dmitry

2010

MIMS EPrint: **2011.72**

Manchester Institute for Mathematical Sciences
School of Mathematics

The University of Manchester

Reports available from: <http://eprints.maths.manchester.ac.uk/>

And by contacting: The MIMS Secretary
School of Mathematics
The University of Manchester
Manchester, M13 9PL, UK

ISSN 1749-9097

VISCOUS-INVISCID INTERACTION IN
A TRANSONIC FLOW
CAUSED BY A DISCONTINUITY IN
WALL CURVATURE

A THESIS SUBMITTED TO THE UNIVERSITY OF MANCHESTER
FOR THE DEGREE OF DOCTOR OF PHILOSOPHY
IN THE FACULTY OF ENGINEERING AND PHYSICAL SCIENCES

2010

Dmitry Yumashev
School of Mathematics

Contents

Abstract	12
Declaration	13
Copyright Statement	14
Acknowledgements	15
Dedication	16
1 Introduction	17
1.1 Asymptotic Theory of Separated Flows	17
1.2 Viscous-Inviscid Interaction in Transonic Flows	21
1.3 Brief Review of The Work	25
2 Inviscid Transonic Flow Near a Curvature Discontinuity	29
2.1 Problem Formulation	29
2.1.1 Governing equations and boundary conditions	29
2.1.2 Asymptotic expansions for local self-similar solutions	31
2.2 Phase Portrait	36
2.2.1 Invariant transformations	36
2.2.2 Stationary points of equations (2.17)	39
2.3 Numerical Solutions of the Karman-Guderley equation	44
2.3.1 Transformation of the variables	44

2.3.2	Numerical results for the phase portrait and the pressure gradients	47
2.4	Hodograph Method	56
2.4.1	Direct and Inverse problems	56
2.4.2	Self-similar solutions of the Triкоми equations	58
2.4.3	Boundary conditions in the Inverse problem	63
2.4.4	Special cases resulting in a singular Jacobian	67
2.4.5	Subsonic flow on the upstream wall	69
2.4.6	Two main limiting cases for oncoming subsonic flows	78
2.4.7	Subcritical supersonic flow on the upstream wall	82
2.4.8	Transonic Prandtl–Meyer flow	85
2.4.9	Supercritical supersonic flow on the upstream wall	89
2.4.10	Passing through the limiting characteristic	92
2.4.11	Shock formation	97
2.4.12	Structure of the flow behind the shock	106
3	Viscous-Inviscid Interaction Caused by a Curvature Break	123
3.1	Boundary Layer Upstream of the Singularity	123
3.1.1	Peculiarities in the boundary layer exposed to the pressure gradient $\partial p/\partial x = G_-(-x)^{-1/3}$	123
3.1.2	Nonlinear logarithmic expansion in the viscous sublayer	135
3.1.3	Special case of a small amplitude in the pressure gradient	140
3.1.4	Displacement effects of the linear viscous sublayer	144
3.2	Interaction Region	152
3.2.1	Main tiers of the interaction region	152
3.2.2	Analytical solution in region 5	163
3.2.3	Analytical solution in region 3	174
3.3	Solution of the Interaction Problem	191
3.3.1	Interaction equation	191
3.3.2	Analytical solution of the interaction equation	193

3.3.3	Skin friction distribution in the interaction region	200
4	Conclusions	207
	Bibliography	211
	Appendix: Navier–Stokes Equations in The Curvilinear Coordinates	214

List of Tables

List of Figures

2.1	Inviscid flow near a discontinuity in wall curvature.	29
2.2	A typical phase trajectory in the (f, g) plane, with P_1, P_2 and P_3 being the stationary points of equations (2.17).	38
2.3	Physical meaning of the limiting characteristic.	41
2.4	Phase trajectories near the saddle point.	43
2.5	Computational domains for ξ and s	46
2.6	Numerical results for the phase trajectories corresponding to different ratios of the curvatures; (a): $\frac{\kappa_+}{\kappa_-} = 1$; (b) and (c): $1 < \frac{\kappa_+}{\kappa_-} < \infty$; (d): $\frac{\kappa_+}{\kappa_-} = \infty$; (e): trajectories which cross the singular line in an illegitimate place and therefore have to be rejected.	49
2.7	Numerical results for the ratio of the curvatures and the ratio of the gradients for different values of the upstream pressure gradient G_-	50
2.8	The ratio of the pressure gradients on the walls as a function of the ratio of the curvatures (plotted for the case of $\frac{\kappa_+}{\kappa_-} > 1$).	51
2.9	Numerical results for the phase trajectories corresponding to different ratios of the curvatures; (a): $\frac{\kappa_+}{\kappa_-} = 1$; (b), (c): $0 < \frac{\kappa_+}{\kappa_-} < 1$; (d): $\frac{\kappa_+}{\kappa_-} = 0$; (e): trajectories which pass through the singular line via the only allowed point P_2 . The dashed lines represent the limiting shape of the trajectories from the family (a), (b), (c) when $\frac{\kappa_+}{\kappa_-} \rightarrow 0^+$, and the so-called <i>critical lines</i> in the supersonic half-plane (see section 2.4.2).	52
2.10	Upstream and downstream pressure gradients as functions of the ratio of the curvatures.	54
2.11	A typical phase trajectory which tunnels through the singular line.	54

2.12	A sheet of the Riemann surface for the many-valued functions in (2.49); a, b, c mark the regions on the real axis which correspond to physically different flow regimes.	60
2.13	Supercritical region in the phase plane.	62
2.14	Tails of the trajectories in the z plane corresponding to a flow near the upstream wall, left, and the downstream wall, right. The trajectories' direction appears to be the opposite for the subcritical and the supercritical flow regimes.	65
2.15	Tails of the z plane trajectories corresponding to a flow near a concave downstream wall.	65
2.16	Arguments of the complex variables z and $1 - z$	68
2.17	First two fragments of the z plane trajectory for an oncoming subsonic flow. The sign of v changes as the trajectory makes a complete turnover around the branching point $z = 0$ and finds itself on the next sheet of the Riemann surface. This is followed by the change of sign of x when $z = r_0$	71
2.18	Left-hand side (LHS) and right-hand side (RHS) of the transcendental equation (2.63) plotted as functions of r_0	72
2.19	Final fragments of the z plane trajectory for an oncoming subsonic flow. The branching point $z = 1$ corresponds to the sonic line ($u = 0$).	74
2.20	Left-hand side (LHS) and right-hand side (RHS) of the first equation in (2.67), plotted as functions of r_- and r_+ respectively.	76
2.21	Regime with a subsonic flow near the upstream wall.	77
2.22	Local structure of the flow around a small break of curvatures, with a slightly flatter upstream wall ($\frac{z_+}{z_-} = 1 + \varepsilon$). Singular pressure gradients are generated in thin layers near both walls ($ \xi \gtrsim \varepsilon^{-3/2}$). The pressure gradients have the small amplitudes $\delta_{\pm} = \mathcal{O}(\varepsilon)$ which are defined in (2.72).	80
2.23	Local structure of the flow around a strong break of curvatures ($\frac{z_+}{z_-} = \frac{1}{\varepsilon} \gg 1$), left, and in the case of a flat upstream wall ($\frac{z_+}{z_-} = \infty$), right.	81

2.24	Phase trajectories approach the saddle point P_3 when $\frac{z_+}{z_-} \rightarrow \infty$; in the limit they coincide with a fragment of the lower critical line $g = -\frac{2}{3} f^{\frac{3}{2}}$.	82
2.25	Regime with a subcritical supersonic flow near the upstream wall. . . .	83
2.26	The ratio of the gradients plotted versus the ratio of the curvatures when $0 < \frac{z_+}{z_-} < 1$	86
2.27	Local structure of the flow in the case of a flat downstream wall. . . .	88
2.28	Initial fragment of the z plane trajectory corresponding to a supercritical supersonic flow near the upstream wall. Note that $z_- = -r_-$ in this case.	89
2.29	Supercritical phase trajectories before passing through the critical point P_2 . The trajectories corresponding to larger values of G_- (stronger adverse pressure gradients on the upstream wall) are closer to the upper critical line $g = \frac{2}{3} f^{\frac{3}{2}}$	93
2.30	Analytical continuation of the solutions through the limiting characteristic is performed when the integration contour \mathcal{L} moves to the infinite circle in the plane of complex z	95
2.31	As a result of the analytical continuation describing how the flow passes through the limiting characteristic, the integration contour \mathcal{L} in the z plane moves to another sheet of the Riemann surface.	95
2.32	The left-hand side (LHS) of equation (2.99), plotted as a function of r_0 , intersects with the shaded area representing all the possible values of the right-hand side (RHS) of (2.99). As a result, the solution for r_0 is confined within a finite interval.	98
2.33	Left-hand side (LHS) and right-hand side (RHS) of equation (2.101) plotted as functions of r . The mutual intersection which takes place when $r = r_s$ corresponds to an illegitimate crossing of the singular line in the phase plane.	100

2.34	Supercritical phase trajectories corresponding to different values of r_- . After passing through the limiting characteristic (point P_2 on the singular line), the trajectories return to the singular line and tend to cross it below P_2	100
2.35	Geometry of an oblique shock wave produced by a wedge.	101
2.36	Geometry of an oblique shock in the cartesian coordinates (x, y)	102
2.37	After passing through the limiting characteristic (l.c.), a supercritical supersonic flow inevitably develops a shock.	103
2.38	In the language of the phase variables, the upstream side of the shock may be located anywhere on the fragment L_1 of the phase trajectory coming from the upstream wall, while the downstream side of the shock lies somewhere on the curve L_2 . The latter is the image of L_1 described by equations (2.107) and (2.108). The grey trajectories represent the flow between the shock and the downstream wall for different values of \varkappa_+ ; the lowermost of these trajectories does not intersect with L_2 and therefore has no physical meaning.	104
2.39	Regime I for the flow behind the shock.	106
2.40	Final fragments of the z plane trajectory in Regime I.	107
2.41	Location of the phase trajectories describing the flow behind the shock in Regime I (shaded area). The trajectories at the boundaries of the shaded area correspond to $r_+ = r_m$ (r_m is defined in (2.109)) and $r_+ = 1$, the latter giving the straight line $g = \frac{2}{3}f$	108
2.42	An illustration of the connection between relative location of the shock ($\frac{\xi_{sh}}{\sqrt{\varkappa_-}}$) and the downstream parameters $\frac{\varkappa_+}{\varkappa_-}$, G_+ . Roman numerals denote physically different regimes for a flow behind the shock. The graphs are plotted for a fixed value of the supercritical upstream pressure gradient G_- , and are invariant with respect to re-scaling of the spatial coordinates.	109
2.43	Regime II for the flow behind the shock, left, and location of the relevant phase trajectories, right.	110

2.44	Final fragment of the z plane trajectory in Regime II for the case when $v < 0$ behind the shock.	111
2.45	Final fragments of the z plane trajectory in Regime II for the case when $v > 0$ behind the shock.	111
2.46	Regime III for the flow behind the shock, left, and location of the relevant phase trajectories, right.	113
2.47	Detachment of the shock from the surface caused by a concave downstream wall (in this illustration $\kappa_+/\kappa_- = -\infty$).	114
2.48	Regime IV for the flow behind the shock, left, and location of the relevant phase trajectories, right.	115
2.49	Connection between the relative location of the shock, the ratio of wall curvatures and the downstream pressure gradient in Regimes III–VI for the flow behind the shock.	116
2.50	Regime V for the flow behind the shock, left, and location of the relevant phase trajectories, right.	117
2.51	Regime VI for the flow behind the shock, left, and location of the relevant phase trajectories, right.	118
2.52	Links between all the possible transonic flow regimes near a discontinuity in wall curvature.	119
2.53	A family of the curves representing the downstream pressure gradient as a function of the curvatures' ratio in the supercritical regime. The curves are plotted for different values of the supercritical upstream pressure gradient G_- ; wider curves correspond to larger values of G_-	120
2.54	Physical interpretation for different fragments of a typical supercritical curve describing the downstream pressure gradient.	121
2.55	The pressure gradients G_{\pm} plotted as functions of the curvatures' ratio for subcritical regimes (solid lines) and supercritical regimes (dashed lines). The non-uniqueness in the supercritical solution is due to an extra degree of freedom gained after passing through the limiting characteristic.	122

3.1	Curvilinear coordinates related to the body surface.	123
3.2	Singular pressure gradients lead to the typical two-tier structure of the boundary layer upstream of the singularity.	127
3.3	Velocity profiles in the overlapping region between tiers 2a and 2b for three characteristic values of λ , obtained in the assumption that the pressure gradient causes nonlinear velocity perturbations in the viscous sublayer 2b.	133
3.4	A typical three-tier structure of the interaction region.	152
3.5	Integration contour in the plane of complex ω	166
3.6	Transformation from the cartesian to the curvilinear coordinates. . .	174
3.7	Regions that had to be considered in order to derive the two integral equations linking F_* and G_*	190
3.8	Viscous-inviscid interaction is taking place on the scale $X \sim 1$ ($s \sim \text{Re}^{-3/10}$) in the innermost part of the interaction region.	193
3.9	Integration contours in the plane of complex ω depending on the sign of X in the inverse Fourier transform.	196
3.10	Pressure gradient distribution across the inner part of the interaction region (solid line). The dashed curves correspond to the singular pressure gradients predicted by the classical boundary layer theory.	198
3.11	Real and imaginary parts of the complex function $K_\omega = \varkappa(\omega) e^{i\theta(\omega)}$ plotted for all real values of ω	200
3.12	Function $J(X)$ describing the skin friction distribution across the innermost part of the interaction region, left, and its first derivative, right.	205
3.13	A typical confined recirculation zone (separation bubble) formed due to an adverse pressure gradient.	206

The University of Manchester

Dmitry Yumashev

Doctor of Philosophy

Viscous-Inviscid Interaction in a Transonic Flow

Caused by a Discontinuity in Wall Curvature

January 30, 2010

The work addresses an important question of whether a discontinuity in wall curvature can cause boundary layer separation at transonic speeds. Firstly an inviscid transonic flow in the vicinity of a curvature break is analyzed. Depending on the ratio of the curvatures, several physically different regimes can exist, including a special type of supersonic flows which decelerate to subsonic speeds without a shock wave, transonic Prandtl–Meyer flow and supersonic flows with a weak shock. It is shown that if the flow can be extended beyond the *limiting characteristic*, it subsequently develops a shock wave. As a consequence, a fundamental link between the local and the global flow patterns is observed in our problem. From an asymptotic analysis of the Karman–Guderley equation it follows that the curvature discontinuity leads to the singular pressure gradients $\partial p/\partial x \sim G_{\mp} (\mp x)^{-1/3}$ upstream and downstream of the break point, respectively. In order to find the amplitude coefficients G_{\mp} , computations are performed and both the *hodograph method* and the *phase portrait technique* are employed.

The focus is then turned to analyzing how the given pressure distribution affects the boundary layer. It is demonstrated that the singular pressure gradient proportional to $(-s)^{-1/3}$ corresponds to a special resonant case for the boundary layer upstream of the singularity. Consequently, the boundary layer approaches the interaction region in a *pre-separated form*. This changes the background on which the viscous-inviscid interaction develops, allowing to construct an asymptotic theory of the *incipient viscous-inviscid interaction* for our particular problem. The analysis of the interaction which takes place near a weak curvature discontinuity leads to a typical three-tier structure. It appears to be possible to obtain analytical solutions in all the tiers of the triple deck when the curvature break is small. As a result, the *interaction equation* may be derived in a closed form. The analytical solution of this equation reveals a local minimum in the *skin friction distribution*, suggesting that a *local recirculation zone* can develop near the curvature break. In fact, the recirculation zone is formed when the ratio of the curvatures satisfies

$$\frac{\varkappa_+}{\varkappa_-} = 1 - \frac{\hat{k}_0}{\ln \text{Re}} + \frac{\hat{k}_1}{(\ln \text{Re})^2} + \dots,$$

where $\text{Re} \gg 1$ is the flow's Reynolds number, \hat{k}_0 is a fixed positive order one quantity which depends on certain physical parameters of the flow, and \hat{k}_1 is an order one *controlling parameter* affecting the size of the recirculation zone. This discovery proves that a discontinuity in wall curvature does evoke boundary layer separation at transonic speeds. The result is fundamentally different from the effect of a curvature break at subsonic and supersonic speeds, as no separation takes place in these two regimes (Messiter & Hu 1975).

Declaration

No portion of the work referred to in this thesis has been submitted in support of an application for another degree or qualification of this or any other university or other institute of learning.

Copyright Statement

- i.** The author of this thesis (including any appendices and/or schedules to this thesis) owns any copyright in it (the “Copyright”) and s/he has given The University of Manchester the right to use such Copyright for any administrative, promotional, educational and/or teaching purposes.
- ii.** Copies of this thesis, either in full or in extracts, may be made **only** in accordance with the regulations of the John Rylands University Library of Manchester. Details of these regulations may be obtained from the Librarian. This page must form part of any such copies made.
- iii.** The ownership of any patents, designs, trade marks and any and all other intellectual property rights except for the Copyright (the “Intellectual Property Rights”) and any reproductions of copyright works, for example graphs and tables (“Reproductions”), which may be described in this thesis, may not be owned by the author and may be owned by third parties. Such Intellectual Property Rights and Reproductions cannot and must not be made available for use without the prior written permission of the owner(s) of the relevant Intellectual Property Rights and/or Reproductions.
- iv.** Further information on the conditions under which disclosure, publication and exploitation of this thesis, the Copyright and any Intellectual Property Rights and/or Reproductions described in it may take place is available from the Head of the School of Mathematics.

Acknowledgements

I would like to thank all the people who have been around me during these exciting years in Manchester for their company, inspiration, help and support. Special thanks go to the ORS Fund and the School of Mathematics for providing the funding which allowed me to come to the UK and undertake this research project. One could hardly underestimate the role of my parents, my grandmother and my former supervisor from the Moscow Institute of Physics and Technology, Alexander V. Fedorov, in persuading me to go abroad. This valuable experience of living in a different cultural environment and expressing thoughts and feelings in a different language will always mean a lot to me.

I would also like to acknowledge the contribution of my supervisor, Anatoly I. Ruban, in providing good scientific advice and, at times, a harsh criticism of my progress. Finally, it needs to be mentioned that it certainly would be impossible for me to work on the PhD without studying classical singing and actively participating in the musical life of Manchester at the same time. Huge thanks here go to Nataliya Kompaniyets for giving me singing lessons and encouraging to develop a career in music. A good progress in this area allowed me to successfully pass an audition for a postgraduate course in opera singing at the Royal Northern College of Music, and I am really looking forward to this new exciting chapter of my life.

Dedication

In loving memory of my mother, Yelena V. Yumasheva (1955 – 2009).

Chapter 1

Introduction

1.1 Asymptotic Theory of Separated Flows

One hundred years passed since the 3rd International Mathematics Congress in Heidelberg, 1904, where Prandtl presented his landmark paper on the *boundary layer theory*. In this paper an important idea was put forward which later became known as the principle of *singular perturbations*. Prandtl's boundary layer theory is applicable for the flows with a high Reynolds number, i.e. with a relatively small viscosity, which is the case for most liquid and gas flows observed in nature and encountered in engineering applications. The viscosity appears to be a small coefficient at the highest order derivatives in the Navier–Stokes equations governing the fluid motion. As a result, viscous forces are insignificant almost everywhere in the flow apart from a thin boundary layer near a rigid body surface where certain flow functions develop strong normal gradients.

Based on these ideas, Prandtl deduced the equations describing the fluid motion in the boundary layer. At the time he did not offer any solutions to these equations; instead, he speculated at length on the *separation phenomenon* (Prandtl 1904). This phenomenon is very common amongst all high Reynolds number flows, and has been observed experimentally on numerous occasions. According to Prandtl, the separation can be expected when the pressure starts to rise in the direction of the flow,

therefore causing the fluid in the boundary layer to decelerate. Should such a situation occur, the separation is going to take place at the point of zero skin friction. The latter may be located by solving the boundary layer equations.

Later, however, it was discovered that the boundary layer theory in its classical form, as given by Prandtl in 1904, leads to a certain mathematical contradiction. Landau & Lifshitz (1944) were the first to point out that a classical boundary layer exposed to a regular adverse pressure gradient develops a singularity as the point x_s of zero skin friction is approached. This was followed by the famous work of Goldstein (1948) who gave a detailed mathematical explanation of the singularity and showed that solutions of the boundary layer equations cannot be extended to the region downstream of x_s . Even though Goldstein's analysis clearly fails to describe the real situation in the vicinity of the boundary layer separation point, it has a great importance in attesting to the impossibility of unseparated flow to exist.

A key element of the separation process, which was not fully appreciated both in Prandtl's classical description and in Goldstein's work, is a mutual interaction between the boundary layer and external inviscid flow, termed the *viscous-inviscid interaction*. It is now known that a typical boundary layer separation takes place not as a result of a gradual growth of pressure in an inviscid flow over a curved body surface (leading to a regular adverse pressure gradient). Instead, it is caused by a sharp pressure rise developing 'spontaneously' due to the viscous-inviscid interaction at a certain location on the body surface where the boundary layer would still be well attached according to Prandtl's classical theory. This kind of a separation has, therefore, been classified as *self-induced*.

The asymptotic theory of the viscous-inviscid interaction, also known as the *triple-deck theory*, was formulated simultaneously by Neiland (1969) and Stewartson & Williams (1969) for the self-induced separation in a supersonic flow. In this case the spontaneous growth in the pressure is due to the formation of a compression wave in the external flow, a wave which in the limit transforms into a shock wave. After undergoing a rapid deceleration because of the rising pressure, the boundary layer separates from the surface along a free streamline and forms a mixing layer with a

recirculation zone behind. The study by Neiland, Stewartson and Williams led to the introduction of a three-tier structure around the point of separation composed of (i) the viscous near-wall sublayer, (ii) the main part of the boundary layer and (iii) the inviscid potential flow region outside the boundary layer.

The interaction process in the triple deck may be described as follows. In the viscous sublayer the fluid motion is relatively slow, and the lower deck exhibits high sensitivity to pressure variations. Even a small pressure rise in the direction of the flow may cause significant deceleration of fluid particles in the sublayer. As a result, the flow filaments become thicker and the streamlines are being displaced from the wall. The slope of the streamlines is then transmitted through the main part of the boundary layer to the potential flow in the upper deck, which converts the displacement into pressure perturbations. The latter are transmitted back to the lower deck and cause extra displacement in it. Therefore, there is mutual interaction between the two outer tiers of the triple deck, and the system adjusts itself until a certain ‘equilibrium’ pressure distribution across the interaction region is achieved. One of the main goals of every study related to boundary layer separation is to find this pressure distribution along with the relevant displacement and skin friction distributions.

The case of a self-induced separation in an incompressible fluid is more complicated because the problem of an incompressible flow around a body is of the elliptic nature and, therefore, is unable to provide the appropriate singular pressure distribution in the vicinity of the separation point. However, if one refers to the theory of ideal fluid flows with free streamlines, one may find that it contains a local solution with the necessary properties (Sychev 1972). In this case the singular pressure gradient

$$\frac{\partial p}{\partial x} \sim k(x_s - x)^{-1/2}$$

is generated upstream of the separation point x_s due to a singularity in local curvature of the free streamline emerging from a smooth surface of the body.¹⁾ According to Sychev (1972), the constant k depends on the Reynolds number of the flow and tends

¹⁾ Note that this streamline does not satisfy the so-called Brillouin–Villat condition of smooth separation.

to zero when $\text{Re} \rightarrow \infty$, being estimated as $k \sim \text{Re}^{-1/16}$.

In addition to the self-induced separation from a smooth rigid body surface, it has long been observed that various irregularities in the shape of a body contour can also lead to viscous-inviscid interaction and, in certain cases, to boundary layer separation. One of the classical examples is the *flow near the trailing edge of a flat plate*; the irregularity develops because the flow undergoes an abrupt change in the boundary condition when the solid surface ends, resulting in viscous-inviscid interaction. Stewartson (1969) and Messiter (1970) described this phenomenon for the case of an incompressible fluid flow by applying the triple deck model to the interaction region.

The most obvious surface irregularities that can cause boundary layer separation include *corner points*,²⁾ *discontinuities in wall curvature* (Messiter & Hu 1975), *humps* (Smith 1973), etc. In all of the above examples an inviscid flow around the body contour develops singular pressure gradients which lead to a breakdown in the classical boundary layer theory. This situation clearly indicates that the viscous-inviscid interaction starts to take place once the irregularity is approached. The interaction acts towards smoothening of the pressure distribution and ultimately enables to obtain continuous solutions for all physical functions of the flow near the irregularity. In contrast to the self-induced separation, the nature of the interaction process appears to be predetermined by the exact type of the surface irregularity.

This year marks the 40th anniversary of the asymptotic theory of separated flows. Since first landmark papers on the subject were published in 1969, many researchers have been involved in the development of the theory, and it is now clear that the viscous-inviscid interaction plays a key role in a wide variety of separation phenomena. Most notably, the triple deck theory has been extended to describe the boundary layer separation from a smooth body surface in an incompressible fluid flow, supersonic flow separation provoked by a shock wave impinging upon the boundary layer, incipient and large scale separations at corner points of the body contour both in subsonic and

²⁾ Separation at corners was studied by Ackerberg (1970), Stewartson (1970), Ruban (1974) for an incompressible fluid and by Neiland (1974) for supersonic flows.

supersonic flows, separation at a trailing edge of a thin airfoil, leading-edge separation, separation of the boundary layer in a hypersonic flow on a hot or cold wall, separation caused by a wall roughness, etc. A detailed account of the fundamentals of the theory and a complete set of references to the now classic papers in this field may be found in the monograph by Sychev, Ruban, Sychev & Korolev (1998).

1.2 Viscous-Inviscid Interaction in Transonic Flows

Despite the significance of the progress made in the asymptotic theory of separated flows since it was established in the late 1960s, a lot of important questions still remain unanswered. Historically the application of the theory has been focused on describing separation at either subsonic or supersonic speeds, but very little is still known about separation of transonic flows. The reason behind this is that the equations of the transonic small perturbation theory, referred to as Karman–Guderley equations, are nonlinear (Cole & Cook 1986), whereas the corresponding sub- and supersonic equations are linear. The latter may be solved to give the so-called *interaction law* in a closed form, which allows to calculate the pressure generated by the inviscid flow in response to the displacement effect of the boundary layer.³⁾

The majority of the studies related to transonic viscous-inviscid interaction has been based on certain simplifications, needed to leave out the nonlinearity in the Karman–Guderley equations.⁴⁾ For example, in the series of works by Bodonyi & Kluwick describing transonic interaction near the trailing edge of a flat plate, the free stream flow was assumed to be supersonic and uniform, leading to a simple analytical solution in the upper tier of the triple deck in the form of a wave integral. These restrictions were removed when Bodonyi & Kluwick (1998) applied a special numerical algorithm of solving Karman–Guderley equations (Cole & Cook 1986).

With the aid of the refined numerical methods, Ruban & Turkyilmaz (2000)

³⁾ For subsonic flows the interaction law is expressed by Cauchy’s integral of the thin aerofoil theory. In supersonic flows it has a much simpler form, being given by the Ackeret formula which establishes a simple local relationship between the streamline slope and the induced pressure.

⁴⁾ See Buldakov & Ruban (2002) for a detailed review.

considered transonic version of the classical problem of a flow near the corner point. Their analysis showed that as the interaction region is approached, the pressure gradient generated by the inviscid transonic flow develops the singularity

$$\frac{\partial p}{\partial x} \sim -(-x)^{-2/3},$$

where the coordinate x is measured from the corner point in the downstream direction. This gradient appears to be strong enough to cause a complete re-structuring of the boundary layer upstream of the interaction region. As a result, the displacement effect of the boundary layer turns out to be mainly due to its inviscid part rather than the viscous sublayer. Contrary to what happens in the subsonic (Ruban 1974) and supersonic (Neiland 1974) analogues of the problem, the transonic flow in the interaction region is governed by a physically different mechanism involving the two upper tiers of the triple deck, which may be called the *inviscid-inviscid interaction*.

This example clearly demonstrates that transonic viscous-inviscid interaction gains its unique features not just through the upper tier of the triple deck where the nonlinear Karman–Guderley equations replace the simple subsonic and supersonic interactive laws. More importantly, the inviscid transonic flow upstream of the interaction region proves to be capable of producing strong variations in the internal structure of the boundary layer approaching the triple deck (such variations will be referred to as the *cumulative effects*). The latter might cause drastic changes in the physical background on which the interaction between the boundary layer and the outer inviscid flow develops, leading to fundamentally different mechanisms of separation as compared to similar sub- and supersonic cases. It turns out that the same situation takes place in the problem considered in the present work (see Chapter 3).

After the work by Ruban & Turkyilmaz (2000) revealed the importance of structural variations in the boundary layer upstream of the transonic interaction region, Buldakov & Ruban (2002) discovered similar effects in the viscous-inviscid interaction caused by a *sonic point* on the surface of a smooth rigid body. They investigated the properties of local self-similar flows near the sonic point in the cases of (i) the *local separation*, when the recirculation zone (forming as a result of the boundary layer

separation) is confined within the dimensions of the interaction region, and (ii) the *global separation*, when a free streamline emerges from the body surface, resulting in a semi-infinite separation region on the scale of the interaction region.⁵⁾ In order to describe local transonic flow close to the sonic point, the authors used standard self-similar expansions of the transonic small perturbations theory (see equations (2.4), (2.5) from section 2.1.1 for details). It was found that for a certain value of the similarity parameter α from the self-similar expansion (2.4), namely $\alpha = \frac{3}{2}$, the boundary layer upstream of the interaction region is exposed to the singular pressure gradient

$$\frac{\partial p}{\partial x} \sim (-x)^{-1/3}, \quad (1.1)$$

where the coordinate x is measured from the sonic point in the downstream direction. According to Buldakov & Ruban (2002), this pressure distribution is responsible for specific cumulative effects in the boundary layer ahead of the singularity, and therefore it affects the background on which the interaction is taking place. It needs to be emphasized that the value $\alpha = \frac{3}{2}$ was considered by the authors mainly because it allowed to obtain solutions with local separation zones. However, from the viewpoint of the inviscid flow outside the interaction region the reasoning behind their choice of this particular value of α is not very convincing. One of the aims of the present work is to address this problem by providing an example of a physical phenomenon which leads to the pressure gradient (1.1) purely from the nature of the potential transonic flow.

Numerical computations of the transonic interaction problem performed by Buldakov & Ruban (2002) involved solving the Karman–Guderley equations in the upper tier of the interaction region, with the upstream pressure distribution given by (1.1). Their results showed the presence of a recirculation zone formed in the interaction region with the longitudinal scale

$$\Delta x \sim \text{Re}^{-3/10} (\ln \text{Re})^{-21/20},$$

⁵⁾ These two physical situations lead to different downstream boundary conditions for the potential transonic flow immediately outside the interaction region, and this affects the pressure distribution acting on the boundary layer.

providing the amplitude of the singular pressure gradient is logarithmically small with respect to Reynolds number:

$$\frac{\partial p}{\partial x} \sim \frac{1}{\ln \text{Re}} (-x)^{-1/3}.$$

The actual extent of the separation region was found to be controlled by a pair of free parameters, the first one being the location of the shock which develops in the outer inviscid flow, and the second one being related to the structure of the pre-separated boundary layer upstream of the interaction region. Both of these two parameters can only be obtained from the global problem of the transonic flow on the scale of the entire body length. The skin friction upstream of the interaction region displayed a characteristic logarithmic decay responsible for an unusual behaviour of the flow inside the interaction region. Moreover, the solution in the interaction region appeared to be non-unique, revealing a hysteresis nature of the transonic separation.

Despite the significance of the above results, not much has been done in this area during the last few years. Most recently, Ruban, Wu & Pereira (2006) considered the viscous-inviscid interaction in transonic Prandtl–Meyer flow. They found that for the local shape of the body contour given by

$$y_w(x) = \begin{cases} 0, & x < 0 \\ cx^{8/5}, & x > 0 \end{cases}$$

the inviscid transonic flow develops a typical expansion fan when the parameter c is negative. As a result, the boundary layer upstream of the interaction region is exposed to the singular pressure gradient

$$\frac{\partial p}{\partial x} \sim (-x)^{-3/5}. \quad (1.2)$$

Remarkably, in this case the displacement is mostly generated in the overlapping region between the viscous sublayer and the main part of the boundary layer, therefore providing yet another example of how the inviscid transonic flow may cause drastic changes in the structure of the boundary layer ahead of the interaction region. As already mentioned before, the restructuring of the boundary layer affects the background on which the interaction develops, and is responsible for the unique nature of separation at transonic speeds.

Nevertheless, it remains unclear whether the fundamental difference between transonic separation and subsonic/supersonic separation appears in other basic cases. In this respect it is worth comparing the effect of a discontinuity in wall curvature on subsonic, transonic and supersonic flows. While the more familiar corner points do affect the flow by causing separation at all speeds, does the curvature break have similar effects?

Messiter & Hu (1975) considered a flow near the joint between a curved and a flat walls, both in subsonic and supersonic regimes. If the wall downstream of the joint is flat, the discontinuity in wall curvature generates an adverse pressure gradient which has logarithmic singularity in the subsonic case and is discontinuous in the supersonic case. As a result, the classical boundary layer theory fails in a small vicinity of the joint, and the flow has to be described by taking viscous-inviscid interaction into the account. The analysis performed by Messiter & Hu shows that the interaction smoothes the singularity in the pressure gradient, producing a continuous skin friction distribution with no separation zones. However, when the flow near a discontinuity in wall curvature is transonic, the situation may change significantly. The main goal of this work is to find out whether the curvature break is capable of causing separation at transonic speeds. If the separation does take place, this would once again demonstrate the originality of transonic separation phenomena.

1.3 Brief Review of The Work

The thesis consists of two main chapters. Because of the well known hierarchical strategy applied to high Reynolds number flows in the classical boundary layer theory, we first of all consider an inviscid transonic flow in a small vicinity of the curvature break (Chapter 2). The local analysis reveals a complicated pattern depending on the ratio of the curvatures before and after the break. It is assumed that the *sonic point* coincides with the curvature discontinuity, simply to ensure that the flow around it is transonic, and that the separation is local (i.e., the separation zone is confined within the small interaction region around the curvature break, as opposed to the

global separation characterized by a free streamline with a semi-infinite separation zone behind it). In this case the irregularity in the shape of the surface leads to the singular pressure gradients $\partial p/\partial x \sim G_{\mp} (\mp x)^{-1/3}$ upstream and downstream of the break respectively, which follows from an asymptotic analysis of the Karman–Guderley equations.⁶⁾ In order to obtain the amplitude coefficients G_{\mp} (and their signs in particular), we perform computations and also employ the *hodograph method* to interpret the numerical results.

Even though the analysis of the inviscid flow in Chapter 2 is just the first step in the study of the boundary layer separation, it has an importance of its own. The earliest results in the classical theory of transonic flows date back to the beginning of the 20th century, and underwent a rapid development in early 1950s, largely due to the works of Frankl and Guderley. A summary of the main theoretical results in this area and the key references may be found in the monograph by Cole & Cook (1986). Guderley (1957) introduced an important technique of analyzing the singular points of the nonlinear Karman–Guderley equations by considering the so-called *phase portrait* of a transonic flow. Combined with the *hodograph method* introduced by Chaplygin (1902) in his famous study of compressible jets, this technique provides a powerful tool for investigating various special cases, for example a *transonic far-field flow*. It turns out that our particular problem of an inviscid transonic flow close to a discontinuity in wall curvature provides a good example of how the two methods can work together.

One of the central concepts of transonic aerodynamics is the *limiting characteristic*. It appears to be an important boundary between physically different regions of transonic flow with respect to a propagation of small perturbations.⁷⁾ Thanks to this property, certain low-speed supersonic flows which have not passed through the limiting characteristic can actually be decelerated to subsonic speeds without forming a *shock wave*. However, once a flow has passed through the limiting characteristic, it can only be decelerated to subsonic speeds by going through a shock. In Chapter 2 we

⁶⁾ It appears that this type of the singular pressure gradient is due to both the curvature break and the sonic point, and not just to the sonic point as suggested previously by Buldakov & Ruban (2002).

⁷⁾ See Liepmann & Roshko (1957), Landau & Lifshitz (1959) and Cole & Cook (1986).

apply the combination of the hodograph method and the phase portrait technique to prove this important result analytically for our specific type of the flow. The analysis also sheds light on the link between the local and the global flow patterns. Even though the phase portrait of the flow appears to be identical to the one obtained by Buldakov & Ruban (2002), our study goes one step further and provides a detailed explanation of all possible flow regimes depending on the ratio of the curvatures.

The effect of the singular pressure gradients on a thin boundary layer which is formed near the wall is discussed in Chapter 3. This is essential for addressing the main question of the work: whether the curvature break is capable of causing flow separation at transonic speeds or not. It turns out that the pressure gradient proportional to $(-s)^{-1/3}$ corresponds to a special resonant case for the boundary layer upstream of the singularity, in agreement with Buldakov & Ruban (2002).⁸⁾ Consequently, the boundary layer approaches the interaction region in a *pre-separated form*, and this affects the background on which the viscous-inviscid interaction develops. The relevant asymptotic solution of the boundary layer equations is obtained by introducing logarithms along with powers of $(-s)$ into the coordinate expansions upstream of the singular point. However, such a solution is real only for a favourable pressure gradient, i.e. for the case of $G_- < 0$, and becomes complex when G_- changes sign to positive, suggesting that the adverse pressure gradient causes separation well ahead of the curvature break. This important result was not mentioned in the study by Buldakov & Ruban (2002).

Since there should always be a smooth transition between different flow regimes, we consider the case of small positive values of G_- encountered when the curvature break is also small (i.e. the ratio of the curvatures is close to 1). This opens up the way to constructing an asymptotic theory of the *incipient viscous-inviscid interaction* in our particular problem. The small but singular pressure gradient upstream of the curvature break still generates a sufficient displacement in the boundary layer which leads to a failure of the classical boundary layer theory. As mentioned in the previous sections, in this kind of a situation one needs to take into account the interaction

⁸⁾ Here s is the curvilinear coordinate measured along the surface from the curvature break.

taking place between the boundary layer and the outer inviscid flow close to the singularity. This leads to a standard three-tier structure of the flow traditionally called the *triple deck*, or simply the *interaction region*.

It appears to be possible to construct analytical solutions in all the tiers of the triple deck when

$$\text{Re}^{-1/6} \ll |G_-| \ll \frac{1}{\ln \text{Re}}, \quad \text{Re} \rightarrow \infty.$$

As a result, the *interaction equation*, describing how the pressure perturbations are converted into the displacement and vice versa, may be derived in a closed form. Remarkably, in this case the displacement proves to be generated mainly in the overlapping region between the viscous sublayer and the main inviscid part of the boundary layer. At the same time the flow in all three tiers of the triple deck has predominantly subsonic features, and the transonic nature of the viscous-inviscid interaction is largely due to certain cumulative effects in the boundary layer upstream of the singularity. The interaction is taking place on the longitudinal spacial scale

$$|s| \sim \text{Re}^{-3/10}$$

which does not depend on G_- (and hence on the ratio of the curvatures).

The analytical solution of the interaction equation reveals a local minimum in the skin friction distribution near the curvature break, indicating that a *local recirculation zone* (also called a *separation bubble*) may develop for stronger discontinuities in wall curvature. In fact, the recirculation zone is formed when the ratio of the curvatures is estimated as

$$\frac{\varkappa_+}{\varkappa_-} = 1 - \frac{\hat{k}_0}{\ln \text{Re}} + \frac{\hat{k}_1}{(\ln \text{Re})^2} + \dots,$$

where \hat{k}_0 is a fixed positive order one quantity depending on certain physical parameters of the flow, and \hat{k}_1 is an order one *controlling parameter* which affects the size of the separation bubble.

Chapter 2

Inviscid Transonic Flow Near a Curvature Discontinuity

2.1 Problem Formulation

2.1.1 Governing equations and boundary conditions

Consider a 2D inviscid transonic flow of a perfect gas near a point of a discontinuity in wall curvature, Fig. 2.1. The local surface shape close to a curvature break may be expressed in the following way:

$$\hat{y}_w(\hat{x}) = -\frac{\hat{\kappa}_{\pm}\hat{x}^2}{2} + \dots, \quad \hat{x} \gtrless 0,$$

where the hat denotes dimensional variables, $\hat{\kappa}_{\pm}$ stand for the wall curvatures, and

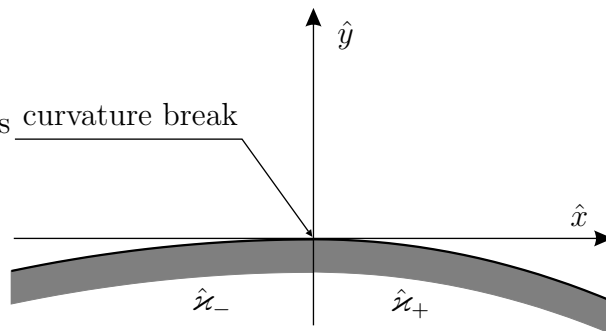


Figure 2.1: Inviscid flow near a discontinuity in wall curvature.

the dots represent higher-order terms in the coordinate expansions. According to our definition, $\hat{\kappa}_{\pm} > 0$ for convex walls. The cartesian coordinates \hat{x} , \hat{y} can be scaled using either of the curvature radii $\hat{\kappa}_{\pm}^{-1}$. Hence, if we take $L = \hat{\kappa}_{-}^{-1}$ as a scale, the body surface will be given by

$$y_w(x) = \begin{cases} -\frac{x^2}{2}, & x < 0, \\ -\left(\frac{\hat{\kappa}_+}{\hat{\kappa}_-}\right) \frac{x^2}{2}, & x > 0 \end{cases}$$

in the scaled dimensionless variables, showing that the behavior of the flow is likely to depend only upon the curvatures' ratio $\hat{\kappa}_+/\hat{\kappa}_-$. However, we are not going to specify the scale since the local inviscid problem considered in this chapter appears to be invariant with respect to re-scaling of spatial coordinates.¹⁾ Furthermore, the scaled curvatures $\kappa_{\pm} = L \hat{\kappa}_{\pm}$ will be used henceforth, because they provide the same curvatures' ratio.

To make sure the flow near the curvature discontinuity is transonic, let us assume that the point $(x, y) = (0, 0)$ where the curvature breaks is also a *sonic point*. We are going to use the velocity at this point, which is by definition equal to the local speed of sound \hat{a}_* , for scaling the velocity components and the speed of sound. Should the sonic point move towards either side of the curvature break, this would imply that the flow around the break has either subsonic or supersonic features, and a boundary layer separation is unlikely to happen (Messiter & Hu 1975). The main goal of the present work, however, is to study a possibility of a transonic flow separation due to the curvature discontinuity, and this justifies our assumption regarding the sonic point location.

Since the flow is inviscid, it also has to be adiabatic (isoentropic). By assuming that the oncoming flow is isoenthalpic, we convert the Euler equations to the system

¹⁾ The problem in the interaction region, discussed in Chapter 3, depends on the spatial scale through the definition of the Reynolds number.

containing only the velocity components U , V and the local speed of sound a :

$$\begin{cases} (a^2 - U^2) \frac{\partial U}{\partial x} + (a^2 - V^2) \frac{\partial V}{\partial y} = UV \left(\frac{\partial U}{\partial y} + \frac{\partial V}{\partial x} \right), \\ \frac{U^2 + V^2}{2} + \frac{a^2}{\gamma - 1} = \frac{\gamma + 1}{2(\gamma - 1)}, \end{cases} \quad (2.1)$$

where γ is the specific heat ratio.²⁾ A further assumption of the flow's isentropy leaves us with potential flows only (due to the 2D Crocco equation linking entropy gradient with vorticity). In this case the velocity components may be expressed through the potential function $\Phi(x, y)$:

$$U = \frac{\partial \Phi}{\partial x}, \quad V = \frac{\partial \Phi}{\partial y}.$$

System (2.1) is solved subject to the impermeability boundary condition upstream and downstream of the curvature discontinuity:

$$\frac{V}{U} \Big|_{y=y_w} = \frac{dy_w}{dx} = -\kappa_{\pm} x, \quad x \gtrless 0. \quad (2.2)$$

The downstream condition is written in the assumption that the separation zone is local, being confined within the interaction region (see Chapter 3).³⁾

2.1.2 Asymptotic expansions for local self-similar solutions

Boundary condition (2.2) may be transferred to the $y = 0$ axis in the leading order of approximation, providing $|\kappa_{\pm} x| \ll 1$ (a small vicinity of the curvature break point as compared to the body scale determined by the curvature radii):

$$V \Big|_{y=0, x \gtrless 0} = -\kappa_{\pm} x. \quad (2.3)$$

This automatically restricts our attention to the upper half-plane, $y \gtrless 0$. As we move closer to the origin, no length scale can be assigned to the problem and the Euler equations are expected to admit self-similar solutions (Cole & Cook 1986); the scaled coordinates (x, y) can be used as small parameters to construct asymptotic expansions in this local region around the discontinuity in wall curvature. Our intention to

²⁾ System (2.1) is written using the dimensionless variables.

³⁾ Note that in a small vicinity of the sonic point $U = 1$ in the leading order.

consider the local behaviour of the inviscid flow is based on the knowledge that typical flow separation phenomena are also local (Sychev et al. 1998).

The fact that $y \geq 0$ in the problem described by (2.1), (2.3) allows to introduce the similarity variable

$$\xi = \frac{x}{y^\alpha},$$

where α is an unknown parameter which is to be determined. The relevant asymptotic expansion of the velocity potential near the sonic point may be written in the form

$$\Phi(x, y) = x + y^\sigma \frac{F(\xi)}{\gamma + 1} + \dots, \quad \sigma = \sigma(\alpha), \quad y \rightarrow 0, \quad \xi = \mathcal{O}(1). \quad (2.4)$$

The first term here corresponds to the main unperturbed flow with $U = 1$, $V = 0$ at the sonic point, whereas the second term represents the leading-order perturbation, with the function $F(\xi)$ being an order one quantity for $\xi = \mathcal{O}(1)$. Substituting this expansion into (2.1) and using the principle of least degeneration results in the following ordinary differential equation (Frankl 1947):

$$[(\alpha\xi)^2 - F']F'' - 5\alpha(\alpha - 1)\xi F' + 3(3\alpha - 2)(\alpha - 1)F = 0, \quad (2.5)$$

and shows that α and σ are related as

$$\sigma = 3\alpha - 2.$$

It can be easily demonstrated that expression (2.4) is, indeed, an asymptotic expansion for $y \rightarrow 0$ as long as $\alpha > 1$ and, consequently, $\sigma > 1$. A more strict argument leading to the introduction of the similarity variable $\xi = x/y^\alpha$ (and the relevant asymptotic form (2.4) with $\sigma = 3\alpha - 2$) in order to describe the local flow is based on *group theory* (Cole & Cook 1986).

All the terms in equation (2.5) correspond only to the left-hand side of the first equation in (2.1), with the right-hand side being of a smaller order of magnitude. Equation (2.5) is nonlinear and has a singular point where the coefficient $(\alpha\xi)^2 - F'$ in front of F'' turns zero. The singular point corresponds to the so-called *limiting characteristic* in the flow (Guderley 1957); upon passing through this characteristic, the flow becomes significantly supersonic and cannot be decelerated without a shock

formation. It is well known that the limiting characteristic is different from the sonic line on which the local Mach number $M = 1$ (Cole & Cook 1986). The flow that has already passed through the sonic line but has not yet reached the limiting characteristic is formally supersonic; however, it may still be decelerated without a shock to become subsonic.⁴⁾

From now on, we shall employ the notations u , v for the leading-order velocity perturbations:

$$\begin{aligned} u &= (\gamma + 1)(U - 1) = (\gamma + 1) \left(\frac{\partial \Phi}{\partial x} - 1 \right) = y^{2\alpha-2} F'(\xi), \\ v &= (\gamma + 1)V = (\gamma + 1) \frac{\partial \Phi}{\partial y} = y^{3\alpha-3} [(3\alpha - 2)F - \alpha \xi F']. \end{aligned} \quad (2.6)$$

Since $y = 0$ corresponds to $\xi = \pm\infty$ depending on the sign of x , boundary condition (2.3) reduces to

$$\alpha [\lambda F - \xi F'] \Big|_{\xi \rightarrow \pm\infty} \sim -(\gamma + 1) \varkappa_{\pm} \left(\frac{x}{y^{3\alpha-3}} \right) \Big|_{y \rightarrow 0}, \quad x \gtrless 0, \quad (2.7)$$

where $\lambda = \frac{\sigma}{\alpha} = 3 - \frac{2}{\alpha}$. It is easily seen from (2.7) that α has to satisfy the constraint $3\alpha - 3 = \alpha$, yielding

$$\alpha = \frac{3}{2}, \quad \lambda = \frac{5}{3}.$$

Hence, boundary condition (2.7) for F is finally written in the form

$$\lim_{\xi \rightarrow \pm\infty} \left[\frac{\lambda F}{\xi} - F' \right] = -\frac{(\gamma + 1) \varkappa_{\pm}}{\alpha}, \quad x \gtrless 0. \quad (2.8)$$

Equation (2.5) with boundary condition (2.8) define a boundary-value problem for the potential function $F(\xi)$, which can be either solved numerically or studied analytically. In the subsequent sections of Chapter 2 we shall solve the problem numerically first and compute the so-called *phase portrait* of the flow (Guderley 1957); the latter is essential in understanding the flow's behavior for different values of \varkappa_+/\varkappa_- . This will be followed by a theoretical explanation of the numerical results using the *hodograph method* (Chaplygin 1902), based on self-similar solutions of the Triкоми equations.

⁴⁾ This is one of the main results of the first part of the thesis, and it is essential for the subsequent analysis of the boundary layer separation. See section (2.4.7) for details.

Our ultimate goal is to find pressure gradients on both upstream and downstream walls as functions of the curvatures' ratio, and to investigate a possibility of a boundary layer separation near the curvature discontinuity. In the subsequent sections it will be shown that the pressure gradients can be obtained from a simple algebraic system of equations containing \varkappa_+/\varkappa_- as a parameter.

The wall pressure gradients are closely related to the asymptotic behavior of $F(\xi)$ at $\xi \rightarrow \pm\infty$; the latter can be easily derived from equation (2.5) to be

$$F(\xi) = C_{\pm}(\pm\xi)^{3-\frac{2}{\alpha}} + D_{\pm}(\pm\xi)^{3-\frac{3}{\alpha}} + \mathcal{O}\left((\pm\xi)^{3-\frac{4}{\alpha}}\right), \quad \xi \rightarrow \pm\infty,$$

where C_{\pm} and D_{\pm} are constants. Since $\alpha = \frac{3}{2}$, the general expression takes the form

$$F(\xi) = C_{\pm}(\pm\xi)^{\lambda} \pm D_{\pm}\xi + \dots, \quad \xi \rightarrow \pm\infty, \quad \lambda = \frac{5}{3}. \quad (2.9)$$

Substituting this into boundary condition (2.8), we get

$$D_{\pm} = \mp(\gamma + 1)\varkappa_{\pm},$$

which means that the second term of the asymptotic form (2.9) is directly related to the impermeability condition on the wall. The first term, on the other hand, describes the pressure distribution on the wall. Indeed, the scaled pressure perturbation

$$p = \frac{\hat{p} - \hat{p}_*}{\hat{\rho}_* \hat{a}_*^2}$$

can be expressed in terms of $F(\xi)$ using the Bernoulli equation:

$$p = -y^{2(\alpha-1)}F' + \dots \sim -u; \quad (2.10)$$

\hat{p}_* and $\hat{\rho}_*$ stand for the pressure and the density at the sonic point. Plugging (2.9) into (2.10) and setting $y = 0$ yields:

$$\left. \frac{\partial p}{\partial x} \right|_{\xi \rightarrow \pm\infty} = -C_{\pm} \frac{2\lambda(\alpha-1)}{\alpha} (\pm x)^{1-\frac{2}{\alpha}}, \quad x \geq 0.$$

For the case of $\alpha = \frac{3}{2}$ the gradient develops a singular behavior of $(\pm x)^{-\frac{1}{3}}$ as long as $C_{\pm} \neq 0$. Therefore, we need to find the relationship between C_{\pm} and \varkappa_+/\varkappa_- , and then see whether a boundary layer separation takes place in these conditions or not.

Finally, it is worth deriving a formula for the local Mach number in terms of $F(\xi)$, based on the second equation from (2.1) and on the self-similar expansions (2.6) for U, V near the sonic point:

$$M = \frac{\sqrt{U^2 + V^2}}{a} = 1 + \frac{1}{2} y^{2(\alpha-1)} F' + \dots \quad (2.11)$$

2.2 Phase Portrait

In this section we are going to introduce the concept of a *phase portrait*, widely used in the theory of transonic flows (Guderley 1957). Even though the phase portrait analysis is considered to be quite well established and has been expounded in various works (see, for example, Cole & Cook (1986) and Ruban et al. (2006)), we find it necessary to give a detailed explanation of it in this thesis. The reason is that the concepts and the techniques introduced while describing the phase portrait will be used throughout the whole work.

2.2.1 Invariant transformations

Let us start from the obvious fact: the self-similar boundary-value problem for $F(\xi)$ described by equation (2.5) and boundary conditions (2.8) has to be invariant with respect to a change in the scaling of the spatial coordinates x and y . The re-scaling leads to the following group transformation:

$$x = B\bar{x}, \quad y = B\bar{y}, \quad (2.12)$$

where $B > 0$ is a “stretch” coefficient, and the bar denotes transformed variables. Since $\alpha > 1$ in the definition of the self-similar variable ξ , transformation (2.12) results in its stretching:

$$\xi = \frac{x}{y^\alpha} = B^{1-\alpha} \frac{\bar{x}}{\bar{y}^\alpha} \equiv A\bar{\xi},$$

with $A = B^{1-\alpha}$ being a new deformation coefficient.

It is easy to notice further that the main equation (2.5) admits the invariant group transformation

$$\xi = A\bar{\xi}, \quad F = A^3\bar{F}. \quad (2.13)$$

We now need to show that boundary conditions (2.8) are also invariant with respect to this transformation. Indeed, the change of the spatial scale described by (2.12) means that dimensionless curvatures undergo the transformation

$$\kappa_\pm = B^{-1}\bar{\kappa}_\pm. \quad (2.14)$$

Plugging (2.13), (2.14) into (2.8) yields

$$\alpha A^2 \left[\frac{\lambda \bar{F}}{\bar{\xi}} - \frac{d\bar{F}}{d\bar{\xi}} \right] \Big|_{\bar{\xi} \rightarrow \pm\infty} = -\frac{1}{B} (\gamma + 1) \bar{x}_{\pm},$$

and from the relationship between A and B it follows that the boundary conditions are invariant when $\alpha = \frac{3}{2}$.

In order to make the solution independent on a choice of the group constant A , we shall introduce two new functions of ξ proportional to the velocity perturbations u, v :⁵⁾

$$\begin{aligned} f(\xi) &= \frac{F'}{\alpha^2 \xi^2} \equiv \frac{(u/y)}{\alpha^2 \xi^2}, \\ g(\xi) &= \frac{\lambda F - \xi F'}{\alpha^2 \xi^3} \equiv \frac{(v/x)}{\alpha^3 \xi^2}. \end{aligned} \tag{2.15}$$

Introducing a new independent variable χ through

$$d\chi = \frac{d\xi}{(f-1)\alpha\xi}, \tag{2.16}$$

one can easily convert equation (2.5) to the following non-singular autonomous system:

$$\begin{cases} \frac{df}{d\chi} = 2f + 3(\alpha - 1)g - 2\alpha f^2, \\ \frac{dg}{d\chi} = 3g + 2(\alpha - 1)f^2 - 3\alpha fg. \end{cases} \tag{2.17}$$

Now each solution of equation (2.5) may be treated as a phase trajectory in the (f, g) plane, as shown in Fig. 2.2. Each such trajectory represents a family of solutions for all possible values of A , i.e. is invariant with respect to coordinate transformation (2.12), and runs in a certain direction as ξ is changing from $-\infty$ to ∞ . However, few difficulties arise immediately.

First of all, transformation (2.16) of the independent variable has two singular points:

$$\xi = 0, \quad f = 1,$$

and passing through either of them alters the direction of changing of χ with respect to the old variable ξ (the latter is increasing monotonely from $-\infty$ to $+\infty$). Hence, the phase plane should have several sheets, with different parts of the trajectory running

⁵⁾ Defined in (2.6), u and v are also invariant with respect to transformation (2.12).

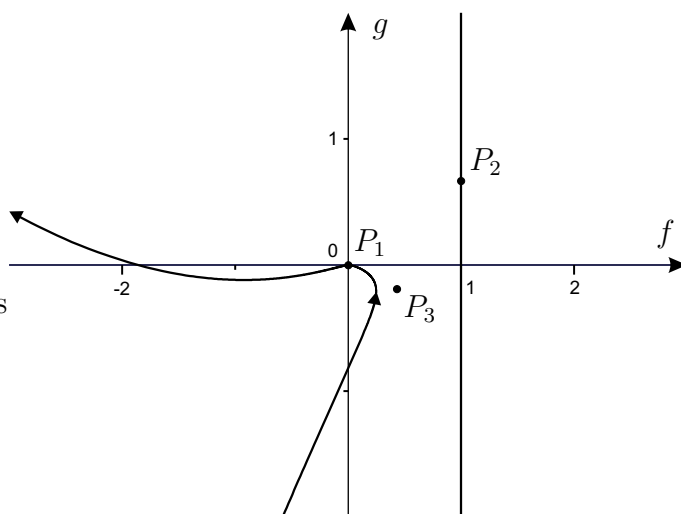


Figure 2.2: A typical phase trajectory in the (f, g) plane, with P_1 , P_2 and P_3 being the stationary points of equations (2.17).

on different sheets according to (2.16).⁶⁾ Since $F(0)$ and $F'(0)$ are not equal to zero in most of the cases, typical phase trajectories stretch to infinity when $\xi \rightarrow 0$ and, in addition to moving onto a new sheet of the phase plane, undergo reflection in the $g = 0$ axis as ξ changes sign. The latter immediately follows from expression (2.15) for the phase variables. The line $f = 1$ (see Fig. 2.2) needs a particular attention. It corresponds to the singular point $F' = \alpha^2 \xi^2$ of equation (2.5), and therefore will be called the *singular line*. Later we shall prove that phase trajectories are only able to pass through the singular line at the point with coordinates $(f, g) = (1, \frac{2}{3})$; the relevant value ξ_c of variable ξ defines the so-called *limiting characteristic* in the physical plane. This characteristic is important because it forms a boundary between two physically different regions, and will be examined comprehensively in section 2.2.2.

Secondly, equations (2.17) are strongly nonlinear and cannot be integrated analytically for the case of $\alpha = \frac{3}{2}$; in this formulation the problem may only be solved numerically. Nevertheless, analyzing *stationary points* of system (2.17) provides an insight regarding several important properties of the transonic flow.

⁶⁾ Note that we are going to plot all the fragments of a single curve (running on different sheets) on the same graph; for example, this was done in Fig. 2.2.

2.2.2 Stationary points of equations (2.17)

Equations (2.17) have three stationary points, where their right-hand sides simultaneously become equal to zero (Guderley 1957). They are $P_1 = (0, 0)$, $P_2 = (1, \frac{2}{3})$ and $P_3 = (\frac{1}{\alpha^2}, -\frac{2}{3\alpha^3})$, as shown in Fig. 2.2.⁷⁾ Let us examine these points one after another, linearizing (2.17) near each point.

1) $P_1 = (0, 0)$. The linearized equations are

$$\begin{cases} \frac{df}{d\chi} = 2f + 3(\alpha - 1)g, \\ \frac{dg}{d\chi} = 3g, \end{cases} \quad (2.18)$$

$|f|, |g| \ll 1$. This system has a pair of positive eigenvalues $\lambda_1 = 2$ and $\lambda_2 = 3$, yielding the local solution

$$f = C |g|^{2/3} + 3(\alpha - 1)g, \quad C = \text{const.}$$

Hence, P_1 is a node with half lines $g = 0$ and $g = \frac{1}{3(\alpha-1)} f$ (the latter becomes $g = \frac{2}{3} f$ when $\alpha = \frac{3}{2}$).

Being the origin in the phase plane, point P_1 corresponds to both the upstream and downstream walls ($\xi \rightarrow \mp\infty$), which can be seen from definition (2.15) of the phase variables and asymptotic form (2.9) of $F(\xi)$. Therefore, the trajectories start from the origin when $\xi = -\infty$ and return to it when $\xi = \infty$. Depending on the sign of f , the flow in the vicinity of the wall can be either subsonic or supersonic. In the limiting cases $C = \infty$ and $C = 0$ the trajectories follow the first and the second half line, respectively. In all other cases $f \sim |g|^{2/3}$ in the leading order, which means that specifying the first two terms of the asymptotic form (2.9) (related to the near-wall pressure gradient and the wall curvature) is equivalent to setting the constant

$$C = \lim_{\xi \rightarrow \pm\infty} \left(\frac{f}{|g|^{2/3}} \right).$$

This result will be used in section 2.4.3 to obtain boundary conditions in the hodograph plane.

⁷⁾ We are not specifying the value of α to make the results look more general.

2) $P_2 = (1, \frac{2}{3})$. Note that this point is located on the singular line. Introducing small deflections $\bar{f} = f - 1$, $\bar{g} = g - \frac{2}{3}$, we get the linearized equations

$$\begin{cases} \frac{d\bar{f}}{d\chi} = 2(1 - 2\alpha)\bar{f} + 3(\alpha - 1)\bar{g}, \\ \frac{d\bar{g}}{d\chi} = 2(\alpha - 2)\bar{f} - 3(\alpha - 1)\bar{g}, \end{cases} \quad (2.19)$$

valid for $|\bar{f}|, |\bar{g}| \ll 1$. The system has a pair of negative eigenvalues $\lambda_1 = -(\alpha + 1)$, $\lambda_2 = -6(\alpha - 1)$, which means that P_2 is a node with half lines $\bar{g} = \bar{f}$ and $\bar{g} = \mu\bar{f}$, where $\mu = \frac{2(2-\alpha)}{3(\alpha-1)}$. In particular, $\mu = \frac{2}{3}$ for $\alpha = \frac{3}{2}$. The trajectories of (2.19) are expressed by the equation

$$\left| \frac{\bar{g} - \mu\bar{f}}{1 - \mu} \right|^{\lambda_1} = C \left| \frac{\bar{f} - \bar{g}}{1 - \mu} \right|^{\lambda_2}, \quad C = \text{const}.$$

The presence of the node P_2 on the singular line leads to important consequences. It appears that the coordinate line $\xi = \xi_c$ in the physical plane, with ξ_c being the common root of the equations $f(\xi_c) = 1$, $g(\xi_c) = \frac{2}{3}$, coincides with a characteristic of the Euler equations. Indeed, at any point of a supersonic flow one can draw a pair of characteristics with local slope

$$\frac{d\hat{y}}{d\hat{x}} = \frac{\hat{U}\hat{V} \pm \sqrt{(\hat{U}^2 + \hat{V}^2) - \hat{a}^2}}{\hat{U}^2 - \hat{a}^2}, \quad (2.20)$$

where the hat denotes unscaled physical variables, \hat{U}, \hat{V} are the velocity components and \hat{a} is the local speed of sound. Transforming to the dimensionless variables introduced in section 2.1.1 and using the asymptotic expansions for u, v and a near the sonic point (resulting from expansion (2.4) of the velocity potential), equation (2.20) may be converted into

$$\frac{dy}{dx} = \frac{\pm 1}{y^{\alpha-1} \alpha \xi \sqrt{f(\xi)}} \equiv \pm \frac{y}{\alpha x \sqrt{f(x/y^\alpha)}}. \quad (2.21)$$

On the other hand, the local slope of a coordinate line $\xi = \text{const}$ is

$$\frac{dy}{dx} = \frac{1}{y^{\alpha-1} \alpha \xi} \Big|_{\xi=\text{const}} \equiv \frac{y}{\alpha x}. \quad (2.22)$$

Comparing (2.21) with (2.22), we see that the characteristics coincide with the coordinate lines when $f = 1$, i.e. on the singular line of the phase plane. In this particular

case $f = f(\xi_c) = 1$ along the entire integral curve of (2.21); otherwise (2.21) and (2.22) lead to different integrals, and the characteristics intersect with the coordinate lines.⁸⁾

However, we also need to make sure that on those coordinate lines which coincide geometrically with the characteristics the so-called *compatibility condition* holds. This is the necessary condition for a solution to exist along the characteristics, and it imposes a certain restriction on the velocity components, leading to the introduction of the *Riemann invariants* (Liepmann & Roshko 1957). Upon substituting the expansions for the velocity components into the compatibility condition and setting $f = 1$, it yields $g = \frac{2}{3}$ in the leading order, thus proving that the only place where the phase trajectories can pass through the singular line is P_2 .

There appears to be a fundamental connection between the limiting characteristic and the way small perturbations propagate in transonic flows. When $\xi < 0$, the coordinate lines have a negative slope and can coincide with the characteristics of the second family; the latter bring information from the outer flow to the wall. Now, if $f < 1$, i.e. the phase trajectory has not yet passed to the right of the singular line, the characteristics are steeper than the coordinate lines (see Fig. 2.3), and the normal component of velocity on these lines is smaller than the local speed of sound.⁹⁾ On

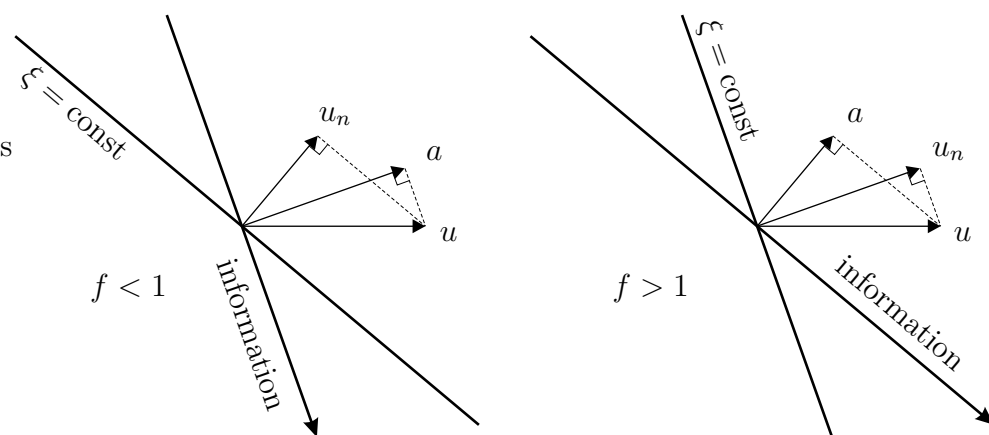


Figure 2.3: Physical meaning of the limiting characteristic.

⁸⁾ Equation (2.21) can only be integrated if the solution for $f(\xi)$ is known.

⁹⁾ The velocity component normal to the characteristics is always equal to the local speed of sound.

the contrary, if $f > 1$, then the characteristics are flatter than the coordinate lines, and the normal component of velocity on these lines is greater than the local speed of sound (Fig. 2.3). Consequently, small perturbations from the downstream regions do not penetrate through the coordinate lines in the upstream direction. It means that if a transonic flow passes through the limiting characteristic (i.e., the phase trajectories tunnel to the right of the singular line through the point P_2), the downstream regions do not affect the flow upstream. In sections 2.4.9–2.4.12 we shall see that this property provides one extra degree of freedom in the local solution, requiring to specify one parameter from the global flow (say, the upstream wall pressure gradient, along with the wall curvatures) in order to describe the local flow uniquely.

When $\xi > 0$, the above results hold for the characteristics of the first family (with a positive slope) transferring information from the wall to the outside flow. Again, in the flow with $f > 1$ there is no influence of the downstream regions on the upstream ones, and that is the reason why the limiting characteristic is so important. In section 2.4.10 it will be shown that for our particular problem $\xi_c < 0$; the value of ξ_c will be obtained analytically.

3) $P_3 = (\frac{1}{\alpha^2}, -\frac{2}{3\alpha^3})$. In the vicinity of this point equations (2.17) are reduced to the following linear system for the small deflections $\bar{f} = f - \frac{1}{\alpha^2}$ and $\bar{g} = g + \frac{2}{3\alpha^3}$:

$$\begin{cases} \frac{d\bar{f}}{d\chi} = \frac{1}{\alpha} [2(\alpha - 2)\bar{f} + 3\alpha(\alpha - 1)\bar{g}] , \\ \frac{d\bar{g}}{d\chi} = \frac{1}{\alpha^2} [2(2\alpha - 1)\bar{f} + 3\alpha(\alpha - 1)\bar{g}] . \end{cases} \quad (2.23)$$

This system has eigenvalues $\lambda_1 = -\frac{\alpha+1}{\alpha}$, $\lambda_2 = \frac{6(\alpha-1)}{\alpha}$ with different signs, which means that P_3 is a saddle point. Its half-lines are directed along the vectors

$$\left\| 1, \frac{2(2\alpha-1)}{3\alpha(\alpha-1)} \right\|^T, \quad \left\| 1, -\frac{1}{\alpha} \right\|^T.$$

When the phase trajectories approach the saddle point, their direction undergoes an abrupt change. In section 2.4.9 we shall see that this affects the physics of the flows by providing a border between the trajectories corresponding to different flow regimes (Fig. 2.4). The saddle point creates an obstacle for those trajectories that move towards the singular line in the lower half-plane $g < 0$ (Fig. 2.2), and makes

them turn either towards the subsonic region, or towards the point P_2 where an intersection with the singular line is allowed. In some special cases the trajectories find themselves moving along the saddle point half-lines. Integrating (2.16) along the first half-line yields

$$\xi = C |\bar{f}|^{-\frac{\alpha+1}{6}}, \quad C = \text{const},$$

and $|\xi| \rightarrow \infty$ when $\bar{f} \rightarrow 0$. This situation contradicts with one of the basic properties of the phase trajectories that $(f, g) \rightarrow (0, 0)$ as $|\xi| \rightarrow \infty$ (on approaching the walls). However, it becomes allowed in the limiting case of $\varkappa_+/\varkappa_- \rightarrow \infty$, interpreted as $\varkappa_+ \rightarrow \infty$, $\varkappa_- = \text{const}$.¹⁰⁾ Integrating (2.16) along the second asymptote gives

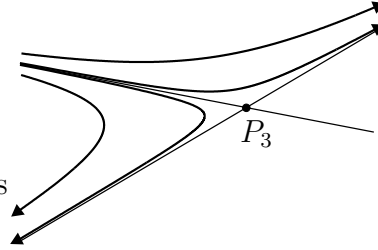


Figure 2.4: Phase trajectories near the saddle point.

$$\xi = C |\bar{f}|^{\alpha-1}, \quad C = \text{const},$$

so that $|\xi| \rightarrow 0$ when $\bar{f} \rightarrow 0$. This refers to the same limiting case of $\varkappa_+/\varkappa_- \rightarrow +\infty$, now interpreted as $\varkappa_- \rightarrow 0$, $\varkappa_+ = \text{const}$, arising from an entirely different flow regime. Due to the fact that the local solution does not depend on the way the coordinates (and, hence, the curvatures) are scaled, these two interpretations are identical, therefore providing an important link between the two completely different flow regimes via the saddle point.

¹⁰⁾ A detailed explanation is given at the end of section 2.4.12.

2.3 Numerical Solutions of the Karman-Guderley equation

The local analysis of the phase trajectories near the stationary points P_1 , P_2 and P_3 gives a valuable information about some basic properties of the flow. However, we need to obtain the phase trajectories for all $\xi \in (-\infty, \infty)$ in order to find the pressure gradients on both walls for a given ratio of the curvatures. The only way to do that, as long as equation (2.5) or system (2.17) are being considered, is to solve the relevant boundary-value problem numerically. In this section we are going to develop a simple numerical technique of solving boundary-value problem (2.5)–(2.8) and calculating the phase trajectories as ξ runs from $-\infty$ to ∞ .

2.3.1 Transformation of the variables

To increase the accuracy of numerical results, a specific transformation of the variable ξ and the function $F(\xi)$ has to be introduced, allowing us to work with a finite computational domain and simpler boundary conditions.

According to the asymptotic behavior (2.9) of $F(\xi)$ at $\xi \rightarrow \pm\infty$, let us introduce a new function $G(s)$:

$$F(\xi) = [(\gamma + 1)\varkappa_-]^{1/\alpha} \text{sign}(\xi) |\xi|^\lambda G(s), \quad (2.24)$$

with the new independent variable s defined as

$$\xi = [(\gamma + 1)\varkappa_-]^{\alpha-1} \text{sign}(s) (\tan|s|)^\alpha \quad (2.25)$$

on the finite domain $-\frac{\pi}{2} \leq s \leq \frac{\pi}{2}$. The $|\xi|^\lambda$ term is used in (2.24) to make $G(s)$ finite when $s = \pm\frac{\pi}{2}$, and taking $\tan|s|$ to the power of α in (2.25) ensures that dG/ds is also finite. Both s and $G(s)$ are invariant with respect to re-scaling (2.13), thanks to the terms with \varkappa_- in the above equations.

Transformation (2.25) monotonely maps the infinite region $-\infty < \xi < \infty$ into the domain $-\frac{\pi}{2} < s < \frac{\pi}{2}$ which is more suitable for numerical computations. As

mentioned before, the new function $G(s)$ is finite at $s = \pm\frac{\pi}{2}$. Its limiting values, defined as

$$G_{\pm} = \mp G\left(\pm\frac{\pi}{2}\right),$$

are directly related to the pressure gradients on the walls:

$$\left.\frac{\partial p}{\partial x}\right|_{y=0, x \geq 0} = G_{\pm} [(\gamma + 1)\varkappa_{\pm}]^{1/\alpha} \frac{2\lambda(\alpha - 1)}{\alpha} (\pm x)^{1 - \frac{2}{\alpha}} + \dots, \quad |x| \ll 1. \quad (2.26)$$

Equation (2.26) is deduced from expansion (2.10) for the pressure and the asymptotic form (2.9) of $F(\xi)$; the latter may be written as

$$F(\xi) = -G_{\pm} [(\gamma + 1)\varkappa_{\pm}]^{2/3} (\pm \xi)^{5/3} - (\gamma + 1)\varkappa_{\pm} \xi + \dots, \quad \xi \rightarrow \pm\infty \quad (2.27)$$

after setting $\alpha = \frac{3}{2}$.

The general expression (2.26) is reduced to

$$\left.\frac{\partial p}{\partial x}\right|_{y=0, x \geq 0} = \mp k G_{\pm} (\pm x)^{-1/3} + \dots, \quad k = \frac{10 [(\gamma + 1)\varkappa_{\pm}]^{2/3}}{9} \quad (2.28)$$

when $\alpha = \frac{3}{2}$, thus yielding the $(\pm x)^{-1/3}$ singularity in the pressure gradients. Our main task now is to find the signs and the absolute values of G_{\pm} for any given ratio of the curvatures.

Transformations (2.24)–(2.25) result in the simple boundary conditions for $G(s)$:

$$\left.\frac{dG}{ds}\right|_{s=\pm\frac{\pi}{2}} = \begin{cases} \frac{\varkappa_{+}}{\varkappa_{-}}, & x > 0, \\ -1, & x < 0, \end{cases} \quad (2.29)$$

and the equation for $G(s)$ is

$$\begin{aligned} \sin^2 s \frac{d}{ds} \left(\sin^2 s \frac{dG}{ds} \right) &= \left(\lambda G + \frac{\sin(2s)}{2\alpha} \frac{dG}{ds} \right). \\ \left[\lambda(\lambda - 1)G + \frac{\lambda \sin(2s)}{2\alpha} \frac{dG}{ds} + \frac{\cos^2 s}{\alpha^2} \frac{d}{ds} \left(\sin^2 s \frac{dG}{ds} \right) \right] &. \end{aligned} \quad (2.30)$$

The solution of the boundary-value problem (2.30)–(2.29) obviously depends only on the ratio of the curvatures. Since the problem does not contain γ , the pressure gradients, according to (2.28), are related to the specific heat ratio via the factor $(\gamma + 1)^{2/3}$.

Equation (2.30) can be integrated numerically for any $s \neq 0$; however, the solution develops a singularity, namely $G(s) \sim |s|^{-\alpha\lambda}$, as $|s| \rightarrow 0$. Thus, original equation (2.5) has to be solved in the vicinity of $\xi = 0$, and the corresponding solution should be matched with $G(s)$ on both sides of $\xi = 0$ at two points of our choice (these points should be located at finite distances from $\xi = 0$ to avoid the singularity in G). By restricting the domain for s (where equation (2.30) is solved) to $-\frac{\pi}{2} < s < -\frac{\pi}{4}$ and $\frac{\pi}{4} < s < \frac{\pi}{2}$, we get the relevant domain for ξ (where equation (2.5) is solved):

$$-\sqrt{(\gamma+1)\varkappa_-} < \xi < \sqrt{(\gamma+1)\varkappa_-},$$

as shown in Fig. 2.5. At the joints, one needs to match $F(\xi)$ with $G(s)$ using (2.24), and $dF/d\xi$ with dG/ds via

$$\left. \frac{dF}{d\xi} \right|_{\xi=\pm\sqrt{(\gamma+1)\varkappa_-}} = \pm (\gamma+1)\varkappa_- \tan s \left[\lambda G + \frac{\sin(2s)}{2\alpha} \frac{dG}{ds} \right] \Big|_{s=\pm\frac{\pi}{4}}.$$

In order to reconstruct the phase trajectories, we use original definition (2.15) within the computational domain for ξ , whereas in the domain of the transformed variables s , $G(s)$ equations

$$\begin{cases} f(s) = \frac{1}{\alpha^2 \tan^2 s} \left[\lambda G + \frac{\sin(2s)}{2\alpha} \frac{dG}{ds} \right], \\ g(s) = -\frac{\sin(2s)}{2\alpha^3 \tan^2 s} \frac{dG}{ds} \end{cases}, \quad (2.31)$$

are employed.

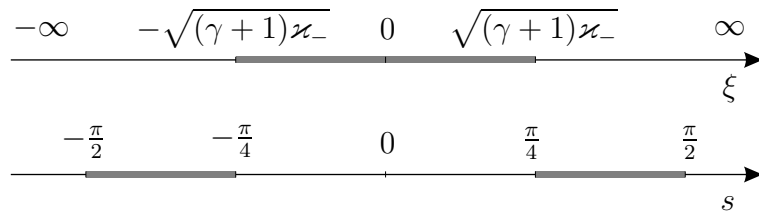


Figure 2.5: Computational domains for ξ and s .

Finally, for those trajectories that happen to pass through the point P_2 both equations (2.5) and (2.30) fail, as the coefficient in front of the second derivative

becomes zero at this point. Therefore, on approaching P_2 equation

$$\frac{dg}{df} = \frac{3g + 2(\alpha - 1)f^2 - 3\alpha fg}{2f + 3(\alpha - 1)g - 2\alpha f^2}, \quad (2.32)$$

obtained from (2.17) and written directly for the phase variables, is solved. In the point P_2 itself both the numerator and the denominator in (2.32) are equal to zero, but their ratio is finite and is equal to 1 when $\alpha = \frac{3}{2}$ (according to the local analysis performed in section 2.2.2). This result is used to eliminate the singularity in (2.32) and pass through the critical point P_2 .

Now we have enough tools to proceed with the numerical technique.

2.3.2 Numerical results for the phase portrait and the pressure gradients

Instead of dealing with the original boundary-value problem which arises when both curvatures are specified, one can consider a different physical situation. Namely, let us assume that we know both the curvature and the pressure gradient on the upstream wall, while the downstream curvature and pressure gradient are unknown. From (2.26) we see that specifying the upstream pressure gradient yields the relevant value of G_- , and along with the upstream condition (2.29) for dG/ds this defines an initial-value problem for $G(s)$. The initial-value problem can be solved numerically using marching with the second-order prediction-correction scheme.

Integrating equation (2.30) for $-\frac{\pi}{2} < s < -\frac{\pi}{4}$, then equation (2.5) for

$$-\sqrt{(\gamma + 1)\varkappa_-} < \xi < \sqrt{(\gamma + 1)\varkappa_-},$$

and then (2.30) again for $\frac{\pi}{4} < s < \frac{\pi}{2}$ (plus equation (2.32) for those trajectories that approach the point P_2), we cover all the values of $\xi \in (-\infty, \infty)$, calculate the phase variables f , g and plot the relevant phase trajectory along the way. Once the final point $s = \frac{\pi}{2}$ is reached, we get the values of G_+ , $\left.\frac{dG}{ds}\right|_+$, and therefore can work out both the downstream pressure gradient and the curvatures ratio from equations (2.28), (2.29). Since \varkappa_- is specified, the latter provides \varkappa_+ .

Notice that for $\alpha = \frac{3}{2}$ equation (2.5) admits a simple analytical solution

$$F(\xi) = C \xi, \quad (2.33)$$

where C is an arbitrary constant. We shall write (2.33) as

$$F(\xi) = -(\gamma + 1)\varkappa \xi, \quad -\infty < \xi < \infty \quad (2.34)$$

and use it as a starting point in our calculations. According to (2.24), this solution yields $G_{\pm} = 0$, i.e. zero pressure gradients on both walls in the leading order. The perturbations of the velocity components, defined in (2.6), in this case are:

$$u = y F' = -(\gamma + 1)\varkappa y, \quad (2.35)$$

$$v = \alpha y^{3/2} [\lambda F - \xi F'] = -(\gamma + 1)\varkappa x.$$

Therefore, (2.34) describes a potential vortex flow outside a wall with a constant curvature $\varkappa = \varkappa_- = \varkappa_+$; for convex walls $\varkappa > 0$ and the flow in the vortex is subsonic. Functions (2.35) are the leading-order terms in the Taylor expansions of the general solution for a potential vortex flow, constructed near any given point of a smooth body surface (with no curvature breaks). The corresponding phase trajectory is simply a straight line $g = \frac{2}{3}f$, $f < 0$, starting from the origin when $\xi = -\infty$, then moving to $(f = -\infty, g = -\infty)$ as $\xi \rightarrow 0$, and finally returning back to the origin when $\xi \rightarrow \infty$ (Fig. 2.6). Note that the reflection rule, derived in section 2.2.1 for a typical trajectory when ξ changes its sign, is not applicable in this case since g appears to be an even function of ξ .¹¹⁾ The $g = \frac{2}{3}f$ line also coincides with one of the half-lines of the stationary point P_1 .

Based on the above results we integrated the initial-value problem for a small negative value of G_- (favorable pressure gradient on the upstream wall), calculating the phase trajectory and the downstream wall parameters in the process. Once the solution was obtained, we increased $|G_-|$ slightly (keeping G_- negative) and solved the problem numerically again. By repeating the procedure, we obtained a family of

¹¹⁾ In most of the cases g is an odd function of ξ in the vicinity of $\xi = 0$, which follows from the definition of g in (2.15). Being proportional to ξ^{-3} if $F(0) \neq 0$, g undergoes a jump from $-\infty$ to ∞ or vice versa when ξ changes sign.

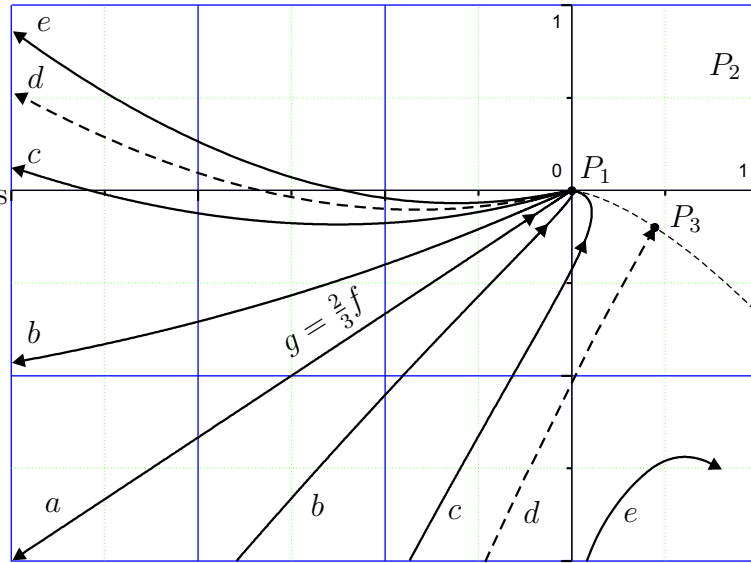


Figure 2.6: Numerical results for the phase trajectories corresponding to different ratios of the curvatures; (a): $\frac{\kappa_+}{\kappa_-} = 1$; (b) and (c): $1 < \frac{\kappa_+}{\kappa_-} < \infty$; (d): $\frac{\kappa_+}{\kappa_-} = \infty$; (e): trajectories which cross the singular line in an illegitimate place and therefore have to be rejected.

the phase trajectories for negative values of G_- (few of them are shown in Fig. 2.6), and plotted κ_+/κ_- versus G_- (Fig. 2.7, left). Fig. 2.6 suggests that when $G_- < 0$, the trajectories start into the subsonic half-plane ($f < 0$), i.e. the oncoming flow with a favorable pressure gradient is subsonic. After crossing the line $g = 0$ (where v changes the sign), the trajectories head on to infinity as $\xi \rightarrow 0$, get reflected in the $g = 0$ line, then enter the supersonic half-plane ($f > 0$) and finally return to the origin, thanks to the presence of the saddle point P_3 . Thus, the flow becomes supersonic near the downstream wall. The larger $|G_-|$ is, the wider the trajectories go with respect to line $g = \frac{2}{3}f$, and their supersonic fragments come closer to the saddle point. As a result, for some $G_- = G_{min} < 0$ the trajectory ends at the saddle point.¹²⁾ The consequences of this kind of a behavior have already been mentioned in section 2.2.2, and will be described in detail in section 2.4.8. Finally, when $|G_-|$ becomes greater than $|G_{min}|$, the trajectories turn to the right of the saddle point and approach the singular line, attempting to cross it at an illegitimate place (Fig. 2.6). Hence, these solutions have to be rejected, which means that no favorable upstream

¹²⁾ Analytical expression for G_{min} will be obtained in section 2.4.5.

pressure gradients stronger than $|G_{min}|$ can exist.

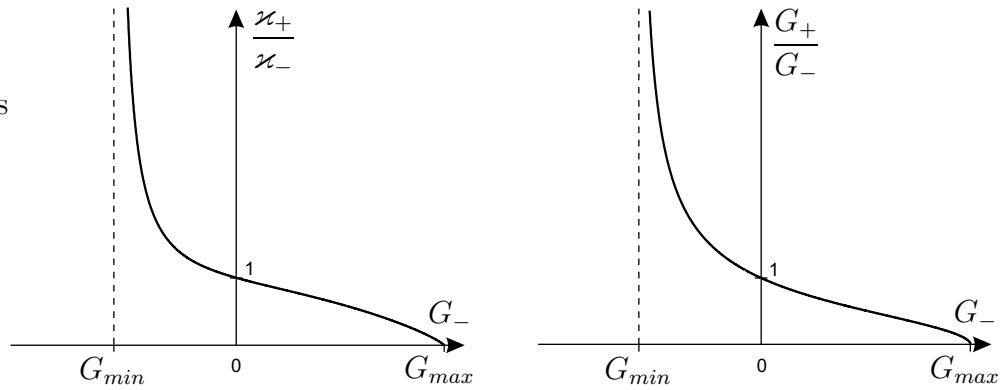


Figure 2.7: Numerical results for the ratio of the curvatures and the ratio of the gradients for different values of the upstream pressure gradient G_- .

From Fig. 2.7, left, we see that oncoming subsonic flows (which have $G_- < 0$) correspond to $\kappa_+/\kappa_- > 1$.¹³⁾ The ratio increases with $|G_-|$, leading to a flatter upstream wall for stronger favorable pressure gradients, and tends to ∞ when $G_- \rightarrow G_{min}^+$. This limit can correspond either to $\kappa_+ \rightarrow \infty$, $\kappa_- > 0$ or $\kappa_- \rightarrow 0^+$, $\kappa_+ > 0$, due to the problem's invariance with respect to re-scaling (2.12). In the first case the size of the region where the self-similar solutions are valid tends to zero;¹⁴⁾ however, for the observer who 'sits' in the self-similar region itself (small enough for the solutions to be valid) the upstream wall becomes a flat plate ($\kappa_- \rightarrow 0$), whereas the downstream wall has $\kappa_+ = O(1)$, thus corresponding to the second interpretation. By choosing

$$L = [\max(\hat{\kappa}_-, \hat{\kappa}_+)]^{-1}$$

as a scale, we can restrict dimensionless curvatures to $0 \leq \kappa_{\pm} \leq 1$ to avoid the infinities and additional re-scaling.

The pressure gradients' ratio G_+/G_- is shown in Fig. 2.7, right, as a function of G_- . As with the curvatures' ratio, it is greater than 1 when $G_- < 0$, suggesting that the downstream pressure gradient is also favorable and is stronger than the

¹³⁾ Positive values of G_- in Fig. 2.7 correspond to a supersonic flow on the upstream wall which will be discussed later.

¹⁴⁾ Recall that transferring boundary condition (2.2) to the $y = 0$ axis is only possible when $|\kappa_{\pm} x| \ll 1$, which means that the regions between the curved walls and the line $y = 0$ are negligible.

upstream gradient. Both gradients vanish in the limit $\kappa_+/\kappa_- \rightarrow 1$ (no discontinuity in the curvature), although the gradient's ratio tends to 1. In the opposite limit $\kappa_+/\kappa_- \rightarrow \infty$ the ratio also tends to infinity. Indeed, on a much flatter upstream wall the pressure gradient should be significantly smaller.

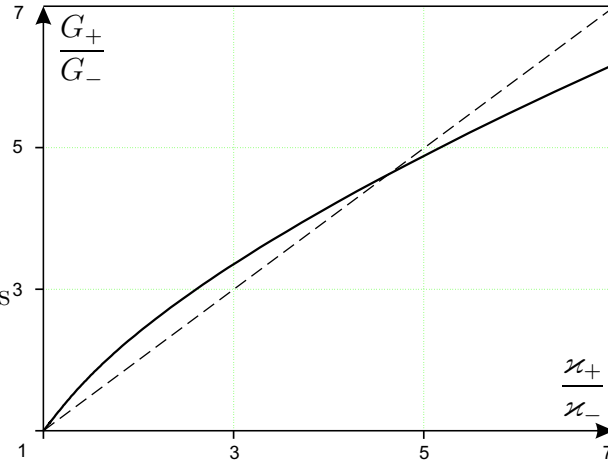


Figure 2.8: The ratio of the pressure gradients on the walls as a function of the ratio of the curvatures (plotted for the case of $\frac{\kappa_+}{\kappa_-} > 1$).

In Fig. 2.8 the gradients' ratio is plotted versus κ_+/κ_- .¹⁵⁾ When κ_+/κ_- is increasing from 1, G_+/G_- at first becomes slightly bigger than the curvatures' ratio, but at $\kappa_+/\kappa_- \approx 4.7$ the situation changes to the opposite, ultimately leading to the following asymptotic behavior:¹⁶⁾

$$\frac{G_+}{G_-} \sim \left(\frac{\kappa_+}{\kappa_-} \right)^{2/3}, \quad \frac{\kappa_+}{\kappa_-} \rightarrow \infty.$$

Let us now move on to positive G_- in the initial value problem; in this case the upstream pressure gradient is adverse; see (2.28). By increasing G_- slightly after each computation, we cover the whole range of possible values of adverse pressure gradients, plot the relevant phase trajectories and obtain the downstream wall parameters (G_+ and κ_+/κ_-). A selection of the trajectories is shown in Fig. 2.9. This time they start into the supersonic half-plane $f > 0$ (i.e. the flow near the upstream

¹⁵⁾ This graph, unlike the previous one, is plotted for the case of a subsonic flow on the upstream wall only, i.e. for $\kappa_+/\kappa_- > 1$.

¹⁶⁾ This comes from the analysis of equations (2.67) in section 2.4.5.

wall is supersonic), but soon after that turn abruptly towards the subsonic half-plane, thanks to the presence of the saddle point. Despite the fact that the flow is originally supersonic, it does decelerate to subsonic speeds without a shock formation. In subsequent sections we shall give a rigorous proof that this is only possible when the phase trajectories remain on the left of the singular line. Recall that in section 2.2.2 we argued that when $f < 1$, small perturbations may penetrate back through the coordinate lines, resulting in an influence of the downstream regions on the upstream ones (essential property of subsonic flows). Therefore, supersonic flows with $0 < f < 1$ are somewhat inferior and allow smooth deceleration. However, once the trajectories find themselves on the right of the singular line ($f > 1$), the only way back is through a shock, which may lead to either a subsonic or a supersonic flow near the downstream wall.

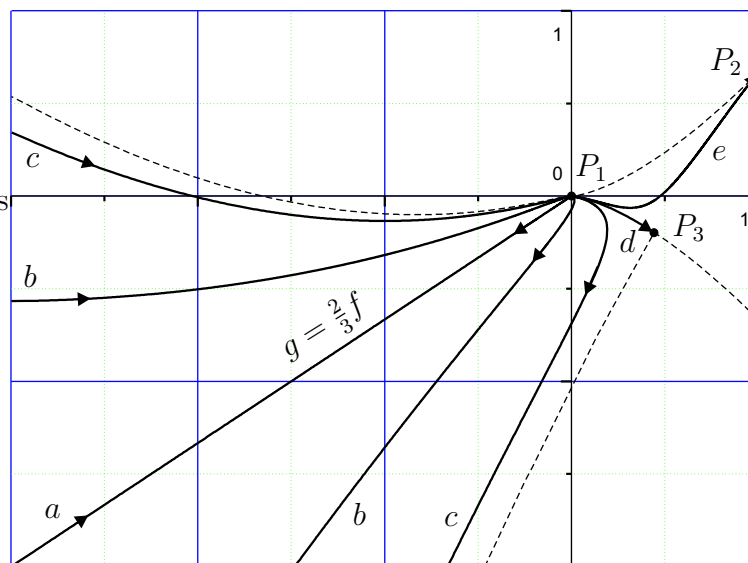


Figure 2.9: Numerical results for the phase trajectories corresponding to different ratios of the curvatures; (a): $\frac{\kappa_+}{\kappa_-} = 1$; (b), (c): $0 < \frac{\kappa_+}{\kappa_-} < 1$; (d): $\frac{\kappa_+}{\kappa_-} = 0$; (e): trajectories which pass through the singular line via the only allowed point P_2 . The dashed lines represent the limiting shape of the trajectories from the family (a), (b), (c) when $\frac{\kappa_+}{\kappa_-} \rightarrow 0^+$, and the so-called *critical lines* in the supersonic half-plane (see section 2.4.2).

After crossing the sonic line, the trajectories travel to $(f = -\infty, g = \infty)$, reflect in the $g = 0$ axis and return back to the origin (crossing line $g = 0$ on the way).

Thus, the behavior totally resembles the one of the trajectories in the previous regime (subsonic oncoming flows), with the only difference in the direction of travelling along the trajectories. Again, the larger the adverse pressure gradient on the upstream wall is, the wider the trajectories go with respect to $g = \frac{2}{3}f$. As for the curvature's ratio, it is plotted versus G_- in Fig. 2.7, left. Now the ratio is within $(0, 1)$ and is diminishing with G_- . From the plot it follows that for some $G_- = G_{max} > 0$ it becomes zero, referring to either $\varkappa_+ \rightarrow 0^+$ or $\varkappa_- \rightarrow \infty$ (with the second curvature being an order-one quantity in both cases).¹⁷⁾ As $G_- \rightarrow G_{max}^-$, the trajectory approaches the saddle point P_3 , and ends up in it when $G_- = G_{max}$. This time it reaches the saddle point when $\xi \rightarrow 0^-$ along the second linear asymptote (section 2.4.8). Later we shall see that this particular phase trajectory then jumps from point P_3 into the origin, creating a weak discontinuity at $\xi = 0$ and a uniform flow for $\xi > 0$ (over a flat plate with $\varkappa_+ = 0$).

For $G_- > 0$ the downstream pressure gradient is also adverse (Fig. 2.7, right), thus yielding the general rule: for subsonic flows on the downstream wall the pressure gradient is always adverse, whereas for supersonic flows near the downstream wall it has to be favorable. However, once the upstream wall is considered, the opposite is true: subsonic flows on the upstream wall lead to favorable pressure gradients, while supersonic flows near the upstream wall develop adverse pressure gradients. Summarizing, in the first regime considered (subsonic upstream flows becoming supersonic downstream) both pressure gradients are favorable, and in the second regime (supersonic upstream flows with $f < 1$, becoming subsonic downstream) both of the gradients are adverse.¹⁸⁾ Overall, there appears to be a symmetry between the two regimes discussed above with respect to the transformation $x \longleftrightarrow -x$; in other words, physical processes in these flows are reversible.

To make the results more clear, it is worth plotting both G_- and G_+ as functions of the curvature's ratio (Fig. 2.10). The two regimes discussed above have a similar property: knowing any pair of the physical parameters, for example $(\varkappa_-, \varkappa_+)$, or

¹⁷⁾ Note that $G_{max} \neq |G_{min}|$; analytical expression for G_{max} will be given in section 2.4.7.

¹⁸⁾ The latter may lead to a separation of the boundary layer.

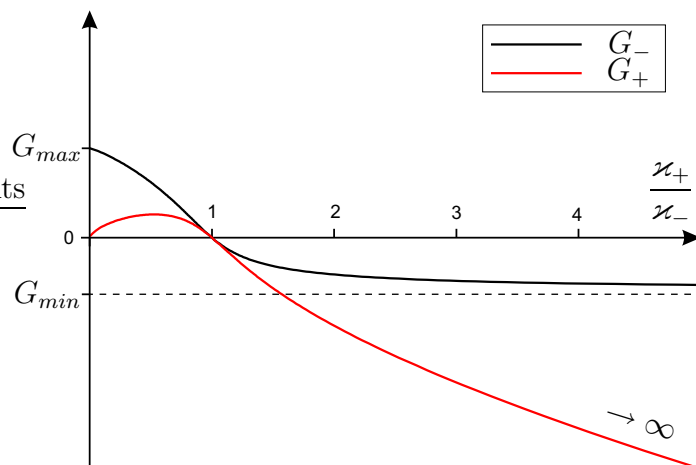


Figure 2.10: Upstream and downstream pressure gradients as functions of the ratio of the curvatures.

(κ_-, G_-) , allows to determine the other two uniquely ((G_-, G_+) or (κ_+, G_+) respectively). It means that by knowing, say, both of the curvatures (which is physically reasonable) one can work out the local flow regardless of the global flow, since no free parameters remain in the local solutions. Later we shall call these two regimes *subcritical* and provide proofs for all the proposals from this section.

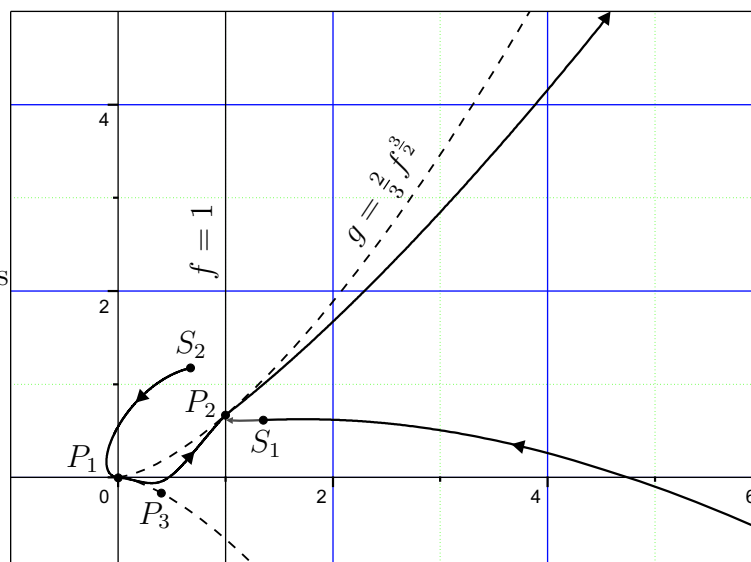


Figure 2.11: A typical phase trajectory which tunnels through the singular line.

Finally, we need to say a few words about what happens when G_- becomes

larger than G_{max} . Recall that in the opposite case when $G_- < G_{min} < 0$ we had physically meaningless solutions with the trajectories trying to cross the singular line in an illegitimate place. However, for $G_- > G_{max}$ the trajectories go above the saddle point; the latter makes them turn upwards and head on towards the node P_2 standing for the limiting characteristic (Fig. 2.9). As already shown previously, this point provides the only possible passage through the singular line, and, being a node, attracts all those trajectories which come close enough. Upon passing through P_2 , the trajectories travel further on the right of the singular line towards $(f = \infty, g = \infty)$ (corresponding to $\xi \rightarrow 0^-$), are reflected in axis $g = 0$ and return back to the singular line, trying to cross it slightly below P_2 (Fig. 2.11). Since this kind of a crossing is prohibited, the only way to return into the origin and satisfy the downstream boundary condition is to undergo a jump to the other side of the singular line. The jump would obviously correspond to a shock in the physical plane. A detailed analysis of such flows (which are irreversible due to the shock formation, and therefore will be called *supercritical*) is given in sections 2.4.9–2.4.12. It appears that the points S_1 and S_2 on Fig. 2.11, referring to the front and the back sides of the shock, are symmetric with respect to the singular line $f = 1$. Moreover, due to the fact that the flow passes through the limiting characteristic before developing the shock, it gains one extra degree of freedom (through the loss of a mutual interaction between the downstream and the upstream regions). In this case one needs to specify any three of the four main parameters \varkappa_- , \varkappa_+ , G_- , G_+ of the local flow to find the remaining one. This is totally different from the situation with the subcritical flows, and may be treated as a dependence of the local solution upon the global solution. Thus, along with both curvatures we now have to specify one of the pressure gradients in order to obtain a unique local flow pattern. Having one extra free parameter results in a greater variety of regimes, for example flows over concave downstream walls with $\varkappa_+ < 0$ (see section 2.4.12).

This completes the numerical analysis, and we can now proceed with a theoretical interpretation of the above results.

2.4 Hodograph Method

In this section we are going to give a theoretical explanation of the numerical results obtained in section 2.3.2. This will provide a better understanding of all the possible scenarios describing how a local inviscid transonic flow generated by a discontinuity in wall curvature may behave depending on the curvatures' ratio. Even though only one specific inviscid flow regime, highlighted in section 2.4.6, will be subsequently chosen for the analysis of a viscous-inviscid interaction in Chapter 3, a complete picture of the inviscid flow has its own scientific significance. Several important proposals regarding the limiting characteristic, shock formation and the link between the local and the global flows will be proved analytically in this section.

2.4.1 Direct and Inverse problems

By analogy with the Quantum Mechanics, our 2D problem admits a *momentum representation*, as opposed to the *coordinate representation* used in previous sections. This implies treating the perturbations u, v of the velocity components as the independent variables, with the spatial coordinates being their functions:

$$x = x(u, v), \quad y = y(u, v).$$

In the coordinate representation the flow in a small vicinity of the sonic point is described by the potential

$$\Phi(x, y) = x + \frac{\phi(x, y)}{(\gamma + 1)} + \dots,$$

where $\phi(x, y)$ is a leading-order perturbation related to u, v and $F(\xi)$ in the following way (see (2.6), (2.4)):

$$u = \frac{\partial \phi}{\partial x}, \quad v = \frac{\partial \phi}{\partial y}, \quad \phi(x, y) = y^{3\alpha-2} F(\xi), \quad y \rightarrow 0, \quad \xi = \mathcal{O}(1).$$

It satisfies the Karman–Guderley equation

$$\frac{\partial \phi}{\partial x} \frac{\partial^2 \phi}{\partial x^2} - \frac{\partial^2 \phi}{\partial y^2} = 0, \tag{2.36}$$

which results from the Euler equations in the assumption of small transonic perturbations (Cole & Cook 1986); (2.36) is equivalent to the system

$$\begin{cases} u \frac{\partial u}{\partial x} - \frac{\partial v}{\partial y} = 0, \\ \frac{\partial u}{\partial y} = \frac{\partial v}{\partial x}. \end{cases} \quad (2.37)$$

After inverting the roles of independent and dependent variables, equations (2.37) are transformed into the so-called Triкоми equations; the latter are linear and describe a flow in its momentum representation:

$$\begin{cases} u \frac{\partial y}{\partial v} - \frac{\partial x}{\partial u} = 0, \\ \frac{\partial x}{\partial v} = \frac{\partial y}{\partial u}. \end{cases} \quad (2.38)$$

These may be easily converted into a pair of linear second order equations for the functions $x(u, v)$ and $y(u, v)$ separately:

$$\begin{cases} u \frac{\partial^2 y}{\partial v^2} - \frac{\partial^2 y}{\partial u^2} = 0, \\ u \frac{\partial^2 x}{\partial v^2} - \frac{\partial^2 x}{\partial u^2} + \frac{1}{u} \frac{\partial x}{\partial u} = 0. \end{cases} \quad (2.39)$$

The transformation from system (2.37) to system (2.38) is possible when the Jacobian

$$\Delta = \det \begin{vmatrix} \frac{\partial x}{\partial u} & \frac{\partial y}{\partial u} \\ \frac{\partial x}{\partial v} & \frac{\partial y}{\partial v} \end{vmatrix} \quad (2.40)$$

is not equal to zero. If $\Delta = 0$ for certain solutions of (2.38), the corresponding functions $u(x, y)$ and $v(x, y)$ are many-valued and these solutions have no physical meaning.¹⁹⁾ On the contrary, if $\Delta = \infty$ at some point, the functions $x(u, v)$, $y(u, v)$ are many-valued, suggesting that the same values of u , v occur in several different places within the flow, which is a normal situation. However, in this case the original equations (2.37) have to be solved in order to avoid the difficulties in transforming $x(u, v)$, $y(u, v)$ to $u(x, y)$, $v(x, y)$.

¹⁹⁾ In fluid mechanics one expects to find a single pair of values of the velocity components u , v at any given point (x, y) unless there is a shock wave.

From now on we shall call the problem described by system (2.37) with boundary conditions (2.2) the *direct problem* (coordinate representation), and the problem described by system (2.38) with the appropriate boundary conditions the *inverse problem* (momentum representation). The (u, v) plane in which the inverse problem is being solved is known as the *hodograph plane*, and gives its name to the method (Chaplygin 1902).

2.4.2 Self-similar solutions of the Triкоми equations

Let us assume that the inverse problem also admits a self-similar solution near the sonic point (in which the wall curvature breaks). Introducing the similarity variable

$$\zeta = \frac{u}{v^\beta}, \quad (2.41)$$

where β is an unknown parameter, we represent $x(u, v)$ and $y(u, v)$ in the form

$$\begin{aligned} x(u, v) &= v \psi(\zeta) + \dots, \\ y(u, v) &= u \varphi(\zeta) + \dots, \end{aligned} \quad (2.42)$$

with the functions $\varphi(\zeta)$, $\psi(\zeta)$ being of the same nature as $F(\xi)$ in the direct problem.²⁰⁾ The quasi-linear structure of these dependencies follows from the fact that v is linear with respect to x according to boundary condition (2.2), and also from the fact that in the limiting case $\varkappa_- = \varkappa_+ = \varkappa$ the direct problem admits the simple solution

$$u = -(\gamma + 1)\varkappa y, \quad v = -(\gamma + 1)\varkappa x;$$

the latter corresponds to a potential vortex flow outside a uniformly curved cylinder (see section 2.3.2). Plugging the ansatz (2.42) into (2.38) it can be shown (based on the least degeneration principle) that the powers of u and v are balanced in the leading order only when

$$\beta = \frac{2}{3} \equiv \frac{1}{\alpha};$$

in this case the equations for $\varphi(\zeta)$ and $\psi(\zeta)$ become self-similar. Note that the similarity parameter of the inverse problem, β , is determined from the similarity

²⁰⁾ From now on we are going to neglect the higher order perturbations in (2.42).

requirement itself, whereas α (the similarity parameter of the direct problem) is obtained from boundary condition (2.2). On the contrary, the powers of u and v in expansions (2.42) follow from the boundary condition as explained above, whereas the power σ in the analogous expansion (2.4) for the direct problem is obtained from the similarity requirement. This ‘cross-relationship’ between the two problems is an important mathematical property.

Substituting (2.42) into the first equation of (2.39), we get the following equation for $\varphi(\zeta)$:²¹⁾

$$(\beta^2\zeta^3 - 1)\varphi'' + \left(\beta(\beta + 1)\zeta^2 - \frac{2}{\zeta}\right)\varphi' = 0, \quad \varphi' = \frac{d\varphi}{d\zeta}.$$

This is a particular case of a *hypergeometric equation*. The transformation from ζ to a new variable z ,

$$z = \frac{1}{1 - \beta^2\zeta^3}, \quad (2.43)$$

yields

$$6z(1 - z)\ddot{\varphi} + (3 - 11z)\dot{\varphi} = 0, \quad \dot{\varphi} = \frac{d\varphi}{dz}. \quad (2.44)$$

The general solution of equation (2.44) can be expressed via an *incomplete beta function* $B(a, b, z)$, see Abramovitz & Stegun (1972):

$$\varphi(z) = C_1 + C_2 B\left(\frac{1}{2}, -\frac{1}{3}, z\right), \quad (2.45)$$

where

$$B(a, b, z) = \int_0^z \omega^{a-1}(1 - \omega)^{b-1}d\omega, \quad (2.46)$$

and C_1, C_2 are arbitrary constants. For the sake of simplicity we will employ a shorter notation for the incomplete beta function from (2.45):

$$B(z) \equiv B\left(\frac{1}{2}, -\frac{1}{3}, z\right) = \int_0^z \frac{d\omega}{\omega^{1/2}(1 - \omega)^{4/3}}. \quad (2.47)$$

The equation for $\psi(\zeta)$ is obtained by substituting (2.42) into the second equation of (2.39):

$$(\beta^2\zeta^3 - 1)\psi'' + \left(\beta(\beta - 1)\zeta^2 + \frac{1}{\zeta}\right)\psi' = 0, \quad \psi' = \frac{d\psi}{d\zeta},$$

²¹⁾ Wherever symbol ‘ β ’ is used instead of its value $2/3$, this is done to make the equations look more general and compact at the same time. This would also be the case with the parameters α and λ .

which can be further transformed using (2.43) to get the general solution in terms of $\psi(z)$:

$$\psi(z) = C_3 + C_4 \left[B(z) - \frac{3}{z^{1/2}(1-z)^{1/3}} \right]. \quad (2.48)$$

The four integration constants in the solutions for ϕ and ψ are not independent; from the second equation in (2.38) and (2.42) it follows that

$$C_1 = C_3, \quad C_2 = C_4,$$

allowing to write the general self-similar solutions for x, y in the form

$$\begin{cases} y = u \cdot [C_1 + C_2 B(z)], \\ x = v \cdot \left[C_1 + C_2 \left(B(z) - \frac{3}{z^{1/2}(1-z)^{1/3}} \right) \right]. \end{cases} \quad (2.49)$$

The functions $B(z)$ and $z^{1/2}(1-z)^{1/3}$ are defined on a 6-sheet Riemann surface, with the sheets joined via brunch-cuts $(-\infty, 0)$ (due to $z^{1/2}$) and $(1, \infty)$ (due to $(1-z)^{1/3}$), as shown in Fig. 2.12. Each sheet is characterized by a pair of integer numbers (n, m) denoting brunches of the functions $z^{1/2}$ and $(1-z)^{1/3}$ accordingly, hence taking on the values $n = 1, 2$ and $m = 1, 2, 3$.

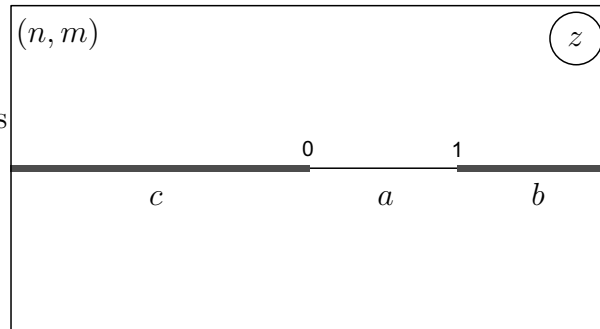


Figure 2.12: A sheet of the Riemann surface for the many-valued functions in (2.49); a, b, c mark the regions on the real axis which correspond to physically different flow regimes.

Let us derive some important properties of solutions (2.49). The variable z may be expressed via u, v explicitly:

$$z = \frac{1}{1 - \beta^2 \frac{u^3}{v^2}}, \quad (2.50)$$

which follows from (2.41) when $\beta = \frac{2}{3}$. It means that physical solutions correspond to real z and are represented by certain trajectories running along the real axis on the Riemann surface. The branching point $z = 0$ corresponds to $v = 0$ (streamlines in the physical plane reach either a local maximum or a minimum at this point), whereas the branching point $z = 1$ corresponds to the sonic line $u = 0$. From (2.50) it can be spotted that subsonic regimes ($u < 0$) are contained in the domain $z \in (0, 1)$, and supersonic regimes are located along the branch cuts $z \in (1, \infty)$ and $z \in (-\infty, 0)$ (regions a , b and c in Fig. 2.12 respectively). The latter, obviously, provides stronger supersonic regimes which will be called *supercritical*. Weaker supersonic regimes are located within the branch-cut $z \in (1, \infty)$ and will be called *subcritical*; a connection between these two types of supersonic solutions is made via the point $z = \infty$ achieved when

$$\zeta^3 = \zeta_c^3, \quad \zeta_c = \left(\frac{1}{\beta^2}\right)^{1/3} \equiv \left(\frac{3}{2}\right)^{2/3}.$$

Using this important value, we can rewrite (2.43) as

$$z = \frac{1}{1 - \left(\frac{\zeta}{\zeta_c}\right)^3}.$$

The equation $(\zeta/\zeta_c)^3 = 1$ is equivalent to $f^3 = \zeta_c^3 g^2$, and defines the two lines

$$g = \pm \frac{2}{3} f^{\frac{3}{2}} \tag{2.51}$$

in the supersonic part of the phase plane ($f > 0$) (see Fig. 2.13). These lines will be called the *critical lines* as they demarcate sub- and supercritical supersonic regimes, with the latter located within the shaded zone in Fig. 2.13. It is easy to show that the upper critical line passes through the node $P_2 = (1, \frac{2}{3})$ (which also lies on the singular line $f = 1$), and the lower critical line passes through the saddle point $P_3 = (\frac{1}{\alpha^2}, -\frac{2}{3\alpha^3})$.

In subsequent sections we are going to formulate and prove several important conjectures for the supercritical flow regimes. One of them says that none of the phase trajectories corresponding to (2.49) can intersect with the critical lines; the trajectories may at best be tangent to the critical lines or coincide with them. Moreover, if the phase trajectory does not completely coincide with either of the critical lines,

functions of z . The original representation in terms of ξ was, in fact, used to derive (2.52). Indeed, according to (2.15),

$$f(\xi) = \frac{F'(\xi)}{\alpha^2 \xi^2} \equiv \frac{u/y}{\alpha^2 \xi^2};$$

this may be rewritten in the form

$$f = \frac{1}{\alpha^2 \xi^2} \frac{1}{y/u},$$

where y/u refers to the general solution of the inverse problem (see (2.49)). Writing ξ^2 as

$$\xi^2 = \frac{x^2}{y^3} \equiv \frac{(x/v)^2}{(y/u)^3} \frac{v^2}{u^3} = \frac{(x/v)^2}{(y/u)^3} \frac{1}{\zeta^3}, \quad (2.53)$$

and recalling (2.50) immediately yields the first equation in (2.52). The expression for $g(z)$ (second equation in (2.52)) is obtained in exactly the same way, through the original definition of $g(\xi)$.

2.4.3 Boundary conditions in the Inverse problem

We now need to formulate boundary conditions for the inverse problem in order to find the constants C_1, C_2 in (2.49). The crucial thing is to determine the values of z which correspond to the physical boundaries $\xi = \pm\infty$. Using the asymptotic form (2.27) of $F(\xi)$, we can work out the velocity perturbations

$$u = yF'(\xi), \quad v = \alpha y^\alpha [\lambda F - \xi F']$$

in the vicinity of both the upstream and the downstream walls, and plug them into the definition of ζ to get the relevant values ζ_\pm :

$$\zeta_\pm^3 = \frac{u^3}{v^2} \Big|_{\xi \rightarrow \pm\infty} = \varkappa_\pm^2 \frac{(\mp \lambda G_\pm)^3}{\varkappa_\pm^2}, \quad \lambda = 3 - \frac{2}{\alpha} = \frac{5}{3}.$$

Along with equation (2.50), this yields the required limiting values of z :

$$z_- = \frac{1}{1 - \beta^2 (\lambda G_-)^3}, \quad z_+ = \frac{1}{1 + \beta^2 (\lambda G_+)^3 \left(\frac{\varkappa_-}{\varkappa_+}\right)^2}, \quad z_\pm \in \mathbb{R}. \quad (2.54)$$

Hence, the boundary conditions for the inverse problem depend upon the curvatures and the pressure gradients' amplitudes on either of the walls.²²⁾ These four parameters play the key role in the entire study, and our main task is to find an analytical relationship between them. Equations (2.54) prove the proposals given in section 2.3.2 (based on the numerical results) for adverse and favorable pressure gradients on both walls. Indeed, if the flow on the upstream wall is subsonic, then $z_- \in (0, 1)$, and according to (2.54) $G_- < 0$, which corresponds to a favorable upstream pressure gradient (see equation (2.28)). The same arguments can be used to prove the proposals for supersonic flows on the upstream wall and for both subsonic and supersonic flows on the downstream wall.

To obtain the trajectories representing the flow in the z plane, we first of all need to know the directions in which they emerge from the starting point z_- and return to the final point z_+ (running along the real axis in between). These may be obtained from the relationship between the differentials dz and $d\xi$ as $\xi \rightarrow \pm\infty$. Since ξ is increasing from $-\infty$ to $+\infty$ along the phase trajectory, $d\xi > 0$ and the sign of dz is the same as of $dz/d\xi$. According to (2.43), $dz = (\beta\zeta)^2 d\zeta^3$; recalling that

$$\zeta^3 = \frac{u^3}{v^2} = \frac{(F')^3}{\alpha^2(\lambda F - \xi F')^2}$$

and using the asymptotic form (2.27) of $F(\xi)$, we arrive at the following equation in the leading order:

$$d\zeta^3 = \pm \frac{C}{\varkappa_{\pm}} \left[1 - \left(\frac{\zeta_{\pm}}{\zeta_c} \right)^3 \right] (\pm\xi)^{-\lambda} d\xi, \quad \xi \rightarrow \pm\infty,$$

where

$$C = (\alpha - 1)(3\beta\lambda G_{\pm})^2 [(\gamma + 1)\varkappa_{\pm}]^{4/3}.$$

Let us assume that on the upstream wall $\varkappa_- > 0$. Thus, the regimes with $\zeta_-^3 < \zeta_c^3$ (oncoming subsonic and subcritical supersonic flows) correspond to $dz < 0$ in the vicinity of z_- – the trajectories in the z plane are leaving to the left of z_- . On the contrary, for $\zeta_-^3 > \zeta_c^3$ (oncoming supercritical supersonic flows) we get $dz > 0$ – the trajectories in the z plane are leaving to the right of z_- (see Fig. 2.14, left).

²²⁾ Recall that the coefficients G_{\pm} are related to the pressure gradients via (2.28).

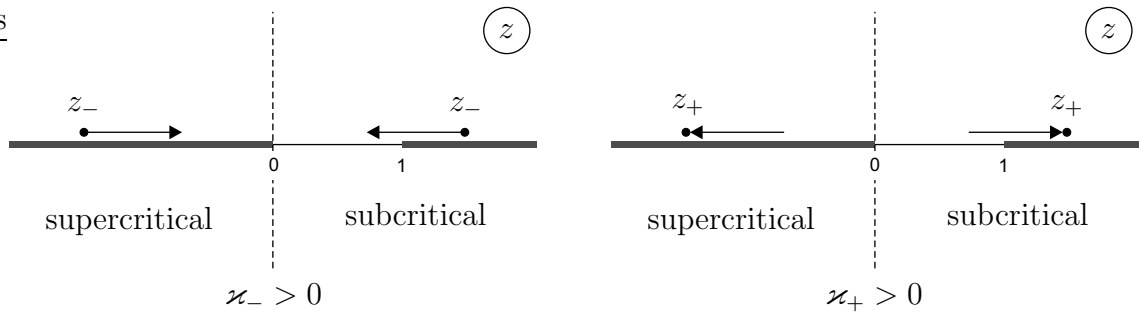


Figure 2.14: Tails of the trajectories in the z plane corresponding to a flow near the upstream wall, left, and the downstream wall, right. The trajectories' direction appears to be the opposite for the subcritical and the supercritical flow regimes.

If on the downstream wall $\kappa_+ > 0$ and $\zeta_+^3 < \zeta_c^3$ (the flow is either subsonic or subcritical supersonic), then the trajectories in the z plane are returning towards z_+ from the left, whereas for $\zeta_+^3 > \zeta_c^3$ (supercritical supersonic flow) the trajectories are returning towards z_+ from the right (see Fig. 2.14, right). However, for concave downstream walls with $\kappa_+ < 0$ the situation is the opposite, as shown in Fig. 2.15.²³⁾

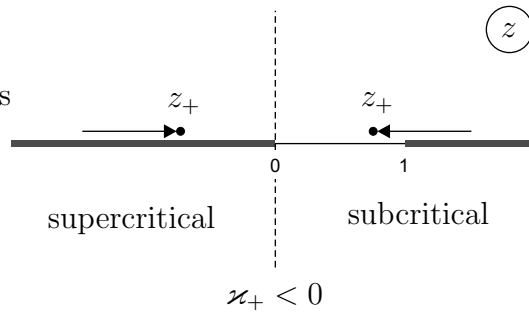


Figure 2.15: Tails of the z plane trajectories corresponding to a flow near a concave downstream wall.

Now we only need to formulate boundary conditions for the functions $x = v\psi(z)$ and $y = u\varphi(z)$ at $z = z_{\pm}$. From the boundary condition (2.3) of the direct problem,

²³⁾ In subsequent sections we will get the same results directly from solutions (2.49) with the appropriate boundary conditions.

which has to be modified slightly according to re-definition (2.6) of v , it follows that

$$\begin{cases} y|_{z=z_{\pm}} = 0, \\ x|_{z=z_{\pm}} = -\frac{v}{(\gamma+1)\kappa_{\pm}}. \end{cases} \quad (2.55)$$

Regardless of the flow regime, we can always apply these conditions at one of the two points z_{\pm} in order to find the constants $C_{1,2}$. Let us choose z_- as it is more natural to start constructing the solutions from the upstream part of the flow. Applying (2.55) (evaluated only at z_-) to (2.49) yields

$$\begin{cases} C_1 = -C_2 B(z_-), \\ C_2 = \frac{z_-^{1/2}(1-z_-)^{1/3}}{3(\gamma+1)\kappa_-}, \end{cases}$$

leading to the following form of the solutions for x, y :

$$\begin{cases} y = u \cdot \frac{z_-^{1/2}(1-z_-)^{1/3}}{3(\gamma+1)\kappa_-} [B(z) - B(z_-)], \\ x = v \cdot \frac{z_-^{1/2}(1-z_-)^{1/3}}{3(\gamma+1)\kappa_-} \left[B(z) - \frac{3}{z^{1/2}(1-z)^{1/3}} - B(z_-) \right]. \end{cases} \quad (2.56)$$

Equations (2.56) are valid subject to an appropriate choice of branches for all the complex-valued functions, including

$$z_-^{1/2}, \quad (1-z_-)^{1/3}, \quad B(z_-)$$

(functions of the constant z_-), and this choice solely depends on the flow regime near the upstream wall. The main criterion is that x and y should always remain real.

As it will be shown later, even for the simplest flow regimes the trajectory in the z plane runs on at least two sheets of the Riemann surface, thus requiring to construct regular branches of all the many-valued functions in (2.56). To do this we shall use the standard exponential representation

$$z = r e^{i\vartheta}$$

of a complex number z , with $-\pi < \vartheta < \pi$ on the sheets $(1, m)$ and $\pi < \vartheta < 3\pi$ on the sheets $(2, m)$. The values $\vartheta = 0, 2\pi$ correspond to real positive $z \in (0, \infty)$ (see

Fig. 2.16). Similarly,

$$(1 - z) = R e^{i\theta},$$

with $-\pi < \theta < \pi$ on the sheets $(n, 1)$, $\pi < \theta < 3\pi$ on the sheets $(n, 2)$ and $3\pi < \theta < 5\pi$ on the sheets $(n, 3)$. The values $\theta = 0, 2\pi, 4\pi$ correspond to real $z \in (-\infty, 1)$ (see Fig. 2.16). The arguments ϑ, θ have been chosen to run through when z moves from one sheet to another because this is convenient for describing transitions between the sheets; however, one can always use local arguments $\bar{\vartheta}, \bar{\theta}$ which are restricted within $(-\pi, \pi)$ on each sheet, thus giving the following expression for the regular branch of

$$z^{1/2}(1 - z)^{1/3}$$

on the sheet (n, m) :

$$z^{1/2}(1 - z)^{1/3} = r^{1/2} R^{1/3} \exp \left\{ \frac{i\bar{\vartheta}}{2} + \frac{i\bar{\theta}}{3} + i\pi(n - 1) + \frac{2\pi i}{3}(m - 1) \right\}, \quad (2.57)$$

$n = \{1, 2\}$, $m = \{1, 2, 3\}$. Finally, R can be expressed in terms of r for real z :

$$R = \begin{cases} 1 + r, & z \in (-\infty, 0), \\ 1 - r, & z \in (0, 1), \\ r - 1, & z \in (1, \infty). \end{cases} \quad (2.58)$$

Now we have enough tools to analyze the main flow regimes, in the order chosen in section 2.3.2 for the numerical computations. But before that it is worth mentioning some important special cases when solutions (2.56) lead to singularities in the Jacobian (2.40).

2.4.4 Special cases resulting in a singular Jacobian

Based upon solutions (2.56) of the inverse problem represented in the form

$$y/u = C \varphi, \quad x/v = C \psi, \quad (2.59)$$

where

$$\varphi(z) = B(z) - B(z_{\pm}), \quad \psi(z) = \varphi(z) - \frac{3}{z^{1/2}(1 - z)^{1/3}}, \quad C = \frac{z_-^{1/2}(1 - z_-)^{1/3}}{3(\gamma + 1)\varkappa_-},$$

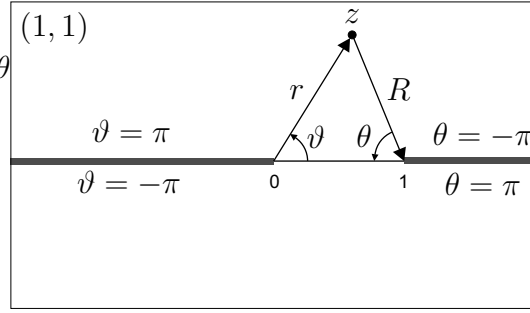


Figure 2.16: Arguments of the complex variables z and $1 - z$.

one can easily derive the following expression for the Jacobian (2.40):

$$\Delta = \left| \frac{\partial(x, y)}{\partial(u, v)} \right| = -C^2 \left[\left(\varphi - \frac{3z^{1/2}}{(1-z)^{1/3}} \right)^2 + 9(1-z)^{1/3} \right] \equiv z \left(\frac{x}{v} \right)^2 (f-1).^{24}$$

(2.60)

The structure of expressions (2.52) for the phase variables suggests that when $|z| \rightarrow \infty$ (with finite z_{\pm}) solutions (2.59) yield the asymptotic forms

$$f = 1 + \mathcal{O}(r^{-5/6}) + \mathcal{O}(r^{-1}), \quad g = \beta + \mathcal{O}(r^{-5/6}) + \mathcal{O}(r^{-1}), \quad r = |z| \rightarrow \infty,$$

i.e. the phase trajectories reach the point P_2 on the singular line. Plugging the above expression for f into (2.60), we see that on approaching P_2 the Jacobian is estimated as $\Delta = \mathcal{O}(r^{1/6})$, and therefore $\Delta \rightarrow \infty$. As it was mentioned at the end of section 2.4.1, an infinite Jacobian does not cause any problems because the functions $x(u, v)$ and $y(u, v)$ are allowed to have multiple values.

However, if the trajectory described by (2.59) crosses the singular line at any point with a finite $z = z_s$ (see section 2.4.11), then from (2.60) it follows that the Jacobian becomes equal to zero, leading to many-valued solutions for $u(x, y)$ and $v(x, y)$. The latter is physically impossible, and makes the crossing illegitimate. This provides an alternative proof that the phase trajectories can only pass through the singular line via the point P_2 which corresponds to the limiting characteristic. The two other singularities occurring in (2.60) when $x \rightarrow 0$ and $v \rightarrow 0$ are removable since in these cases $f \sim x^{-2}$ and $z \sim v^2$ respectively.

²⁴⁾ We used expression (2.52) for f to obtain the last equality.

The Jacobian may also be represented in terms of the phase variables only:²⁵⁾

$$\Delta = \frac{y^{6-4\alpha}}{\alpha^4 \xi^4 (\alpha - 1)^2} \left[\frac{f - 1}{9g^2 - 4f^3} \right].$$

From this it follows that on both critical lines, defined in (2.51), $\Delta = \infty$. Therefore, in the case when a phase trajectory coincides with one of the critical lines, solutions (2.59) do not work, and we have to solve the direct problem (section 2.4.8).

Finally, an immediate connection between the self-similar solutions of the direct and the inverse problems (the latter given by (2.59)) is described by the one-dimensional Jacobian²⁶⁾

$$\frac{d\xi}{d\zeta} = \frac{\beta u z}{y^{1/2} v^{1/3}} \left[\frac{f - 1}{f} \right],$$

which has only one nontrivial singularity when $f = 1$ for a finite z , again referring to the illegitimate crossing of the singular line (the singularity associated with the branching point $z = 0$ is eliminated by moving the trajectory to the next sheet of the Riemann surface, see section 2.4.5). In other words, whenever the Jacobian $d\xi/d\zeta$, treated as a function of z , becomes zero at any finite point of the trajectory in the z plane (except for the origin), the transformation $\xi(\zeta)$ is no longer monotonic, thus creating physically unfeasible multiple values in the functions $u(x, y)$ and $v(x, y)$.²⁷⁾

We shall now move on to describe all the possible local flow regimes which can develop near the curvature break.

2.4.5 Subsonic flow on the upstream wall

In section 2.4.2 it was shown that subsonic flows correspond to $z \in (0, 1)$. Hence, for the regime considered in this section, the upstream boundary conditions are applied at $z_- \in (0, 1)$, and the trajectory leaves to the left if this point towards $z = 0$, due to the property discussed above. To make general solutions (2.56) real in the subsonic region, one needs to use the branch with $n = 1$, $m = 1$ of the function $z^{1/2}(1 - z)^{1/3}$

²⁵⁾ Note that Δ becomes self-similar when $\alpha = \frac{3}{2}$.

²⁶⁾ This formula is deduced from equations (2.53) and (2.52).

²⁷⁾ The point $z = \infty$ is excluded because it corresponds to the removable singularity associated with a limiting characteristic.

(see 2.57). Since $\vartheta = \theta = 0$ for $z \in (0, 1)$, equations (2.57), (2.58) yield

$$z^{1/2}(1-z)^{1/3} = r^{1/2}(1-r)^{1/3}, \quad 0 < r < 1.$$

The function $B(z)$ contains exactly the same regular branch and is real:

$$B(z) \equiv B(r) = \int_0^r \frac{d\rho}{\rho^{1/2}(1-\rho)^{4/3}}, \quad \rho \in \mathbb{R};$$

this is also true for the coefficient $z_-^{1/2}(1-z_-)^{1/3}$, in which z_- can simply be replaced by r_- . Applying these results to (2.56), we get the following solutions in the vicinity of the upstream wall:

$$\begin{cases} y = u \cdot \frac{r_-^{1/2}(1-r_-)^{1/3}}{3(\gamma+1)\varkappa_-} [B(r) - B(r_-)], \\ x = v \cdot \frac{r_-^{1/2}(1-r_-)^{1/3}}{3(\gamma+1)\varkappa_-} \left[B(r) - \frac{3}{r^{1/2}(1-r)^{1/3}} - B(r_-) \right]. \end{cases} \quad (2.61)$$

Since

$$\frac{dB(r)}{dr} = \frac{1}{r^{1/2}(1-r)^{4/3}} \geq 0, \quad 0 < r < 1,$$

$B(r)$ grows steadily with r . Together with the inequality $u < 0$ valid for all subsonic flows and the first equation in (2.61), this implies that the restriction $y \geq 0$ holds for $0 < r \leq r_- < 1$, which means that the trajectory in the z plane indeed goes to the left of r_- . At the same time the second equation in (2.61) gives $x < 0$ when $v > 0$, which is, indeed, the case near a convex upstream wall.

Once the trajectory has left the point r_- , its further behavior in the z plane is quite obvious. First of all, the trajectory cannot turn backwards at any regular point because the transformation $\xi(z)$, as expected, appears to be monotonic for solutions (2.61) (see end of section 2.4.4). Hence, the trajectory goes towards the origin $z = 0$ (which is also the branching point of function $z^{1/2}$). When $z = 0$ is reached, it means that $v = 0$ and the sign of v is to be changed, as it can be seen from the relevant computations in section 2.3.2 (Fig. 2.6). Without a loss of generality, one can say that the change of the sign leads to $\Delta \arg v = +\pi$. Writing the Taylor expansion of (2.50) when $v \rightarrow 0$, $u \neq 0$ yields

$$z = -\frac{v^2}{\beta^2 u^3} (1 + \mathcal{O}(v^2)).$$

Therefore, the change in sign of v corresponds to $\Delta \arg z = +2\pi$, which means that the trajectory makes a single turnover along an infinitesimal circle around the point $z = 0$, and finds itself in the subsonic region on the sheet $(2, 1)$, as shown in Fig. 2.17.

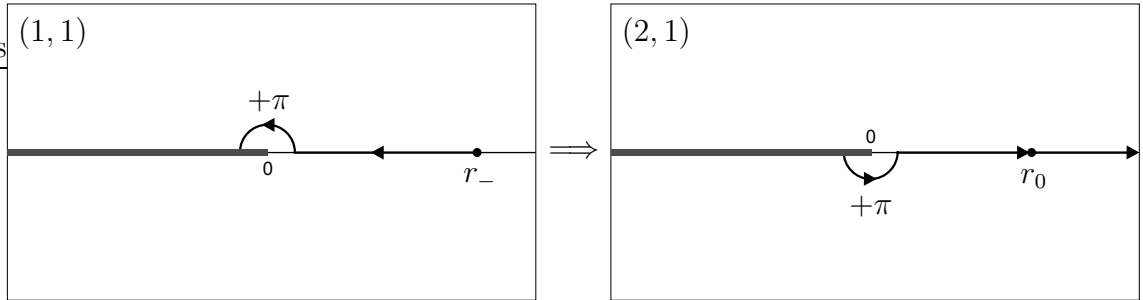


Figure 2.17: First two fragments of the z plane trajectory for an oncoming subsonic flow. The sign of v changes as the trajectory makes a complete turnover around the branching point $z = 0$ and finds itself on the next sheet of the Riemann surface. This is followed by the change of sign of x when $z = r_0$.

There is a theoretical explanation for the fact that v must change sign, based upon the following requirements: a z plane trajectory should always remain on the real axis and cannot turn backwards at any point, while the corresponding solutions for x and y , given by (2.61), should be real for all values of z along the trajectory. The only possibility for a trajectory to comply with these requirements is to make a single turnover around the origin and find itself in the subsonic region on the second sheet of the function $z^{1/2}$, thus providing a change in sign of v . Moreover, the above arguments suggest that a flow which is originally subsonic or subcritical supersonic cannot accelerate to become supercritical supersonic. Should this happen, solutions (2.61) would lead to complex x and y . Due to the same reason supercritical flows cannot decelerate to subcritical supersonic or subsonic speeds. The latter also means that for supercritical supersonic flows the phase trajectories always remain in the supercritical region (Fig. 2.13) unless the flow undergoes a shock, and the relevant trajectories in the z plane have to stay within the left branch-cut.

In the subsonic region on the sheet $(2, 1)$, according to (2.57) and (2.58), $z^{1/2} = -r^{1/2}$, $(1 - z)^{1/3} = (1 - r)^{1/3}$, and from (2.47) $B(z) = -B(r)$. Hence, the turnover

transforms solutions (2.61) into

$$\begin{cases} y = -u \cdot \frac{r_-^{1/2}(1-r_-)^{1/3}}{3(\gamma+1)\varkappa_-} [B(r) + B(r_-)], \\ x = v \cdot \frac{r_-^{1/2}(1-r_-)^{1/3}}{3(\gamma+1)\varkappa_-} \left[\frac{3}{r^{1/2}(1-r)^{1/3}} - (B(r) + B(r_-)) \right]. \end{cases} \quad (2.62)$$

These are the analytical continuations of (2.61) through the singular point $z = 0$ in the equations for $\varphi(z)$ and $\psi(z)$ (see (2.44)). The singularity is trivial, because the relevant solutions in the physical plane are regular near the line $v = 0$, and is simply due to the transformation of the variables associated with the inverse problem. That is the reason why it is removed by means of the analytical continuation.

After the turnover, the trajectory in the z plane leaves to the right of $z = 0$ and travels towards $z = 1$ (see Fig. 2.17) as $\xi(z)$, according to (2.53), continues to grow when r is increasing in (2.62). The expression for y in (2.62) is guaranteed to be positive for $0 < r < 1$ because $u < 0$. However, the solution for x changes its sign from negative to positive at some point $r_0 \in (0, 1)$ which satisfies the transcendental equation

$$\frac{3}{r_0^{1/2}(1-r_0)^{1/3}} = B(r_0) + B(r_-). \quad (2.63)$$

The latter has a clear graphic solution for certain values of the parameter r_- (see Fig. 2.18). This solution appears to be unique and exists when $r_- \in (r_*, 1)$, with

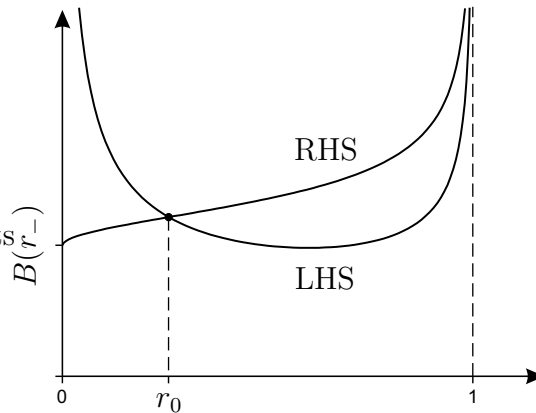


Figure 2.18: Left-hand side (LHS) and right-hand side (RHS) of the transcendental equation (2.63) plotted as functions of r_0 .

$r_* \approx 0.3039$ being the only root of the equation

$$B(r_*) = \frac{3\sqrt{\pi}\Gamma(2/3)}{\Gamma(1/6)}. \quad (2.64)$$

Here

$$\Gamma(s) = \int_0^\infty t^{s-1} e^{-t} dt$$

is the Euler's *Gamma function*.²⁸⁾ The corresponding trajectory in the phase plane stretches into infinity when $r \rightarrow r_0^-$, and reflects itself from the $g = 0$ axis when x changes sign (Fig. 2.6).

Upon passing through r_0 , the trajectory in the z plane approaches the branching point $z = 1$ on the sheet $(2, 1)$. This branching point corresponds to the sonic line ($u = 0$). From the numerical solution we already know that the phase trajectories cross this line and enter the supersonic region, i.e. u needs to change sign once the sonic point $z = 1$ is reached in the plane of complex z . Applying the Taylor expansion to (2.50) when $u \rightarrow 0$, $v \neq 0$ yields

$$z = 1 + \frac{\beta^2 u^3}{v^2} + \mathcal{O}(u^6).$$

Hence, the change in sign of u , which can be expressed as $\Delta \arg u = +\pi$ without a loss of generality, results in $\Delta \arg(1 - z) = +3\pi$. The latter is equivalent to the trajectory making one and a half revolutions along an infinitesimal circle around $z = 1$, finding itself at the lower side of the branch cut $(1, \infty)$ on the sheet $(2, 2)$, as shown in Fig. 2.19.²⁹⁾

To continue the function $B(z)$ analytically through singular point $z = 1$, we use its equivalent representation on the sheet (n, m) :³⁰⁾

$$B(z) = (-1)^n \frac{3\sqrt{\pi}\Gamma(2/3)}{\Gamma(1/6)} + \frac{3}{2} \int_1^z \frac{d\omega}{\omega^{3/2}(1-\omega)^{1/3}} + \frac{3}{z^{1/2}(1-z)^{1/3}}. \quad (2.65)$$

Setting $n = m = 2$, $\tilde{\vartheta} = 0$, $\tilde{\theta} = \pi$ in (2.57), (2.58) and substituting the results into (2.65) gives the real expression for $B(z)$ at the lower side of the branch cut $(1, \infty)$ on

²⁸⁾ Equation (2.64) follows from the asymptotic behavior of $B(z)$ when $z \rightarrow 1^-$.

²⁹⁾ Again, there is a theoretical explanation for this, similar to the one given previously for the change in sign of v .

³⁰⁾ This formula implies using expression (2.57) for $z^{1/2}(1-z)^{1/3}$ and $\omega^{1/2}(1-\omega)^{1/3}$ on the sheet (n, m) .

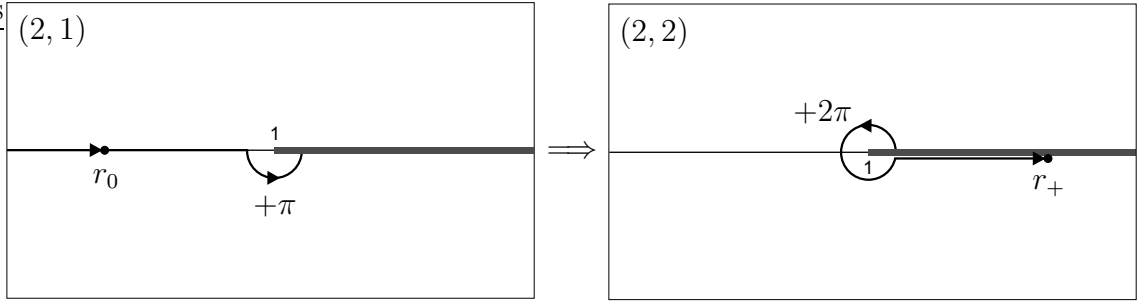


Figure 2.19: Final fragments of the z plane trajectory for an oncoming subsonic flow. The branching point $z = 1$ corresponds to the sonic line ($u = 0$).

the sheet (2, 2):

$$B(z) = \frac{3\sqrt{\pi}\Gamma(2/3)}{\Gamma(1/6)} + \frac{3}{2} \int_1^r \frac{d\rho}{\rho^{3/2}(\rho-1)^{1/3}} + \frac{3}{r^{1/2}(r-1)^{1/3}}, \quad \rho \in \mathbb{R}, \quad 1 < r < \infty.$$

With this expression in mind, one can write down the solutions for x, y in this region, describing a subcritical supersonic flow:

$$\begin{cases} y = u \cdot \frac{r_-^{1/2}(1-r_-)^{1/3}}{3(\gamma+1)\varkappa_-} \left[-B(r_-) + \frac{9\sqrt{\pi}\Gamma(2/3)}{\Gamma(1/6)} + I(r) \right], \\ x = v \cdot \frac{r_-^{1/2}(1-r_-)^{1/3}}{3(\gamma+1)\varkappa_-} \left[-B(r_-) + \frac{9\sqrt{\pi}\Gamma(2/3)}{\Gamma(1/6)} + I(r) - \frac{3}{r^{1/2}(r-1)^{1/3}} \right], \end{cases} \quad (2.66)$$

where

$$I(r) = \int_r^\infty \frac{d\rho}{\rho^{1/2}(\rho-1)^{4/3}}, \quad 1 < r < \infty.$$

Now we have $u > 0, v < 0$. Again, the functions in (2.66) are the analytical continuations of (2.62) through the singular point $z = 1$.

In order to provide a monotonic increase of ξ with x and y given by (2.66), the trajectory in the z plane has to move further to the right of $z = 1$ along the branch cut. It can be easily proved that x remains positive when r is increasing, whereas y becomes zero at some finite point $r_+ > 1$ corresponding to the downstream wall (see Fig. 2.19).³¹⁾ Applying boundary conditions (2.55) to solutions (2.66) at this point,

³¹⁾ Note that the trajectory returns to r_+ from the left, in agreement with the general rule derived earlier.

we arrive at the following algebraic system of two equations:

$$\begin{cases} B(r_-) = \frac{9\sqrt{\pi}\Gamma(2/3)}{\Gamma(1/6)} + I(r_+), \\ \frac{\varkappa_+}{\varkappa_-} = \frac{r_+^{1/2}(r_+ - 1)^{1/3}}{r_-^{1/2}(1 - r_-)^{1/3}}. \end{cases} \quad (2.67)$$

These equations allow to determine any two of the three parameters r_- , r_+ , \varkappa_+/\varkappa_- for a given value of the third one. The most physically meaningful case is when the curvatures' ratio \varkappa_+/\varkappa_- is known and r_{\pm} are expressed as functions of it, yielding the coefficients G_{\pm} related to the wall pressure gradients.

Let us discuss some basic properties of equations (2.67). First of all, the first of them, which implicitly sets a functional dependence $r_+(r_-)$ (or vice versa), admits the limit

$$r_- \rightarrow 1^-, \quad r_+ \rightarrow 1^+,$$

and the rate of the approach is the same from both sides:

$$\lim_{r_- \rightarrow 1^-} \left[\frac{r_+(r_-) - 1}{1 - r_-} \right] = 1.$$

This limit corresponds to $\varkappa_+/\varkappa_- \rightarrow 1$ due to the second equation, and reduces solutions (2.61), (2.62), (2.66) to

$$y = -\frac{u}{(\gamma + 1)\varkappa}, \quad x = -\frac{v}{(\gamma + 1)\varkappa},$$

where $\varkappa = \varkappa_- = \varkappa_+$. The flow described by these linear functions is nothing else than a potential vortex outside a convex cylindrical surface (with no curvature break), and is related to the simple analytical solution $F(\xi) = -(\gamma + 1)\varkappa\xi$ of the direct problem, thus being an important reference point for the whole study.³²⁾ One of the properties of this flow is that there is no pressure gradient on both walls in the leading order, i.e. $G_{\pm} = 0$.

Secondly, system (2.67) also admits the limit $r_+ \rightarrow \infty$, for which r_- tends to a finite value $r_{**} \approx 0.8302$, the latter being the only root of the transcendental equation

$$B(r_{**}) = \frac{9\sqrt{\pi}\Gamma(2/3)}{\Gamma(1/6)}. \quad (2.68)$$

³²⁾ This basic flow regime has already being used in section 2.3.2 to prepare the ground for the computations.

This property is illustrated graphically in Fig. 2.20, where the left-hand side of the first equation in (2.67) is plotted as a function of r_- , and the right-hand side of the same equation – as a function of r_+ . Hence, we get the important restriction for the possible values of r_- (within this particular regime):

$$r_{**} < r_- \leq 1. \tag{2.69}$$

As r_+ increases from 1^+ to ∞ , r_- decreases steadily from 1^- to r_{**} (because both

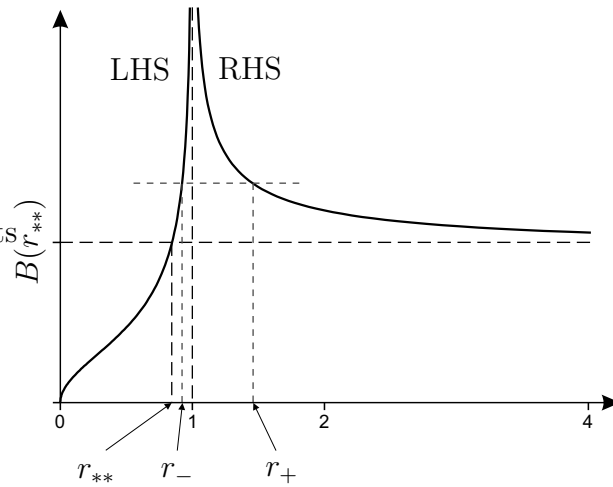


Figure 2.20: Left-hand side (LHS) and right-hand side (RHS) of the first equation in (2.67), plotted as functions of r_- and r_+ respectively.

curves plotted in Fig. 2.20 are monotonic functions of their arguments). Applying this result to the second equation in (2.67), it can be shown that \varkappa_+/\varkappa_- increases monotonely from 1 to ∞ with r_+ , thus covering all the possible values of the curvatures' ratio for the oncoming subsonic flows. Essentially, the upstream flow is subsonic whenever $\varkappa_+/\varkappa_- > 1$, i.e. when the upstream wall is flatter compared to the downstream wall.³³⁾ The limiting value G_{min} of the upstream pressure gradient discovered in section 2.3.2 numerically is then given by

$$G_{min} = \lim_{r_- \rightarrow r_{**}^+} G_- = -\frac{1}{\lambda\beta^{2/3}} \left[\frac{1 - r_{**}}{r_{**}} \right]^{1/3},$$

according to the first equation in (2.54).

³³⁾ For certain supercritical supersonic flows the curvatures' ratio may also be greater than one, although the wall pressure gradients would be completely different (section 2.4.12).

The relevant flow structure in the physical plane is shown in Fig. 2.21. The oncoming subsonic flow (i.e., the subsonic flow near the upstream wall) firstly passes through the line where $v = 0$, and the streamlines reach a local maximum. This line corresponds to

$$\xi = \xi|_{v=0} = -\frac{2}{[B(r_-)]^{\frac{3}{2}}} \left(\frac{3(\gamma+1)\kappa_-}{r_-^{1/2}(1-r_-)^{1/3}} \right)^{1/2},$$

which follows from both (2.61) and (2.62) after applying the limit $v \rightarrow 0$, $r \sim v^2 \rightarrow 0$. The flow then passes through the symmetry axis $x = 0$ and accelerates, transforming to a subcritical supersonic flow; this transition takes place at the sonic line with the position

$$\xi = \xi|_{u=0} = \beta \left[\frac{1}{3} B(r_-) - \frac{\sqrt{\pi} \Gamma(2/3)}{\Gamma(1/6)} \right] \left(\frac{(\gamma+1)\kappa_-}{r_-^{1/2}(1-r_-)^{1/3}} \right)^{1/2},$$

obtained from both (2.62) and (2.66) by taking the limit

$$u \rightarrow 0, \quad r = 1 + \mathcal{O}(u^3) \rightarrow 1.$$

The subcritical supersonic flow occupies the entire space between the sonic line and the downstream wall (see Fig. 2.21).

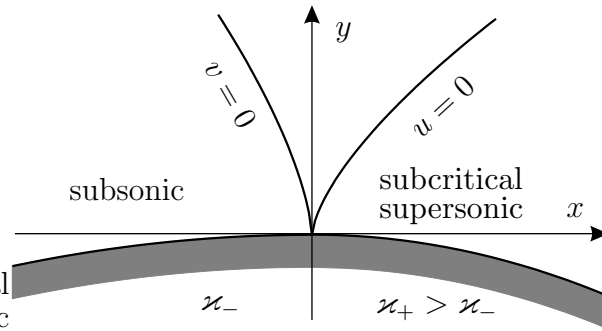


Figure 2.21: Regime with a subsonic flow near the upstream wall.

For the particular flow regime described in this section, the two following limiting cases prove to be important and can be studied analytically:

$$\frac{\kappa_+}{\kappa_-} = 1 + \varepsilon, \quad \frac{\kappa_+}{\kappa_-} = \frac{1}{\varepsilon},$$

where $0 < \varepsilon \ll 1$. Let us discuss them separately.

2.4.6 Two main limiting cases for oncoming subsonic flows

a) $\frac{\varkappa_+}{\varkappa_-} = 1 + \varepsilon$ – a small difference between the curvatures. In this case the set of equations (2.67) yields

$$\begin{cases} (1 - r_-) = C \varepsilon^3 \cdot (1 + \mathcal{O}(\varepsilon)), \\ (r_+ - 1) = C \varepsilon^3 \cdot (1 + \mathcal{O}(\varepsilon)), \end{cases} \quad (2.70)$$

where

$$C = \left(\frac{\Gamma(1/6)}{2\sqrt{\pi}\Gamma(2/3)} \right)^3.$$

The asymptotic expansion of $F(\xi)$ at large $|\xi|$, represented as

$$F(\xi \rightarrow \pm\infty) = \delta_{\pm} |\xi|^{\frac{5}{3}} - (\gamma + 1)\varkappa_{\pm} \xi + \mathcal{O}(\delta_{\pm}^2 |\xi|^{\frac{1}{3}}), \quad (2.71)$$

has the small coefficient

$$\delta_{\pm}(\varepsilon) = \varepsilon \cdot \frac{\Gamma(1/6)}{2\sqrt{\pi}\Gamma(2/3)} \frac{[(\gamma + 1)\varkappa_{\pm}]^{2/3}}{\lambda\beta^{2/3}} (1 + \mathcal{O}(\varepsilon)) \ll 1 \quad (2.72)$$

in front of the leading term.³⁴⁾ Hence, if $|\xi|$ is not large enough, the second term of the expansion actually dominates, and the flow is close to a potential vortex outside a cylinder with a constant curvature (solutions (2.35)). However, in small vicinities of both walls the $|\xi|^{5/3}$ term, which is responsible for the singular pressure gradients, comes into play. The first two terms in the asymptotic expansion of $F(\xi)$ are of the same order when $|\xi| \sim \varepsilon^{-3/2}$, thus giving an estimate for the size of the *perturbed* regions where the flow is essentially different from the potential vortex and generates the singularities in the pressure gradients (see Fig. 2.22). Outside of these regions, i.e. in the rest of the space corresponding to the estimate $|\xi| < \varepsilon^{-3/2}$, we have the leading-order solution³⁵⁾

$$F(\xi) = -(\gamma + 1)\varkappa \xi \cdot (1 + \mathcal{O}(\varepsilon)). \quad (2.73)$$

This important result will be used in chapter 3 to prove that small breaks in wall curvature may lead to a boundary layer separation. Therefore, it is worth providing another argument in support of the simplified expression (2.73).

³⁴⁾ This is deduced from (2.70), (2.54) and (2.27).

³⁵⁾ One can use either \varkappa_- or \varkappa_+ for \varkappa .

Indeed, let us find out what happens with the function

$$y = u \cdot \frac{r_-^{1/2}(1-r_-)^{1/3}}{3(\gamma+1)\varkappa_-} \left[B(r) - B(r_-) \right] \quad (2.74)$$

from solutions (2.61) for the upstream flow when $r_- \rightarrow 1^-$. In this limit the incomplete beta function $B(r_-)$ has the asymptotic form

$$B(r_-) = \frac{3}{(1-r_-)^{1/3}} - \frac{3\sqrt{\pi}\Gamma(2/3)}{\Gamma(1/6)} + \mathcal{O}((1-r_-)^{2/3}). \quad (2.75)$$

Unless the variable r in (2.74) is close to 1 itself, which would correspond to one of the above mentioned perturbed regions with $|\xi| \gtrsim \varepsilon^{-3/2}$, the leading-order term in (2.75) is going to dominate the expression for y . Solution (2.74) is then reduced to

$$y = -u \cdot \frac{r_-^{1/2}}{(\gamma+1)\varkappa_-} \left[1 - (1-r_-)^{\frac{1}{3}} \left(\frac{1}{3} B(r) + \frac{\sqrt{\pi}\Gamma(2/3)}{\Gamma(1/6)} \right) + \mathcal{O}(1-r_-) \right]; \quad (2.76)$$

since $(1-r_-)^{1/3} = \mathcal{O}(\varepsilon)$ according to (2.70), this yields

$$y = -\frac{u}{(\gamma+1)\varkappa_-} [1 + \mathcal{O}(\varepsilon)],$$

as long as $B(r) = \mathcal{O}(1)$. The same result obviously follows from the downstream solutions (2.62), and it is in agreement with the simplified expression (2.73) for $F(\xi)$ outside the small perturbed regions near the wall.

The $(\gamma+1)\varkappa\xi$ term clearly dominates the asymptotic form (2.71) for relatively large $|\xi|$, providing

$$|\xi| \ll \varepsilon^{-3/2}.$$

According to (2.76), however, its dominance is also extended to the values $|\xi| \lesssim 1$, because in this case $B(r) = \mathcal{O}(1)$. As a result, the potential vortex solution works for all ξ from

$$-\varepsilon^{-3/2} \ll \xi \ll \varepsilon^{-3/2},$$

and is suppressed by the $|\xi|^{5/3}$ term only when $|\xi| \gtrsim \varepsilon^{-3/2}$. Thus, the first two asymptotic terms in (2.71) may be used to construct a simplified *composite* solution for $F(\xi)$ which is uniformly valid for all $\xi \in (-\infty, \infty)$ and matches the exact solution with the given accuracy:

$$F(\xi) = \left(\delta_-(\pm\xi)^{\frac{5}{3}} - (\gamma+1)\varkappa_-\xi \right) [1 + \mathcal{O}(\varepsilon)], \quad \delta_- = \mathcal{O}(\varepsilon).$$

This will be exploited in Chapter 3.

The value of ξ corresponding to $v = 0$ in the case of $\frac{\kappa_+}{\kappa_-} = 1 + \varepsilon$ is

$$\xi|_{v=0} = -\varepsilon \beta \sqrt{(\gamma+1)\kappa} \frac{\Gamma(1/6)}{2\sqrt{\pi}\Gamma(2/3)} (1 + \mathcal{O}(\varepsilon)) \sim -\varepsilon,$$

and this coordinate line is close to the symmetry axis $x = 0$, whereas the sonic line approaches the downstream surface:

$$\xi|_{u=0} = \frac{\beta \sqrt{(\gamma+1)\kappa}}{\varepsilon^{3/2}} \left(\frac{2\sqrt{\pi}\Gamma(2/3)}{\Gamma(1/6)} \right)^{3/2} (1 + \mathcal{O}(\varepsilon)) \sim \frac{1}{\varepsilon^{3/2}}.$$

Therefore, a small supersonic region is created near the downstream wall, and its size coincides with the size of the downstream perturbed region (where the singular pressure gradient develops). The relevant flow structure is shown in Fig. 2.22.

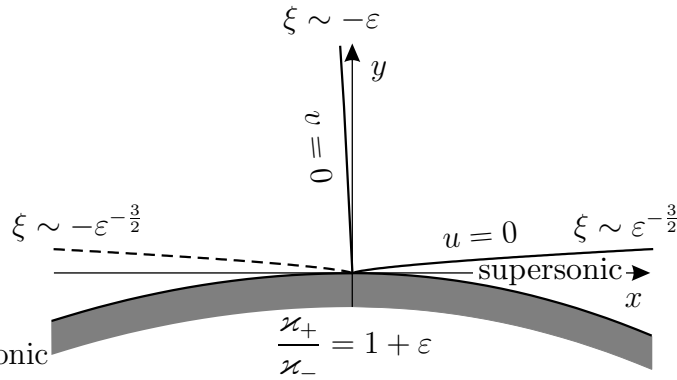


Figure 2.22: Local structure of the flow around a small break of curvatures, with a slightly flatter upstream wall ($\frac{\kappa_+}{\kappa_-} = 1 + \varepsilon$). Singular pressure gradients are generated in thin layers near both walls ($|\xi| \gtrsim \varepsilon^{-3/2}$). The pressure gradients have the small amplitudes $\delta_{\pm} = \mathcal{O}(\varepsilon)$ which are defined in (2.72).

b) $\frac{\kappa_+}{\kappa_-} = \frac{1}{\varepsilon}$ – the upstream surface is close to a flat plate, assuming that κ_+ is an order one quantity. In this case equations (2.67) yield the following asymptotic solutions for the parameters r_{\pm} :

$$\begin{cases} r_- = r_{**} + \frac{6}{5}\varepsilon + \mathcal{O}(\varepsilon^2), \\ r_+ = \left[\frac{r_{**}^{1/2}(1-r_{**})^{1/3}}{\varepsilon} \right]^{6/5} (1 + \mathcal{O}(\varepsilon)) \sim \frac{1}{\varepsilon^{6/5}}, \end{cases}$$

with r_{**} given by (2.68). The lines on which $v = 0$ and $u = 0$ are given, respectively, by

$$\xi|_{v=0} = -2\varepsilon^{1/2} \left(\frac{\Gamma(1/6)}{9\sqrt{\pi}\Gamma(2/3)} \right)^{3/2} \left[\frac{3(\gamma+1)\kappa_+}{r_{**}^{1/2}(1-r_{**})^{1/3}} \right]^{1/2} (1 + \mathcal{O}(\varepsilon)) \sim -\varepsilon^{1/2},$$

$$\xi|_{u=0} = \beta\varepsilon^{1/2} \frac{2\sqrt{\pi}\Gamma(2/3)}{\Gamma(1/6)} \left[\frac{(\gamma+1)\kappa_+}{r_{**}^{1/2}(1-r_{**})^{1/3}} \right]^{1/2} (1 + \mathcal{O}(\varepsilon)) \sim \varepsilon^{1/2},$$

and the flow structure is shown in Fig. 2.23, left. Hence, when $\varepsilon \rightarrow 0$, interpreted as $\kappa_- \rightarrow 0$ with $\kappa_+ = O(1)$, the upstream wall becomes a flat plate, and the flow above it becomes uniform, i.e. $u = v = 0$ for $x < 0$. It can be further shown that this kind of a flow develops a weak discontinuity at $x = 0$, with a break in the second derivatives of the velocity components, and becomes supersonic in the region $x > 0$ (where the wall is curved). This situation is demonstrated in Fig. 2.23, right, and corresponds to the phase trajectory which coincides with lower critical line $g = -\frac{2}{3}f^{\frac{3}{2}}$. In section

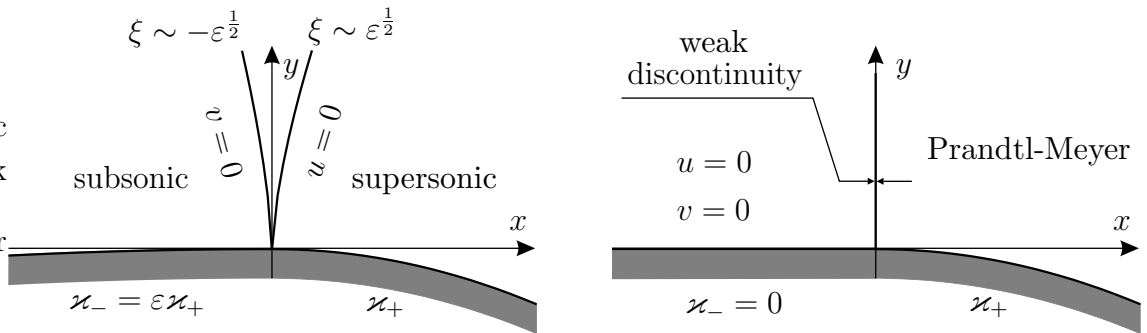


Figure 2.23: Local structure of the flow around a strong break of curvatures ($\frac{\kappa_+}{\kappa_-} = \frac{1}{\varepsilon} \gg 1$), left, and in the case of a flat upstream wall ($\frac{\kappa_+}{\kappa_-} = \infty$), right.

2.4.4 it was shown that the Jacobian (2.40) becomes equal to ∞ on the critical lines, and the flow has to be expressed in the physical variables only, being essentially a transonic Prandtl–Meyer flow (see section 2.4.8). As $\varepsilon \rightarrow 0$, the phase trajectory approaches the saddle point P_3 , and splits into two fragments when $\varepsilon = 0$: the point $P_1 = (0, 0)$ itself which represents the uniform flow ($u, v = 0$) above the plane with $\kappa_- = 0$, and the fragment of the lower critical line between the saddle point and the origin (Fig. 2.24). The weak discontinuity at $x = 0$ is represented by the trajectory’s

jump from the origin to the saddle point. Once in the saddle point, the trajectory returns back to the origin along the lower critical line when the downstream wall is approached. The relevant solution for the velocity potential will be given in section 2.4.8, along with a more rigorous proof of the above results.

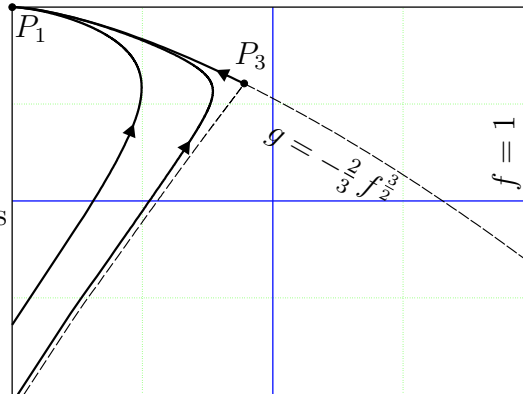


Figure 2.24: Phase trajectories approach the saddle point P_3 when $\frac{\kappa_+}{\kappa_-} \rightarrow \infty$; in the limit they coincide with a fragment of the lower critical line $g = -\frac{2}{3} f^{\frac{3}{2}}$.

This completes our study of the limiting cases within the oncoming subsonic flow regime, for which $1 < \frac{\kappa_+}{\kappa_-} < \infty$. Let us now move to the next flow regime.

2.4.7 Subcritical supersonic flow on the upstream wall

The phase trajectories obtained for the oncoming subsonic flows can be run in the opposite direction, because they stay within the subcritical zone and do not develop discontinuities (except for the trivial jump at $\xi = 0$). Indeed, the substitution $\xi \rightarrow -\xi$ does not change the variable χ in (2.16), and any continuous trajectory described by autonomous system (2.17) can be run in both directions while ξ changes from $-\infty$ to ∞ . These arguments suggest that there should exist a regime which is symmetrical with respect to the oncoming subsonic flow, i.e. with a subcritical supersonic flow on the upstream wall decelerating to subsonic speeds without a shock formation. From the reflection rule it follows that such a flow would exist when $0 < \frac{\kappa_+}{\kappa_-} < 1$ (flatter downstream wall).³⁶⁾

³⁶⁾ This result was also obtained in the computations, see section 2.3.2.

Mathematically the reflection requires the following substitutions in all the analytical solutions derived for the subsonic upstream flows in section 2.4.5:

$$r_- \longleftrightarrow r_+, \quad \varkappa_- \longleftrightarrow \varkappa_+.$$

Now $r_- \in (1, \infty)$, $r_+ \in (r_{**}, 1)$, and the trajectory in the z plane travels in the opposite direction. The whole flow pattern again comprises of three regions. In the first one the solution of the inverse problem is given by

$$\begin{cases} y = u \cdot \frac{r_+^{1/2}(1-r_+)^{1/3}}{3(\gamma+1)\varkappa_+} \left[-B(r_+) + \frac{9\sqrt{\pi}\Gamma(2/3)}{\Gamma(1/6)} + I(r) \right], \\ x = v \cdot \frac{r_+^{1/2}(1-r_+)^{1/3}}{3(\gamma+1)\varkappa_+} \left[-B(r_+) + \frac{9\sqrt{\pi}\Gamma(2/3)}{\Gamma(1/6)} + I(r) - \frac{3}{r^{1/2}(r-1)^{1/3}} \right], \end{cases} \quad (2.77)$$

with $u > 0$, $v > 0$, $r_- \geq r > 1$, corresponding to the subcritical supersonic flow near the upstream wall (see Fig. 2.25). The z plane trajectory starts from the point r_-

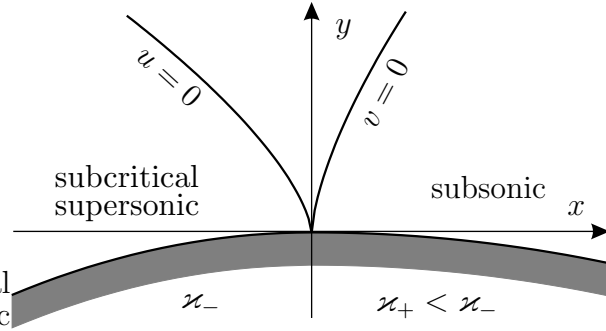


Figure 2.25: Regime with a subcritical supersonic flow near the upstream wall.

on the lower side of the branch cut $(1, \infty)$ on the sheet $(2, 2)$, and moves to the left of r_- towards $z = 1$, where u changes sign. The sonic line is located at

$$\xi = \xi|_{u=0} = -\beta \left(\frac{(\gamma+1)\varkappa_+}{r_+^{1/2}(1-r_+)^{1/3}} \right)^{1/2} \left[\frac{1}{3} B(r_+) - \frac{\sqrt{\pi}\Gamma(2/3)}{\Gamma(1/6)} \right].$$

Passing through the sonic line is equivalent to one and a half turnovers around $z = 1$ along an infinitesimal circle, which brings the trajectory into the subsonic region on the sheet $(2, 1)$. The trajectory then continues to move to the left towards $z = 0$,

with the solutions of the inverse problem given by

$$\begin{cases} y = -u \cdot \frac{r_+^{1/2}(1-r_+)^{1/3}}{3(\gamma+1)\varkappa_+} [B(r_+) + B(r)], \\ x = -v \cdot \frac{r_+^{1/2}(1-r_+)^{1/3}}{3(\gamma+1)\varkappa_+} \left[B(r_+) + B(r) - \frac{3}{r^{1/2}(1-r)^{1/3}} \right]. \end{cases} \quad (2.78)$$

Now $u < 0$, $v > 0$ and $1 > r > 0$. It is this region that contains the point r_0 where $x = 0$ (symmetry axis in the physical plane); r_0 can be found from the transcendental equation

$$\frac{3}{r_0^{1/2}(1-r_0)^{1/3}} = B(r_0) + B(r_+).$$

Once the branching point $z = 0$ is reached, the trajectory makes a single turnover around it, moving to the subsonic zone on the sheet $(1, 1)$. Thus, v changes sign, and the streamlines reach local maxima on the line

$$\xi = \xi|_{v=0} = \frac{2}{[B(r_+)]^{3/2}} \left(\frac{3(\gamma+1)\varkappa_+}{r_+^{1/2}(1-r_+)^{1/3}} \right)^{1/2}$$

in the physical plane. After that the z plane trajectory moves to the right towards the final point r_+ on the sheet $(1, 1)$ (the downstream wall), and the solutions in this region are

$$\begin{cases} y = u \cdot \frac{r_+^{1/2}(1-r_+)^{1/3}}{3(\gamma+1)\varkappa_+} [B(r) - B(r_+)], \\ x = v \cdot \frac{r_+^{1/2}(1-r_+)^{1/3}}{3(\gamma+1)\varkappa_+} \left[B(r) - \frac{3}{r^{1/2}(1-r)^{1/3}} - B(r_+) \right], \end{cases} \quad (2.79)$$

with $u < 0$, $v < 0$ and $0 < r < r_+$. This completes the construction of the analytical solutions for the given regime. The relevant phase trajectories are shown in Fig. 2.9; as mentioned above, they match with the trajectories for the oncoming subsonic flow regime, but run in the opposite direction. Therefore, the two regimes discussed in sections 2.4.5 and 2.4.7 provide the flow patterns which are symmetrical with respect to the $x = 0$ line.

Finally, satisfying the upstream boundary conditions in (2.77) (as the downstream condition is already satisfied in (2.79)), we arrive at the system of two algebraic

equations similar to (2.67):

$$\begin{cases} B(r_+) = \frac{9\sqrt{\pi}\Gamma(2/3)}{\Gamma(1/6)} + I(r_-), \\ \frac{\varkappa_+}{\varkappa_-} = \frac{r_+^{1/2}(1-r_+)^{1/3}}{r_-^{1/2}(r_- - 1)^{1/3}}. \end{cases} \quad (2.80)$$

As before, this system allows to determine the parameters r_{\pm} for a given ratio of the curvatures, and has the same properties as (2.67) (in particular, the two limiting cases discussed in section 2.4.6). The curvatures' ratio is now changing between 1^- (when $r_- = 1^+$, $r_+ = 1^-$) and 0^+ (when $r_- \rightarrow \infty$, $r_+ \rightarrow r_{**}^+$). Solving (2.80) numerically with respect to r_{\pm} finally yields the coefficients G_{\pm} (related to the wall pressure gradients) as functions of the curvatures' ratio; these are plotted in Fig. 2.10. This time the pressure gradients on both walls are adverse (and singular), and a boundary layer separation is expected to take place for this regime. The limiting value G_{max} of the upstream pressure gradient discovered in section 2.3.2 numerically is given by

$$G_{max} = \lim_{r_- \rightarrow \infty} G_- = \frac{1}{\lambda\beta^{2/3}} > |G_{min}|,$$

again following from the first equation in (2.54). In Fig. 2.26 the gradients' ratio is shown as a function of the curvatures' ratio when $0 < \frac{\varkappa_+}{\varkappa_-} < 1$.³⁷⁾

2.4.8 Transonic Prandtl–Meyer flow

Let us now consider the limiting case $\frac{\varkappa_+}{\varkappa_-} = \varepsilon \rightarrow 0$ (interpreted as $\varkappa_- = O(1)$, $\varkappa_+ \rightarrow 0^+$), which is symmetrical as compared to the limit $\frac{\varkappa_+}{\varkappa_-} = \frac{1}{\varepsilon}$ discussed in section 2.4.6. Now $r_- \rightarrow \infty$, $r_+ \rightarrow r_{**}^+$, and solution (2.77) yields that the Jacobian (2.40) tends to infinity as $r \rightarrow \infty$. It means that the inverse transformation $(u, v) \rightarrow (x, y)$ is not uniquely defined, and one has to solve the direct problem (either for $F(\xi)$ or for $f(\xi)$, $g(\xi)$).

To understand this limiting case better, we need to look at the behavior of the corresponding phase trajectories. For small $\frac{\varkappa_+}{\varkappa_-}$ the trajectory, after leaving the origin, is located slightly below the lower critical line $g = -\frac{2}{3}f^{\frac{3}{2}}$ in the supersonic region.

³⁷⁾ This graph is the inversion of Fig. 2.8 plotted for $1 < \frac{\varkappa_+}{\varkappa_-} < \infty$.

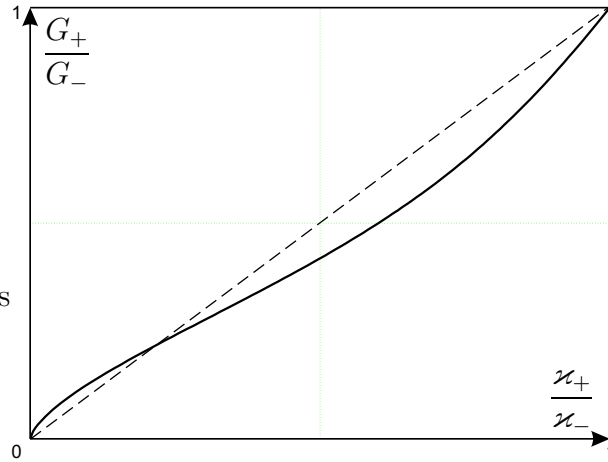


Figure 2.26: The ratio of the gradients plotted versus the ratio of the curvatures when $0 < \frac{\kappa_+}{\kappa_-} < 1$.

When approaching the saddle point P_3 , it abruptly turns to the left and moves towards the subsonic region, see Fig. 2.9. However, in the limit $\frac{\kappa_+}{\kappa_-} \rightarrow 0$ the trajectory merges with the lower critical line, being confined within the fragment of the line between the origin and the saddle point (Fig. 2.9, trajectory d). The Jacobian is equal to ∞ on the critical lines, and, as already mentioned above, in this case one has to solve the direct problem. Luckily, this solution can be obtained analytically.

For this purpose we integrate system (2.17) along the lower critical line. On this line f and g are related through $g = -\frac{2}{3}f^{\frac{3}{2}}$, and both equations in (2.17) are reduced to

$$\frac{df}{d\chi} = 2f - f^{3/2} - 3f^2.$$

Introducing a new function $q(\xi) = 1 + f^{1/2}$ and returning to the original variable ξ via (2.16), we arrive at the following equation:

$$(q - 2)\xi \frac{dq}{d\xi} = (\lambda - q)(q - 1), \quad \lambda = \frac{5}{3},$$

which has the general solution

$$\frac{\lambda - q}{(q - 1)^3} = C \xi^2, \quad C = \text{const}. \quad (2.81)$$

For the fragment of the lower critical line between the origin and the saddle point we have $0 \leq f \leq \frac{1}{\alpha^2}$, so that $1 \leq q \leq \lambda$. Applying this result to (2.81), we see that

$C > 0$. Therefore, (2.81) yields the implicit algebraic equation for $f(\xi)$:

$$\frac{\beta - f^{1/2}}{f^{3/2}} = C \xi^2. \quad (2.82)$$

Once $f(\xi)$ has been obtained from (2.82), $F(\xi)$ can be calculated using the first of equations (2.15). The constant C has to be determined from the boundary condition at $\xi \rightarrow -\infty$ (upstream wall with $\varkappa_- = O(1)$). Indeed, the relevant asymptotic form of $F(\xi)$ is

$$F(\xi) = -\kappa G_- (-\xi)^\lambda - \kappa^\alpha \xi + \dots, \quad \xi \rightarrow -\infty, \quad \kappa = [(\gamma + 1)\varkappa_-]^{1/\alpha},$$

with $G_- > 0$ for the oncoming supersonic flow. Differentiating once and dividing by $\alpha^2 \xi^2$ gives the asymptotic form of $f(\xi)$ near the upstream wall, which can be plugged into (2.82):

$$\frac{\alpha^2 \xi^2}{(\kappa \lambda G_-)^\alpha} + \frac{\alpha^2 (-\xi)^{2-\beta}}{\kappa} \left[\frac{\alpha}{(\lambda G_-)^{\alpha+1}} - \frac{1}{\lambda G_-} \right] + \dots = C \xi^2.$$

This allows to find the parameters G_- and C :

$$G_- = \frac{\alpha^{1/\alpha}}{\lambda} \equiv G_{max}, \quad C = \frac{\alpha}{(\gamma + 1)\varkappa_-}. \quad (2.83)$$

The exact solution may then be represented in one of the following ways:

$$\frac{\beta}{f^{3/2}} - \frac{1}{f} = \frac{\alpha \xi^2}{(\gamma + 1)\varkappa_-}, \quad \frac{\beta}{g} + \frac{\alpha}{f} = -\frac{\alpha^2 \xi^2}{(\gamma + 1)\varkappa_-}. \quad (2.84)$$

From the local analysis of the trajectory's behavior in the vicinity of the saddle point one can find that the critical line $g = -\frac{2}{3} f^{\frac{3}{2}}$ coincides with the second half-line of the saddle (see end of section 2.2.2). Moreover, the trajectory arrives to the saddle point strictly when $\xi = 0$, which can also be obtained from (2.84). All other trajectories, which do not coincide with the lower critical line, either turn to the left (subcritical supersonic flows) or to the right (supercritical supersonic flows) when approaching the saddle point, as shown in Fig. 2.9. Hence, the point somewhat acts as a switch between two physically different regimes. The only trajectory coinciding with the lower critical line may therefore be called the *critical trajectory*, and the relevant solution for $f(\xi)$, given by (2.84), describes the transonic Prandtl–Meyer compression wave (Liepmann & Roshko 1957).

Once this trajectory reaches the saddle point, it cannot go further along the critical line as this would lead to an illegitimate intersection with the singular line $f = 1$. Instead, the trajectory jumps back into the origin and stays there for all $\xi \in (0, \infty)$, thus giving a uniform flow with $u = v = 0$ above the flat downstream wall (see Fig. 2.27). The jump leads to a weak discontinuity along the $x = 0$ line

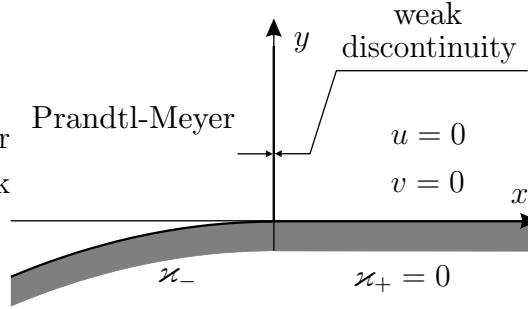


Figure 2.27: Local structure of the flow in the case of a flat downstream wall.

in the physical plane; namely, the second derivatives of the velocity components are broken. Indeed, since the solution for $F(\xi)$ near the saddle point is given by

$$F(\xi) = \frac{\xi^3}{3} (1 + \mathcal{O}(\xi^2)), \quad \xi \rightarrow 0^-,$$

the second derivatives

$$\frac{\partial^2(u, v)}{\partial x^n y^{2-n}} \sim F'''(\xi) \rightarrow 2, \quad n = 0, 1, 2.$$

Therefore, we have the nonzero second derivatives when $\xi \rightarrow 0^-$ and zero second derivatives when $\xi \rightarrow 0^+$ because the flow is uniform for all $\xi > 0$.

The downstream wall pressure gradient (proportional to G_+) is obviously zero in the uniform flow over a flat downstream wall. By applying the limit $\frac{\varkappa_+}{\varkappa_-} \rightarrow 0$ to the flow regime described in section 2.4.7 it can be shown that

$$\lim_{\varkappa_+ \rightarrow 0} \left[\frac{G_+}{\varkappa_+^{2/3}} \right] = \frac{1}{\lambda} \left(\frac{1}{\beta \varkappa_-} \right)^{2/3} \left(\frac{1 - r_{**}}{r_{**}} \right)^{1/3}, \quad \varkappa_- = \mathcal{O}(1),$$

with r_{**} defined in (2.68). Thus, $G_+ \sim \varkappa_+^{2/3} \rightarrow 0$ when $\varkappa_+ \rightarrow 0$.

All these results are symmetric to the case of $\varkappa_- = 0$, $\varkappa_+ = \mathcal{O}(1)$, which was considered qualitatively in section 2.4.6. This is, in fact, the last regime with the

reversibility property with respect to the transformation $x \rightarrow -x$. The next regime to follow (when the phase trajectory is slightly above the critical line and turns to the right upon passing by the saddle point) involves supercritical supersonic flows. The latter inevitably develop shock waves and therefore cannot be inverted.

2.4.9 Supercritical supersonic flow on the upstream wall

This regime takes place when phase trajectories start into the supercritical region (Fig. 2.13), i.e. when $G_- > G_{max}$, $\zeta_-^3 > \zeta_c^3$ and z_- is somewhere within the branch cut $(-\infty, 0)$. Without losing generality, we can continue solutions (2.56) analytically to the lower side of the branch cut on the sheet $(1, 1)$ to get the following solution near the upstream wall:

$$\begin{cases} y = u \cdot \frac{r_-^{1/2}(1+r_-)^{1/3}}{3(\gamma+1)\alpha_-} [J(r_-) - J(r)], \\ x = v \cdot \frac{r_-^{1/2}(1+r_-)^{1/3}}{3(\gamma+1)\alpha_-} \left[J(r_-) - J(r) - \frac{3}{r^{1/2}(1+r)^{1/3}} \right]; \end{cases} \quad (2.85)$$

here

$$J(r) = \int_0^r \frac{d\rho}{\rho^{1/2}(1+\rho)^{4/3}}.$$

Since $y \geq 0$ and $u > 0$ in the oncoming supersonic flow, $r \leq r_-$ in (2.85), and the z plane trajectory leaves to the right of z_- , travelling towards the origin (see Fig. 2.28). This result has already been obtained in section 2.4.3.

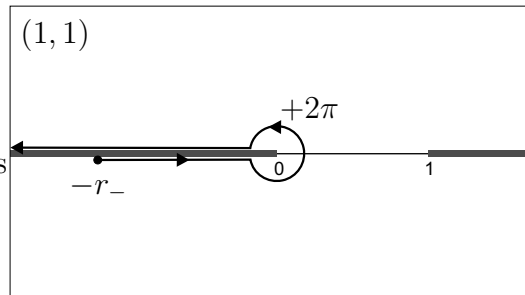


Figure 2.28: Initial fragment of the z plane trajectory corresponding to a supercritical supersonic flow near the upstream wall. Note that $z_- = -r_-$ in this case.

The subsequent behavior of the z plane trajectory is obvious. Due to presence of the saddle point P_3 the relevant phase trajectory gradually turns upwards and crosses the line $g = 0$, i.e. the sign of v changes. This can be clearly seen from the computations in section 2.3.2. Hence, in the z plane the trajectory reaches the point $z = 0$, and makes a single turnover along an infinitesimal circle around it, finding itself on the upper side of the supercritical branch cut $(-\infty, 0)$. The turnover transforms solutions (2.85) into

$$\begin{cases} y = u \cdot \frac{r_-^{1/2}(1+r_-)^{1/3}}{3(\gamma+1)\varkappa_-} [J(r_-) + J(r)], \\ x = v \cdot \frac{r_-^{1/2}(1+r_-)^{1/3}}{3(\gamma+1)\varkappa_-} \left[J(r_-) + J(r) + \frac{3}{r^{1/2}(1+r)^{1/3}} \right]. \end{cases} \quad (2.86)$$

Now $v < 0$, and x is still negative. The trajectory then moves from the origin to the left along the upper side of the branch cut, and runs towards $z = -\infty$ (see Fig. 2.28). From solutions (2.86) and the general formulae (2.52) for the phase variables, one can easily obtain that $f \rightarrow 1$, $g \rightarrow \frac{2}{3}$ when $r \rightarrow \infty$. It means that the phase trajectory is moving towards the point $P_2 = (1, \frac{2}{3})$ located at the intersection of the upper critical line $g = \frac{2}{3} f^{\frac{3}{2}}$ and the singular line $f = 1$ (Fig. 2.9, trajectory e). A detailed study of this point was performed in section 2.2.2; P_2 is one of the three stationary points of equations (2.17) and is a node. The latter means that all the trajectories in the supercritical zone eventually tend to pass through this point. Moreover, P_2 is the only point where the phase trajectories are allowed to cross the singular line, and it corresponds to the limiting characteristic.

To understand how the trajectories behave near the critical point P_2 and what happens after they have passed through this point, let us consider the asymptotic behavior of (2.86) as $r \rightarrow \infty$. By introducing

$$C = \frac{r_-^{1/2}(1+r_-)^{1/3}}{3(\gamma+1)\varkappa_-}, \quad \sigma = J(r_-) + J(\infty), \quad (2.87)$$

where

$$J(\infty) = \frac{3\sqrt{3\pi}\Gamma(2/3)}{\Gamma(1/6)},$$

we get:

$$\begin{cases} y/u = C\sigma \left[1 - \frac{6}{5\sigma} r^{-5/6} + \dots \right], \\ x/v = C\sigma \left[1 + \frac{9}{5\sigma} r^{-5/6} + \dots \right], \end{cases} \quad r \rightarrow \infty. \quad (2.88)$$

It immediately follows from these equations that

$$\xi^2 = \frac{x^2}{y^3} = \frac{\beta^2}{C\sigma} \left[1 + \frac{36}{5\sigma} r^{-5/6} + \dots \right], \quad r \rightarrow \infty. \quad (2.89)$$

Therefore, $\xi \rightarrow \xi_c^-$ when $r \rightarrow \infty$, where

$$\xi_c = -\frac{\beta}{[J(r_-) + J(\infty)]^{1/2}} \left(\frac{3(\gamma + 1)\varkappa_-}{r_-^{1/2}(1 + r_-)^{1/3}} \right)^{1/2} \quad (2.90)$$

refers to the position of the limiting characteristic in the physical plane.³⁸⁾ Note that ξ_c may only be obtained if both \varkappa_- and r_- (or \varkappa_- and G_-) are known.

Plugging (2.88) into (2.52) yields the relevant asymptotic forms for the phase variables near P_2 :

$$\begin{cases} f = 1 - \frac{6}{\sigma} r^{-5/6} + r^{-1} + \dots, \\ g = \beta \left[1 + \frac{9}{\sigma} r^{-5/6} + r^{-1} + \dots \right], \end{cases} \quad r \rightarrow \infty. \quad (2.91)$$

From these we can work out dg/df and d^2g/df^2 along the phase trajectories approaching P_2 from the left:

$$\begin{cases} \frac{dg}{df} = 1 + \frac{\sigma}{15} r^{-1/6} + \dots, \\ \frac{d^2g}{df^2} = -\frac{\sigma^2}{2(15)^2} r^{2/3} + \dots, \end{cases} \quad r \rightarrow \infty. \quad (2.92)$$

The first equation in (2.92) suggests that the trajectories become tangent to the upper critical line when they reach the critical point. Indeed, the line has the equation $g = \frac{2}{3} f^{\frac{3}{2}}$ which yields $dg/df = \sqrt{f} = 1$ when $f = 1$.³⁹⁾ According to the second equation in (2.92), the trajectories' curvature has a singularity at this point. Hence, the function $g(f)$ is likely to have fractional powers of f in its expansion near P_2 , making $f = 1$ a branching point in the plane of complex f (the latter is obviously different from the phase plane). We now need to continue the solutions analytically through this point, so that they would remain real when $f > 1$.

³⁸⁾ In our case $\xi_c < 0$ because $x < 0$ in (2.86).

³⁹⁾ One of the node's half lines also corresponds to $dg/df = 1$, see section 2.2.2.

2.4.10 Passing through the limiting characteristic

Let us perform the analytical continuation of the function $g(f)$ through the singular line via the point P_2 . Equation (2.32) yields the following expansion of $\bar{g} = g - \frac{2}{3}$ over the powers of $\bar{f} = f - 1$:

$$\bar{g}(\bar{f}) = \bar{f} \left[G_1(\bar{f}) + (-\bar{f})^\nu G_2(\bar{f}) \right], \quad \bar{f} < 0, \quad |\bar{f}| \ll 1, \quad (2.93)$$

where

$$\nu = \frac{5\alpha - 7}{\alpha + 1},$$

and the functions

$$G_1(\bar{f}) = 1 + \sum_{n=1}^{\infty} a_n \bar{f}^n, \quad G_2(\bar{f}) = \sum_{n=0}^{\infty} b_n \bar{f}^n$$

are analytical functions of their argument. It is clearly seen that $\bar{f} = 0$ is a branching point in the complex plane \bar{f} unless ν is an integer. Since $\nu = \frac{1}{5}$ when $\alpha = \frac{3}{2}$, the function $\bar{g}(\bar{f})$ has a total of 5 branches due to this point, defined on the relevant Riemann surface.

Writing the first two of terms of (2.93) explicitly gives

$$\bar{g}(\bar{f}) = \bar{f} + b_0 (-\bar{f})^{6/5} + \mathcal{O}(\bar{f}^2).$$

The constant b_0 remains a free parameter upon substituting (2.93) into the equation (2.32) for the direct problem; analytical expression for b_0 can only be obtained from the inverse problem. Indeed, by plugging the last expression into the asymptotic expansions (2.92) we get the equation

$$\nu(\nu + 1)b_0 = -\frac{(\sigma/15)^6}{2 [(\nu + 1)b_0]^4},$$

which has the single real root ⁴⁰⁾

$$b_0 = -\frac{1}{3} \left(\frac{\sigma}{6} \right)^{6/5}.$$

As expected, b_0 depends upon the value of r_- on the upstream wall (via σ). In other words, the phase trajectories corresponding to different upstream boundary

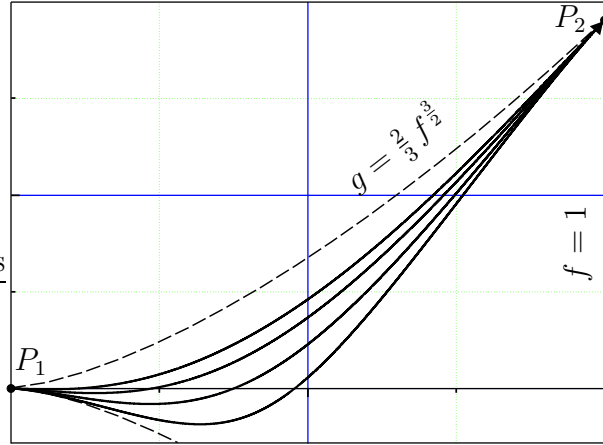


Figure 2.29: Supercritical phase trajectories before passing through the critical point P_2 . The trajectories corresponding to larger values of G_- (stronger adverse pressure gradients on the upstream wall) are closer to the upper critical line $g = \frac{2}{3} f^{3/2}$.

conditions enter the point P_2 slightly differently, although $dg/df \rightarrow 1^+$ and $d^2g/df^2 \rightarrow -\infty$ when $f \rightarrow 1^-$ anyway (Fig. 2.29).

Expansion (2.93) is equivalent to the following asymptotic form of the function $F(\xi)$ as $\xi \rightarrow \xi_c^-$:

$$F(\xi) = F_c + F'_c(\xi - \xi_c) + \frac{F''_c}{2}(\xi - \xi_c)^2 + A(\xi_c - \xi)^{11/5} + \dots; \quad (2.94)$$

here

$$F_c = \frac{5\alpha^2\xi_c^3}{3\lambda}, \quad F'_c = \alpha^2\xi_c^2, \quad F''_c = \alpha(\alpha - 1)\xi_c, \quad A = \frac{15}{88} \frac{\xi_c}{|\xi_c|^{1/5}} \left(\frac{5\sigma}{18} \right)^{6/5}.$$

The fractional power term leads to a singularity in F''' , causing singularities in the second derivatives of u, v . The function $(\xi - \xi_c)^{1/5}$ also has 5 branches defined on the relevant 5-sheet Riemann surface, and needs to be continued analytically to the right of ξ_c .

To perform the continuation, we are going to employ the general solutions (2.56) of the inverse problem, which take the form of (2.86) just before the phase trajectories reach the point P_2 . For example, the first expression in (2.56) may be written as

$$y/u = \tilde{C} \int_{\mathcal{L}} \frac{d\omega}{\omega^{1/2}(1-\omega)^{4/3}}, \quad \tilde{C} = \frac{z_-^{1/2}(1-z_-)^{1/3}}{3(\gamma+1)\varkappa_-}, \quad (2.95)$$

⁴⁰⁾ σ is defined in (2.87).

where the contour \mathcal{L} (also called ‘the z plane trajectory’ in previous sections) is shown in Fig. 2.30 and represents the supercritical supersonic upstream flow before passing through the limiting characteristic.⁴¹⁾ The regular branches of the functions

$$\omega^{1/2}(1-\omega)^{1/3}, \quad z_-^{1/2}(1-z_-)^{1/3}$$

are defined according to (2.57). Splitting the integral in (2.95) into two fragments along the lower and then the upper side of the branch cut $(-\infty, 0)$ on the sheet $(1, 1)$ ($n = m = 1, \bar{\theta} = 0$), and substituting $\bar{\vartheta} = \mp\pi$ respectively into (2.57), we obtain the regular branches of $\omega^{1/2}(1-\omega)^{1/3}$ on these sides. This immediately yields (2.86).

When \mathcal{L} reaches $-\infty$, solution (2.95) is reduced to

$$y/u = C \left[J(r_-) + J(\infty) \right], \quad C = \tilde{C} e^{i\pi/2} \equiv \frac{r_-^{1/2}(1+r_-)^{1/3}}{3(\gamma+1)\varkappa_-} \in \mathbb{R}.$$

Once at $-\infty$, the only possibility for the contour to move further is to join the infinite circle centered at the origin (Fig. 2.30) and make several turnovers until the function $\omega^{1/2}(1-\omega)^{1/3}$ becomes real again on a different sheet of the Riemann surface. The minimal required change of $\arg z$ in these turnovers is simply equal to the least common multiple of 2 and 3 times π , thus giving $\Delta \arg z = 6\pi$ (three turnovers). Indeed, the function $z^{1/2}$ requires the transitions with $\Delta \arg z = 2\pi k, k \in \mathbb{Z}$ to keep solution (2.95) real, and the function $(1-z)^{1/3}$ needs $\Delta \arg(1-z) = 3\pi k, k \in \mathbb{Z}$. On the infinite circle $\Delta \arg z = \Delta \arg(1-z)$, which means that $z^{1/2}(1-z)^{1/3}$ takes a minimum of three turnovers along the circle to provide another real solution for y .

It can be easily shown that the three turnovers bring the z plane trajectory to the upper side of the branch cut $(-\infty, 0)$ on the sheet $(2, 1)$ (Fig. 2.31); as a result, the function $\omega^{1/2}(1-\omega)^{1/3}$ gains an extra multiple of $e^{i\pi} \equiv -1$. Now the contour has to move along the branch cut from $-\infty$ to the right as there is no other alternative of how to keep y real and ensure that the transformation $\xi(z)$ is monotonic. Since the integral along the infinite circle vanishes, solution (2.95) takes the form of

$$y/u = C \left[J(r_-) + J(\infty) - \int_{\infty}^r \frac{d\rho}{\rho^{1/2}(1+\rho)^{4/3}} \right] \equiv C \left[J(r_-) + 2J(\infty) - J(r) \right] \quad (2.96)$$

⁴¹⁾ The contour starts at the point z_- , ends at any given point z (upper limit of the integral), and has to stay within the real axis everywhere in between.

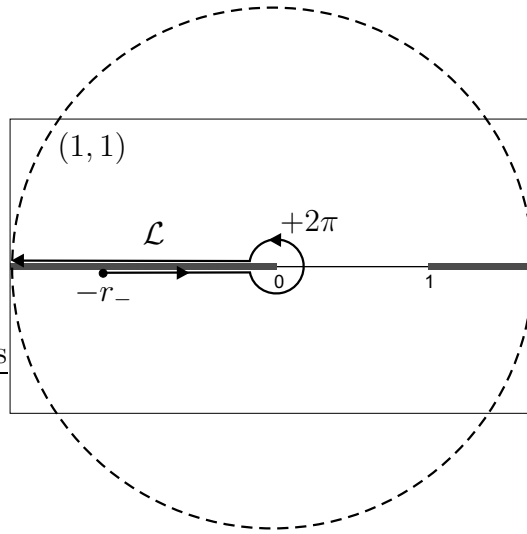


Figure 2.30: Analytical continuation of the solutions through the limiting characteristic is performed when the integration contour \mathcal{L} moves to the infinite circle in the plane of complex z .

after the transition. The structure of this expression, which is the analytical continuation of (2.86) from the upper side of the branch cut $(-\infty, 0)$ on the sheet $(1, 1)$ to the upper side of the branch cut $(-\infty, 0)$ on the sheet $(2, 1)$, is due to the additive property of an integral, and also due to the change in sign of the integrand upon the three turnovers. Expression (2.96) is, in fact, the only nontrivial continuation of (2.86), as the next possible transition, characterized by $\Delta \arg z = 12\pi$, brings the trajectory back to where it started and yields (2.86) again; a transition with $\Delta \arg z = 18\pi$ results in (2.96), and so on.

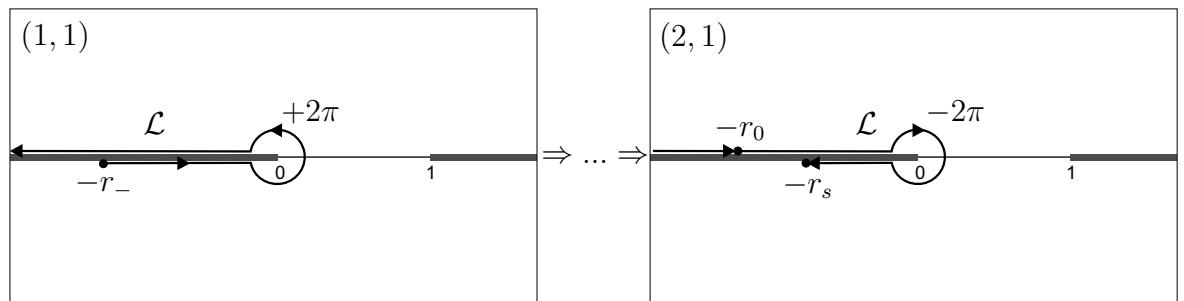


Figure 2.31: As a result of the analytical continuation describing how the flow passes through the limiting characteristic, the integration contour \mathcal{L} in the z plane moves to another sheet of the Riemann surface.

Let us now find out what happens with the expansion (2.93) for $\bar{g}(\bar{f})$ when the z plane trajectory makes three turnovers along the infinite circle. From (2.91) it follows that $\bar{f} \sim z^{-5/6}$ when $z \rightarrow \infty$. Thus,

$$|\bar{f}| \rightarrow 0, \quad \Delta \arg \bar{f} = -\frac{5}{6} \Delta \arg z = -5\pi,$$

which means the complex variable \bar{f} makes two and a half turnovers along an infinitesimal circle around the point $\bar{f} = 0$ (in the plane of complex \bar{f}), and finds itself on the right of this point, having moved 2 sheets down on the relevant Riemann surface. The move produces $\Delta \arg(\bar{f}^{6/5}) = -6\pi$, transforming expansion (2.93) into

$$\bar{g}(\bar{f}) = \bar{f} [G_1(\bar{f}) + \bar{f}^\nu G_2(\bar{f})] = \bar{f} + b_0 \bar{f}^{6/5} + O(\bar{f}^2), \quad 0 < \bar{f} \ll 1.$$

Hence, the phase trajectories tunnel through P_2 to the right of the singular line, with $dg/df \rightarrow 1^-$ and $d^2g/df^2 \rightarrow -\infty$ when $\bar{f} \rightarrow 0^+$ (Fig. 2.11). They literally get reflected from the upper critical line and stay within the supercritical region. The latter can also be seen from the fact that the z plane trajectory always remains on the branch cut $(-\infty, 0)$ unless a shock is developed (creating a jump in both the phase and the z plane trajectories – see section 2.4.11). Indeed, should it leave the branch cut for either the subsonic region $z \in (0, 1)$ or the subcritical supersonic region $z \in (1, \infty)$, solution (2.95) would become complex.

As the z plane trajectory makes three turnovers along the infinite circle, the complex variable ξ also undergoes two and a half turnovers around the point ξ_c and moves to the right of ξ_c along an infinitesimal ark, which follows from expansion (2.89). The asymptotic form (2.94) of $F(\xi)$ then yields the right-hand side expansion

$$F(\xi) = F_c + F'_c(\xi - \xi_c) + \frac{F''_c}{2}(\xi - \xi_c)^2 - A(\xi - \xi_c)^{11/5} + \dots, \quad 0 < (\xi - \xi_c) \ll 1, \quad (2.97)$$

characterized by the opposite sign in front of the singular term as compared to the left-hand side expansion (2.94).

This completes the continuation of the main functions through the singular line.

Based upon (2.96), we write the analytically continued solutions of the inverse problem in the form

$$\begin{cases} y/u = C [J(r_-) + 2J(\infty) - J(r)] , \\ x/v = C \left[J(r_-) + 2J(\infty) - J(r) - \frac{3}{r^{1/2}(1+r)^{1/3}} \right] , \end{cases} \quad (2.98)$$

with the contour \mathcal{L} running along the upper side of the branch cut $(-\infty, 0)$ on the sheet $(2, 1)$ from $-\infty$ towards the origin (Fig. 2.31, right). These solutions express the flow immediately after passing through the limiting characteristic.

2.4.11 Shock formation

It has already been observed in the computations that, after passing through the point P_2 , the phase trajectory travels to (∞, ∞) and reflects in the $g = 0$ axis when x (and ξ) changes sign (Fig. 2.11). This is exactly what solutions (2.98) give; rewriting them as

$$\begin{cases} y/u = C \left[-J(r) + J(r_0) + \frac{3}{r_0^{1/2}(1+r_0)^{1/3}} \right] , \\ x/v = C \left[-J(r) - \frac{3}{r^{1/2}(1+r)^{1/3}} + J(r_0) + \frac{3}{r_0^{1/2}(1+r_0)^{1/3}} \right] , \end{cases}$$

where

$$C = \frac{r_-^{1/2}(1+r_-)^{1/3}}{3(\gamma+1)\varkappa_-}$$

and r_0 satisfies the equation

$$J(r_0) + \frac{3}{r_0^{1/2}(1+r_0)^{1/3}} = J(r_-) + 2J(\infty), \quad (2.99)$$

we see that x , indeed, changes sign. This happens when the z plane trajectory passes through the point $z_0 = -r_0$ on the upper side of the branch cut $(-\infty, 0)$ (Fig. 2.31, right). Since $u > 0$, $v < 0$ in the region considered, x is negative for $\infty > r > r_0$ and positive for $r_0 > r > 0$, in agreement with the requirement that $\xi(z)$ should grow monotonely along the contour \mathcal{L} . Equation (2.99) has a clear graphic solution which depends on the value of r_- , as shown in Fig. 2.32. When r_- decreases from the infinity to zero, r_0 increases steadily and remains finite for all the values of r_- .

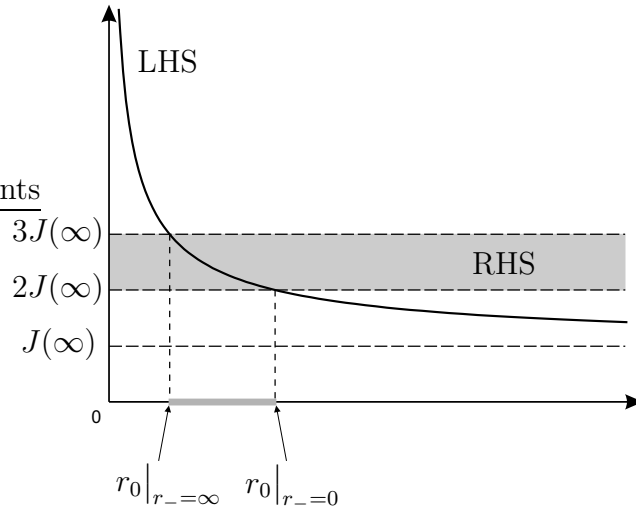


Figure 2.32: The left-hand side (LHS) of equation (2.99), plotted as a function of r_0 , intersects with the shaded area representing all the possible values of the right-hand side (RHS) of (2.99). As a result, the solution for r_0 is confined within a finite interval.

After passing through the point z_0 , the z plane trajectory keeps moving towards the origin. Once in the origin, it makes a single turnover along an infinitesimal circle, funding itself on the lower side of the brunch cut (see Fig. 2.31, right). Thus, v changes sign for the second time, as predicted in the computations, with the loci of streamlines minima at

$$\xi = \xi|_{v=0} = \frac{2}{[J(r_-) + 2J(\infty)]^{\frac{3}{2}}} \left(\frac{3(\gamma + 1)\varkappa_-}{r_-^{1/2}(1 + r_-)^{1/3}} \right)^{1/2};$$

in comparison, the first change of sign of v corresponds to

$$\xi|_{v=0} = -\frac{2}{[J(r_-)]^{\frac{3}{2}}} \left(\frac{3(\gamma + 1)\varkappa_-}{r_-^{1/2}(1 + r_-)^{1/3}} \right)^{1/2}.$$

The relevant phase trajectory crosses the axis $g = 0$, still remaining on the right of the singular line. In fact, the f -coordinate of the point where $g = 0$ is given by

$$f|_{g=0} = \left[\frac{J(r_-) + 2J(\infty)}{3} \right]^2 \geq \left[\frac{2J(\infty)}{3} \right]^2 \approx 2.231 > 1 \quad \forall r_-.$$

As shown in the computations, the phase trajectory then moves towards the node point P_2 , but never reaches it. Instead it tries to cross the singular line below P_2

(Fig. 2.11). This behavior can be explained theoretically. Indeed, after the turnover around the origin solutions (2.98) are transformed into

$$\begin{cases} y/u = C \left[J(r) + J(r_-) + 2J(\infty) \right], \\ x/v = C \left[J(r) + \frac{3}{r^{1/2}(1+r)^{1/3}} + J(r_-) + 2J(\infty) \right], \end{cases} \quad (2.100)$$

with $u > 0$, $v > 0$. The z plane trajectory now moves along the lower side of the supercritical branch cut to the left, so that r is increasing in (2.100). Plugging (2.100) into the expression (2.60) for the Jacobian and setting it to zero, we get the equation

$$\left[J(r) - \frac{3r^{1/2}}{(1+r)^{1/3}} + J(r_-) + 2J(\infty) \right]^2 = 9(1+r)^{1/3}, \quad (2.101)$$

which again has a clear graphical solution at some finite point r_s , see Fig. 2.33.⁴²⁾

This is because the function

$$J(r) - \frac{3r^{1/2}}{(1+r)^{1/3}}$$

decreases steadily from 0 to $-\infty$ with r ; therefore, the left-hand side of (2.101) decreases from $[J(r_-) + 2J(\infty)]^2$ to 0 (when the whole expression in the brackets becomes equal to zero) and then starts to grow again. On the way down it crosses the right-hand side of (2.101) which goes lower than the left-hand side at $r = 0$ since $9 < [J(r_-) + 2J(\infty)]^2$ for all r_- , but then monotonely grows with r .

After setting $r = r_s$ and performing a few trivial transformations, equation (2.101) can be rewritten as

$$J(r_s) + J(r_-) + 2J(\infty) = \frac{3}{(1+r_s)^{1/3}} \left[r_s^{1/2} + (1+r_s)^{1/2} \right].$$

Solutions (2.100) then yield the following values of f and g when $r = r_s$:

$$f|_{r=r_s} = 1, \quad g|_{r=r_s} = \frac{2}{3} \sqrt{\frac{r_s}{1+r_s}} < \frac{2}{3}. \quad (2.102)$$

Therefore, the trajectory is trying to pass through the singular line where it is not allowed to do so (which is, basically, at any point except for P_2 , see sections 2.2.2, 2.4.4). This is illustrated in Fig. 2.34 for the supercritical phase trajectories cor-

⁴²⁾ The graph is plotted in a logarithmic scale.

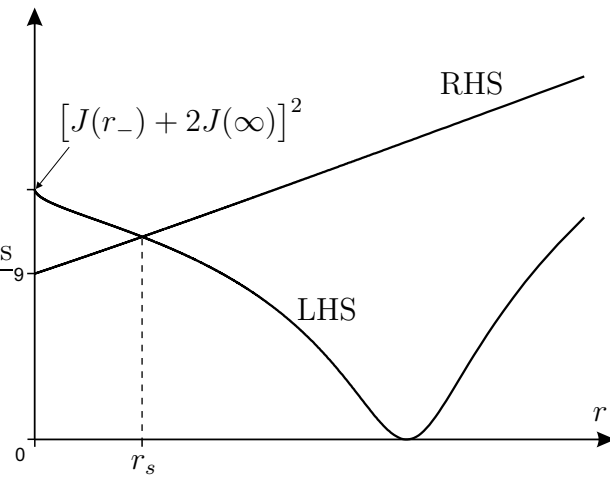


Figure 2.33: Left-hand side (LHS) and right-hand side (RHS) of equation (2.101) plotted as functions of r . The mutual intersection which takes place when $r = r_s$ corresponds to an illegitimate crossing of the singular line in the phase plane.

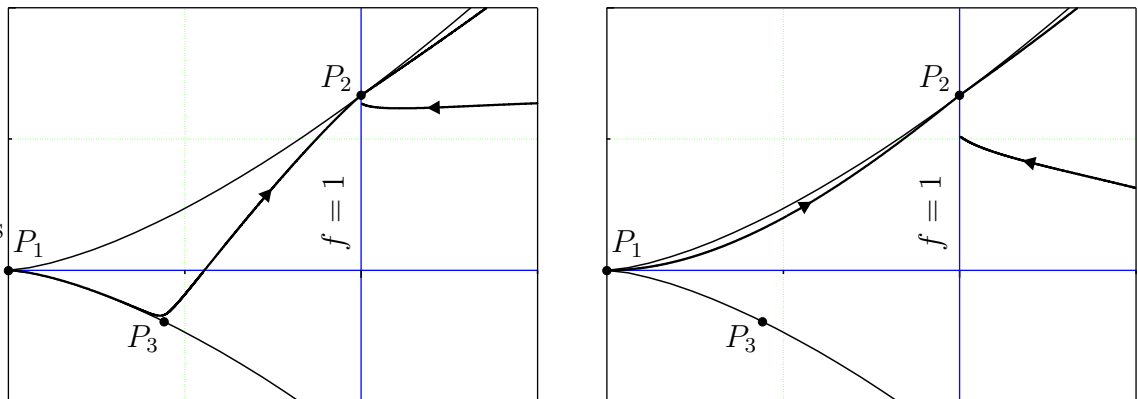


Figure 2.34: Supercritical phase trajectories corresponding to different values of r_- . After passing through the limiting characteristic (point P_2 on the singular line), the trajectories return to the singular line and tend to cross it below P_2 .

responding to different values of r_- . The only way to resolve this situation is to introduce a shock at a certain point $r_1 < r_s$ on the z plane trajectory, before the prohibited intersection with the singular line occurs.

The above results prove that *any oncoming supercritical supersonic flow necessarily leads to a shock formation*. Now we need to perform a local analysis of the

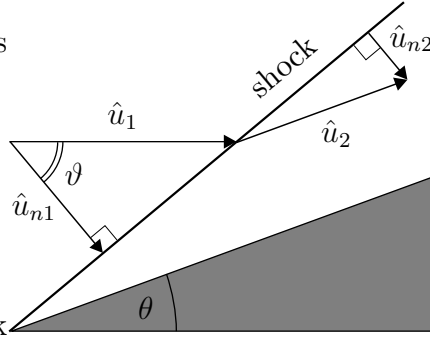


Figure 2.35: Geometry of an oblique shock wave produced by a wedge.

Hugoniot equations in order to continue the solutions through the shock.⁴³⁾ Introducing the angles shown in Fig. 2.35, these equations can be written in the form (Liepmann & Roshko 1957)

$$\left\{ \begin{array}{l} \frac{\sin(\vartheta)}{M_2^2 \cos(\vartheta + \theta)} - \frac{\sin(\vartheta + \theta)}{M_1^2 \cos(\vartheta)} = \gamma \sin(\theta), \\ \frac{1 + \frac{\gamma-1}{2} M_1^2}{1 + \frac{\gamma-1}{2} M_2^2} = \frac{\frac{\tan(\vartheta)}{\tan(\vartheta + \theta)} - \left(\frac{\gamma+1}{\gamma-1}\right)}{\frac{\tan(\vartheta + \theta)}{\tan(\vartheta)} - \left(\frac{\gamma+1}{\gamma-1}\right)}, \\ \hat{U}_{\tau 1} = \hat{U}_{\tau 2}, \\ \frac{\hat{a}_1^2}{\gamma - 1} + \frac{\hat{U}_{n1}^2}{2} = \frac{\gamma + 1}{2(\gamma - 1)} \hat{U}_{n1} \hat{U}_{n2}, \end{array} \right. \quad (2.103)$$

where the indices 1 and 2 correspond to the parameters before and after the shock respectively, the indices n and τ refer to the normal and tangent directions with respect to the shock, the hat denotes the dimensional (unscaled) variables, and $M_{1,2} = \hat{U}_{1,2}/\hat{a}_{1,2}$.⁴⁴⁾ In the physical coordinates (x, y) the flow before and after the shock forms the angles θ_1 and θ_2 with the x axis; the shock itself is inclined and forms the angle χ with the y axis (see Fig. 2.36). Hence,

$$\left\{ \begin{array}{l} \vartheta = \chi + \theta_1, \\ \theta = \theta_2 - \theta_1. \end{array} \right. \quad (2.104)$$

⁴³⁾ Even though this has been done in various works (Cole & Cook 1986), it is worth giving a detailed explanation here.

⁴⁴⁾ We used the Prandtl's law, $\hat{a}_{n*}^2 = \hat{U}_{n1} \hat{U}_{n2}$, in order to derive the last equation in (2.103), with \hat{a}_{n*} being the critical speed of the flow normal to the shock.

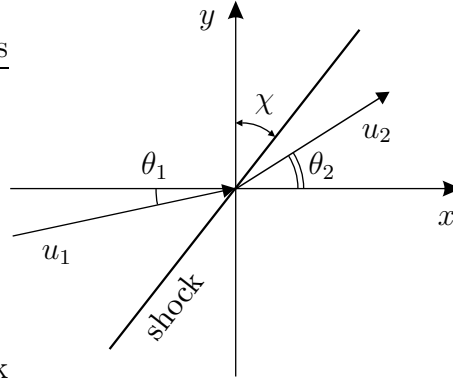


Figure 2.36: Geometry of an oblique shock in the cartesian coordinates (x, y) .

By further assuming that the shock is attached to the wall and coincides with the coordinate line $\xi = \xi_{sh} = \text{const}$ (Fig. 2.37), we get in the leading order of approximation:

$$\chi = \chi(y) = \alpha \xi_{sh} y^{1/2} \ll 1,$$

as $y \ll 1$ in the local problem. Similarly,

$$\theta_{1,2} \approx \frac{\hat{v}}{\hat{u}} \approx \frac{\frac{v}{\gamma+1}}{1 + \frac{u}{\gamma+1}} \approx \frac{v}{\gamma+1},$$

where $u = yF'(\xi)$, $v = \alpha y^\alpha [\lambda F - \xi F']$ are our main velocity perturbations. We see that all the angles in (2.104) are small, and this allows to simplify (2.103) significantly using χ as a small parameter. From equation (2.11) for the local Mach number

$$M_{1,2}^2 = [1 + yF'(\xi) + \dots]_{1,2} = 1 + \chi^2 f_{1,2} + \dots, \quad (2.105)$$

with $f_{1,2}$ referring to the values of f immediately before and after the shock. Note that the corresponding entropy change in the shock is of order of χ^6 , and the flow behind the shock can be treated as potential with the accuracy provided by asymptotic expansions (2.4), (2.10) and (2.11).

The trigonometric functions in (2.103) can also be expanded:

$$\begin{aligned} \tan(\chi + \theta_{1,2}) &= \chi \left[1 + \chi^2 \left(\frac{g_{1,2}}{\gamma+1} + \frac{1}{3} \right) + \dots \right], \\ \sin(\chi + \theta_{1,2}) &= \chi \left[1 + \chi^2 \left(\frac{g_{1,2}}{\gamma+1} - \frac{1}{6} \right) + \dots \right], \\ \cos(\chi + \theta_{1,2}) &= 1 - \frac{1}{2} \chi^2 + \dots, \end{aligned} \quad (2.106)$$

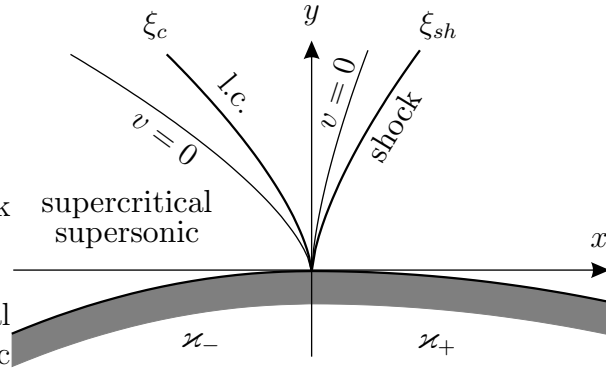


Figure 2.37: After passing through the limiting characteristic (l.c.), a supercritical supersonic flow inevitably develops a shock.

$g_{1,2}$ being the values of g immediately before and after the shock. Substituting expansions (2.105), (2.106) into the first three equations of (2.103) leads to the same equation

$$f_1 + g_1 = f_2 + g_2 \tag{2.107}$$

in the leading order. On the other hand, the last equation of (2.103) yields

$$f_1 + f_2 = 2. \tag{2.108}$$

The above analysis shows that the 2D Hugoniot system, containing four equations (continuity equation, two momentum equations and energy equation), is degenerated into the system of only two equations ((2.107) and (2.108)) when the asymptotic limit $x, y \ll 1$ is considered. System (2.107)–(2.108) describes the jump of the phase trajectories due to the shock. The second equation determines the shock strength and suggests that the points (f_1, g_1) and (f_2, g_2) are symmetric with respect to the singular line $f = 1$, whereas the first one provides the relevant change $g_2 - g_1$ of the vertical velocity component.

This result gives a basic understanding of how the supercritical supersonic flows behave. As opposed to the case of the subsonic and the subcritical supersonic flows, we shall assume that both of the parameters κ_- and G_- for the oncoming flow are known, therefore defining r_- uniquely according to (2.54) (provided that the upstream pressure gradient G_- is strong enough for the starting point z_- to be located in the

supercritical region, i.e. on the branch cut $(-\infty, 0)$). In this case solutions (2.85), (2.86), (2.98) and (2.100) allow to construct the relevant phase trajectory until the illegitimate crossing with the singular line (occurring at $z = -r_s$), and to determine the values of ξ along this trajectory (see equations (2.52), (2.53) for f , g and ξ in terms of the inverse problem solutions). Theoretically the shock can form at any point of the final fragment L_1 of the phase trajectory with positive ξ (see Fig. 2.38). Note that we only consider shocks originated at the wall, which have $\xi_{sh} > 0$.⁴⁵⁾

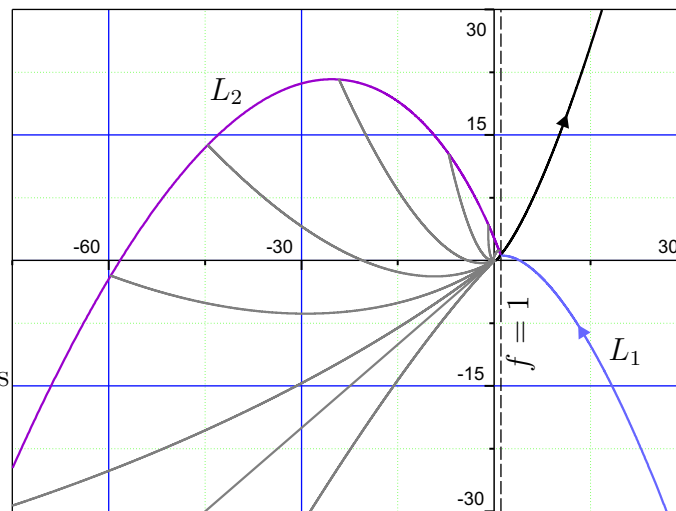


Figure 2.38: In the language of the phase variables, the upstream side of the shock may be located anywhere on the fragment L_1 of the phase trajectory coming from the upstream wall, while the downstream side of the shock lies somewhere on the curve L_2 . The latter is the image of L_1 described by equations (2.107) and (2.108). The grey trajectories represent the flow between the shock and the downstream wall for different values of \varkappa_+ ; the lowermost of these trajectories does not intersect with L_2 and therefore has no physical meaning.

Thus, for any given supercritical pair of the parameters \varkappa_- and G_- , the locus L_1 of the points (f_1, g_1) (possible locations of the left-hand side of the shock in the phase plane) is uniquely defined. Due to (2.107) and (2.108) this yields the corresponding locus L_2 of the points (f_2, g_2) (possible locations of the right-hand side of the shock in the phase plane), as shown in Fig. 2.38. The latter has a clear maximum, and then goes towards $(f_2, g_2) = (-\infty, -\infty)$.

⁴⁵⁾ The shocks induced by other sources and impinging upon the wall are located at $\xi_{sh} < 0$; they are excluded from our study.

The final fragment of the phase trajectory starts somewhere on L_2 and returns to the origin, but the available data (\varkappa_-, G_-) is insufficient for obtaining the exact position of this curve (Fig. 2.38). Depending on the value of z_+ , which is responsible for the asymptotic behavior of the trajectory close to the origin, the last fragment may either be completely subsonic, partially or completely subcritical supersonic, or entirely supercritical supersonic. Hence, to get a unique solution one has to fix z_+ along with \varkappa_-, G_- , therefore leading to the fundamental difference between the supercritical flows and all other flows. Recall that for the oncoming subsonic and the subcritical supersonic flows it was sufficient to set any two of the four parameters $\{\varkappa_-, r_-, \varkappa_+, r_+\}$, or $\{\varkappa_-, G_-, \varkappa_+, G_+\}$, in order to get the remaining two from either (2.67) or (2.80). Now we need to fix any three parameters from these sets, say $\{\varkappa_-, r_-, r_+\}$, to find the fourth one (in this case \varkappa_+). In other words, passing through the limiting characteristic (which inevitably leads to the shock formation) gives one extra degree of freedom to the supercritical supersonic flows. The local solution cannot be constructed based upon \varkappa_{\pm} only (as it was clearly the case for the subsonic and the subcritical supersonic regimes), and requires one parameter from the global solution, be it a value of the pressure gradient on the upstream wall or a location of the shock.

When r_- and r_+ are specified, the phase trajectory can be constructed uniquely. If, in addition, \varkappa_- is known, the relevant value of \varkappa_+ can be obtained from an obvious condition that ξ should be continuous at the shock. Indeed, the curvatures drop out of the expressions (2.52) for the phase variables, and therefore do not affect the phase trajectory. However, they are present in formula (2.53) which provides the values of ξ along the trajectory. It means that knowing r_-, r_+ , together with the shock conditions (2.107)–(2.108), is sufficient for reconstructing both fragments of the phase trajectory (before and after the shock), whereas the values of ξ along these fragments depend upon \varkappa_- before the shock and upon \varkappa_+ after the shock respectively. Thus, the continuity condition $\xi_1 = \xi_2 \equiv \xi_{sh}$ at the shock provides the required link between the curvatures.

2.4.12 Structure of the flow behind the shock

Let us now perform a detailed analysis of all the possible phase trajectories after the shock. Since ξ monotonely increases from 0 along L_1 , it also increases along L_2 when moving from the left to the right (Fig. 2.38), due to the continuity of ξ at the shock. The increase of ξ_{sh} means that the shock becomes more inclined, and its intensity drops (this can also be seen from the decrease of the parameter $H = f_1 - 1 = 1 - f_2$ while moving along L_2 to the right). Based on this result, we shall list all the regimes which occur as ξ_{sh} keeps increasing.

1) Regime I – a subsonic flow immediately behind the shock, transforming into a subcritical supersonic flow on the downstream wall with $\varkappa_+ > 0$, see Fig. 2.39. The

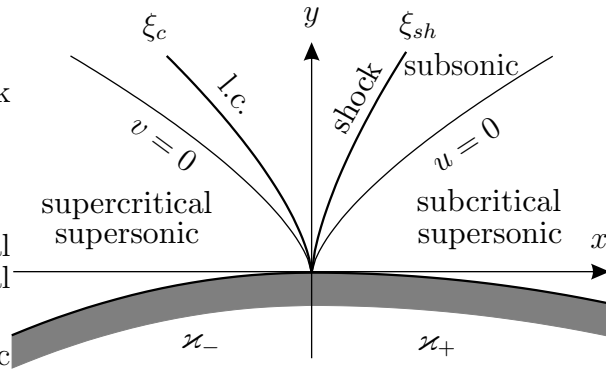


Figure 2.39: Regime I for the flow behind the shock.

relevant phase trajectory behind the shock consists of two fragments (Fig. 2.41). The first one is subsonic (the flow right behind the shock), with the solutions

$$\begin{cases} y = -u D \left[B(r) + I(r_+) + \frac{9\sqrt{\pi} \Gamma(2/3)}{\Gamma(1/6)} \right], \\ x = -v D \left[B(r) - \frac{3}{r^{1/2}(1-r)^{1/3}} + I(r_+) + \frac{9\sqrt{\pi} \Gamma(2/3)}{\Gamma(1/6)} \right], \end{cases}$$

where

$$D = \frac{r_+^{1/2}(r_+ - 1)^{1/3}}{3(\gamma + 1)\varkappa_+},$$

$u < 0, v < 0$ and $r_2 \leq r < 1$,⁴⁶⁾. The second fragment is supersonic (the flow near

⁴⁶⁾ The point r_2 corresponds to the right-hand side of the shock.

the downstream wall), with the solutions

$$\begin{cases} y = u D \left[I(r) - I(r_+) \right], \\ x = v D \left[I(r) - \frac{3}{r^{1/2}(r-1)^{1/3}} - I(r_+) \right], \end{cases}$$

$u > 0$, $v < 0$, $1 < r \leq r_+$. For this final fragment of the phase trajectory the corresponding z plane trajectory runs on two separate sheets of the Riemann surface, shown in Fig. 2.40.⁴⁷⁾

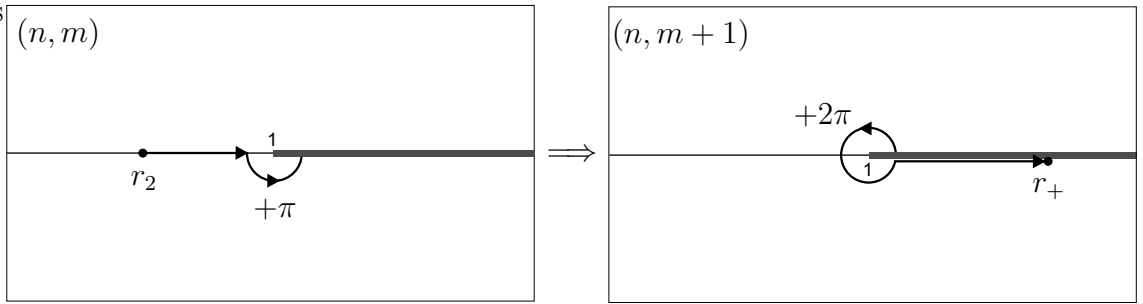


Figure 2.40: Final fragments of the z plane trajectory in Regime I.

If r_+ is large, the phase trajectory described by the above solutions moves downwards fairly quickly (Fig. 2.38), and no intersection with L_2 occurs. However, as r_+ decreases, the minimal distance between the trajectory and L_2 also decreases, leading to the intersection at the infinite point ($f = -\infty$, $g = -\infty$) when $r_+ = r_m$ (see Fig. 2.41). It may be shown that r_m is the only root of the equation

$$I(r_m) = \frac{3}{r_{00}^{1/2}(1-r_{00})^{1/3}} - B(r_{00}) - \frac{9\sqrt{\pi}\Gamma(2/3)}{\Gamma(1/6)}, \quad r_m > 1, \quad (2.109)$$

where

$$r_{00} = \frac{r_0}{1+2r_0}, \quad (2.110)$$

and r_0 is defined in (2.99) for a given r_- . Thus, r_m is itself a function of r_- . The intersection between L_2 and the last fragment of the phase trajectory at the infinite point means $f_1 \rightarrow \infty$, $f_2 \rightarrow -\infty$, corresponding to the normal shock with $\xi_{sh} = 0$.

⁴⁷⁾ Note that v remains negative both before the shock (on L_1) and after she shock.

The relevant curvatures' ratio can also be obtained analytically:

$$\left(\frac{\varkappa_+}{\varkappa_-}\right)_m = \frac{r_m^{1/2}(r_m - 1)^{1/3}}{r_-^{1/2}(1 + r_-)^{1/3}} \frac{r_0^{1/2}(1 + r_0)^{1/3}}{r_{00}^{1/2}(1 - r_{00})^{1/3}}. \quad (2.111)$$

Equation (2.111), together with (2.99), (2.109) and (2.110), shows that $(\varkappa_+/\varkappa_-)_m$ is a function of r_- ; it monotonely decreases from ∞ to 0 while r_- is increasing from 0 to ∞ .

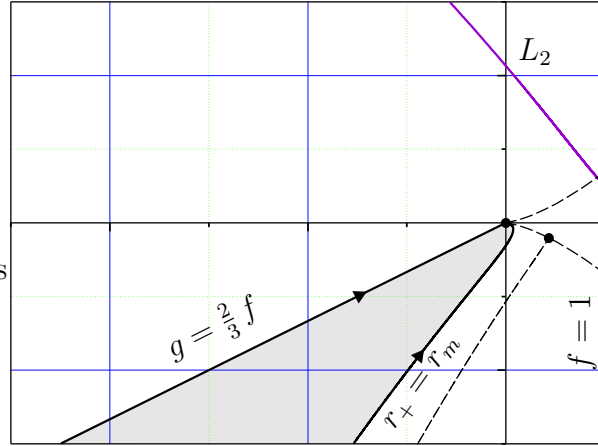


Figure 2.41: Location of the phase trajectories describing the flow behind the shock in Regime I (shaded area). The trajectories at the boundaries of the shaded area correspond to $r_+ = r_m$ (r_m is defined in (2.109)) and $r_+ = 1$, the latter giving the straight line $g = \frac{2}{3}f$.

As r_+ diminishes further, so that $r_m > r_+ > 1$, the final fragment of the phase trajectory comes closer to the line $g = \frac{2}{3}f$. Its intersection point with L_2 moves upwards (Fig. 2.38), resulting in a monotonic increase in ξ_{sh} . The curvatures' ratio can now be expressed via

$$\bar{\varkappa}_+ \equiv \frac{\varkappa_+}{\varkappa_-} = \frac{r_+^{1/2}(r_+ - 1)^{1/3}}{r_-^{1/2}(1 + r_-)^{1/3}} \left(\frac{\chi_1}{\chi_2}\right),$$

with

$$\chi_1 = \frac{1}{f_1} \left[-J(r_1) + J(r_-) + 2J(\infty) \right]^{-1}, \quad f_1 = f(r_1),$$

$$\chi_2 = -\frac{1}{f_2} \left[B(r_2) + I(r_+) + \frac{9\sqrt{\pi}\Gamma(2/3)}{\Gamma(1/6)} \right]^{-1}, \quad f_2 = f(r_2).$$

To illustrate how $\bar{\varkappa}_+$ behaves when r_+ is decreasing, it is plotted versus the scaled shock position $\bar{\xi}_{sh} = \frac{\xi_{sh}}{\sqrt{\varkappa_-}}$ in Fig. 2.42, left, for all the possible flow regimes behind the

shock.⁴⁸⁾ The curve, which appears to be invariant with respect to transformation (2.12), corresponds to one particular value of r_- (or G_-); one can plot a family of such curves for different r_- , and they would all look similar, simply being stretched along both axes in a certain way. We see that within the regime I the curvatures' ratio decreases steadily with ξ_{sh} . Moving a few steps forward, it is worth mentioning that the function $\bar{\kappa}_+(\bar{\xi}_{sh})$ has a distinct minimum, therefore providing two different shock locations for any given curvatures' ratio: a strong shock ($\bar{\xi}_{sh} < \bar{\xi}_{min}$) and a weak shock ($\bar{\xi}_{sh} > \bar{\xi}_{min}$).⁴⁹⁾ It is also clearly seen from Fig. 2.42 that $\bar{\xi}_{sh}$ does not exceed a certain maximum value $\bar{\xi}_{max}$, the latter obviously corresponding to the shock's degeneration into a characteristic of a supersonic flow (Liepmann & Roshko 1957).

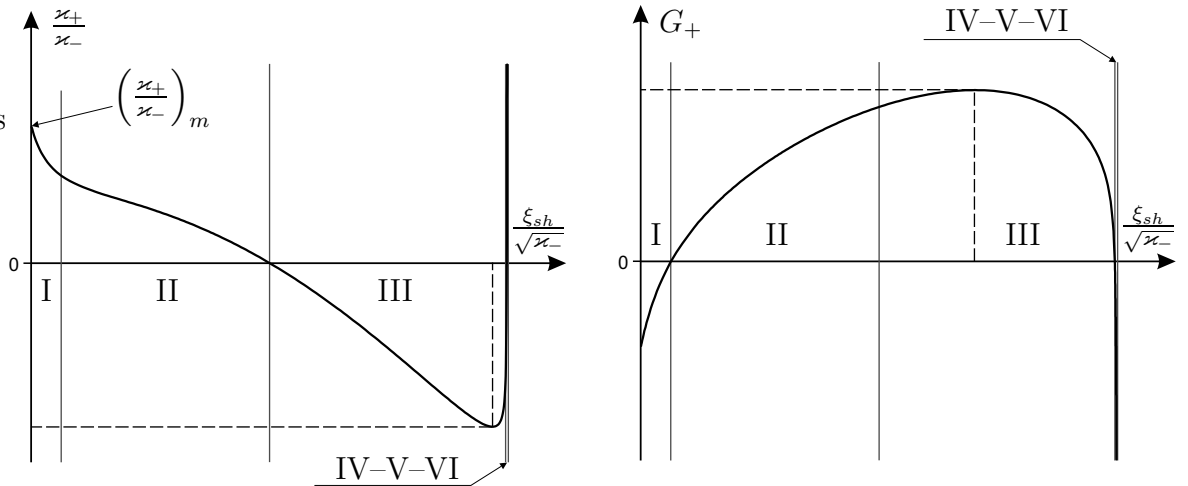


Figure 2.42: An illustration of the connection between relative location of the shock ($\frac{\xi_{sh}}{\sqrt{\kappa_-}}$) and the downstream parameters $\frac{\kappa_+}{\kappa_-}$, G_+ . Roman numerals denote physically different regimes for a flow behind the shock. The graphs are plotted for a fixed value of the supercritical upstream pressure gradient G_- , and are invariant with respect to re-scaling of the spatial coordinates.

The pressure gradient on the downstream wall has the amplitude

$$G_+ = -\frac{1}{\lambda\beta^{2/3}} \left(\frac{\kappa_+}{\kappa_-}\right)^{2/3} \left(\frac{r_+ - 1}{r_+}\right)^{1/3}, \quad (2.112)$$

and is favorable (as it is for any supersonic flow on the downstream wall, see section 2.4.5); G_+ plotted in Fig. 2.42, right, as a function of $\bar{\xi}_{sh}$ for all the regimes behind

⁴⁸⁾ The rest of them, denoted by the Roman numerals II–VI, will be examined below.

⁴⁹⁾ Note that the regimes IV, V and VI could not be shown in Fig. 2.42 properly and require a zooming which will be given later (see Fig. 2.49).

the shock. Again, the curve shown in Fig. 2.42 corresponds to one particular value of G_- , which is due to the fact that supercritical flows have one extra degree of freedom. In the regime I the gradient is always favorable, but its absolute value decreases with ξ_{sh} and becomes equal to zero when $r_+ = 1^+$.

2) Regime II – an entirely subsonic flow between the shock and the downstream wall with $\varkappa_+ > 0$. The flow structure is shown in Fig. 2.43, left. Depending on the value of $r_+ \in (0, 1)$, the last fragment of the phase trajectory either runs completely in the lower half-plane $g < 0$, or starts in the upper half-plane (immediately after the shock) and then crosses the line $g = 0$ before returning to the origin (see Fig. 2.38).⁵⁰ In the first case, v stays negative both before and after the shock, and the final fragment of the phase trajectory is described by the solutions

$$\begin{cases} y = u D [B(r) - B(r_+)], \\ x = v D \left[B(r) - \frac{3}{r^{1/2}(1-r)^{1/3}} - B(r_+) \right], \end{cases} \quad (2.113)$$

where

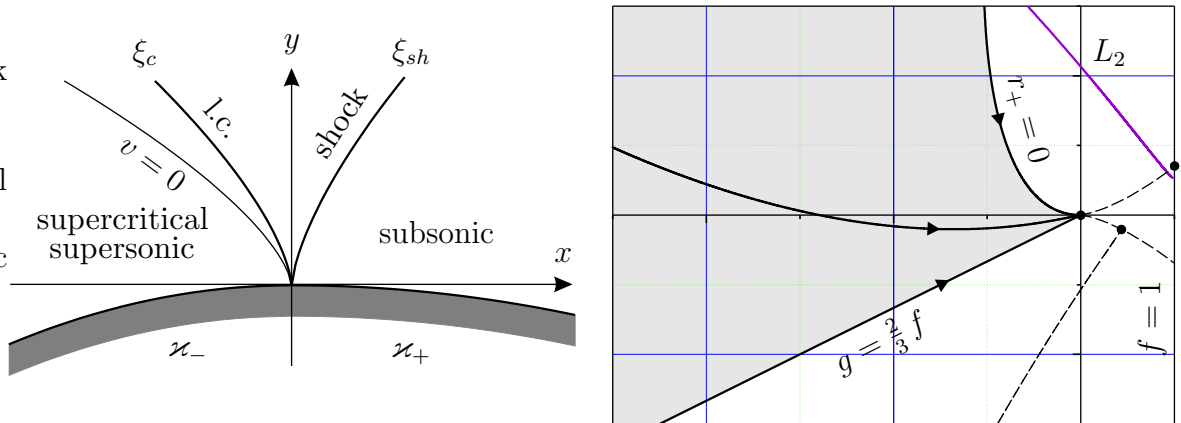


Figure 2.43: Regime II for the flow behind the shock, left, and location of the relevant phase trajectories, right.

$$D = \frac{r_+^{1/2}(1-r_+)^{1/3}}{3(\gamma+1)\varkappa_+},$$

and $r_2 \leq r \leq r_+$ (the relevant z plane trajectory is shown in Fig. 2.44). In the second

⁵⁰ The trajectories' location near the origin is sketched in Fig. 2.43, right.

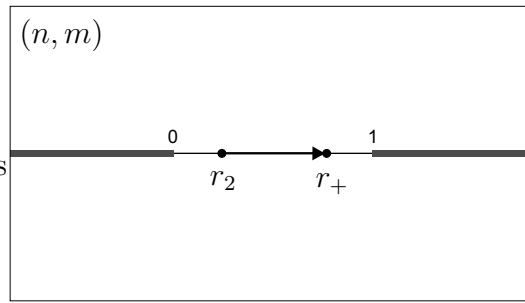


Figure 2.44: Final fragment of the z plane trajectory in Regime II for the case when $v < 0$ behind the shock.

case v changes sign in the shock first (becoming positive), and then once again in the downstream subsonic flow. The fragment of the phase trajectory with $v > 0$ (just after the shock) corresponds to the solutions

$$\begin{cases} y = -u D [B(r) + B(r_+)], \\ x = -v D \left[B(r) - \frac{3}{r^{1/2}(1-r)^{1/3}} + B(r_+) \right], \end{cases} \quad (2.114)$$

$r_2 \geq r > 0$, and the final fragment is given by (2.113) with $0 < r \leq r_+$. Now the z plane trajectory runs on two sheets of the Riemann surface (Fig. 2.45).

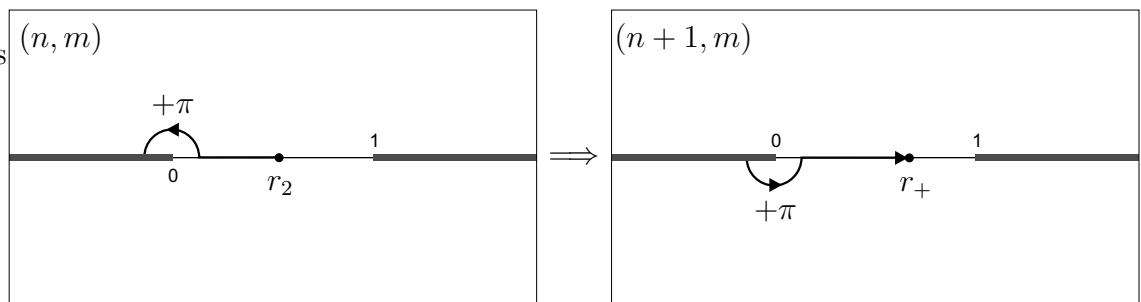


Figure 2.45: Final fragments of the z plane trajectory in Regime II for the case when $v > 0$ behind the shock.

As r_+ decreases from 1 to 0, ξ_{sh} keeps increasing (the shock becomes more oblique and weakens), the curvatures' ratio decreases to 0; at the same time the downstream pressure gradient is adverse (as it should be for any subsonic flow) and increases

monotonely (see Fig. 2.42). The two limiting cases are important: $r_+ = 1^-$ corresponds to a potential vortex flow and leads to a zero pressure gradient on the wall,⁵¹⁾ while $r_+ \rightarrow 0^+$ yields $\varkappa_+ \sim \sqrt{r_+} \rightarrow 0$, i.e. a flat downstream wall. However, in the second case the downstream pressure gradient (proportional to G_+) is not equal to zero and depends upon \varkappa_- , r_- ; solutions (2.114) are degenerated into

$$\begin{cases} y = -u \frac{B(r)}{2(\lambda G_+)^{3/2}}, \\ x = -v \frac{1}{2(\lambda G_+)^{3/2}} \left(B(r) - \frac{3}{r^{1/2}(1-r)^{1/3}} \right), \end{cases} \quad (2.115)$$

$r_2 \geq r > 0 \equiv r_+$. Therefore, the subsonic flow between the shock and the flat downstream wall with $\varkappa_+ = 0$ is not uniform, as opposed to a similar special case for the oncoming subcritical supersonic flow discussed in section 2.4.6.

It is also worth mentioning that the trajectory described by solutions (2.114) changes its behavior significantly when $r_+ = r_*$, with $r_* \approx 0.3039$ defined in (2.64). For $1 > r_+ > r_*$ it stays in the subsonic half-plane, and, if not restricted by L_2 , would go towards $(-\infty, \infty)$. On the other hand, for $r_* > r_+ > 0$ it starts turning right at a certain point, enters the subcritical supersonic region, and attempts to cross the singular line in an illegitimate place above P_2 . However, the restricting curve L_2 (on which the trajectory must terminate) is well below the place where the described turning takes place, and the last fragment of the phase trajectory remains entirely subsonic for all $r_+ \in (0, 1)$.⁵²⁾

Finally, the curvatures' ratio is given by

$$\frac{\varkappa_+}{\varkappa_-} = \frac{r_+^{1/2}(1-r_+)^{1/3}}{r_-^{1/2}(1+r_-)^{1/3}} \left(\frac{\chi_1}{\chi_2} \right),$$

where

$$\chi_1 = \frac{1}{f_1} \left[-J(r_1) + J(r_-) + 2J(\infty) \right]^{-1}, \quad f_1 = f(r_1),$$

$$\chi_2 = -\frac{1}{f_2} \left[\pm B(r_2) + B(r_+) \right]^{-1}, \quad f_2 = f(r_2),$$

and \pm corresponds to $v \geq 0$ immediately behind the shock.

⁵¹⁾ The phase trajectory in this case coincides with the line $g = \frac{2}{3}f$.

⁵²⁾ Note that for the subsonic and the subcritical supersonic oncoming flows there was a natural restriction $r_{\pm} > r_{**}$ due to the saddle point, with $r_{**} \approx 0.8302$ defined in (2.68); since $r_{**} > r_*$, this kind of a turning never happened.

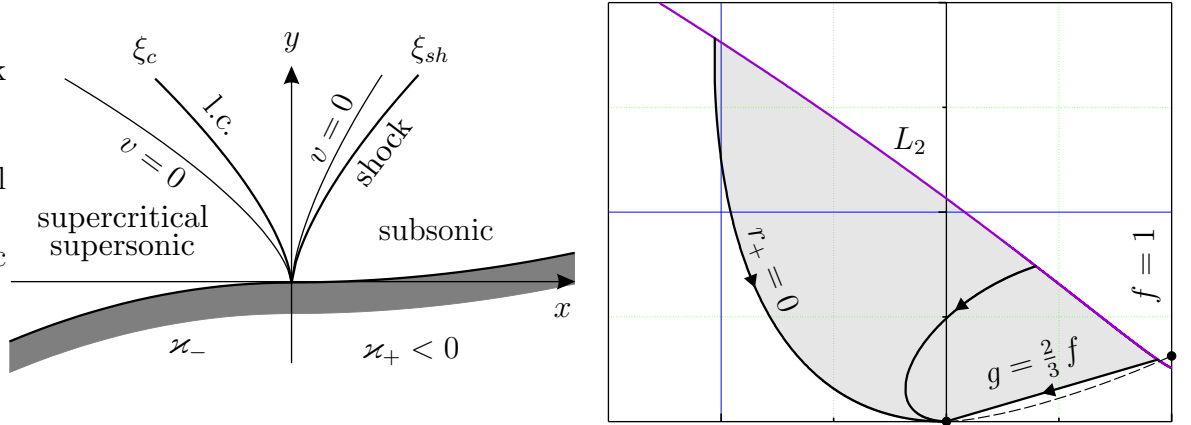


Figure 2.46: Regime III for the flow behind the shock, left, and location of the relevant phase trajectories, right.

3) Regime III – a subsonic flow on the downstream wall with $\alpha_+ < 0$. The flow structure is shown in Fig. 2.46, left. Depending on the value of r_+ , the phase trajectory can either run entirely in the subsonic half-plane, or start from the subcritical supersonic region (see Fig. 2.46, right). In the first case the inverse problem solutions are

$$\begin{cases} y = u D \left[B(r_+) - B(r) \right], \\ x = v D \left[B(r_+) - B(r) + \frac{3}{r^{1/2}(1-r)^{1/3}} \right], \end{cases} \quad (2.116)$$

where

$$D = \frac{r_+^{1/2}(1-r_+)^{1/3}}{3(\gamma+1)|\alpha_+|},$$

and $r_2 \geq r \geq r_+$. The sign of v changes either in the shock itself when

$$f_1 > \left(\frac{J(r_-) + 2J(\infty)}{3} \right)^2,$$

or in the flow just before the shock when

$$f_1 < \left(\frac{J(r_-) + 2J(\infty)}{3} \right)^2,$$

so that v is positive on the concave downstream wall anyway. In the second case there is a subcritical supersonic flow immediately after the shock corresponding to

the solutions

$$\begin{cases} y = u D \left[B(r_+) + \frac{9\sqrt{\pi}\Gamma(2/3)}{\Gamma(1/6)} + I(r) \right], \\ x = v D \left[B(r_+) + \frac{9\sqrt{\pi}\Gamma(2/3)}{\Gamma(1/6)} + I(r) - \frac{3}{r^{1/2}(r-1)^{1/3}} \right], \end{cases} \quad (2.117)$$

$r_2 \geq r > 1$; this flow then decelerates to a subsonic regime without a shock formation, and is described by solutions (2.116) with $1 > r \geq r_+$. In the z plane the relevant trajectory runs on two sheets of the Riemann surface.⁵³⁾

As r_+ increases from 0 to 1, ξ_{sh} increases monotonically. From Fig. 2.42 it can be seen that, firstly, the downstream wall pressure gradient reaches its maximum and starts decreasing (remaining adverse throughout the entire regime), and, secondly, the ratio of the curvatures, now being negative, reaches its minimum and starts increasing. The latter yields the largest possible value of $|\kappa_+/\kappa_-|$ for a concave downstream wall ($\kappa_+ < 0$) at which the attached shock can exist, and creates a demarcation line between the strong and the weak solutions for the shock.⁵⁴⁾ This also provides an explanation for a well known experimental result that for a supersonic flow above a flat plate transforming into a concave wall the shock is always detached (see Fig. 2.47). Indeed, in this case $\kappa_+/\kappa_- = -\infty$, whilst the largest possible value of $|\kappa_+/\kappa_-|$ resulting in the attached shock is finite.

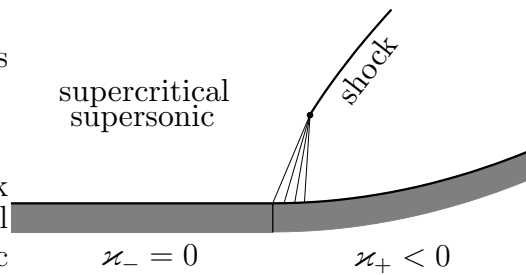


Figure 2.47: Detachment of the shock from the surface caused by a concave downstream wall (in this illustration $\kappa_+/\kappa_- = -\infty$).

The regime ends with the limiting case of $r_+ = 1^-$, when the entire trajectory is in the supersonic region and coincides with $g = \frac{2}{3}f$. This kind of a flow is essentially

⁵³⁾ We are skipping the plot of the z plane trajectory for the sake of simplicity.

⁵⁴⁾ However, the value $(\kappa_+/\kappa_-)_{min}$ and the corresponding shock location ξ_{min} cannot be obtained analytically.

a potential vortex flow over a *concave* wall, and there is no pressure gradient on the downstream wall in this case.

Finally, the analytical expression for \varkappa_+/\varkappa_- is structurally similar to the ones in the previous regimes, with $\chi_{1,2}$ depending on the exact solutions immediately before and after the shock. From now on we are going to skip it, in order to save paper and the reader's patience.

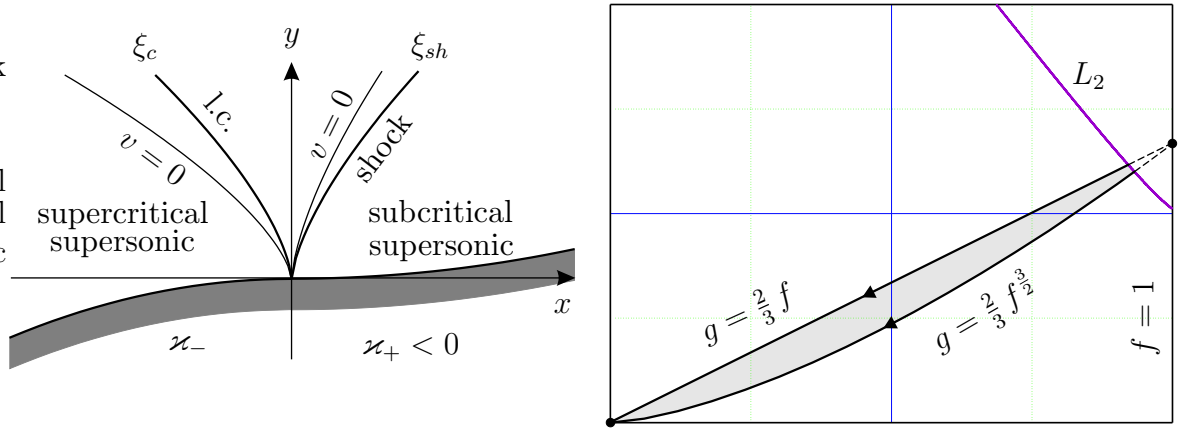


Figure 2.48: Regime IV for the flow behind the shock, left, and location of the relevant phase trajectories, right.

4) Regime IV – a subcritical supersonic flow between the shock and the downstream wall with $\varkappa_+ < 0$ (Fig. 2.48, left). The final fragment of the phase trajectory is located in the region confined between the three lines: $g = \frac{2}{3}f$ (corresponding to $r_+ = 1$), $g = \frac{2}{3}f^{\frac{3}{2}}$ (the upper critical line, $r_+ = \infty$) and L_2 , as shown in Fig. 2.48, right; therefore, $r_+ \in (1, \infty)$. The inverse problem solutions are

$$\begin{cases} y = u D \left[I(r_+) - I(r) \right], \\ x = v D \left[I(r_+) - I(r) + \frac{3}{r^{1/2}(r-1)^{1/3}} \right], \end{cases}$$

where

$$D = \frac{r_+^{1/2}(r_+ - 1)^{1/3}}{3(\gamma + 1)|\varkappa_+|},$$

and $r_2 \geq r \geq r_+$. In the limiting cases, when the phase trajectory coincides either with $g = \frac{2}{3}f$ or with $g = \frac{2}{3}f^{\frac{3}{2}}$, $r_2 \rightarrow r_+ \rightarrow 1^+$ and $r_+ \rightarrow r_2 \rightarrow \infty$ respectively.

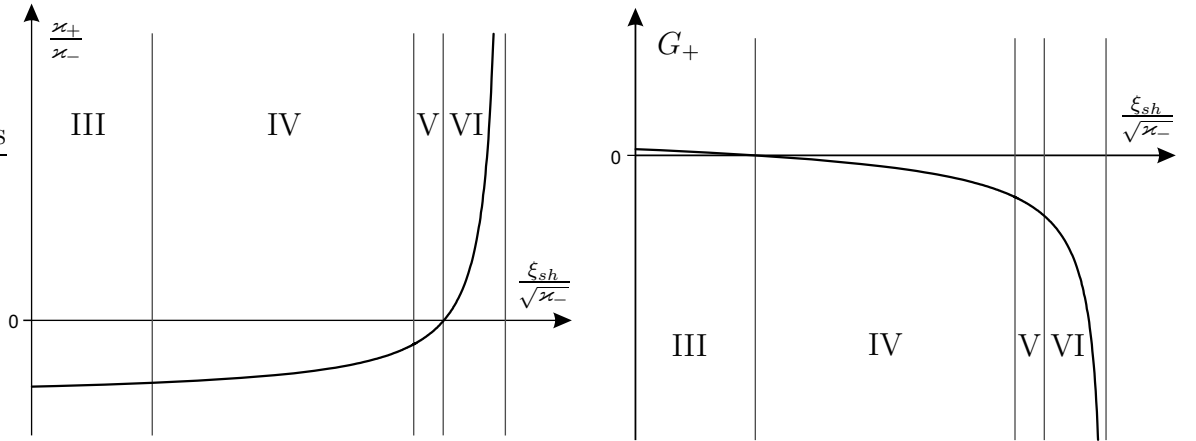


Figure 2.49: Connection between the relative location of the shock, the ratio of wall curvatures and the downstream pressure gradient in Regimes III–VI for the flow behind the shock.

As r_+ is increasing from 1 to ∞ , ξ_{sh} continues to increase monotonely. At the same time $|\varkappa_+/\varkappa_-|$ is diminishing (the ratio itself is negative, because $\varkappa_+ < 0$), while $|G_+|$ is increasing (the downstream pressure gradient is now favorable) – see Fig. 2.49.

5) Regime V – a supercritical supersonic flow between the shock and the downstream wall with $\varkappa_+ < 0$ (Fig. 2.50, left). The phase trajectories for this regime are shown in Fig. 2.50, right. The relevant value of r_+ is decreasing from ∞ to 0, and the inverse problem solutions are given by

$$\begin{cases} y = u D [J(r) - J(r_+)], \\ x = v D \left[J(r) + \frac{3}{r^{1/2}(1+r)^{1/3}} - J(r_+) \right], \end{cases}$$

where

$$D = \frac{r_+^{1/2}(1+r_+)^{1/3}}{3(\gamma+1)|\varkappa_+|},$$

and $r_2 \geq r \geq r_+$.

With the decrease of r_+ , ξ_{sh} increases monotonely, $|\varkappa_+/\varkappa_-|$ continues to decrease (becoming zero when $r_+ = 0$) and the absolute value of the downstream wall pressure gradient (which is favorable) keeps increasing, see Fig. 2.49. In the limiting case $r_+ \rightarrow 0$ we have $\varkappa_+ = 0^-$; however, the flow above the flat downstream wall is not uniform, as opposed to the subcritical flow for the same wall geometry considered in

section 2.4.8, and the wall pressure gradient is non zero, being a function of \varkappa_- , r_- .

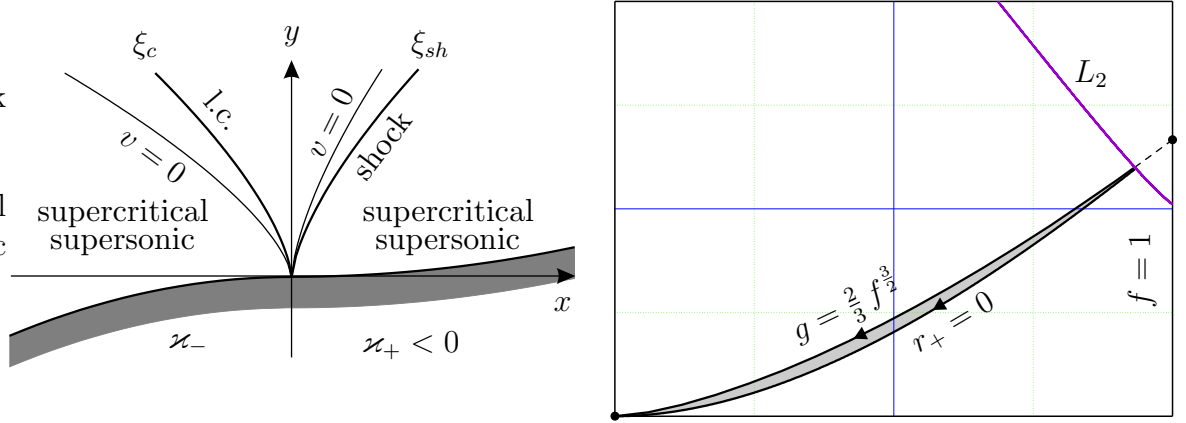


Figure 2.50: Regime V for the flow behind the shock, left, and location of the relevant phase trajectories, right.

6) Regime VI (final) – a supercritical supersonic flow between the shock and the downstream wall with $\varkappa_+ > 0$ (Fig. 2.51, left). The phase trajectories are now crossing the line $g = 0$ (Fig. 2.51, right), so that the z plane trajectory runs on both sides of the supercritical branch cut. The solutions on the upper side of the branch cut (for which $v > 0$) are

$$\begin{cases} y = u D \left[J(r_+) + J(r) \right], \\ x = v D \left[J(r_+) + J(r) + \frac{3}{r^{1/2}(1+r)^{1/3}} \right], \end{cases}$$

where

$$D = \frac{r_+^{1/2}(1+r_+)^{1/3}}{3(\gamma+1)\varkappa_+},$$

and $r_2 \geq r > 0$. On the lower side (corresponding to $v < 0$)

$$\begin{cases} y = u D \left[J(r_+) - J(r) \right], \\ x = v D \left[J(r_+) - J(r) - \frac{3}{r^{1/2}(1+r)^{1/3}} \right], \end{cases}$$

$0 < r \leq r_+$. The parameter r_+ is now increasing from 0 to ∞ , followed by a monotonic increase of $\bar{\xi}_{sh}$ right up to the largest possible value $(\bar{\xi}_{sh})_{max}$ for a given upstream

pressure gradient G_- .⁵⁵⁾ At the same time \varkappa_+/\varkappa_- is increasing from 0 to ∞ (see Fig. 2.49, left), and the absolute value of the favorable downstream pressure gradient keeps increasing (Fig. 2.49, right); the latter has the following asymptotic behavior:

$$G_+ \sim -\frac{1}{\lambda\beta^{2/3}} \left(\frac{\varkappa_+}{\varkappa_-}\right)^{2/3} \rightarrow -\infty \quad (2.118)$$

as $\varkappa_+/\varkappa_- \rightarrow \infty$. Equation (2.118) does not contain G_- (or r_-), suggesting that in the limit $\varkappa_+/\varkappa_- \rightarrow \infty$ the flow near the downstream wall depends only upon the curvatures' ratio. In other words, the additional degree of freedom, typical for the supercritical flows, vanishes, which makes the supercritical flow behave like the subcritical.

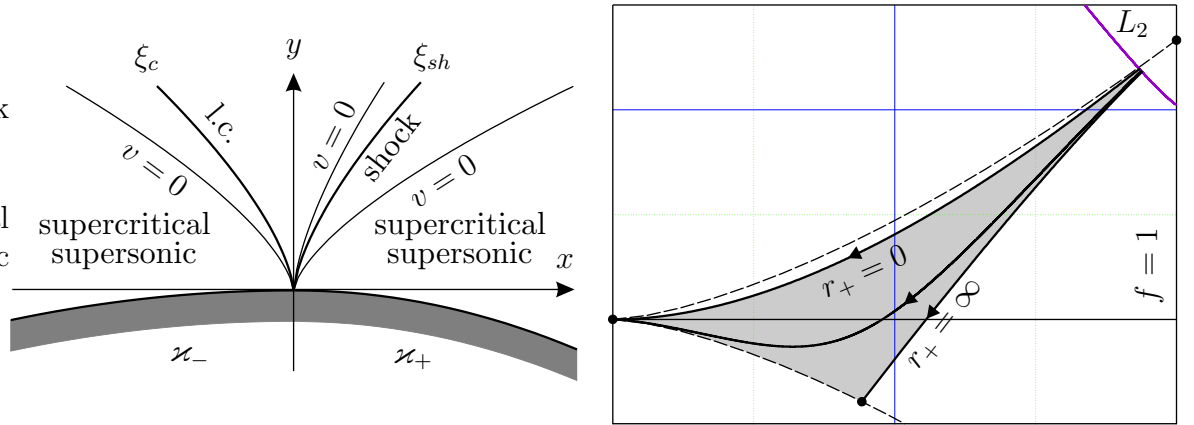


Figure 2.51: Regime VI for the flow behind the shock, left, and location of the relevant phase trajectories, right.

In this limiting case of $\varkappa_+/\varkappa_- \rightarrow \infty$ the phase trajectory moves towards the saddle point along its first asymptote (Fig. 2.51). It means that the flow asymptotically becomes the Prandtl–Meyer flow as the downstream wall with $\varkappa_+ \rightarrow \infty$ is approached (assuming $\varkappa_- = \mathcal{O}(1)$), thus being the only case when the phase trajectory does not return to the origin. However, the domain of the applicability of the above solutions in the physical plane is being degenerated to a point, and we need to perform a re-scaling. Indeed, since the problem is invariant with respect to transformation (2.12), the above limiting case may be treated as $\varkappa_- \rightarrow 0$ for $\varkappa_+ = \mathcal{O}(1)$. It can be shown

⁵⁵⁾ This value cannot be represented as an explicit function of G_- .

that this re-normalization leads to a uniform flow with $u = v = 0$ above the upstream wall with $\varkappa_- \rightarrow 0$, and the three coordinate lines where $v = 0$, as well as the limiting characteristic (ξ_c) and the shock (ξ_{sh}), all tighten to the vertical axis $x = 0$ (see Fig. 2.23, right). The shock itself degenerates to a weak discontinuity located at $x = 0$, whereas the flow in region $x > 0$ corresponds to the phase trajectory running along the lower critical line $g = -\frac{2}{3} f^{\frac{3}{2}}$ from the saddle point to the origin (Fig. 2.24). This regime has already been considered previously in section 2.4.6, but at that time it appeared as the limiting case for the oncoming subsonic flow (when $\varkappa_- \rightarrow 0$).

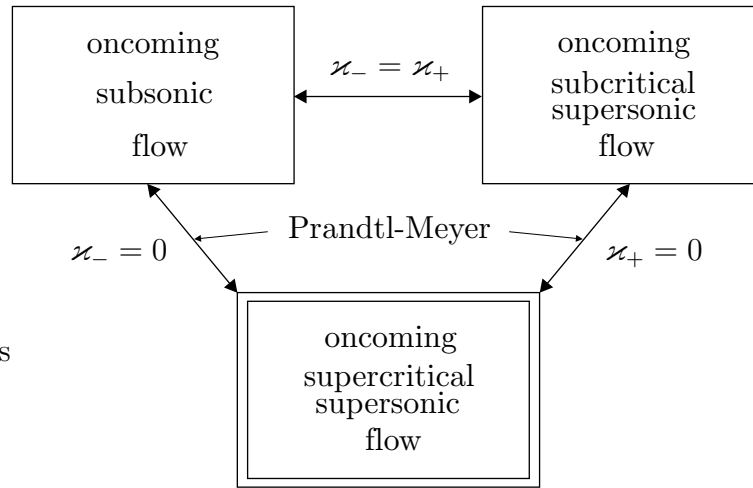


Figure 2.52: Links between all the possible transonic flow regimes near a discontinuity in wall curvature.

We have just derived a fundamental property linking all the transonic flows near the curvature-break point, which is illustrated in Fig. 2.52. The oncoming subsonic flows (for which $\varkappa_+/\varkappa_- > 1$) are succeeded by the subcritical supersonic flows, with the special case $\varkappa_- = \varkappa_+$ in between. The subcritical supersonic flows upstream, taking place for $0 < \varkappa_+/\varkappa_- < 1$, are succeeded by the supercritical supersonic flows when $\varkappa_+ \rightarrow 0$. As it was shown in sections 2.4.9–2.4.11, the supercritical regimes are physically different from all other regimes because they require one extra parameter in order to determine the local flow pattern. In the limiting case $\varkappa_+ \rightarrow 0$ the supercritical flow pattern is completely different from the one obtained for the similar limit in the subcritical flows. Therefore, the local flow parameters (in

particular the downstream wall pressure gradient) show a bifurcation-like behavior at the turn of the subcritical and the supercritical supersonic regimes. The supercritical regimes also allow the solutions with $\varkappa_+ < 0$ (concave downstream walls), and are linked with the subsonic regimes via the limiting case $\varkappa_- \rightarrow 0$.⁵⁶⁾ Therefore, we have a sequence of the possible regimes transforming from one into another, depending on the values of the basic input parameters (for example, \varkappa_- and G_-).

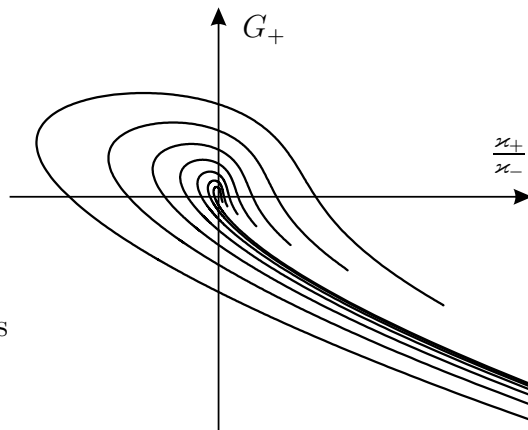


Figure 2.53: A family of the curves representing the downstream pressure gradient as a function of the curvatures' ratio in the supercritical regime. The curves are plotted for different values of the supercritical upstream pressure gradient G_- ; wider curves correspond to larger values of G_- .

Finally, let us summarize the results obtained for the supercritical flows by plotting the downstream wall pressure gradient G_+ (Fig. 2.53) versus the curvatures' ratio for different values of G_- (or r_-). As opposed to the subcritical regimes, now we have a family of the curves, which is due to the presence of one extra degree of freedom in the supercritical flows (for the subsonic and the subcritical supersonic flows there was only one such curve, shown in Fig. 2.8 and Fig. 2.26 respectively). All the curves in Fig. 2.53 have the same asymptotic behavior when $\varkappa_+/\varkappa_- \rightarrow \infty$, in accordance with (2.118); they match with the appropriate curve for G_+ in subsonic regimes

⁵⁶⁾ In this limiting case one extra degree of freedom degenerates, since the (physical) downstream pressure gradient $\partial p/\partial x$, according to (2.118) and (2.28), is finite and proportional to $\varkappa_+^{2/3}$ only. Although G_- still remains a free parameter in the supercritical solutions, the latter are reduced to a uniform flow upstream and the Prandtl–Meyer flow downstream of the curvature break. It can also be seen from (2.28) that the (physical) upstream pressure gradient is proportional to $G_- \varkappa_-^{2/3}$, and it vanishes with \varkappa_- regardless of the value of G_- .

(Fig. 2.10), therefore providing a link between the supercritical supersonic and the subsonic regimes discussed above. The clearly observed pair of the solutions for the pressure gradient within certain values of κ_+/κ_- corresponds to the strong and the weak shocks (Fig. 2.54). However, the strong solution seems to be physically unreasonable for our particular problem because it leads to

$$\frac{d\bar{\xi}_{sh}}{d\bar{\kappa}_+} < 0, \quad \bar{\xi}_{sh} = \frac{\xi_{sh}}{\sqrt{\kappa_-}}, \quad \bar{\kappa}_+ = \frac{\kappa_+}{\kappa_-},$$

and might be linked to a flow with an impinging shock. Moreover, it is the weak solution that yields the important limiting case $\kappa_+/\kappa_- \rightarrow \infty$, bringing the whole pattern back to the subsonic flows. On the weak branch in Fig. 2.54 the downstream pressure gradient monotonely decreases with $\bar{\kappa}_+$, and can be either adverse (for the most negative values of $\bar{\kappa}_+$, close to the shock's detachment from the wall) or favorable (for all other values of $\bar{\kappa}_+$).

Both the subcritical and the supercritical solutions for the coefficients G_{\pm} are plotted in Fig. 2.55 as functions of the curvatures' ratio. This plot completes our study of the inviscid flow generated by a discontinuity in wall curvature. Now we can move on to the boundary layer, and find out how the latter is affected by the singular pressure gradients.

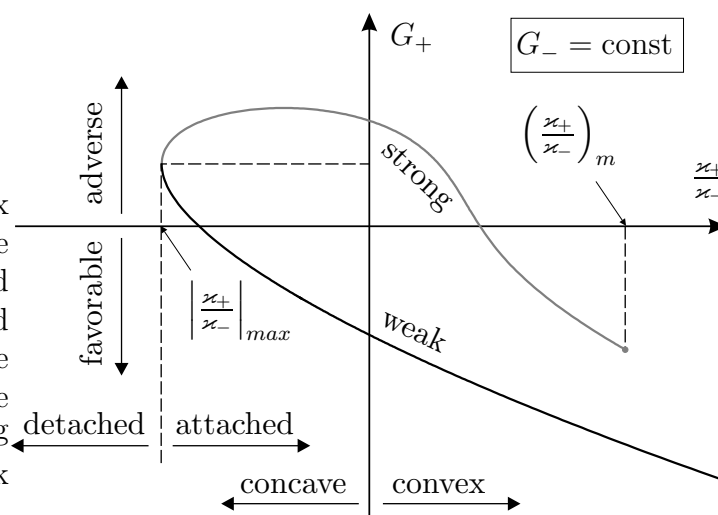


Figure 2.54: Physical interpretation for different fragments of a typical supercritical curve describing the downstream pressure gradient.

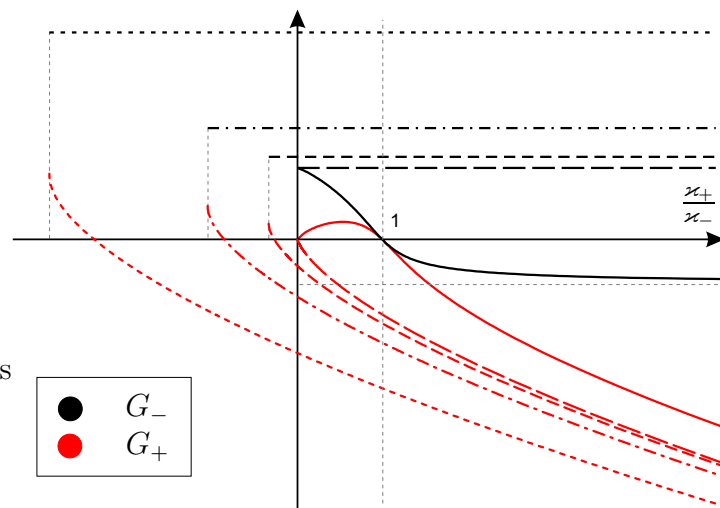


Figure 2.55: The pressure gradients G_{\pm} plotted as functions of the curvatures' ratio for subcritical regimes (solid lines) and supercritical regimes (dashed lines). The non-uniqueness in the supercritical solution is due to an extra degree of freedom gained after passing through the limiting characteristic.

Chapter 3

Viscous-Inviscid Interaction Caused by a Curvature Break

3.1 Boundary Layer Upstream of the Singularity

Having obtained a complete picture of the outer inviscid flow near a break in wall curvature, let us now turn our focus to the boundary layer and find out how it responds to the singular pressure gradients (2.28) generated by the break.

3.1.1 Peculiarities in the boundary layer exposed to the pressure gradient $\partial p/\partial x = G_-(-x)^{-1/3}$

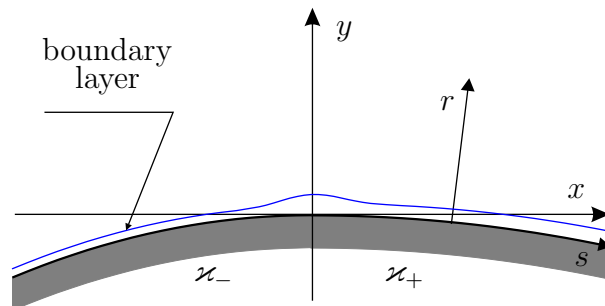


Figure 3.1: Curvilinear coordinates related to the body surface.

From now on we are going to use the curvilinear coordinates (s, r) related to the

body surface (see Fig. 3.1). According to the classical boundary layer theory, we introduce the following asymptotic expansions of the functions describing a compressible flow of a Newtonian fluid:

$$\begin{aligned}
 U(s, r, \text{Re}) &= U_0(s, Y) + \mathcal{O}(\text{Re}^{-1/2}), \\
 V(s, r, \text{Re}) &= \text{Re}^{-1/2}V_0(s, Y) + \mathcal{O}(\text{Re}^{-1}), \\
 p(s, r, \text{Re}) &= P_0(s, Y) + \mathcal{O}(\text{Re}^{-1/2}), \\
 h(s, r, \text{Re}) &= h_0(s, Y) + \mathcal{O}(\text{Re}^{-1/2}), \\
 \rho(s, r, \text{Re}) &= R_0(s, Y) + \mathcal{O}(\text{Re}^{-1/2}), \\
 \mu(s, r, \text{Re}) &= \mu_0(s, Y) + \mathcal{O}(\text{Re}^{-1/2}).
 \end{aligned} \tag{3.1}$$

Here $\text{Re} = \frac{\hat{\rho}_* \hat{a}_* L}{\hat{\mu}_*} \gg 1$ is Reynolds number referred to the sonic point (*), L is the spatial scale related to curvature radii (see section 2.1.1), $Y = r \text{Re}^{1/2}$ is a standard scaled normal coordinate, U and V stand for velocity components, p for pressure, h for enthalpy, ρ for density and μ for dynamic viscosity. All the functions have been non-dimensionalised using their values in the sonic point:

$$\hat{U} = \hat{a}_* U, \quad \hat{V} = \hat{a}_* V, \quad \hat{p} = \hat{p}_* + \hat{\rho}_* \hat{a}_*^2 p, \quad \hat{\rho} = \hat{\rho}_* \rho, \quad \hat{h} = \hat{a}_*^2 h, \quad \hat{\mu} = \hat{\mu}_* \mu,$$

with the hat denoting physical variables. Index ‘0’ in all the functions on the right-hand side of (3.1) indicates that they are the leading-order terms of the correspondent expansions based on powers of $\text{Re}^{-1/2}$.

Plugging (3.1) into the Navier–Stokes equations written in the curvilinear coordinates (s, r) (see Appendix), we obtain the classical boundary layer equations in the

leading order:

$$\left\{ \begin{array}{l} \frac{\partial(R_0 U_0)}{\partial s} + \frac{\partial(R_0 V_0)}{\partial Y} = 0 \\ R_0 \left(U_0 \frac{\partial U_0}{\partial s} + V_0 \frac{\partial U_0}{\partial Y} \right) = -\frac{\partial p_0}{\partial s} + \frac{\partial}{\partial Y} \left(\mu_0 \frac{\partial U_0}{\partial Y} \right) \\ \frac{\partial p_0}{\partial Y} = 0 \\ R_0 \left(U_0 \frac{\partial h_0}{\partial s} + V_0 \frac{\partial h_0}{\partial Y} \right) = U_0 \frac{\partial p_0}{\partial s} - \frac{1}{\text{Pr}} \frac{\partial}{\partial Y} \left(\mu_0 \frac{\partial h_0}{\partial Y} \right) + \mu_0 \left(\frac{\partial U_0}{\partial Y} \right)^2 \\ h_0 = \frac{1 + \gamma p_0}{(\gamma - 1)R_0}, \end{array} \right. \quad (3.2)$$

where $\text{Pr} = \mathcal{O}(1)$ is Prandtl's number.¹⁾ The absence of centrifugal terms in the system suggests that the effects of wall curvature do not affect the leading-order boundary layer. As a result, the pressure remains constant across the boundary layer and is a function of s only, prescribed by the outer inviscid flow. Transforming the known pressure distribution (2.28), originally obtained in the cartesian coordinates (x, y) , to the curvilinear coordinates yields

$$\frac{\partial p(s, r, \text{Re})}{\partial s} = k G_{\pm} (\pm s)^{-1/3} + \dots + \mathcal{O}(\text{Re}^{-1/2}),$$

so that

$$\frac{\partial p_0}{\partial s} = k G_{\pm} (\pm s)^{-1/3} + \dots, \quad 0 \leq Y < \infty, \quad |s| \rightarrow 0. \quad (3.3)$$

Here “ \pm ” corresponds to $s \gtrless 0$, the dots stand for higher-order terms of the coordinate expansion within the framework of the classical boundary layer theory (these terms also include the effects of the coordinate transformation itself), while the $\mathcal{O}(\text{Re}^{-1/2})$ terms represent the leading-order displacement effects.

On the wall the no-slip condition should hold:

$$U_0|_{Y=0} = V_0|_{Y=0} = 0,$$

which means that in a small vicinity of the wall the motion is relatively slow and the gas behaves like an incompressible fluid. Slow fluid particles near the wall are

¹⁾ To close the system, we need to specify how the viscosity depends on the enthalpy, i.e. to set the function $\mu_0(h_0)$. However, this will not be required for the analysis below.

the ones mostly affected by singular pressure gradient (3.3), the latter trying either to accelerate or to decelerate the gas (depending on the signs of G_{\pm}). Therefore, for the no-slip conditions to hold, the singular pressure gradient must be balanced by viscous forces and inertial terms, which may be expressed as

$$R_0 U_0 \frac{\partial U_0}{\partial s} \sim \frac{\partial p_0}{\partial s} \sim \frac{\partial}{\partial Y} \left(\mu_0 \frac{\partial U_0}{\partial Y} \right). \quad (3.4)$$

If we assume that the wall is not heated/cooled artificially, then the value of enthalpy on the wall is an order one quantity: $h_w = h_0|_{Y=0} = \mathcal{O}(1)$. Due to the equation of state, gas density near the wall is then estimated as $R_w = R_0|_{Y=0} = \mathcal{O}(1)$, and the viscosity $\mu_w = \mu_0|_{Y=0} \equiv \mu_0(h_w) = \mathcal{O}(1)$ (Goldstein 1930). Changing the differentials to finite differences in (3.4), and assuming further that $\Delta U_0 \sim U_0$, i.e. the pressure gradient is strong enough to cause nonlinear perturbations of the velocity, we find:

$$R_w \frac{(\Delta U_0)^2}{\Delta s} \sim \mu_w \frac{\Delta U_0}{(\Delta Y)^2} + \frac{\Delta U_0}{\Delta Y} \frac{\Delta \mu_0}{\Delta Y} \sim \frac{\partial p_0}{\partial s} \sim |\Delta s|^{-1/3}, \quad (3.5)$$

where Δs and ΔY are small deviations from $s = 0$ and $Y = 0$ respectively.²⁾ Finally, it is obvious that $\Delta \mu_0 \ll \mu_w \sim 1$, and (3.5) yields the following closed system of estimates:

$$\frac{(\Delta U_0)^2}{\Delta s} \sim \frac{\Delta U_0}{(\Delta Y)^2} \sim |\Delta s|^{-1/3}.$$

This system can be easily solved to give

$$\Delta U_0 \sim \Delta Y \sim |\Delta s|^{1/3} \quad (3.6)$$

Therefore, the so-called *viscous sublayers* are formed upstream and downstream of the singularity, with their thickness vanishing according to (3.6). This physical mechanism allows to generate strong viscous and inertial forces capable of balancing the singular pressure gradient.

Let us now focus on the sublayer upstream of the singularity. The parabolic nature of the boundary layer equations suggests that information is carried downstream, thus

²⁾We used the same value of ΔU_0 to approximate both $\partial U_0/\partial s$ and $\partial^2 U_0/\partial Y^2$ because each of these terms has to balance the singular pressure gradient in the momentum equation; as a result, velocity increments in the two different directions are not independent. Similar ideology was used when swapping U_0 with ΔU_0 in the inertial term.

requiring to consider regions upstream of the singularity first. Due to the second estimate in (3.6) the relevant solution should depend on the similarity variable

$$\eta = \frac{Y}{(-s)^{1/3}}.$$

In the sublayer itself $\eta = \mathcal{O}(1)$; $\eta = 0$ corresponds to the wall, and $\eta \rightarrow \infty$ when the main part of the boundary layer is reached (it is denoted as region 2a in Fig. 3.2). It turns out that the latter is mostly inviscid and only inertial terms balance the pressure gradient (the flow is fast enough, so that $U_0 \gg \Delta U_0$ in the main inertial term). To simplify the analysis in the sublayer, we introduce a compressible stream function $\psi_0(s, Y)$:

$$\frac{\partial \psi_0}{\partial Y} = R_0 U_0, \quad \frac{\partial \psi_0}{\partial s} = -R_0 V_0. \quad (3.7)$$

With (3.7) the continuity equation is satisfied automatically, while the no-slip con-

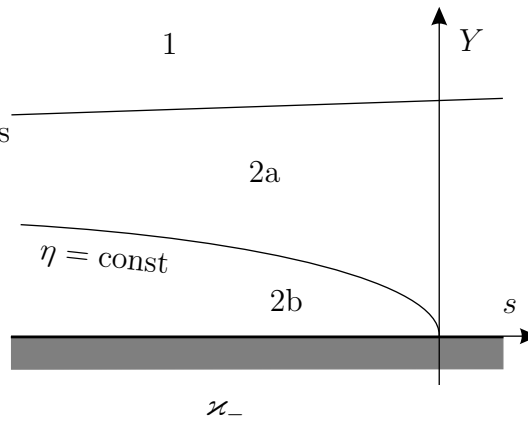


Figure 3.2: Singular pressure gradients lead to the typical two-tier structure of the boundary layer upstream of the singularity.

dition reduces to

$$\psi_0|_{Y=0} = \frac{\partial \psi_0}{\partial Y}|_{Y=0} = 0. \quad (3.8)$$

With this in mind, one can obtain an estimate

$$\psi_0 = \Delta \psi_0 \sim R_0 U_0 \Delta Y \sim R_w \Delta U_0 \Delta Y \sim (\Delta Y)^2 \sim |\Delta s|^{2/3}$$

for the stream function in the sublayer. Therefore, we write an asymptotic expansion for ψ_0 in the sublayer as

$$\psi_0(s, Y) = (-s)^{2/3} \psi(\eta) + \dots \quad (3.9)$$

The leading order term here represents a response to the singular pressure gradient, while the higher-order terms (not shown explicitly) stand for the eigen modes of the sublayer (see Goldstein (1948) for details). From now on we are going to neglect the eigen modes because in our case the main physical effect proves to be described by the leading-order term in (3.9).

Strictly speaking, we also need to consider a thermal sublayer and construct the appropriate expansions for the remaining functions R_0 , h_0 and μ_0 . Simple estimates in the energy equation from (3.2) suggest that the heat generated by internal friction is balanced by heat conductivity when $\Delta h_0 \sim |\Delta s|^{1/3}$. On the other hand, convective terms and mechanical work produced by the pressure are in balance with the heat generation when $\Delta Y \sim |\Delta s|^{1/3}$. Thus, the thermal and dynamical sublayers coincide. The relevant expansions for R_0 , h_0 and μ_0 are

$$\begin{aligned} h_0 &= h_w + (-s)^{2/3} \tilde{h}(\eta) + \dots, \\ R_0 &= R_w + (-s)^{2/3} \tilde{R}(\eta) + \dots, \\ \mu_0 &= \mu_w + (-s)^{2/3} \tilde{\mu}(\eta) + \dots; \end{aligned} \tag{3.10}$$

parameters R_w , h_w and μ_w are assumed to be known from the global solution of the boundary layer equations (3.2). Plugging these expansions along with (3.9) into the momentum equation in (3.2) yields a single equation for $\psi(\eta)$ in the leading order approximation:

$$\mu_w \psi''' - \frac{2}{3} \psi \psi'' + \frac{1}{3} (\psi')^2 = R_w k G_-, \quad \psi' = \frac{d\psi}{d\eta}, \tag{3.11}$$

suggesting that the gas, indeed, behaves like an incompressible fluid in the sublayer. The energy equation and the equation of state split from the system, and equation (3.11) (which combines the continuity and the momentum equations) can be solved independently.

We need three boundary condition to obtain a unique solution of (3.11). Two of them come from no-slip condition (3.8) after applying it to (3.9):

$$\psi|_{\eta=0} = \psi'|_{\eta=0} = 0. \tag{3.12}$$

The remaining condition states that $\psi(\eta)$ is not allowed to grow exponentially when $\eta \rightarrow \infty$. Should such a growth occur, we won't be able to obtain a finite solution for the main part of the boundary layer, making it impossible to perform matching with the outer inviscid flow when $Y \rightarrow \infty$ (Goldstein 1948). The asymptotic form of $\psi(\eta)$ at infinity can still have positive powers of η as well as $\ln \eta$.

It is easy to spot that equation (3.11) admits an exact solution in terms of a quadratic polynomial

$$\psi(\eta) = a_0\eta^2 + a_1\eta + a_2,$$

as long as the constant coefficients satisfy a constraint $a_1^2 - 4a_0a_2 = 3R_w kG_-$. However, the no-slip condition (3.12) requires $a_1 = a_2 = 0$, leading to a contradiction with the constraint when $G_- \neq 0$. Therefore, if we want to obtain a solution for ψ corresponding to a non-zero pressure gradient, we need to assume that $\psi(\eta) \neq a_0\eta^2 + a_1\eta + a_2$; the latter implies there is a nontrivial solution for ψ''' . Differentiating (3.11) once we get

$$\mu_w \psi^{(4)} - \frac{2}{3} \psi \psi''' = 0, \quad \psi^{(4)} = \frac{d^4 \psi}{d\eta^4}.$$

Introducing a new function

$$\chi(\eta) = \int_0^\eta \psi(\xi) d\xi,$$

this equation may be represented in the form

$$\mu_w \frac{d\chi^{(4)}}{d\chi} - \frac{2}{3} \chi^{(4)} = 0, \quad \chi^{(4)} = \frac{d^4 \chi}{d\eta^4},$$

and so

$$\psi''' = \frac{d^4 \chi}{d\eta^4} = C e^{\frac{2\chi}{3\mu_w}}. \quad (3.13)$$

In order to find the integration constant C , we simply need to set $\eta = 0$ in (3.11), and note that with $\eta = 0$, (3.13) reduces to $\psi'''|_{\chi=0} = C$. Thus,

$$C = \frac{R_w k G_-}{\mu_w};$$

(3.13) may be rewritten as

$$\psi''' = \frac{d^4 \chi}{d\eta^4} = \frac{R_w k G_-}{\mu_w} e^{\frac{2\chi}{3\mu_w}}. \quad (3.14)$$

This equation is equivalent to (3.11) along with no-slip condition (3.12). It suggests that, unless we consider solutions describing a reverse flow, any polynomial representation of ψ fails when $\eta \rightarrow \infty$. Indeed, we are expecting to have a well attached boundary layer upstream of the interaction region, especially in the case of $G_- < 0$, and therefore need to restrict our attention to the solutions which give $U_0 > 0$ across the sublayer 2b (no reverse flow). The latter means $\psi' > 0$ for all $\eta \in (0, \infty)$, and both ψ and χ grow steadily with η . As a result, the matching condition with the main part of the boundary layer 2a implies that χ , treated as a function of η , tends to $+\infty$ according to a certain power dependence when $\eta \rightarrow \infty$.³⁾ But this generates exponentially growing terms due to (3.14), and we are unable to perform the required matching. Moreover, equation (3.14) may simply have no solutions that would grow indefinitely with η .

The contradiction hints that the boundary-value problem for $\psi(\eta)$ has no solutions when $G_- \neq 0$ (i.e., when there is a discontinuity in wall curvature). To find out what causes this situation and how to obtain a suitable solution for the sublayer, we shall consider a more general pressure gradient

$$\frac{\partial p}{\partial s} = G (-s)^{-\lambda};$$

in our case $\lambda = 1/3$. Again, assuming that the pressure gradient is strong enough to cause nonlinear effects in the viscous sublayer, we can estimate

$$\Delta U_0 \sim U_0 \tag{3.15}$$

in the convective terms; balancing them with the viscous forces and the pressure therefore requires

$$\Delta U_0 \sim |\Delta s|^{\frac{1-\lambda}{2}}, \quad \Delta Y \sim |\Delta s|^{\frac{1+\lambda}{4}}. \tag{3.16}$$

This indicates that a viscous sublayer is formed close to the wall when the singularity is approached ($\Delta s \rightarrow 0$).

According to (3.15) and (3.16), the stream function is estimated as

$$\psi_0 = \Delta \psi_0 \sim U_0 \Delta Y \sim |\Delta s|^{\frac{3-\lambda}{4}},$$

³⁾ To be more specific, χ should be proportional to η^3 in the overlapping region between the viscous sublayer and the main part of the boundary layer, which gives a linear profile for $U_0(Y)$.

resulting in the following asymptotic expansion:

$$\psi_0 = (-s)^{\frac{3-\lambda}{4}} \psi(\eta) + \dots, \quad \eta = \frac{Y}{(-s)^{\frac{1+\lambda}{4}}}. \quad (3.17)$$

Plugging this into the momentum equation gives

$$\mu_w \psi''' - \frac{3-\lambda}{4} \psi \psi'' + (1-\lambda) (\psi')^2 = 2R_w G. \quad (3.18)$$

The boundary conditions for $\psi(\eta)$ are same as before, i.e. $\psi|_{\eta=0} = \psi'|_{\eta=0} = 0$, plus no exponential growth as $\eta \rightarrow \infty$.

To be able to see how variations in λ affect the solution of the boundary-value problem, it is helpful to consider the asymptotic behaviour of $\psi(\eta)$ when $\eta \rightarrow \infty$. Equation (3.18) can be transformed to

$$\mu_w \sqrt{\omega} \frac{d^2 \omega}{d\psi^2} - \frac{3-\lambda}{4} \psi \frac{d\omega}{d\psi} + (1-\lambda) \omega = 2R_w G, \quad \omega(\psi) = (\psi')^2, \quad (3.19)$$

with the no-slip condition requiring that

$$\omega|_{\psi=0} = 0. \quad (3.20)$$

We now need to look at the asymptotic form of $\omega(\psi)$ when $\psi \rightarrow \infty$ in terms of power functions, which corresponds to having powers of η in $\psi(\eta)$ when $\eta \rightarrow \infty$:

$$\omega(\psi) = A\psi^\alpha + \frac{2R_w G}{1-\lambda} + \frac{B}{\psi^\beta} + \dots, \quad \psi \rightarrow \infty. \quad (3.21)$$

Here $\alpha = \frac{4(1-\lambda)}{3-\lambda}$, $\beta = \frac{4\lambda}{3-\lambda}$, the free parameter A can be determined by solving equation (3.19) numerically for all ψ and satisfying the no-slip condition on the wall, and

$$B = -\frac{4\mu_w A^{3/2} (1-\lambda)(1-3\lambda)}{(3-\lambda)^2}. \quad (3.22)$$

The first two terms in (3.21) come from balancing the convective terms with the pressure gradient, while B/ψ^β corresponds to the viscous forces. It can be clearly seen from (3.22) that $B \rightarrow 0$ if $\lambda \rightarrow 1/3$, indicating that power expansion (3.21) fails to include viscous effects when $\lambda = 1/3$. Since the latter are necessary to satisfy the no-slip condition when integrating (3.19) down to the wall, the only way to keep the viscosity alive is to introduce specific terms into (3.21) decaying with ψ much faster than power functions (for example, exponentially small terms).

There is also a possibility that $\lambda = 1/3$ is a real degenerate case, when the boundary value problem for $\omega(\psi)$ has no solutions. A better understanding of what happens when $\lambda \rightarrow 1/3$ can be achieved by solving the problem (3.19), (3.20), (3.21) numerically. Introducing a small deviation ε :

$$\lambda = \frac{1}{3} + \varepsilon, \quad |\varepsilon| \ll 1.$$

and setting A in (3.21), we integrated (3.19) starting from large ψ (when (3.21) holds) down to the wall. By means of an iteration process the only value of A , denoted as A_* , which allows to satisfy the no-slip condition (3.20) was obtained. Repeating the procedure for different values of ε , we computed the function $A_*(\varepsilon)$; it turned out to be a straight line with a negative slope close to $-3/4$ when plotted in logarithmic scale. Thus,

$$A_*(\varepsilon) = |\varepsilon|^{-\nu}, \quad \nu \approx 0.75, \quad |\varepsilon| \ll 1,$$

and $A_* \rightarrow \infty$ when $|\varepsilon| \rightarrow 0$. This situation resembles a resonance and suggests that $\lambda = 1/3$ is, indeed, a degenerate case. As a result, certain logarithmic terms should be added to the power functions in the original expansion (3.17) when $\lambda = 1/3$.

To make the effect even more clear, let us use asymptotic form (3.21) to obtain the velocity profile $U_0(Y)$ at the bottom of the main inviscid part of the boundary layer (i.e. in the overlapping region with the viscous sublayer) for various λ . First of all, since $\omega = (d\psi/d\eta)^2$, (3.21) yields

$$d\eta = \frac{d\psi}{A^{1/2} \psi^{\alpha/2}} \left[1 - \frac{1}{\lambda - 1} \frac{R_w G}{A \psi^\alpha} - \frac{B}{2A \psi^{\alpha+\beta}} + \dots \right].$$

Secondly, $\alpha = 1 + \mathcal{O}(\varepsilon)$ when $\lambda = \frac{1}{3} + \varepsilon$, and the integration simply results in

$$\eta = \frac{2 \psi^{1-\alpha/2}}{A^{1/2}(2-\alpha)} (1 + \dots). \quad (3.23)$$

Now, from (3.17)

$$U_0 \sim \frac{1}{R_w} \frac{\partial \psi_0}{\partial Y} \sim \frac{1}{R_w} (-s)^{\frac{1-\lambda}{2}} \frac{d\psi}{d\eta} \equiv \frac{1}{R_w} (-s)^{\frac{1-\lambda}{2}} \sqrt{\omega}.$$

Using (3.21) for $\omega(\psi)$ when $\psi \rightarrow \infty$, and expressing ψ via η according to (3.23), we get in the leading order:

$$U_0 \sim (-s)^{\frac{1-\lambda}{2}} \eta^{\frac{\alpha}{2-\alpha}} \sim Y^{\frac{2(1-\lambda)}{1+\lambda}}. \quad (3.24)$$

This profile (describing the flow in the overlapping region) is plotted in Fig. 3.3 for $\lambda > 1/3$, $\lambda = 1/3$ and $\lambda < 1/3$. The illustration clearly shows that the $\lambda = 1/3$ case demarcates two physically different regimes. Stronger gradients ($\lambda > 1/3$) lead to $\partial^2 U_0 / \partial Y^2 < 0$, which means viscous forces are slowing fast fluid particles down, so that the no-slip condition can hold. Weaker gradients ($\lambda < 1/3$), however, result in $\partial^2 U_0 / \partial Y^2 > 0$ regardless of whether the gradient is favourable or adverse, suggesting that viscous forces actually accelerate fluid particles which is an unlikely situation for our particular problem. Finally, when $\lambda = 1/3$, we get $\partial^2 U_0 / \partial Y^2 = 0$; this leads to the degeneration of viscous forces in equation (3.11) for the sublayer, and hence to the inability to satisfy the no-slip condition.

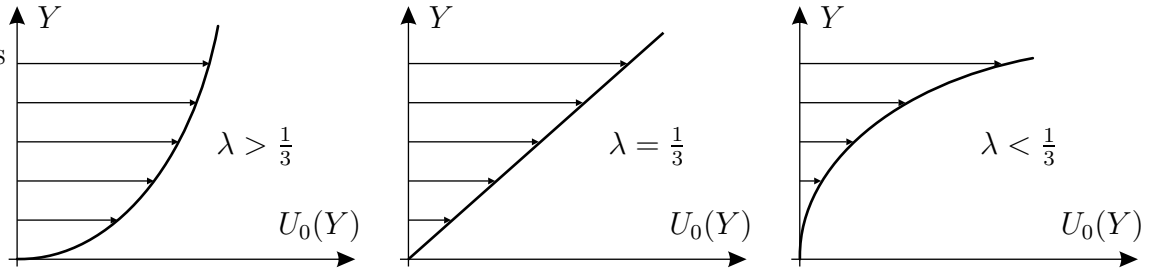


Figure 3.3: Velocity profiles in the overlapping region between tiers 2a and 2b for three characteristic values of λ , obtained in the assumption that the pressure gradient causes nonlinear velocity perturbations in the viscous sublayer 2b.

The regime with $\lambda < 1/3$, which results in $\partial^2 U_0 / \partial Y^2 > 0$, can still have a physical meaning. For example, in the theory of *marginal separation* the flow, after being exposed to a regular adverse pressure gradient acting along the upper surface of an airfoil, enters the interaction region in a pre-separated state (Sychev et al. 1998). In this case the leading-order velocity profile is $U_0 \sim Y^2$, which corresponds to $\lambda = 0$ in our analysis of the effects produced by the singular pressure gradient $\partial p / \partial s \sim (-s)^{-\lambda}$. Therefore, $\partial^2 U_0 / \partial Y^2 > 0$, and the velocity profile has the shape shown in Fig. 3.3, right.⁴⁾

Nevertheless, if a pre-separated state does not develop, one has to reconsider the

⁴⁾ The pre-separated solution $U_0 \sim Y^2$ providing the background for marginal separation is valid everywhere inside the viscous sublayer, and not just in the overlapping region with the main part of the boundary layer.

estimates made for the local pressure gradient with $\lambda < 1/3$. Indeed, by saying that ΔU_0 is of the same order as U_0 in convective terms, i.e. that the perturbations are nonlinear, we actually bound the velocity value directly to the pressure gradient. However, when $\lambda < 1/3$ the pressure gradient apparently is not strong enough to cause nonlinear perturbations (locally) – hence the physically unreasonable solution with $\partial^2 U_0 / \partial Y^2 > 0$. A more meaningful estimate in this case is $\Delta U_0 \ll U_0$, so that the velocity perturbation generated in the viscous sublayer by the weaker pressure gradient is much smaller than a ‘regular’ velocity near the wall in the absence of this gradient. The ‘regular’ velocity profile may be given, for example, by the well-known Blasius solution, and has to be linear close to the wall:

$$U_0 = \tau_w Y + \mathcal{O}(Y^2), \quad Y \rightarrow 0.$$

When the singularity is approached, the viscous sublayer is still formed, but the estimates for ΔU_0 and ΔY as functions of Δs are different from those that we had previously. Indeed, balancing terms in the momentum equation requires

$$U_0 \frac{\Delta U_0}{\Delta s} \sim |\Delta s|^{-\lambda} \sim \frac{\Delta U_0}{(\Delta Y)^2},$$

where $U_0 \sim Y \sim \Delta Y$. Thus, $\Delta Y \sim |\Delta s|^{1/3}$ regardless of λ , and

$$\Delta U_0 \sim |\Delta s|^{-\lambda+2/3} \sim (\Delta Y)^{2-3\lambda},$$

so that $\Delta U_0 / U_0 \sim (\Delta Y)^{1-3\lambda} \ll 1$ when $\lambda < 1/3$.

Once again, we see that the singular pressure gradient with $\lambda = 1/3$ is a special case. The two physically different solutions which exist when $\lambda < 1/3$ (corresponding to either $\Delta U_0 \sim U_0$ or $\Delta U_0 \ll U_0$) are expected to coincide in the limit $\lambda \rightarrow (1/3)^-$, because only one solution exists for $\lambda > 1/3$. Therefore, we expect to get an intermediate situation when $\lambda = 1/3$, with weak cumulative effects upstream of the singularity actually being prescribed by the nature of the singularity. This clearly resembles a resonance, and would require logarithmic terms in the original coordinate expansion (3.9) in order to obtain the solution of the relevant boundary-value problem.

In the case of $\lambda < 1/3$ and no cumulative effects, the estimate $\Delta U_0 \ll U_0$ leads to the following expansion for ψ_0 :

$$\psi_0 = \frac{\tau_w Y^2}{2} + (-s)^{1-\lambda} \psi(\eta) + \dots, \quad \eta = \frac{Y}{(-s)^{1/3}}. \quad (3.25)$$

Plugging this into the momentum equation results in a linear equation for $\psi(\eta)$:

$$\mu_w \psi''' - \frac{\tau_w}{3} \left[\eta^2 \psi'' - 3(1-\lambda) \eta \psi' + 3(1-\lambda) \psi \right] = R_w G.$$

The asymptotic form of $\psi(\eta)$ as $\eta \rightarrow \infty$ is then given by

$$\psi(\eta) = A \eta^{3(1-\lambda)} + B \eta - \frac{R_w G}{\tau_w (1-\lambda)} + C \eta^{-3\lambda} + \dots,$$

where A, B are independent constants obtained from the no-slip condition on the wall, and C can be expressed via A . If we substitute this into (3.25) and differentiate with respect to Y once, it will provide velocity profile in the overlapping region between the sublayer and the main part of the boundary layer:

$$U_0 = \tau_w Y + 3A(1-\lambda) Y^{2-3\lambda} + B(-s)^{-\lambda+2/3} + \dots$$

Thus, when $\lambda = \frac{1}{3}(1-\varepsilon)$, $0 < \varepsilon \ll 1$, a weak logarithmic term is generated:

$$Y^{2-3\lambda} = Y^{1+\varepsilon} = Y (1 + \varepsilon \ln Y + \mathcal{O}(\varepsilon^2)).$$

The $Y \ln Y$ term is expected to replace the simple linear profile $U_0 \sim Y$ which was obtained previously for the case of $\lambda = 1/3$, thereby removing the degeneration of viscous forces.

3.1.2 Nonlinear logarithmic expansion in the viscous sub-layer

To verify the above predictions for the case when $\partial p_0 / \partial s \sim (-s)^{-1/3}$, let us introduce logarithms of $(-s)$ into the original coordinate expansion (3.9) for the sublayer (Buldakov & Ruban 2002):

$$\psi_0(s, Y) = (-s)^{2/3} \left[(-\ln(-s))^\kappa \psi(\eta) + (-\ln(-s))^{\kappa-1} \varphi(\eta) + \dots \right], \quad (3.26)$$

where

$$\eta = \frac{Y}{(-s)^{1/3}(-\ln(-s))^\nu},$$

and κ, ν are constants. Taking into the account the cumulative effects in the resonant case of $\partial p_0/\partial s \sim (-s)^{-1/3}$, we choose κ and ν in such a way that, upon plugging (3.26) into the momentum equation, the pressure gradient only appears in the second order approximation based on the powers of logarithms. This proves to be the only way to obtain the solutions for $\psi(\eta)$ and $\varphi(\eta)$ which satisfy all the boundary conditions. Simple estimates, therefore, lead to the unique set of values of κ and ν :

$$\kappa = \frac{1}{4}, \quad \nu = -\frac{1}{4},$$

in agreement with Buldakov & Ruban (2002). Once these values have been chosen, the leading order function $\psi(\eta)$ should satisfy the homogeneous equation

$$\mu_w \psi''' - \frac{2}{3} \psi \psi'' + \frac{1}{3} (\psi')^2 = 0,$$

which is a particular case of equation (3.11) when $G_- = 0$. Since (3.11) and the no-slip conditions are equivalent to (3.14), setting $G_- = 0$ in the latter results in

$$\chi^{(4)} = \frac{d^3 \psi}{d\eta^3} = 0.$$

Integrating this simple equation and taking into the account the no-slip conditions, we obtain the only suitable solution for ψ :

$$\psi(\eta) = \frac{\tau_w \eta^2}{2}.$$

Parameter τ_w (related to the leading order skin friction) will be determined from the next order problem describing $\varphi(\eta)$. The equation for φ is linear and contains the pressure gradient:

$$\varphi''' - \frac{\tau_w}{3\mu_w} \left[\eta^2 \varphi'' - 2\eta \varphi' + 2\varphi \right] = \frac{R_w k G_-}{\mu_w} + \frac{3\tau_w^2}{\mu_w} \eta^2. \quad (3.27)$$

The second term on the right-hand side comes from the solution for $\psi(\eta)$ (leading order problem), thanks to the nonlinearity of the original momentum equation. It is this term that allows to construct the solution for φ which satisfies the no-slip

condition and does not grow exponentially when $\eta \rightarrow \infty$. Differentiating (3.27) once, we get an integrable equation for $W(\eta) = \varphi'''$, and can therefore reconstruct φ :

$$\varphi(\eta) = \frac{1}{2} \int_0^\eta (\eta - \zeta)^2 W(\zeta) d\zeta + C\eta^2, \quad W(\zeta) = \frac{3\tau_w^2}{4\mu_w} \int_\infty^\zeta \xi e^{-\alpha_w(\xi^3 - \zeta^3)} d\xi. \quad (3.28)$$

Here constant C is expected to be determined from the next order problem, and parameter $\alpha_w = \frac{\tau_w}{9\mu_w}$.

Solution (3.28) obviously satisfies all of the three boundary conditions. However, the differentiation of equation (3.27) while deriving (3.28) resulted in a loss of the constant $R_w k G_- / \mu_w$. Therefore, a certain condition should hold for (3.28) to actually satisfy (3.27). Plugging (3.28) into (3.27) gives

$$-\frac{3\tau_w^2}{4} \int_0^\infty \xi e^{-\alpha_w \xi^3} d\xi = R_w k G_-; \quad (3.29)$$

the integral can be transformed to $\Gamma(2/3)$, and (3.29) eventually takes the form

$$\tau_w = \frac{1}{3\sqrt{\mu_w}} \left[-\frac{4R_w k G_-}{\Gamma(2/3)} \right]^{3/4}. \quad (3.30)$$

This expression defines the leading order skin friction τ_w as a function of G_- and other known parameters of the flow.

According to (3.30), real values of τ_w exist only when $G_- \leq 0$, i.e. for favourable pressure gradients. Any adverse pressure gradient ($G_- > 0$) results in complex τ_w , suggesting that an early separation takes place long before the singularity is reached.⁵⁾ Once again, it demonstrates why the viscous sublayer is extremely sensitive to the singular pressure gradient proportional to $(-s)^{-1/3}$. However, basic physical intuition says that there should not be an abrupt change in the flow structure when kG_- switches from negative to small positive values.⁶⁾ In other words, it should be possible to extend real solutions for τ_w to at least small positive kG_- . This opens up the way to constructing a *linear theory* which will be the focus of our attention henceforth. But before we proceed with the theory, let us find out what happens with the logarithmic expansion (3.26) when $kG_- \rightarrow 0^-$.

⁵⁾ This phenomenon was not mentioned in the earlier work by Buldakov & Ruban (2002), and is one of the main results of this thesis.

⁶⁾ Both of the parameters k and G_- can be small – see section 3.1.3.

Since $\psi(\eta) = \frac{\tau_w \eta^2}{2}$, (3.26) yields:

$$U_0(s, Y) \sim \frac{\partial \psi_0}{\partial Y} = (-\ln(-s))^{3/4} \tau_w Y + \mathcal{O}\left[(-\ln(-s))^{-1/4}\right],$$

so that the corresponding coordinate expansion of U_0 in the main part of the boundary layer starts with $(-\ln(-s))^{3/4} U_{00}(Y)$, where $U_{00}(Y)$ sets the leading order velocity profile across the boundary layer near the singularity. On the other hand, there have to be no logarithmic terms in the solution for U_0 when $Y \rightarrow \infty$. Indeed,

$$U_0|_{Y \rightarrow \infty} = U_e(s) = 1 + \mathcal{O}((-s)^{2/3}),$$

as prescribed by the matching condition with the outer inviscid flow. Thus, $U_{00}(Y) \rightarrow 0$ when $Y \rightarrow \infty$. It means that the coordinate expansion for U_0 should also have a term without logarithms or powers of $(-s)$, i.e. a function of Y only, which tends to 1 in the overlapping region with the outer flow:

$$U_0(s, Y) = (-\ln(-s))^{3/4} U_{00}(Y) + U_{01}(Y) + \mathcal{O}\left[(-\ln(-s))^{-1/4}\right], \quad U_{01}(\infty) = 1. \quad (3.31)$$

The fact that there is a relatively large logarithmic term in front of the ‘natural’ boundary layer velocity profile $U_{01}(Y)$ is a result of the cumulative effects taking place in the resonant case.

When we enter the sublayer ($Y \rightarrow 0$), (3.31) reduces to

$$U_0 = (-\ln(-s))^{3/4} \tau_w Y + \tau_0 Y + \dots, \quad (3.32)$$

where $\tau_0 Y$ stands for the leading term in the Taylor expansion of $U_{01}(Y)$ near the wall; its presence in (3.32) is dictated by the matching condition with the outer flow. However, if we look at what the original expansion (3.26) gives in the overlapping region between the sublayer and the main part of the boundary layer, we will get:

$$U_0(s, Y) \sim Y(-\ln(-s))^{3/4} \left\{ (\tau_w - a_\infty) + \frac{3a_\infty}{\ln(-s)} \left[\ln Y + \frac{1}{4} \ln(-\ln(-s)) + \dots \right] + \dots \right\},$$

$a_\infty = 3\tau_w/4$. This expansion is due to the asymptotic behaviour of $\varphi(\eta)$ when $\eta \rightarrow \infty$, and clearly does not contain a function of Y on its own. Therefore, it does not match with what comes from the main part of the boundary layer (expansion (3.32)).

The contradiction is resolved by inserting the ‘intermediate’ $\frac{\tau_0 Y^2}{2}$ term between the two leading order terms of (3.26):

$$\psi_0(s, Y) = (-s)^{2/3} (-\ln(-s))^{1/4} \psi(\eta) + \frac{\tau_0 Y^2}{2} + (-s)^{2/3} (-\ln(-s))^{-3/4} \varphi(\eta) + \dots, \quad (3.33)$$

with

$$\eta = \frac{Y (-\ln(-s))^{1/4}}{(-s)^{1/3}}.$$

It can be easily shown that this modified expansion leads to the same equations for $\psi(\eta)$ and $\varphi(\eta)$ as before, and the relevant solutions obtained for these functions previously remain valid. Hence, expression (3.30) for τ_w is not affected by the introduction of the τ_0 term, and $\tau_w \sim (-kG_-)^{3/4}$. Since $\psi(\eta) = \frac{\tau_w \eta^2}{2}$, the leading order term in (3.33) is

$$\left(C_0 \left[(-kG_-) (-\ln(-s)) \right]^{3/4} + \frac{\tau_0}{2} \right) Y^2,$$

where constant C_0 is proportional to τ_w . This expression has an important consequence: if we are working on a spatial scale $(-s) \sim \text{Re}^{-\chi}$ (as it usually is the case in the problems involving viscous-inviscid interaction), $\chi = \text{const}$, then the first term in the above expression becomes an order one quantity when

$$-kG_- \sim \frac{1}{\ln \text{Re}} \ll 1.$$

With any further diminishing of $|kG_-|$ the $\frac{\tau_0 Y^2}{2}$ term begins to dominate expansion (3.33) on the given spatial scale for s , and the entire mathematical description of the flow in the sublayer has to be reconsidered. Thus, nonlinear solution (3.30) for τ_w is not valid when $|kG_-|$ is smaller than $\mathcal{O}(1/\ln \text{Re})$, explaining why (3.30) provides the abrupt change in the physics of the flow as soon as G_- changes the sign to positive.

To summarize, small values of $|kG_-|$ need a special consideration. This detail was missed by Buldakov & Ruban (2002), and therefore their results obtained for the case of a logarithmically-small pressure gradient can only be treated as approximate. In the subsequent sections we are going to develop an asymptotic theory which yields real τ_w for small positive $kG_- \lesssim 1/\ln \text{Re}$. This theory will be different from the one obtained by Buldakov & Ruban, and cannot be viewed simply as an extension of the

latter to the case of small singular pressure gradients. In order to proceed, we need to recall the inviscid flow theory developed in Chapter 2 and find out what regimes correspond to $|kG_-| \ll 1$.

3.1.3 Special case of a small amplitude in the pressure gradient

According to (2.28), the pressure gradient upstream of the singularity generated by the outer inviscid flow is

$$\frac{\partial p_0}{\partial s} = kG_-(-s)^{-1/3}, \quad k = \frac{10[(\gamma + 1)\kappa_-]^{2/3}}{9},$$

with G_- being a function of the curvatures' ratio. It was demonstrated previously in Chapter 2 that this function (along with G_+) has a unique subcritical solution and a family of supercritical solutions (see Fig. 2.55). After looking at how G_- behaves for different values of κ_+/κ_- , it is clear that $|kG_-|$ can be small in the two following cases:

- $\kappa_- = \mathcal{O}(1)$, $|G_-| \ll 1$, corresponding to a subcritical flow near a small break in wall curvature. This inviscid flow regime will be in the focus during the subsequent study of the viscous-inviscid interaction. It was first mentioned in section 2.4.6.
- $\kappa_- \ll 1$, $G_- = \mathcal{O}(1)$, corresponding to a supercritical flow over a strong break of curvatures, with a much flatter upstream wall ($\kappa_+/\kappa_- \gg 1$). This regime was described in section 2.4.12, and features a supercritical supersonic flow near the upstream and the downstream walls, plus a weak shock in between. Studying viscous-inviscid interaction in this case may be a subject of an independent theoretical work.

From now on we are going to consider the first case only. In section 2.4.6 it was shown that if

$$\frac{\kappa_+}{\kappa_-} - 1 = \varepsilon_0, \quad |\varepsilon_0| \ll 1,$$

then

$$G_- = -\frac{\alpha^{5/3} \Gamma(1/6) \varepsilon_0}{2(3\alpha - 2)\sqrt{\pi} \Gamma(2/3)} (1 + \mathcal{O}(\varepsilon_0)), \quad \alpha = \frac{3}{2},$$

and \varkappa_- is an order one quantity. Defining the parameters ε , G as

$$\varepsilon = \frac{5\alpha^{5/3} \Gamma(1/6) [(\gamma + 1)\varkappa_-]^{2/3} |\varepsilon_0|}{9(3\alpha - 2)\sqrt{\pi} \Gamma(2/3)} (1 + \mathcal{O}(\varepsilon_0)), \quad 0 < \varepsilon \ll 1, \quad (3.34)$$

$$G = -\text{sign}(\varepsilon_0),$$

we can write

$$kG_- = \varepsilon G = \begin{cases} \varepsilon, & \frac{\varkappa_+}{\varkappa_-} < 1, \\ -\varepsilon, & \frac{\varkappa_+}{\varkappa_-} > 1, \end{cases}$$

so that the pressure gradient

$$\frac{\partial p_0}{\partial s} = \varepsilon G (-s)^{-1/3}.$$

The small parameter ε allows to construct asymptotic expansions and linearize the theory.

Since $\varepsilon = 0$ corresponds to a continuous curvature, there is no singular pressure gradient in this case, and the relevant stream function in the sublayer is expected to have the $\frac{\tau_w Y^2}{2}$ term in the leading order. This term can be treated as the asymptotic form of a regular solution of the boundary layer equations near the wall; the constant $\tau_w = \mathcal{O}(1)$ is assumed to be known from the global problem (along with R_w and μ_w). When $\varepsilon \neq 0$, the presence of the small but singular pressure gradient requires all the terms in the momentum equation to be balanced in the $\mathcal{O}(\varepsilon)$ approximation, thus leading to the following expansion for the stream function:

$$\psi_0(s, Y, \varepsilon) = \frac{\tau_w Y^2}{2} + \varepsilon \left[(-s)^{2/3} \psi(\eta) + \dots \right] + \mathcal{O}(\varepsilon^2), \quad \eta = \frac{Y}{(-s)^{1/3}}.$$

Substituting this into the momentum equation yields

$$\mu_w \psi''' - \frac{\tau_w}{3} \left[\eta^2 \psi'' - 2\eta \psi' + 2\psi \right] = R_w G. \quad (3.35)$$

Function $\psi(\eta)$ should satisfy the no-slip condition on the wall and is not allowed to grow exponentially when $\eta \rightarrow \infty$. It turns out that this boundary-value problem still

has no solution, even despite the linearization. Indeed, differentiating (3.35) once, we obtain an integrable equation for $W(\eta) = \psi'''$:

$$\frac{dW}{d\eta} - \frac{\tau_w}{3\mu_w} \eta^2 W = 0.$$

A quadruple integration leads to a general solution

$$\psi(\eta) = C_0 \int_0^\eta (\eta - \zeta)^2 e^{\alpha_w \eta^3} d\zeta + C_1 \eta^2 + C_2 \eta + C_3, \quad \alpha_w = \frac{\tau_w}{9\mu_w},$$

where C_0 , C_1 , C_2 and C_3 are constants. Since it has been obtained by differentiating (3.35) and, therefore, neglecting the constant on the right-hand side of (3.35), a certain restriction has to be imposed on one of the integration constants for this solution to satisfy (3.35):

$$C_3 = -\frac{3R_w G}{2\tau_w} \neq 0.$$

However, the boundary conditions require $C_0 = C_2 = C_3 = 0$, suggesting that there appears to be a conflict between the two different expressions for C_3 , and the boundary value problem for ψ has no solution.

This degeneration is similar to the one taking place in the case of strong pressure gradients (see section 3.1.2), and is resolved by introducing logarithmic terms into the coordinate expansion for ψ_0 . Due to the linearity of the order ε problem, we expect $\ln(-s)$ to appear linearly, so that the required expansion has the form:

$$\psi_0(s, Y, \varepsilon) = \frac{\tau_w Y^2}{2} + \varepsilon (-s)^{2/3} \left[\ln(-s) \psi(\eta) + \varphi(\eta) + \dots \right] + \mathcal{O}(\varepsilon^2), \quad \eta = \frac{Y}{(-s)^{1/3}}. \quad (3.36)$$

The presence of $\ln(-s)$ in front of $\psi(\eta)$ leads to the homogeneous version of equation (3.35):

$$\mu_w \psi''' - \frac{\tau_w}{3} \left[\eta^2 \psi'' - 2\eta \psi' + 2\psi \right] = 0;$$

according to the above analysis, the only solution of this equation which satisfies all the boundary conditions is

$$\psi(\eta) = \frac{a\eta^2}{2}, \quad a = \text{const}.$$

The logarithmic term in (3.36) not only allows to obtain the solution for ψ , but also brings additional terms into the equation for $\varphi(\eta)$:

$$\mu_w \varphi''' - \frac{\tau_w}{3} \left[\eta^2 \varphi'' - 2\eta \varphi' + 2\varphi \right] = R_w G + \tau_w (\psi - \eta \psi') \equiv R_w G - \frac{\tau_w a \eta^2}{2}. \quad (3.37)$$

We are now going to show that the η^2 term on the right-hand side makes it possible to construct a suitable solution for φ , providing a certain value of the constant a is chosen. Differentiating (3.37) once and denoting $W(\eta) = \psi'''$, we get:

$$\frac{dW}{d\eta} - \frac{\tau_w}{3\mu_w} \eta^2 W = -\frac{\tau_w a \eta}{\mu_w}.$$

The general solution is

$$W(\eta) = -\frac{\tau_w a}{\mu_w} \int_{\eta_0}^{\eta} \xi e^{-\alpha_w(\xi^3 - \eta^3)} d\xi.$$

Integration constant η_0 should be adjusted in such a way that no exponential growth occurs when $\eta \rightarrow \infty$; this is only possible if $\eta_0 = \infty$, thus giving

$$W(\eta) = \frac{\tau_w a}{\mu_w} \int_{\eta}^{\infty} \xi e^{-\alpha_w(\xi^3 - \eta^3)} d\xi. \quad (3.38)$$

Integrating this three times and applying the no-slip conditions yields

$$\varphi(\eta) = \frac{1}{2} \int_0^{\eta} (\eta - \zeta)^2 W(\zeta) d\zeta + b\eta^2, \quad b = \text{const}. \quad (3.39)$$

We still need to make sure that this solution satisfies (3.37) with the $R_w G$ term on the right-hand side (the constant term was dropped due to the differentiation while deriving (3.39)). Plugging (3.39) into (3.37) leaves

$$\tau_w a \int_0^{\infty} \xi e^{-\alpha_w \xi^3} d\xi = R_w G.$$

This constraint provides a simple linear algebraic equation for a , and its solution may be expressed in the form

$$a = \frac{3\alpha_w^{2/3} R_w G}{\tau_w \Gamma(2/3)}. \quad (3.40)$$

Unlike the previous solution (3.30) for τ_w , the constant a is real for both adverse ($G = +1$) and favourable ($G = -1$) pressure gradients, while τ_w is now a given parameter ($\tau_w = \mathcal{O}(1)$).

Using the explicit solution for ψ , we can rewrite the original expansion for ψ_0 in the following way:

$$\psi_0(s, Y, \varepsilon) = \frac{\tau_w Y^2}{2} + \varepsilon \left[\ln(-s) \frac{a Y^2}{2} + (-s)^{2/3} \varphi(\eta) + \dots \right] + \mathcal{O}(\varepsilon^2), \quad (3.41)$$

$\varphi(\eta)$ is defined in (3.38)–(3.39).⁷⁾ The skin friction on the upstream wall is given by

$$t_w = \frac{\mu_w}{R_w} \frac{\partial^2 \psi_0}{\partial Y^2} \Big|_{Y=0} = \frac{\mu_w}{R_w} \left(\tau_w + \varepsilon [a \ln(-s) + 2b + \dots] + \mathcal{O}(\varepsilon^2) \right). \quad (3.42)$$

If $G = 1$ (adverse pressure gradient) and, hence, $a > 0$ according to (3.40), it may happen so that on a certain spatial scale $(-s) = \sigma \ll 1$ the logarithmic term will become large enough to cancel τ_w in the leading order:

$$\tau_w + \varepsilon a \ln \sigma = 0.$$

If σ , in its turn, represents the size of the interaction region, the latter normally estimated as $\text{Re}^{-\chi}$, $\chi = \text{const}$, then the above equation is going to provide an estimate for the value of ε which gives zero leading-order skin friction:

$$\varepsilon = \frac{\tau_w}{a\chi \ln \text{Re}} \sim \frac{1}{\ln \text{Re}}. \quad (3.43)$$

Thus, a boundary layer separation may take place in this case. Strictly speaking, asymptotic expansions (3.36), (3.42) fail when the leading order term with τ_w gets cancelled due to the growth of the logarithmic term, and the description of the flow has to be re-considered yet again. The flow regime corresponding to the estimate (3.43) is weakly nonlinear, demarcating the two logarithmic representations ((3.26) and (3.36)) introduced so far.

In subsequent sections, however, we are going to focus on the linear case when expansion (3.36) is valid, which is true for

$$\varepsilon \ll \frac{1}{\ln \text{Re}}.$$

The linear theory is expected to provide a better understanding of how the *incipient* viscous-inviscid interaction caused by a weak curvature break develops into boundary layer separation.

3.1.4 Displacement effects of the linear viscous sublayer

Let us now find the displacement generated in the linear viscous sublayer which is described by asymptotic solution (3.41). To do this, we need to look at the asymptotic

⁷⁾ The constant b is a free parameter which controls the structure of the boundary layer ahead of the interactions region; it is similar to the controlling parameter A_1 introduced by Buldakov & Ruban (2002) for the nonlinear case.

form of (3.41) when $\eta \rightarrow \infty$ and determine the structure of the relevant coordinate expansions in the main part of the boundary layer. It can be easily shown from (3.38)–(3.39) that

$$\varphi(\eta) = \frac{3a}{2} \eta^2 \ln \eta + (a_1 + b)\eta^2 + a_2\eta + a_3 + \frac{a_4}{\eta} + \dots, \quad \eta \rightarrow \infty. \quad (3.44)$$

Here constants a_n , $n = 1, 2, \dots$, are all non-zero order one quantities related to the main parameter a . In particular, $a_3 = -\frac{3R_w G}{2\tau_w}$, $a_4 = \frac{3\mu_w a}{2\tau_w}$, and, what is most important,

$$a_2 = 3a \int_0^\infty \zeta e^{\alpha_w \zeta^3} \int_\zeta^\infty \frac{e^{-\alpha_w \xi^3}}{\xi^2} d\xi d\zeta \equiv \frac{a}{3\alpha_w^{1/3}} \int_0^\infty \frac{e^\zeta}{\zeta^{1/3}} \int_\zeta^\infty \frac{e^{-\xi}}{\xi^{4/3}} d\xi d\zeta. \quad (3.45)$$

The integrand from this expression will be reduced to a special case of a *hypergeometric function* in section 3.2.2, therefore allowing to obtain a simple numerical value for a_2 and confirm that it is an order one quantity.

Plugging (3.44) into (3.41) and noticing that $\ln \eta = \ln Y - \frac{1}{3} \ln(-s)$ due to the definition of η , one can spot that the $\ln(-s)$ terms cancel. As a result, the coordinate expansion of ψ_0 in the overlapping region between the sublayer 2b and the main part of the boundary layer 2a only contains powers of $(-s)$:⁸⁾

$$\begin{aligned} \psi_0(s, Y, \varepsilon) &= \frac{\tau_w Y^2}{2} + \\ &+ \varepsilon \left[\frac{3a}{2} Y^2 \ln Y + (a_1 + b) Y^2 + (-s)^{1/3} a_2 Y + (-s)^{2/3} a_3 + \dots \right] + \mathcal{O}(\varepsilon^2). \end{aligned} \quad (3.46)$$

This expression suggests the form of the coordinate expansions in the main part of

⁸⁾ In this kind of a situation one could say that the displacement effect of the boundary layer upstream of the singularity is mainly due to the overlapping region rather than to the viscous sublayer.

the boundary layer:

$$\begin{aligned}
U_0(s, Y, \varepsilon) &= U_0^{(0)}(s, Y) + \varepsilon \left[U_{00}^{(1)}(Y) + (-s)^{1/3} U_{01}^{(1)}(Y) + (-s)^{2/3} U_{02}^{(1)}(Y) + \dots \right] + \mathcal{O}(\varepsilon^2), \\
V_0(s, Y, \varepsilon) &= V_0^{(0)}(s, Y) + \varepsilon \left[(-s)^{-2/3} V_{01}^{(1)}(Y) + (-s)^{-1/3} V_{02}^{(1)}(Y) + \dots \right] + \mathcal{O}(\varepsilon^2), \\
R_0(s, Y, \varepsilon) &= R_0^{(0)}(s, Y) + \varepsilon \left[R_{00}^{(1)}(Y) + (-s)^{1/3} R_{01}^{(1)}(Y) + (-s)^{2/3} R_{02}^{(1)}(Y) + \dots \right] + \mathcal{O}(\varepsilon^2), \\
h_0(s, Y, \varepsilon) &= h_0^{(0)}(s, Y) + \varepsilon \left[h_{00}^{(1)}(Y) + (-s)^{1/3} h_{01}^{(1)}(Y) + (-s)^{2/3} h_{02}^{(1)}(Y) + \dots \right] + \mathcal{O}(\varepsilon^2), \\
\mu_0(s, Y, \varepsilon) &= \mu_0^{(0)}(s, Y) + \varepsilon \left[\mu_{00}^{(1)}(Y) + (-s)^{1/3} \mu_{01}^{(1)}(Y) + (-s)^{2/3} \mu_{02}^{(1)}(Y) + \dots \right] + \mathcal{O}(\varepsilon^2).
\end{aligned} \tag{3.47}$$

Here the first digit in the subscript (which is zero everywhere) corresponds to the leading-order approximation based on powers of $\text{Re}^{-1/2}$ in the classical boundary layer theory, the second digit in the subscript shows the number of an approximation in the coordinate expansion based on the fractional powers of $(-s)$, and the superscript refers to the power of ε in a given approximation. The leading-order functions, denoted commonly as $f_0^{(0)}(s, Y)$, describe an unperturbed regular boundary layer over a smooth wall ($\varepsilon = 0$); they are assumed to be known from the global problem.⁹⁾ The analyticity of these functions implies that their coordinate expansions around $s = 0$ only have positive integer powers of $(-s)$:

$$U_0^{(0)}(s, Y) = U_{00}^{(0)}(Y) + (-s) U_{01}^{(0)}(Y) + \mathcal{O}((-s)^2),$$

the same being true for the other functions. Comparing this to the fractional powers of $(-s)$ in the order- ε terms shown explicitly in (3.47), we see that the latter give larger derivatives with respect to s . This becomes crucial when substituting (3.47) into the Navier–Stokes equations and collecting terms with different powers of $(-s)$.

In the order ε^0 approximation we get standard boundary layer equations with

⁹⁾ For example, these can be the well-known self-similar solutions for a compressible boundary layer written in the Dorodnitsyn-Lees variables (Sychev et al. 1998).

zero pressure gradient:

$$\left\{ \begin{array}{l} \frac{\partial(R_0^{(0)}U_0^{(0)})}{\partial s} + \frac{\partial(R_0^{(0)}V_0^{(0)})}{\partial Y} = 0 \\ R_0^{(0)} \left(U_0^{(0)} \frac{\partial U_0^{(0)}}{\partial s} + V_0^{(0)} \frac{\partial U_0^{(0)}}{\partial Y} \right) = \frac{\partial}{\partial Y} \left(\mu_0^{(0)} \frac{\partial U_0^{(0)}}{\partial Y} \right) \\ R_0^{(0)} \left(U_0^{(0)} \frac{\partial h_0^{(0)}}{\partial s} + V_0^{(0)} \frac{\partial h_0^{(0)}}{\partial Y} \right) = -\frac{1}{\text{Pr}} \frac{\partial}{\partial Y} \left(\mu_0^{(0)} \frac{\partial h_0^{(0)}}{\partial Y} \right) + \mu_0^{(0)} \left(\frac{\partial U_0^{(0)}}{\partial Y} \right)^2 \\ R_0^{(0)} h_0^{(0)} = \frac{1}{(\gamma - 1)}. \end{array} \right. \quad (3.48)$$

In the order ε^1 approximation one obtains fractional powers of $(-s)$ in the first two terms of the relevant coordinate expansions, namely $(-s)^{-2/3}$ and $(-s)^{-1/3}$; this results in two independent sets of equations. The $\mathcal{O}(\varepsilon(-s)^{-2/3})$ terms yield

$$\left\{ \begin{array}{l} -\frac{1}{3} \left(R_{00}^{(0)} U_{01}^{(1)} + U_{00}^{(0)} R_{01}^{(1)} \right) + \frac{d}{dY} \left(R_{00}^{(0)} V_{01}^{(1)} \right) = 0 \\ -\frac{1}{3} U_{00}^{(0)} U_{01}^{(1)} + \frac{dU_{00}^{(0)}}{dY} V_{01}^{(1)} = 0 \\ -\frac{1}{3} U_{00}^{(0)} h_{01}^{(1)} + \frac{dh_{00}^{(0)}}{dY} V_{01}^{(1)} = 0 \\ R_{00}^{(0)} h_{01}^{(1)} + h_{00}^{(0)} R_{01}^{(1)} = 0, \end{array} \right. \quad (3.49)$$

where the functions with common notation $f_{00}^{(0)}(Y)$ represent the leading-order regular flow profiles in the cross-section $s = 0$. Similarly, for the $\mathcal{O}(\varepsilon(-s)^{-1/3})$ terms we get:

$$\left\{ \begin{array}{l} -\frac{2}{3} \left(R_{00}^{(0)} U_{02}^{(1)} + U_{00}^{(0)} R_{02}^{(1)} \right) + \frac{d}{dY} \left(R_{00}^{(0)} V_{02}^{(1)} \right) = 0 \\ R_{00}^{(0)} \left[-\frac{2}{3} U_{00}^{(0)} U_{02}^{(1)} + \frac{dU_{00}^{(0)}}{dY} V_{02}^{(1)} \right] = -G \\ R_{00}^{(0)} \left[-\frac{2}{3} U_{00}^{(0)} h_{02}^{(1)} + \frac{dh_{00}^{(0)}}{dY} V_{02}^{(1)} \right] = U_{00}^{(0)} G \\ R_{00}^{(0)} h_{02}^{(1)} + h_{00}^{(0)} R_{02}^{(1)} = -\frac{3\gamma}{2} h_{00}^{(0)} R_{00}^{(0)} G. \end{array} \right. \quad (3.50)$$

The function $V_{01}^{(1)}(Y)$ described by system (3.49) is obviously responsible for the leading-order displacement effects. However, this system does not contain the pressure gradient, as the latter only appears in the next-order system (3.50). This hierarchy is the consequence of the cumulative effects taking place in the viscous sublayer

2b, and it will be crucial for the subsequent analysis of the viscous-inviscid interaction.

Excluding $U_{01}^{(1)}$, $R_{01}^{(1)}$ and $h_{01}^{(1)}$ from the last three equations in (3.49) leads to a first order differential equation for $V_{01}^{(1)}(Y)$, the solution being $V_{01}^{(1)}(Y) = C U_{00}^{(0)}(Y)$. The integration constant C is determined from matching this solution with the appropriate term in the asymptotic form (3.46) which comes from the sublayer. Indeed, (3.46) suggests that

$$V_{01}^{(1)} \sim \frac{a_2 Y}{3R_w}, \quad U_{00}^{(0)} \sim \frac{\tau_w Y}{R_w}$$

when $Y \rightarrow 0$. Hence, $C = \frac{a_2}{3\tau_w}$, and

$$V_{01}^{(1)}(Y) = \frac{a_2}{3\tau_w} U_{00}^{(0)}(Y).$$

This solution illustrates how the original displacement produced in the viscous sublayer 2b is transmitted into the outer flow via the predominantly inviscid main part 2a of the boundary layer. Now recall that in region 2a, according to (3.47),

$$V_0(s, Y, \varepsilon) = V_0^{(0)}(s, Y) + \varepsilon \left[(-s)^{-2/3} V_{01}^{(1)}(Y) + (-s)^{-1/3} V_{02}^{(1)}(Y) + \dots \right] + \mathcal{O}(\varepsilon^2). \quad (3.51)$$

The $V_0^{(0)}$ term represents natural displacement produced by the ‘unperturbed’ boundary layer over a smooth wall, and is an order-one quantity when $Y \sim 1$. It is followed by the singular term $\varepsilon(-s)^{-2/3} V_{01}^{(1)}$ corresponding to the displacement generated by the sublayer 2b in response to the singular pressure gradient (3.3). On the spatial scale $(-s) \sim \varepsilon^{3/2}$ both terms are order one quantities, making the above expansion for V_0 invalid.

In order to continue V_0 into the region $(-s) \lesssim \varepsilon^{3/2}$, we are going to introduce a

local variable $\bar{s} = s \varepsilon^{-3/2}$. Re-expanding (3.47) over the new scale yields:

$$\begin{aligned}
 U_0(s, Y, \varepsilon) &= U_{00}^{(0)}(Y) + \mathcal{O}(\varepsilon) + \varepsilon^{3/2} \bar{U}_0^{(1)}(\bar{s}, Y) + \mathcal{O}(\varepsilon^2), \\
 V_0(s, Y, \varepsilon) &= \bar{V}_0^{(1)}(\bar{s}, Y) + \mathcal{O}(\varepsilon^{1/2}), \\
 R_0(s, Y, \varepsilon) &= R_{00}^{(0)}(Y) + \mathcal{O}(\varepsilon) + \varepsilon^{3/2} \bar{R}_0^{(1)}(\bar{s}, Y) + \mathcal{O}(\varepsilon^2), \\
 h_0(s, Y, \varepsilon) &= h_{00}^{(0)}(Y) + \mathcal{O}(\varepsilon) + \varepsilon^{3/2} \bar{h}_0^{(1)}(\bar{s}, Y) + \mathcal{O}(\varepsilon^2), \\
 \mu_0(s, Y, \varepsilon) &= \mu_{00}^{(0)}(Y) + \mathcal{O}(\varepsilon) + \varepsilon^{3/2} \bar{\mu}_0^{(1)}(\bar{s}, Y) + \mathcal{O}(\varepsilon^2),
 \end{aligned} \tag{3.52}$$

where the functions with common notation $f_{00}^{(0)}(Y)$ represent the known unperturbed profiles in the $s = 0$ cross-section. The intermediate terms denoted as $\mathcal{O}(\varepsilon)$ do not affect the displacement, and therefore were not written explicitly. Plugging (3.52) into the Navier–Stokes equations (written in the (\bar{s}, Y) variables), we obtain the following four PDEs for the functions $\bar{f}_0^{(1)}(\bar{s}, Y)$ in the $\mathcal{O}(\varepsilon^{3/2})$ approximation:

$$\left\{ \begin{array}{l}
 R_{00}^{(0)} \frac{\partial \bar{U}_0^{(1)}}{\partial \bar{s}} + U_{00}^{(0)} \frac{\partial \bar{R}_0^{(1)}}{\partial \bar{s}} + \frac{\partial}{\partial Y} \left(R_{00}^{(0)} \bar{V}_0^{(1)} \right) = 0 \\
 R_{00}^{(0)} \left[U_{00}^{(0)} \frac{\partial \bar{U}_0^{(1)}}{\partial \bar{s}} + \frac{dU_{00}^{(0)}}{dY} \bar{V}_0^{(1)} \right] = \frac{d}{dY} \left(\mu_{00}^{(0)} \frac{dU_{00}^{(0)}}{dY} \right) \\
 R_{00}^{(0)} \left[U_{00}^{(0)} \frac{\partial \bar{h}_0^{(1)}}{\partial \bar{s}} + \frac{dh_{00}^{(0)}}{dY} \bar{V}_0^{(1)} \right] = -\frac{1}{\text{Pr}} \frac{d}{dY} \left(\mu_{00}^{(0)} \frac{dh_{00}^{(0)}}{dY} \right) + \mu_{00}^{(0)} \left(\frac{dU_{00}^{(0)}}{dY} \right)^2 \\
 R_{00}^{(0)} \bar{h}_0^{(1)} + h_{00}^{(0)} \bar{R}_0^{(1)} = 0.
 \end{array} \right.$$

Differentiating the second and the third equations with respect to \bar{s} cancels the right-hand sides since they only depend on Y . The system can then be reduced to a single PDE for the leading-order displacement function $\bar{V}_0^{(1)}(\bar{s}, Y)$, ultimately leading to the general solution

$$\bar{V}_0^{(1)}(\bar{s}, Y) = C(\bar{s}) U_{00}^{(0)}(Y) + D(Y).$$

Matching this solution with the first two terms in (3.51) when $\bar{s} \rightarrow -\infty$, we obtain the functions $C(\bar{s})$, $D(Y)$:

$$C(\bar{s}) = \frac{a_2}{3\tau_w} (-\bar{s})^{-2/3}, \quad D(Y) = V_{00}^{(0)}(Y).$$

Consequently, the uniformly-valid (with respect to s) asymptotic expansion for V_0 has the form:

$$V_0(s, Y, \varepsilon) = \frac{a_2}{3\tau_w} (-\bar{s})^{-2/3} U_{00}^{(0)}(Y) + V_{00}^{(0)}(Y) + \mathcal{O}(\varepsilon^{1/2}), \quad \bar{s} = s \varepsilon^{-3/2}.$$

The above result allows to calculate the classical displacement angle in region 2a:

$$\Theta = \text{Re}^{-1/2} \frac{V_0}{U_0} + \mathcal{O}(\text{Re}^{-1}) = \text{Re}^{-1/2} \left[\frac{a_2}{3\tau_w} (-\bar{s})^{-2/3} + \frac{V_{00}^{(0)}}{U_{00}^{(0)}} + \mathcal{O}(\varepsilon^{1/2}) \right] + \mathcal{O}(\text{Re}^{-1}). \quad (3.53)$$

In this expression the first term (in the square brackets) represents the displacement generated in response to the singular pressure gradient, while the second one stands for the natural displacement generated by the regular boundary layer. We are interested in the case when the first term dominates, leading to a typical viscous-inviscid interaction. Therefore, let us assume that $|\bar{s}| \ll 1$ in (3.53), and estimate an excessive pressure Δp_0 produced by the inviscid flow in response to the boundary layer displacement.

According to the classical transonic theory of a thin body (see Chapter 2), $\Delta p_0 \sim \Theta^{2/3}$, as opposed to the Akkeret's formula $\Delta p_0 \sim \Theta$ in the supersonic case. Substituting the singular term for Θ from (3.53) gives the estimate

$$\Delta p_0 \sim \text{Re}^{-1/3} (-\bar{s})^{-4/9}.$$

On the other hand, the original pressure produced by the inviscid transonic flow near the curvature break is

$$p_0 = -\frac{3}{2} \varepsilon G(-s)^{2/3} \equiv -\frac{3}{2} \varepsilon^2 G(-\bar{s})^{2/3}.$$

From these two estimates one can easily spot that as \bar{s} becomes smaller, Δp_0 increases while p_0 decreases. Eventually, they become of the same order of magnitude when

$$(-\bar{s}) \sim (\varepsilon^6 \text{Re})^{-3/10},$$

indicating that viscous-inviscid interaction starts to take place on this scale. For the singular term to dominate in (3.53), $(-\bar{s})$ should be small, which leads to the following restriction on ε :

$$\varepsilon \gg \text{Re}^{-1/6}.$$

If $\varepsilon \lesssim \text{Re}^{-1/6}$, then the natural displacement of the regular boundary layer (second term in (3.53)) dominates, making the singular effects of the weak curvature break insignificant in the leading order. Thus, from now on we are going to assume that ε satisfies the restriction

$$\text{Re}^{-1/6} \ll \varepsilon \ll \frac{1}{\ln \text{Re}}, \quad \text{Re} \rightarrow \infty, \quad (3.54)$$

where the upper estimate was mentioned in section 3.1.4 and corresponds to the situation when the skin friction vanishes in the leading order due to the adverse pressure gradient.

Finally, recalling that $s = \varepsilon^{3/2}\bar{s}$, we obtain the scale of the interaction region for the original variable s :

$$(-s) \sim \sigma(\varepsilon, \text{Re}) = (\varepsilon \text{Re})^{-3/10}. \quad (3.55)$$

The lower estimate in (3.54) suggests that $\sigma \ll 1$. According to (3.55), the small parameter ε effectively diminishes the Reynold's number. This is due to the nonlinearity of the transonic analogue of the Akkeret's formula describing the transformation of streamlines' displacement into pressure: $\Delta p_0 \sim \Theta^{2/3}$. Indeed, if we were operating in the supersonic regime, then the displacement $\Theta \sim \varepsilon \text{Re}^{-1/2}(-s)^{-2/3}$ would have generated the pressure $\Delta p_0 \sim \Theta$, which would become of the same order as the original pressure $p_0 \sim \varepsilon(-s)^{2/3}$ when $(-s) \sim \text{Re}^{-3/8}$.

3.2 Interaction Region

3.2.1 Main tiers of the interaction region

Now we have everything in order to introduce an interaction region, known as *triple deck*. It has a typical 3-tier structure, with the lower deck 5 being a continuation of the sublayer 2b, the intermediate region 4 being an extension of the main part of the boundary layer 2a, and the upper tier 3 located in the outer inviscid flow 1 (see Fig. 3.4). As it normally is the case in the problems involving triple deck, the lower tier 5 generates a displacement in response to the pressure gradient; this displacement is then transferred via the passive region 4 into the upper deck 3, and the latter converts it back into the pressure, therefore creating a system with a feedback. The mechanism is usually referred to as *viscous-inviscid interaction*. We are going to start the analysis of the interaction from the lower tier, and will then move upwards.

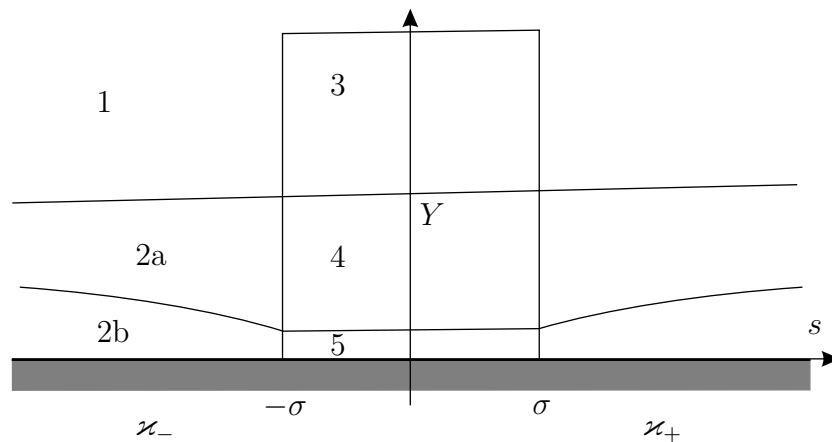


Figure 3.4: A typical three-tier structure of the interaction region.

Region 5 is the continuation of the viscous sublayer. The length of this region has been estimated in the previous section as $(-s) \sim \sigma = (\varepsilon \text{Re})^{-3/10}$, which corresponds to the failure of the classical boundary layer theory. The height of tier 5 is obtained from the fact that $\eta \sim 1$ in the overlapping region between 2b and 5, yielding $Y \sim (-s)^{1/3} \sim \sigma^{1/3} = (\varepsilon \text{Re})^{-1/10}$. Therefore, we can introduce the internal variables s_* ,

Y_* :

$$s = \sigma s_*, \quad Y = \sigma^{1/3} Y_*, \quad (3.56)$$

with $Y = r \cdot \text{Re}^{1/2}$ referring to the classical boundary layer coordinate in the normal direction. The expansions for the flow-field functions in region 5 follow from solution (3.41) in region 2b:

$$\begin{aligned} U(s, r, \text{Re}, \varepsilon) &= \sigma^{1/3} \left[U_*^{(0)}(s_*, Y_*) + \varepsilon U_*^{(1)}(s_*, Y_*) + \mathcal{O}(\varepsilon^2) \right] + \dots \equiv \sigma^{1/3} U_*(s_*, Y_*, \varepsilon) + \dots, \\ V(s, r, \text{Re}, \varepsilon) &= \text{Re}^{-1/2} \sigma^{-1/3} \left[\varepsilon V_*^{(1)}(s_*, Y_*) + \mathcal{O}(\varepsilon^2) \right] + \dots \equiv \text{Re}^{-1/2} \sigma^{-1/3} V_*(s_*, Y_*, \varepsilon) + \dots, \\ P(s, r, \text{Re}, \varepsilon) &= \sigma^{2/3} \left[\varepsilon P_*^{(1)}(s_*, Y_*) + \mathcal{O}(\varepsilon^2) \right] + \dots \equiv \sigma^{2/3} P_*(s_*, Y_*, \varepsilon) + \dots, \\ R(s, r, \text{Re}, \varepsilon) &= R_w + \dots, \\ h(s, r, \text{Re}, \varepsilon) &= h_w + \dots, \\ \mu(s, r, \text{Re}, \varepsilon) &= \mu_w + \dots, \end{aligned} \quad (3.57)$$

where dots stand for the higher-order powers of σ . The asterisk in the subscripts indicates that these double expansions replace classical boundary layer expansions (3.1) once the interaction region is approached, and the superscript corresponds to the power of ε in the inner expansions.

The leading-order terms in (3.57) should match with (3.41) when $s_* \rightarrow -\infty$ (matching condition between regions 2b and 5). Note that the pressure P is no longer assumed to be a given function, and is expected to be obtained from the interaction problem. However, when $s_* \rightarrow -\infty$, function P has to match with the known pressure distribution upstream of the interaction region, i.e. $P|_{s_* \rightarrow -\infty} \sim -\frac{3}{2} \varepsilon G(-s)^{2/3}$.

Plugging (3.57) into the Navier–Stokes equations written in variables (3.56), we get:

$$\left\{ \begin{array}{l} \frac{\partial U_*^{(0)}}{\partial s_*} = 0, \quad \frac{\partial^2 U_*^{(0)}}{\partial Y_*^2} = 0, \\ \frac{\partial U_*^{(1)}}{\partial s_*} + \frac{\partial V_*^{(1)}}{\partial Y_*} = 0, \\ R_w \left[U_*^{(0)} \frac{\partial U_*^{(1)}}{\partial s_*} + \frac{\partial U_*^{(0)}}{\partial Y_*} V_*^{(1)} \right] = -\frac{\partial P_*^{(1)}}{\partial s_*} + \mu_w \frac{\partial^2 U_*^{(1)}}{\partial Y_*^2}, \\ \frac{\partial P_*^{(1)}}{\partial Y_*} = 0. \end{array} \right. \quad (3.58)$$

The thermodynamic equations have split from the system in the leading order because the flow in region 5 is slow and is close to incompressible. Note that $P_*^{(1)}$ is a function of s_* only, according to the last equation. The first two equations in (3.58) imply

$$U_*^{(0)} = U_*^{(0)}(Y_*) = C_1 Y_* + C_2;$$

matching with (3.41) yields

$$U_*^{(0)} = \frac{\tau_w Y_*}{R_w}.$$

With this in mind, we introduce the scaled stream function

$$\psi_*(s_*, Y_*, \varepsilon) = \sigma^{-2/3} \psi = \psi_*^{(0)}(s_*, Y_*) + \varepsilon \psi_*^{(1)}(s_*, Y_*) + \mathcal{O}(\varepsilon^2), \quad (3.59)$$

where ψ is the physical stream function. Comparing $\psi_*^{(0)}$ and $\psi_*^{(1)}$ with the corresponding terms in expansions (3.57) for the velocity components gives:

$$\psi_*^{(0)} = \psi_*^{(0)}(Y_*) = \frac{\tau_w Y_*^2}{2}, \quad \frac{\partial \psi_*^{(1)}}{\partial Y_*} = R_w U_*^{(1)}, \quad \frac{\partial \psi_*^{(1)}}{\partial s_*} = -R_w V_*^{(1)}.$$

Therefore, system (3.58) can be reduced to the single linear equation for $\psi_*^{(1)}$:

$$\tau_w \left[Y_* \frac{\partial^2 \psi_*^{(1)}}{\partial s_* \partial Y_*} - \frac{\partial \psi_*^{(1)}}{\partial s_*} \right] = -R_w \frac{dP_*^{(1)}}{ds_*} + \mu_w \frac{\partial^3 \psi_*^{(1)}}{\partial Y_*^3}. \quad (3.60)$$

As mentioned before, its solution should match with (3.41) when $s_* \rightarrow -\infty$ for every fixed Y_* (overlapping region between 2b and 5). In particular, the asymptotic form of $\psi_*^{(1)}$ at $Y_* \rightarrow \infty$ has to match with (3.46). Re-writing (3.46) in the inner variables of region 5 yields:

$$\psi_0 = \sigma^{2/3} \left[\frac{\tau_w Y_*^2}{2} + \varepsilon \left(\frac{3a}{2} Y_*^2 \ln Y_* + c Y_*^2 + (-s_*)^{1/3} a_2 Y_* + (-s_*)^{2/3} a_3 + \dots \right) \right] + \dots, \quad (3.61)$$

where

$$c = \frac{a}{2} \ln \sigma + a_1 + b. \quad (3.62)$$

Comparing this with (3.59) and recalling that $\psi = \psi_0 + \mathcal{O}(\text{Re}^{-1/2})$, we get:

$$\psi_*^{(1)} = \frac{3a}{2} Y_*^2 \ln Y_* + c Y_*^2 + F_*(s_*) Y_* + G_*(s_*) + \dots, \quad Y_* \rightarrow \infty. \quad (3.63)$$

Functions $F_*(s_*)$ and $G_*(s_*)$ are order-one quantities in the interaction region (i.e. when $|s_*| \sim 1$). They should match with the relevant terms in (3.61) when $s_* \rightarrow -\infty$:

$$F_*(s_*) \sim a_2(-s_*)^{1/3}, \quad G_*(s_*) \sim a_3(-s_*)^{2/3}, \quad s_* \rightarrow -\infty. \quad (3.64)$$

It is worth mentioning that the problem formulation in region 5 does not require $F_*(s_*)$ and $G_*(s_*)$ to depend on ε . However, according to the analysis of the flow in region 3 performed in section 3.2.3, G_* (as well as F_*) needs to be treated as a function of ε with the following expansion:

$$G_*(s_*, \varepsilon) = G_0(s_*) + \sqrt{\varepsilon} G_1(s_*) + \mathcal{O}(\varepsilon),$$

suggesting that the original expansion (3.59) has fractional powers of ε . The results obtained for $G_*(s_*)$ by solving equation (3.60) in region 5 will obviously remain valid for the G_0 and G_1 ; only the $\mathcal{O}(\varepsilon)$ terms in G_* are going to coincide with the $\mathcal{O}(\varepsilon^2)$ terms from (3.59) which are ignored in the current study. Knowing both G_0 and G_1 appears to be sufficient for describing the onset of the separation. The analysis of these two leading-order functions from the expansion of G_* (section 3.3.1) leads to introduction of the inner scale X :

$$s_* = \varepsilon^{3/10} X,$$

with the relevant scaling for G_* :

$$G_*(s_*, \varepsilon) = \varepsilon^{1/5} A(X).$$

The problem for $A(X)$ does not depend on ε and describes the interaction taking place in the region $|X| \sim 1$. It may be deduced directly by replacing $\varepsilon \psi_*^{(1)}(s_*, Y_*)$ in (3.59) with $\varepsilon^{6/5} \psi_*^{(1)}(X, \mathcal{Y})$, where $\mathcal{Y} = \varepsilon^{-1/10} Y_*$. This additional re-scaling does not

affect the results obtained in sections 3.2.1–3.2.3 using s_* as the main inner variable of the interaction region.

If we plug (3.63) into (3.60), the latter will reduce to

$$\frac{dG_*}{ds_*} = \frac{R_w}{\tau_w} \frac{dP_*^{(1)}}{ds_*}$$

in the leading order. Integrating this with respect to s_* and taking into the account matching condition (3.64), we get a simple relationship between $G_*(s_*)$ and the leading-order pressure distribution across the interaction region:

$$G_*(s_*) = \frac{R_w}{\tau_w} P_*^{(1)}(s_*). \quad (3.65)$$

On the other hand, function $F_*(s_*)$ represents the leading-order displacement generated in region 5 in response to this pressure distribution. In section 3.2.2 we are going to derive a relationship between F_* and G_* by solving equation (3.60) analytically, with the obvious no-slip conditions

$$\psi_*^{(1)} \Big|_{Y_*=0} = \frac{\partial \psi_*^{(1)}}{\partial Y_*} \Big|_{Y_*=0} = 0.$$

Region 4 is the continuation of the main part of the boundary layer 2a into the interaction region. Therefore, $|s_*| \sim 1$ and $Y \sim 1$ in this tier. The structure of the expansions in region 4 can be deduced either from the relevant expansions (3.47) in region 2a by setting $s = \sigma s_*$ in the latter, or from the asymptotic form (3.63) which comes from region 5 by setting $Y_* = \sigma^{-1/3} Y$ in it. However, it is the matching condition with region 2a that allows to associate more terms from the required expansions in region 4 with certain terms already known from (3.47). Thus,

we obtain the double-expansions in region 4:

$$\begin{aligned}
 U(s, r, \text{Re}, \varepsilon) &= U_{00}^{(0)}(Y) + \varepsilon \left[U_{00}^{(1)}(Y) + \sigma^{1/3} \tilde{U}_{01}^{(1)}(s_*, Y) + \sigma^{2/3} \tilde{U}_{02}^{(1)}(s_*, Y) + \dots \right] + \dots, \\
 V(s, r, \text{Re}, \varepsilon) &= \text{Re}^{-1/2} \varepsilon \left[\sigma^{-2/3} \tilde{V}_{01}^{(1)}(s_*, Y) + \sigma^{-1/3} \tilde{V}_{02}^{(1)}(s_*, Y) + \dots \right] + \dots, \\
 R(s, r, \text{Re}, \varepsilon) &= R_{00}^{(0)}(Y) + \varepsilon \left[R_{00}^{(1)}(Y) + \sigma^{1/3} \tilde{R}_{01}^{(1)}(s_*, Y) + \sigma^{2/3} \tilde{R}_{02}^{(1)}(s_*, Y) + \dots \right] + \dots, \\
 P(s, r, \text{Re}, \varepsilon) &= \varepsilon \left[\sigma^{2/3} \tilde{P}_{02}^{(1)}(s_*, Y) + \dots \right] + \dots, \\
 h(s, r, \text{Re}, \varepsilon) &= h_{00}^{(0)}(Y) + \varepsilon \left[h_{00}^{(1)}(Y) + \sigma^{1/3} \tilde{h}_{01}^{(1)}(s_*, Y) + \sigma^{2/3} \tilde{h}_{02}^{(1)}(s_*, Y) + \dots \right] + \dots, \\
 \mu(s, r, \text{Re}, \varepsilon) &= \mu_{00}^{(0)}(Y) + \varepsilon \left[\mu_{00}^{(1)}(Y) + \sigma^{1/3} \tilde{\mu}_{01}^{(1)}(s_*, Y) + \sigma^{2/3} \tilde{\mu}_{02}^{(1)}(s_*, Y) + \dots \right] + \dots.
 \end{aligned} \tag{3.66}$$

Here the powers of σ appear instead of the powers of $(-s)$ in (3.47), the subscript/superscript notation follows the conventions adopted in region 2a (see section 3.1.4), the dots represent the higher-order terms, and the tilde denotes the functions unique to region 4 (they have to be obtained from the interaction problem). The rest of the functions, for example $U_{00}^{(0)}(Y)$, come from region 2a. Note that the $\mathcal{O}(\varepsilon^0)$ term in the expression for V has been omitted, because the natural displacement of a regular boundary layer is assumed to be insignificant (this is true when $\varepsilon \gg \text{Re}^{-1/6}$, see section 3.1.4).

Plugging (3.66) into the Navier–Stokes equations written in variables s_* and Y , we get the following system of homogeneous equations for the leading order functions

$$\tilde{f}_{01}^{(1)}(s_*, Y): \quad \left\{ \begin{array}{l} R_{00}^{(0)} \frac{\partial \tilde{U}_{01}^{(1)}}{\partial s_*} + U_{00}^{(0)} \frac{\partial \tilde{R}_{01}^{(1)}}{\partial s_*} + \frac{\partial}{\partial Y} \left(R_{00}^{(0)} \tilde{V}_{01}^{(1)} \right) = 0, \\ U_{00}^{(0)} \frac{\partial \tilde{U}_{01}^{(1)}}{\partial s_*} + \frac{dU_{00}^{(0)}}{dY} \tilde{V}_{01}^{(1)} = 0, \\ U_{00}^{(0)} \frac{\partial \tilde{h}_{01}^{(1)}}{\partial s_*} + \frac{dh_{00}^{(0)}}{dY} \tilde{V}_{01}^{(1)} = 0, \\ R_{00}^{(0)} \tilde{h}_{01}^{(1)} + h_{00}^{(0)} \tilde{R}_{01}^{(1)} = 0. \end{array} \right. \tag{3.67}$$

The pressure only appears in the next order problem for the functions $\tilde{f}_{02}^{(1)}(s_*, Y)$; there is no need to write all the relevant equations down because the pressure actually

splits from the system, being described by

$$\frac{\partial P_{02}^{(1)}}{\partial Y} = 0.$$

Thus, it does not change across the region, and is simply equal to the leading-order pressure distribution in region 5:

$$P_{02}^{(1)}(s_*) \equiv P_*^{(1)}(s_*) = \frac{\tau_w}{R_w} G_*(s_*).$$

To sum up, the two main functions of the flow in region 4 are, firstly, to transmit the displacement generated in the sublayer 5 to the outer flow (this process is described by (3.67) and does not depend on the pressure in the leading order), and, secondly, to transmit the pressure generated by the outer flow in response to the displacement back into region 5.

Equations (3.67) can be integrated easily, resulting in the following solution for the leading-order displacement function $\tilde{V}_{01}^{(1)}$:

$$\tilde{V}_{01}^{(1)}(s_*, Y) = C_*(s_*) U_{00}^{(0)}(Y).$$

To find the distribution function $C_*(s_*)$, we need to match this with the asymptotic form (3.63) valid in the overlapping region between tiers 4 and 5. Since

$$\psi = \sigma^{2/3} \psi_* = \sigma^{2/3} [\psi_*^{(0)} + \varepsilon \psi_*^{(1)} + \dots],$$

equation (3.63), along with the solution $\psi_*^{(0)} = \frac{\tau_w Y_*^2}{2}$, gives

$$\psi = \frac{\tau_w Y^2}{2} + \varepsilon \left[\frac{3a}{2} Y^2 \ln Y + (a_1 + b) Y^2 + \sigma^{1/3} Y F_*(s_*) + \sigma^{2/3} G_*(s_*) + \dots \right] + \dots,$$

where Y_* has been swapped with $\sigma^{-1/3} Y$. Differentiating with respect to $s = \sigma s_*$, and comparing the result with the expansions for V and R from (3.66), we get:

$$\tilde{V}_{01}^{(1)} \sim -\frac{Y}{R_w} \frac{dF_*}{ds_*}, \quad Y \rightarrow 0.$$

Finally, recalling that $U_{00}^{(0)} \sim \frac{\tau_w}{R_w} Y$ when $Y \rightarrow 0$, one can obtain:

$$C_*(s_*) = -\frac{1}{\tau_w} \frac{dF_*}{ds_*},$$

so that

$$V(s_*, Y) = \varepsilon \operatorname{Re}^{-1/2} \sigma^{-2/3} \left[-\frac{U_{00}^{(0)}(Y)}{\tau_w} \frac{dF_*(s_*)}{ds_*} + \mathcal{O}(\sigma^{1/3}) \right] + \dots \quad (3.68)$$

This provides an estimate for the displacement generated in region 5 and transmitted via the intermediate region 4 to the inviscid flow in region 3 (upper tier of the triple deck). Let us now turn our focus to the latter.

Region 3 is an extension of the interaction region into the outer inviscid flow, and replaces region 4 when $Y \rightarrow \infty$. It has the same length, $|s_*| = \sigma^{-1}|s| \sim 1$, with the two other tiers of the triple deck. Since $U_{00}^{(0)} \rightarrow 1$ when $Y \rightarrow \infty$, and $|F_*| \sim 1$ for $|s_*| \sim 1$, the leading order displacement angle, according to (3.68), is estimated as

$$|\Theta| = |V/U|_{Y \rightarrow \infty} \sim \delta(\varepsilon, \operatorname{Re}) = \varepsilon \operatorname{Re}^{-1/2} \sigma^{-2/3} \equiv \varepsilon^{6/5} \operatorname{Re}^{-3/10} \ll 1.$$

The estimate $\delta \ll 1$ is a consequence of the original assumption that $\varepsilon \gg \operatorname{Re}^{-1/6}$.

Note that the small parameters σ and δ are closely related to one another:

$$\delta = \varepsilon^{3/2} \sigma,$$

i.e. they depend on Re in exactly the same way.

From the classical transonic theory of a thin body it follows that the $\mathcal{O}(\delta)$ displacement generates an order $\delta^{2/3}$ perturbation in the pressure, longitudinal velocity component, density, enthalpy and viscosity. However, the viscosity may be neglected because the flow in region 3 turns out to be inviscid in the two leading orders of approximation based on δ , and the relevant asymptotic expansions take the form

$$\begin{aligned} U &= 1 + \delta^{2/3} u_1(s_*, y_*) + \delta^{4/3} u_2(s_*, y_*) + \dots, \\ V &= \delta v_1(s_*, y_*) + \delta^{5/3} v_2(s_*, y_*) + \dots, \\ p &= \delta^{2/3} p_1(s_*, y_*) + \delta^{4/3} p_2(s_*, y_*) + \dots, \\ \rho &= 1 + \delta^{2/3} \rho_1(s_*, y_*) + \delta^{4/3} \rho_2(s_*, y_*) + \dots, \\ h &= \frac{1}{\gamma - 1} + \delta^{2/3} h_1(s_*, y_*) + \delta^{4/3} h_2(s_*, y_*) + \dots \end{aligned} \quad (3.69)$$

We have introduced the local normal coordinate y_* in region 3 according to

$$r = \nu(\varepsilon, \text{Re}) y_*, \quad \nu \ll 1,$$

where r is the original curvilinear coordinate in the normal direction. The scale ν is obtained from the requirement that the normal momentum equation is not degenerated (as opposed to what happens in the boundary layer), therefore allowing to convert the normal velocity component (which represents the displacement effects) into the pressure perturbation on the scale $y_* \sim 1$. Using the estimate

$$U \frac{\partial V}{\partial s} \sim \frac{\partial p}{\partial r},$$

and recalling (3.69), one may easily get the required expression for ν :

$$\nu = \sigma \delta^{-1/3} \equiv \varepsilon^{-7/10} \text{Re}^{-1/5} \ll 1.$$

Again, the estimate $\nu \ll 1$ follows from the assumption that $\varepsilon \gg \text{Re}^{-1/6}$. The newly obtained scaling implies

$$\frac{r}{|s|} = \frac{y_*}{|s_*|} \delta^{-1/3} \sim \delta^{-1/3} \gg 1$$

in region 3, suggesting that it has a shape of a vertically stretched rectangular in the ‘physical’ coordinates (s, r) . Expressing y_* via the classical normal boundary layer coordinate Y yields:

$$y_* = \varepsilon \sigma Y,$$

so that $Y \gg 1$ when $y_* \sim 1$, as expected.

Note that asymptotic expansions (3.66) and (3.57) in regions 4 and 5 are double, being explicitly based on the independent small parameters ε and $\sigma(\varepsilon, \text{Re})$ (or implicitly on ε and Re). Thus, expansions (3.69) should also be double, which means each term in the main expansion based on $\delta(\varepsilon, \text{Re})$, for example $u_1(s_*, y_*)$, is actually an expansion itself; these inner expansions should be based on any small parameter other than δ . This is going to be crucial for the problem in region 3, allowing to linearize the governing equations and obtain an analytical solution (see section 3.2.3).

The fact that region 3 is significantly stretched in the normal direction results in the elimination of the viscous forces in the two leading-order problems, but on the

other hand reanimates some of the centrifugal terms in the Navier–Stokes equations (written in the scaled curvilinear coordinates (s_*, y_*) – see Appendix). Namely, it is the $-\varkappa v_7^2$ term in the second momentum equation that balances the pressure gradient and other convective terms in the leading-order problem with respect to δ .¹⁰⁾ Therefore, plugging (3.69) into the Navier–Stokes equations yields the following systems in the first two approximations based on the powers of δ :

$$\left\{ \begin{array}{l} \frac{\partial u_1}{\partial s_*} + \frac{\partial \rho_1}{\partial s_*} = 0, \\ \frac{\partial u_1}{\partial s_*} + \frac{\partial p_1}{\partial s_*} = 0, \\ \frac{\partial v_1}{\partial s_*} + \frac{\partial p_1}{\partial y_*} = \frac{\varkappa}{\varepsilon^{3/2}}, \\ \frac{\partial h_1}{\partial s_*} - (\gamma - 1) \frac{\partial p_1}{\partial s_*} = 0, \\ \rho_1 + h_1 - \gamma p_1 = 0; \end{array} \right. \quad (3.70)$$

$$\left\{ \begin{array}{l} \frac{\partial u_2}{\partial s_*} + \frac{\partial \rho_2}{\partial s_*} = -\frac{\partial v_1}{\partial y_*} - \frac{\partial(\rho_1 u_1)}{\partial s_*}, \\ \frac{\partial u_2}{\partial s_*} + \frac{\partial p_2}{\partial s_*} = -(u_1 + \rho_1) \frac{\partial u_1}{\partial s_*}, \\ \frac{\partial v_2}{\partial s_*} + \frac{\partial p_2}{\partial y_*} = -(u_1 + \rho_1) \frac{\partial v_1}{\partial s_*} + \frac{\varkappa}{\varepsilon^{3/2}} \left[u_1 - y_* \frac{\partial p_1}{\partial y_*} \right], \\ \frac{\partial h_2}{\partial s_*} - (\gamma - 1) \frac{\partial p_2}{\partial s_*} = -(u_1 + \rho_1) \frac{\partial h_1}{\partial s_*} + (\gamma - 1) u_1 \frac{\partial p_1}{\partial s_*}, \\ \rho_2 + h_2 - \gamma p_2 = -\rho_1 h_1. \end{array} \right. \quad (3.71)$$

Integrating the first two equations of (3.70), and taking into the account that the solutions should match with the known outer inviscid flow in region 1 when $|s_*| \rightarrow \infty$, we get:

$$p_1 = \rho_1 = -u_1.$$

The equation of state is then reduced to $h_1 = (\gamma + 1) p_1$, which makes the energy equation trivial. It means that system (3.70) is under-defined, and is reduced to the

¹⁰⁾ \varkappa is the local curvature of the wall.

single differential equation

$$\frac{\partial v_1}{\partial s_*} - \frac{\partial u_1}{\partial y_*} = \frac{\varkappa}{\varepsilon^{3/2}} \quad (3.72)$$

for the two functions u_1 and v_1 . As it usually is the case for many problems in fluid mechanics, the missing equation is obtained by considering the next-order problem described by system (3.71). Indeed, the left-hand sides of the equations in (3.71) are the same as in (3.70), and therefore are linearly dependent. However, the system is now inhomogeneous, and for it to have a solution, the right-hand sides must satisfy a compatibility condition. Imposing this condition results in the required second relationship between u_1 and v_1 :

$$(\gamma + 1) u_1 \frac{\partial u_1}{\partial s_*} - \frac{\partial v_1}{\partial y_*} = 0. \quad (3.73)$$

Equations (3.72), (3.73) are the well-known Karman–Guderley equations for an inviscid transonic flow of a perfect gas. The first one is nothing more than the zero vorticity condition written in curvilinear coordinates. The presence of the small parameter ε on the right-hand side means that functions u_1, v_1 (and, consequently, p_1, ρ_1, h_1) contain ε and may be expanded with respect to it, making the original expansions (3.69) double as predicted before. Thus, the two independent small parameters in region 3 are δ (outer expansion) and ε (inner expansions). Having ε in u_1, v_1 will be crucial for linearizing equation (3.73) in order to obtain analytical solution of the interaction problem.

It only remains to formulate boundary conditions for the functions u_1, v_1 . Firstly, they should match with the outer solutions in region 1 when $s_*^2 + y_*^2 \rightarrow \infty$; the latter were obtained in Chapter 2 and have a self-similar form. Secondly, as $y_* \rightarrow 0$, u_1 and v_1 should match with the relevant terms in the asymptotic forms of U and V in region 4 when $Y \rightarrow \infty$. Recalling that $u_1 = -p_1$ in region 3, and that the pressure is constant across regions 4 and 5, we get the first boundary condition:

$$u_1 \Big|_{y_*=0} = -P_*(s_*) \equiv -\frac{\tau_w}{R_w} G_*(s_*), \quad (3.74)$$

where $P_*(s_*)$ is the unknown pressure distribution across the interaction region. Finally, matching v_1 with (3.68) when $y_* \rightarrow 0$ and $Y \rightarrow \infty$ respectively, yields the

second boundary condition:

$$v_1|_{y_*=0} = -\frac{1}{\tau_w} \frac{dF_*(s_*)}{ds_*}. \quad (3.75)$$

Boundary-value problem (3.72)–(3.75), plus the matching condition with the outer flow in region 1, is going to provide the second relationship between the functions $F_*(s_*)$ and $G_*(s_*)$, therefore allowing to deduce a single equation for either F_* or G_* which describes the viscous-inviscid interaction taking place in regions 3, 4 and 5.

Let us turn our attention to the problem in region 5 first. The problem is linear and should have a relatively straightforward solution.

3.2.2 Analytical solution in region 5

We start with subtracting the cumulative effects from the stream function $\psi_*^{(1)}$ in region 5 by introducing a new function φ_* :

$$\varphi_*(s_*, Y_*) = \psi_*^{(1)}(s_*, Y_*) - \frac{3a}{2} Y_*^2 \ln Y_* - c Y_*^2. \quad (3.76)$$

The transformation obviously does not affect the no-slip condition at the wall, so that

$$\varphi_*|_{Y_*=0} = \frac{\partial \varphi_*}{\partial Y_*}|_{Y_*=0} = 0. \quad (3.77)$$

However, the equation for φ_* gains an extra term from the third derivative of $Y_*^2 \ln Y_*$:

$$\tau_w \left[Y_* \frac{\partial^2 \varphi_*}{\partial s_* \partial Y_*} - \frac{\partial \varphi_*}{\partial s_*} \right] = -R_w \frac{dP_*}{ds_*} + \mu_w \left[\frac{3a}{Y_*} + \frac{\partial^3 \varphi_*}{\partial Y_*^3} \right], \quad (3.78)$$

where $P_*(s_*) \equiv P_*^{(1)}(s_*)$ is the leading-order pressure distribution across tier 5. Finally, from (3.63) and (3.76) it follows that

$$\varphi_* = F_*(s_*) Y_* + G_*(s_*) + \frac{H_*(s_*)}{Y_*} + \mathcal{O}(Y_*^{-2}), \quad Y_* \rightarrow \infty; \quad (3.79)$$

the $\mathcal{O}(Y_*^{-1})$ term has been written explicitly for convenience. If we plug (3.79) into (3.78), this will yield (3.65), and also provide a simple equation for $H_*(s_*)$:

$$\frac{dH_*}{ds_*} = -\frac{3a\mu_w}{2\tau_w}.$$

Consequently,

$$H_*(s_*) = -\frac{3a\mu_w}{2\tau_w} s_* + \text{const}. \quad (3.80)$$

Differentiating equation (3.78) with respect to Y_* , we introduce the function

$$\Phi(s_*, Y_*) = \frac{\partial^2 \varphi_*}{\partial Y_*^2}; \quad (3.81)$$

it satisfies the equation

$$\frac{\partial^2 \Phi}{\partial Y_*^2} - \frac{\tau_w Y_*}{\mu_w} \frac{\partial \Phi}{\partial s_*} = \frac{3a}{Y_*^2}, \quad (3.82)$$

and has the following asymptotic behaviour:

$$\begin{aligned} \Phi &= -3a \ln Y_* + \mathcal{O}(1), & Y_* \rightarrow 0, \\ \Phi &= \frac{2H_*(s_*)}{Y_*^3} + \mathcal{O}(Y_*^{-4}), & Y_* \rightarrow \infty. \end{aligned} \quad (3.83)$$

The first formula in (3.83) is deduced directly from (3.76) and (3.81), taking into the account that $\psi_*^{(1)} \sim Y_*^2$ when $Y_* \rightarrow 0$ due to the no-slip conditions; the second equation in (3.83) results from (3.79).

Function Φ should also match with with the relevant solution in sublayer 2b when $s_* \rightarrow -\infty$. Since the scaling used in region 5 does not change the variable η , i.e.

$$\eta = \frac{Y}{(-s)^{1/3}} \equiv \frac{Y_*}{(-s_*)^{1/3}},$$

certain terms in solution (3.41) for the sublayer can be related to Φ , yielding the required matching condition:

$$\Phi \sim 3a \int_{\eta}^{\infty} e^{\alpha_w \zeta^3} \int_{\zeta}^{\infty} \frac{e^{-\alpha_w \xi^3}}{\xi^2} d\xi d\zeta, \quad (3.84)$$

$$\eta = \text{const}, \quad s_* \rightarrow -\infty, \quad Y_* = \eta(-s_*)^{1/3} \rightarrow \infty.$$

In this formula parameter η is a constant from the range $0 < \eta < \infty$.

Boundary-value problem (3.82)–(3.84) is solved using a Fourier transform with respect to s_* . Equation (3.82) is linear and has an obvious particular solution

$$\Phi = -3a \ln Y_*. \quad (3.85)$$

Therefore, we only need to apply the transform to the respective homogeneous equation for Φ , which gives the ordinary differential equation

$$\frac{d^2 \Phi_\omega}{dY_*^2} - i\omega \frac{\tau_w Y_*}{\mu_w} \Phi_\omega = 0$$

for the Fourier image function

$$\Phi_\omega = \int_{-\infty}^{\infty} \Phi(s_*, Y_*) e^{-i\omega s_*} ds_*.$$

Introducing a new variable

$$z = \lambda(\omega) Y_*, \quad \lambda(\omega) = \left(\frac{i\omega \tau_w}{\mu_w} \right)^{1/3}, \quad (3.86)$$

the above equation is reduced to the canonical Airy equation:

$$\frac{d^2 \Phi_\omega}{dz^2} - z \Phi_\omega = 0. \quad (3.87)$$

Its general solution may be expressed in terms of the Airy functions:

$$\Phi_\omega(z) = C_\omega \text{Ai}(z) + D_\omega \text{Bi}(z), \quad (3.88)$$

C_ω and D_ω being integration constants.

Let us now find out what happens with (3.88) when ω changes from $-\infty$ to ∞ along the real axis in the inverse transform

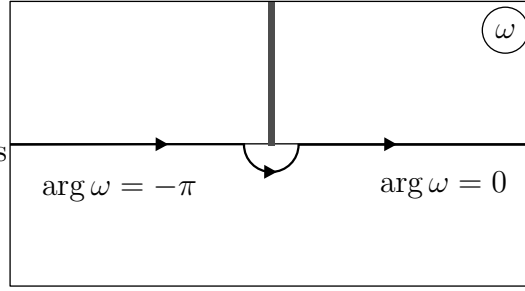
$$\Phi(s_*, Y_*) = \frac{1}{2\pi} \int_{-\infty}^{\infty} \Phi_\omega(\lambda(\omega) Y_*) e^{i\omega s_*} d\omega. \quad (3.89)$$

Since $\lambda(\omega) \sim (i\omega)^{1/3}$, we need to make a branch-cut in the plane of complex ω and choose the appropriate regular branches, so that $\Phi_\omega(z)$ does not grow exponentially when $|z| \rightarrow \infty$. If the branch-cut runs along the imaginary axis in the upper half-plane (Fig. 3.5), then $-\frac{3\pi}{2} < \arg \omega < \frac{\pi}{2}$. For the regular branch of $\lambda(\omega)$ defined according to the rule

$$\arg \lambda = \frac{1}{3} \left(\frac{\pi}{2} + \arg \omega \right)$$

we obtain the restriction

$$-\frac{\pi}{3} < \arg \lambda < \frac{\pi}{3}.$$


 Figure 3.5: Integration contour in the plane of complex ω .

The same constraint holds for $\arg z$ since $z = \lambda(\omega) Y_*$ and Y_* is a positive real number. Now, when $|z| \rightarrow \infty$ and $|\arg z| < \pi$, the first Airy function has the following asymptotic form (Abramovitz & Stegun 1972):

$$\text{Ai}(z) = \frac{e^{-\zeta}}{2\pi^{1/2} z^{1/4}} [1 + \mathcal{O}(\zeta^{-1})], \quad \zeta = \frac{2}{3} z^{3/2}.$$

Therefore, for the given branch of $\lambda(\omega)$ we have $-\frac{\pi}{2} < \arg \zeta < \frac{\pi}{2}$, and $\text{Ai}(z)$ exponentially decays in this sector. On the other hand,

$$\text{Bi}(z) \equiv e^{i\pi/6} \text{Ai}(z e^{2i\pi/3}) + e^{-i\pi/6} \text{Ai}(z e^{-2i\pi/3})$$

always has at least one component which grows exponentially in the same sector. The only way to avoid this growth is to set $D_\omega = 0$ in (3.88), leaving $\Phi_\omega(z) = C_\omega \text{Ai}(z)$. Applying the inverse transform and adding (3.85), we obtain the required solution of the original equation (3.82) for Φ :

$$\Phi(s_*, Y_*) = \frac{1}{2\pi} \int_{-\infty}^{\infty} C_\omega \text{Ai}(\lambda(\omega) Y_*) e^{i\omega s_*} d\omega - 3a \ln Y_*. \quad (3.90)$$

It remains to check whether this solution is in agreement with asymptotic forms (3.83) and (3.84). The first condition in (3.83), corresponding to $Y_* \rightarrow 0$, directly follows from (3.90), providing that the Fourier integral converges in this limit.¹¹⁾ For Φ to be of the order of Y_*^{-3} when $Y_* \rightarrow \infty$ (second condition in (3.83)), the integral should first of all tend to $3a \ln Y_*$. By considering

$$\frac{\partial \Phi}{\partial Y_*} = \frac{1}{2\pi} \int_{-\infty}^{\infty} C_\omega \lambda(\omega) \text{Ai}'(\lambda(\omega) Y_*) e^{i\omega s_*} d\omega - \frac{3a}{Y_*}, \quad \text{Ai}'(z) = \frac{d\text{Ai}(z)}{dz} \quad (3.91)$$

¹¹⁾ This requirement actually leads to a slightly modified form of the general solution for Φ – see section 3.3.3.

instead of Φ for the matter of convenience, one can easily show that the required asymptotic behaviour occurs if $C_\omega \sim |\omega|^{-1}$ for real $\omega \rightarrow 0$.¹²⁾ Therefore, we introduce a new complex function

$$K_\omega = \varkappa(\omega) e^{i\theta(\omega)}, \quad \varkappa(\omega) = |K_\omega|, \quad \theta(\omega) = \arg K_\omega, \quad (3.92)$$

that is not necessarily analytical, in order to extract the $|\omega|^{-1}$ singularity in C_ω :

$$C_\omega = \frac{C_0}{|\omega|} K_\omega, \quad C_0 = \text{const}. \quad (3.93)$$

All the functions here are originally defined for real ω , but may be analytically continued into the entire complex plane. The normalization constant C_0 in (3.93) allows to impose a simple restriction on the value of K_ω at $\omega = 0$:

$$K_\omega(0) = 1 \quad \Longleftrightarrow \quad \begin{cases} \varkappa(0) = 1, \\ \theta(0) = 0. \end{cases} \quad (3.94)$$

Now we need to fix the value of C_0 for which the integral in (3.91) tends to $3a/Y_* + \mathcal{O}(Y_*^{-4})$ when $Y_* \rightarrow \infty$. Simple calculations yield:

$$C_0 = -\frac{\pi a}{\text{Ai}(0)}, \quad \text{Ai}(0) = \frac{1}{3^{2/3} \Gamma(2/3)}, \quad (3.95)$$

thereby allowing to match solution (3.91) in sublayer 5 with the relevant solution in tier 4.

The last matching condition (3.84) may be transformed to the following form:

$$-\frac{\partial \Phi}{\partial Y_*} \frac{Y_*}{3a} \sim f_1(\eta) = \eta e^{\alpha_w \eta^3} \int_\eta^\infty \frac{e^{-\alpha_w \zeta^3}}{\zeta^2} d\zeta, \quad \eta = \frac{Y_*}{(-s_*)^{1/3}} = \text{const}, \quad Y_* \rightarrow \infty. \quad (3.96)$$

Integrating the right-hand side of solution (3.91) by parts, and taking into the account (3.93), (3.94) and (3.95), we obtain:

$$-\frac{\partial \Phi}{\partial Y_*} \frac{Y_*}{3a} \sim f_2(\eta) = \frac{1}{\text{Ai}(0)} \int_0^\infty \text{Ai}(\xi(\eta, t)) e^{-t} dt, \quad \xi(\eta, t) = \eta \left(\frac{\tau_w t}{\mu_w} \right)^{1/3}, \quad (3.97)$$

¹²⁾ The fact that the asymptotic form of the integral at $Y_* \rightarrow \infty$ is related to the asymptotic form of C_ω close to $\omega = 0$ is due to the presence of the rapidly decaying Airy function. The $|\omega|^{-1}$ singularity can be treated as an image of the cumulative effects in the ω -plane, since it provides the logarithmic term in the stream function.

again for $\eta = \text{const}$ and $Y_* \rightarrow \infty$. Therefore, condition (3.84) is equivalent to proving that $f_1(\eta) \equiv f_2(\eta)$ for all $\eta \in [0, \infty)$.

First of all, a simple check yields $f_1(0) = f_2(0) = 1$. For $\eta > 0$ we are going to use a well-known representation of the Airy function via the modified Bessel functions (Abramovitz & Stegun 1972):

$$\text{Ai}(\xi) = \frac{\sqrt{\xi}}{3} \left[I_{-\frac{1}{3}}(z) - I_{\frac{1}{3}}(z) \right], \quad z = \frac{2}{3} \xi^{3/2}.$$

The latter are related to the original Bessel function of the first kind:

$$I_\nu(z) = e^{-\frac{i\pi\nu}{2}} J_\nu\left(z e^{\frac{i\pi}{2}}\right),$$

which may be further expressed via the Kummer function of the first kind, denoted as $M(a, b, z)$:

$$\int_0^\infty e^{-(au)^2} u^{\mu-1} J_\nu(bu) du = \frac{\Gamma\left(\frac{1}{2}(\nu+\mu)\right) \left(\frac{b}{2a}\right)^\nu}{2a^\mu \Gamma(\nu+1)} M\left(\frac{1}{2}(\nu+\mu), (\nu+\mu), -\frac{b^2}{4a^2}\right).$$

By setting $\mu = \frac{7}{3}$, $\nu = \pm\frac{1}{3}$, $a = 1$ and $b = b(\eta) = \frac{2}{3} \eta^{\frac{3}{2}} e^{\frac{i\pi}{2}} \sqrt{\frac{\tau_w}{\mu_w}}$, we arrive at the following expression for $f_2(\eta)$:

$$f_2(\eta) = \frac{1}{\text{Ai}(0)} \int_0^\infty \text{Ai}(\xi(\eta, t)) e^{-t} dt = M\left(1, \frac{2}{3}, \alpha_w \eta^3\right) - \alpha_w^{1/3} \Gamma(2/3) \eta M\left(\frac{4}{3}, \frac{4}{3}, \alpha_w \eta^3\right).$$

The Kummer function of the second kind, $U(a, b, z)$, is defined according to the formula

$$U(a, b, z) = \frac{\pi}{\sin(\pi b)} \left[\frac{M(a, b, z)}{\Gamma(1+a-b) \Gamma(b)} - z^{1-b} \frac{M(1+a-b, 2-b, z)}{\Gamma(a) \Gamma(2-b)} \right];$$

setting $a = 1$, $b = \frac{2}{3}$, $z = \alpha_w \eta^3$ yields:

$$U\left(1, \frac{2}{3}, \alpha_w \eta^3\right) = 3f_2(\eta).$$

To associate this with $f_1(\eta)$, we need to employ another representation for the Kummer function of the second kind:

$$\Gamma(a) U(a, b, z) = e^z \int_1^\infty e^{-zt} (t-1)^{a-1} t^{b-a-1} dt,$$

where $a = 1$, $b = \frac{2}{3}$, $z = \alpha_w \eta^3$ as before. Simple transformations in the integral reduce it to

$$3\eta e^{\alpha_w \eta^3} \int_\eta^\infty \frac{e^{-\alpha_w t^3}}{t^2} dt = 3f_1(\eta).$$

Hence,

$$U\left(1, \frac{2}{3}, \alpha_w \eta^3\right) = 3f_1(\eta) \equiv 3f_2(\eta)$$

for all $\eta \geq 0$, thereby proving the required identity.

The above result confirms that (3.91) is, indeed, the correct solution in region 5 which satisfies all the matching conditions. Moreover, the two different representations of $U(a, b, z)$ from the proof of the equivalency between $f_1(\eta)$ and $f_2(\eta)$ allow to find a simple numerical value of the constant a_2 describing the leading-order displacement effects in sublayer 2b. According to (3.45),

$$a_2 = a \int_0^\infty U\left(1, \frac{2}{3}, \alpha_w \eta^3\right) d\eta.$$

Using the Airy function representation of the integrand, we have:

$$a_2 = \frac{3a}{\text{Ai}(0)} \int_0^\infty e^{-t} \int_0^\infty \text{Ai}\left((9t)^{\frac{1}{3}} \alpha_w \eta\right) d\eta dt.$$

Since

$$\int_0^\infty \text{Ai}(x) dx = \frac{1}{3},$$

the required value of a_2 is

$$a_2 = \frac{a [\Gamma(2/3)]^2}{\alpha_w^{1/3}}.$$

The ultimate goal of the analysis in region 5 is to find a relationship between the functions $F_*(s_*)$ and $G_*(s_*)$. This can be done by expressing both of these functions via the newly obtained solution (3.90) for Φ . Let us recall that $\Phi = \frac{\partial^2 \varphi_*}{\partial Y_*^2}$, where the function φ_* is defined in (3.76). Integrating this twice and taking into the account the no-slip conditions for φ_* yields:

$$\varphi_*(s_*, Y_*) = \int_0^{Y_*} (Y_* - t) \Phi(s_*, t) dt. \quad (3.98)$$

Both components of the integral converge when $Y_* \rightarrow \infty$, which is due to the second asymptotic form in (3.83), and give the estimates

$$\int_\infty^{Y_*} \Phi(s_*, t) dt \sim -\frac{H_*(s_*)}{Y_*^2}, \quad \int_0^{Y_*} t \Phi(s_*, t) dt \sim -\frac{2H_*(s_*)}{Y_*}, \quad Y_* \rightarrow \infty.$$

With this in mind, we compare (3.98) with the asymptotic form (3.79) of φ_* to obtain the following important relationships:

$$\begin{aligned} F_*(s_*) &= \int_0^\infty \Phi(s_*, Y_*) dY_*, \\ G_*(s_*) &= - \int_0^\infty Y_* \Phi(s_*, Y_*) dY_*. \end{aligned} \quad (3.99)$$

It, therefore, remains to utilize the known solution for Φ and express F_* via G_* .

Thanks to the asymptotic forms (3.83), the integrals in (3.99) can be further transformed to include $\partial\Phi/\partial Y_*$:

$$\begin{aligned} F_*(s_*) &= - \int_0^\infty Y_* \frac{\partial\Phi}{\partial Y_*} dY_*, \\ G_*(s_*) &= \frac{1}{2} \int_0^\infty Y_*^2 \frac{\partial\Phi}{\partial Y_*} dY_*. \end{aligned} \quad (3.100)$$

Using (3.91), along with, (3.93), (3.94) and (3.95), we get:

$$Y_* \frac{\partial\Phi}{\partial Y_*} = \frac{3a}{2\text{Ai}(0)} \left[\int_{0^-}^{-\infty} \text{Ai}(\lambda(\omega)Y_*) \frac{d}{d\omega} [K_\omega e^{i\omega s_*}] d\omega + \int_{0^+}^{\infty} \text{Ai}(\lambda(\omega)Y_*) \frac{d}{d\omega} [K_\omega e^{i\omega s_*}] d\omega \right]. \quad (3.101)$$

The integration is originally performed along the real axis in the plane of complex ω .

For this expression to be real, function K_ω should satisfy the condition

$$K_\omega(\omega) = \overline{K_\omega(-\omega)}, \quad \omega \in \mathbb{R},$$

equivalent to

$$\begin{cases} |K_\omega| = \varkappa(\omega) = \varkappa(-\omega), \\ \arg(K_\omega) = \theta(\omega) = -\theta(-\omega), \end{cases} \quad (3.102)$$

where $\omega \in \mathbb{R}$. This enables to combine the two complex integrals in (3.101), which, upon plugging them into (3.100) and swapping the integration with respect to Y_* and ω , yield the following real Fourier integrals for F_* and G_* :

$$\begin{aligned} F_*(s_*) &= - \frac{a \Gamma(2/3)}{\alpha_w^{1/3}} \int_0^\infty \frac{1}{\omega^{1/3}} \frac{d}{d\omega} [\varkappa(\omega) \cos(\theta(\omega) + \omega s_* - \pi/6)] d\omega, \\ G_*(s_*) &= \frac{a \Gamma(2/3)}{2\alpha_w^{2/3} \Gamma(1/3)} \int_0^\infty \frac{1}{\omega^{2/3}} \frac{d}{d\omega} [\varkappa(\omega) \cos(\theta(\omega) + \omega s_* - \pi/3)] d\omega. \end{aligned} \quad (3.103)$$

Before arriving at (3.103), we used the identities

$$\int_0^\infty \text{Ai}(x) dx = \frac{1}{3}, \quad z \text{Ai}(z) = \frac{d^2 \text{Ai}(z)}{dz^2}$$

to calculate the integrals with respect to Y_* ; this provided the $\omega^{-1/3}$ and $\omega^{-2/3}$ multiples in (3.103). Differentiating (3.103) with respect to s_* and integrating by parts gives:

$$\begin{aligned} \frac{dF_*}{ds_*} &= \frac{a \Gamma(2/3)}{3\alpha_w^{1/3}} \int_0^\infty \frac{\varkappa(\omega) \sin(\theta(\omega) + \omega s_* - \pi/6)}{\omega^{1/3}} d\omega, \\ \frac{dG_*}{ds_*} &= -\frac{a \Gamma(2/3)}{3\alpha_w^{2/3} \Gamma(1/3)} \int_0^\infty \frac{\varkappa(\omega) \sin(\theta(\omega) + \omega s_* - \pi/3)}{\omega^{2/3}} d\omega. \end{aligned} \quad (3.104)$$

With the aim to find the link between F_* and G_* , let us introduce complex functions $f_*(s_*) = f_r + i f_i$ and $g_*(s_*) = g_r + i g_i$:¹³⁾

$$\begin{aligned} f_*(s_*) &= \frac{a \Gamma(2/3)}{3\alpha_w^{1/3}} \int_0^\infty \omega^{2/3} \varkappa(\omega) e^{i(\theta(\omega) + \omega s_* - \pi/6)} d\omega, \\ g_*(s_*) &= -\frac{a \Gamma(2/3)}{3\alpha_w^{2/3} \Gamma(1/3)} \int_0^\infty \omega^{1/3} \varkappa(\omega) e^{i(\theta(\omega) + \omega s_* - \pi/3)} d\omega, \end{aligned} \quad (3.105)$$

assuming the integrals converge due to a decay of $\varkappa(\omega)$ when $\omega \rightarrow \infty$. It can be easily seen that

$$f_r = \Re(f_*) = \frac{d^2 F_*}{ds_*^2}, \quad g_r = \Re(g_*) = \frac{d^2 G_*}{ds_*^2}.$$

Applying a Fourier transform \mathcal{F} to (3.105), we have:

$$\begin{aligned} f_\omega &= \mathcal{F}(f_*) = \frac{2\pi a \Gamma(2/3)}{3\alpha_w^{1/3}} \omega^{2/3} \varkappa(\omega) e^{i(\theta(\omega) - \pi/6)} H(\omega), \\ g_\omega &= \mathcal{F}(g_*) = -\frac{2\pi a \Gamma(2/3)}{3\alpha_w^{2/3} \Gamma(1/3)} \omega^{1/3} \varkappa(\omega) e^{i(\theta(\omega) - \pi/3)} H(\omega), \end{aligned}$$

where $H(\omega)$ is the Heaviside step function. These two equations yield a direct relationship between f_ω and g_ω :

$$g_\omega = -\frac{f_\omega}{\alpha_w^{1/3} \Gamma(1/3) e^{i\pi/6} \omega^{1/3}}.$$

The inverse Fourier transform then gives

$$g_*(s_*) = \frac{\Gamma(2/3)}{\alpha_w^{1/3} \Gamma(1/3)} \left[i \int_0^\infty \frac{f_*(s_* + t)}{t^{2/3}} dt + e^{i\pi/6} \int_0^\infty \frac{f_*(s_* - t)}{t^{2/3}} dt \right]. \quad (3.106)$$

¹³⁾ The entire interaction problem could be solved in the Fourier space without referring to the ‘intermediate’ integral relationships between F_* and G_* in regions 3 and 5 written in physical variables. However, we are going to spend some time deriving these formulae in order to have a better understanding of a physical nature of the interaction in each tier.

We obviously need to find a connection between f_r and g_r only; since

$$if_* = if_r - f_i, \quad e^{i\pi/6} f_* = \frac{1}{2} (\sqrt{3} f_r - f_i) + \frac{i}{2} (f_r + \sqrt{3} f_i),$$

f_i has to be expressed via f_r using the Sokhotski-Plemelj formulae. The latter provide a link between real and imaginary parts of an analytical function $f(z)$ evaluated on the real axis $x = \Re(z)$:

$$\begin{aligned} f_r(x) &= \frac{1}{\pi} \int_{-\infty}^{\infty} \frac{f_i(\xi) d\xi}{\xi - x}, \\ f_i(x) &= -\frac{1}{\pi} \int_{-\infty}^{\infty} \frac{f_r(\xi) d\xi}{\xi - x}. \end{aligned} \tag{3.107}$$

We are going to use the second formula in (3.107) to express f_i via f_r . Taking the real part of (3.106) yields:

$$g_r(s_*) = -\frac{\Gamma(2/3)}{\alpha_w^{1/3} \Gamma(1/3)} \left[\int_0^{\infty} \frac{f_i(s_* + t)}{t^{2/3}} dt + \frac{1}{2} \int_0^{\infty} \frac{[\sqrt{3} f_r(s_* - t) - f_i(s_* - t)]}{t^{2/3}} dt \right]. \tag{3.108}$$

Therefore, the two following double integrals emerge:

$$\begin{aligned} I_1(s_*) &= \int_0^{\infty} \frac{f_i(s_* + t)}{t^{2/3}} dt = -\frac{1}{\pi} \int_{s_*}^{\infty} \frac{1}{(x - s_*)^{2/3}} \left[\int_{-\infty}^{\infty} \frac{f_r(\xi) d\xi}{\xi - x} \right] dx, \\ I_2(s_*) &= \int_0^{\infty} \frac{f_i(s_* - t)}{t^{2/3}} dt = \frac{1}{\pi} \int_{-\infty}^{s_*} \frac{1}{(s_* - x)^{2/3}} \left[\int_{-\infty}^{\infty} \frac{f_r(\xi) d\xi}{\xi - x} \right] dx. \end{aligned}$$

It can be shown that swapping the integration order creates double principal value integrals:

$$\begin{aligned} I_1(s_*) &= -\frac{1}{\pi} \int_{-\infty}^{\infty} f_r(s_* + \xi) \left[\int_0^{\infty} \frac{dt}{t^{2/3}(\xi - t)} \right] d\xi, \\ I_2(s_*) &= \frac{1}{\pi} \int_{-\infty}^{\infty} f_r(s_* - \xi) \left[\int_0^{\infty} \frac{dt}{t^{2/3}(\xi - t)} \right] d\xi. \end{aligned}$$

Here the outer principal value integral eliminates the point $\xi = 0$ in which the inner integral is not defined. Simple calculations give

$$\int_0^{\infty} \frac{dt}{t^{2/3}(\xi - t)} = \begin{cases} \frac{\pi}{\sqrt{3}} \frac{1}{\xi^{2/3}}, & \xi > 0, \\ -\frac{2\pi}{\sqrt{3}} \frac{1}{(-\xi)^{2/3}}, & \xi < 0, \end{cases}$$

so that $I_{1,2}$ may be transformed to

$$I_1(s_*) = \frac{2}{\sqrt{3}} \int_{-\infty}^{\infty} \frac{f_r(s_* + \xi)}{|\xi|^{2/3}} d\xi - \sqrt{3} \int_0^{\infty} \frac{f_r(s_* + \xi)}{\xi^{2/3}} d\xi,$$

$$I_2(s_*) = -\frac{2}{\sqrt{3}} \int_{-\infty}^{\infty} \frac{f_r(s_* - \xi)}{|\xi|^{2/3}} d\xi + \sqrt{3} \int_0^{\infty} \frac{f_r(s_* - \xi)}{\xi^{2/3}} d\xi.$$

Plugging these into (3.108), we obtain the required relationship between f_r and g_r :

$$g_r(s_*) = -\frac{1}{\alpha_w^{1/3} [\Gamma(1/3)]^2} \int_0^{\infty} \frac{f_r(s_* - \xi)}{\xi^{2/3}} d\xi. \quad (3.109)$$

Thus, the value of g_r at any given point s_* is determined only by the values of f_r upstream of this point, and is not affected by the values of f_r downstream. Equation (3.109), written as

$$\frac{d^2 G_*(s_*)}{ds_*^2} = -\frac{1}{\alpha_w^{1/3} [\Gamma(1/3)]^2} \int_{-\infty}^{s_*} \frac{d^2 F_*(\xi)}{d\xi^2} \frac{d\xi}{(s_* - \xi)^{2/3}},$$

can be integrated once to give an expression directly for the pressure gradient:

$$\frac{dG_*(s_*)}{ds_*} = -\frac{1}{\alpha_w^{1/3} [\Gamma(1/3)]^2} \int_{-\infty}^{s_*} \frac{dF_*(\xi)}{d\xi} \frac{d\xi}{(s_* - \xi)^{2/3}}; \quad (3.110)$$

we used initial conditions (3.64) while deriving (3.110). As mentioned before, only the values of the displacement function F_* upstream of s_* contribute to the pressure G_* in this point, which is due to the parabolic nature of the original boundary layer equations solved in region 5. The non-locality of (3.110) stems from the fact that the flow in region 5 is nearly incompressible.

Finally, the Abel-type integral in (3.110) may be inverted, yielding the following formula for the displacement function:

$$\frac{dF_*(s_*)}{ds_*} = -\frac{\alpha_w^{1/3} \Gamma(1/3)}{\Gamma(2/3)} \int_{-\infty}^{s_*} \frac{d^2 G_*(\xi)}{d\xi^2} \frac{d\xi}{(s_* - \xi)^{2/3}}. \quad (3.111)$$

Again, the quantity on the left-hand side is determined using only the values of the function on the right-hand side upstream of a given point. In this particular case, the displacement at a point s_* is generated by the pressure distribution ahead of s_* . However, there is a principal difference between (3.110) and its inverse (3.111), since it is $d^2 G_*/ds_*^2$ and not dG_*/ds_* that contributes to dF_*/ds_* .

Having obtained the required relationships between the pressure distribution and displacement across region 5, we can move to the upper tier 3.

3.2.3 Analytical solution in region 3

First of all, let us recall how the coordinates and the velocity components in the outer region 1 are transformed when moving from the cartesian coordinates (x, y) to the curvilinear coordinates (s, r) related to the surface of the body. The coordinate transformation is written as

$$\begin{cases} \varkappa x = -(1 + \varkappa r) \sin \vartheta(s), \\ \varkappa y = -1 + (1 + \varkappa r) \cos \vartheta(s), \end{cases} \quad (3.112)$$

where $\varkappa = \varkappa_{\pm}$ when $x \gtrless 0$, and

$$\vartheta(s) = -\varkappa s, \quad |\vartheta| \sim \sigma \ll 1,$$

as shown in Fig. 3.6. Using the notations U and V for the curvilinear velocity components from the boundary layer analysis in previous sections, we can construct the following expansions for the inviscid flow close to the sonic point:

$$U = 1 + \frac{v_{\tau}}{\gamma + 1} + \dots, \quad V = \frac{v_n}{\gamma + 1} + \dots,$$

v_{τ} and v_n being the leading-order perturbations. The corresponding cartesian veloc-

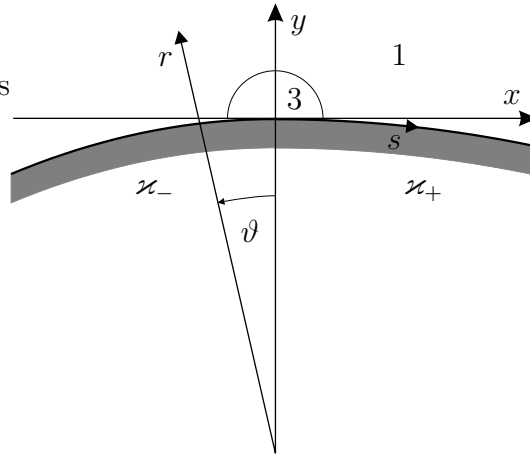


Figure 3.6: Transformation from the cartesian to the curvilinear coordinates.

ity components u_x and u_y are

$$\begin{aligned} u_x &= \left[1 + \frac{v_{\tau}}{\gamma + 1} \right] \cos \vartheta - \frac{v_n}{\gamma + 1} \sin \vartheta, \\ u_y &= \left[1 + \frac{v_{\tau}}{\gamma + 1} \right] \sin \vartheta + \frac{v_n}{\gamma + 1} \cos \vartheta. \end{aligned}$$

Comparing this to the definition of the cartesian velocity perturbations u, v used in the inviscid analysis in region 1 (see (2.6)), we obtain:

$$\begin{aligned} u &= v_\tau \cos \vartheta - v_n \sin \vartheta, \\ v &= [(\gamma + 1) + v_\tau] \sin \vartheta + v_n \cos \vartheta. \end{aligned}$$

Note that the trigonometric functions should actually be expanded, since $|\vartheta| \ll 1$ and only the leading order terms have to remain in the expressions on the right-hand side; higher order terms contribute to higher order velocity perturbations which are neglected in the analysis. The inverse of the above equations is

$$\begin{aligned} v_\tau &= u \cos \vartheta + v \sin \vartheta - (\gamma + 1) \sin^2 \vartheta, \\ v_n &= -u \sin \vartheta + v \cos \vartheta - (\gamma + 1) \sin \vartheta \cos \vartheta, \end{aligned} \tag{3.113}$$

the last two terms representing the projections of the main horizontal velocity onto the curvilinear axes. Again, the right-hand side has to be linearized, because v_τ and v_n are only the leading-order perturbations; we are going to do the linearization later.

To illustrate how transformations (3.113) work, let us consider the exact impermeability condition $v_n|_{r=0} = 0$ and obtain the relevant condition in the cartesian coordinates. Since u is a perturbation itself, the second equation in (3.113) yields

$$v|_{r=0} = -(\gamma + 1) \varkappa s$$

in the leading order approximation (after expanding the trigonometric functions). A subsequent shift from the body surface ($r = 0$) to the $y = 0$ axis provides an order $1 - \cos \vartheta = \mathcal{O}((\varkappa s)^2)$ correction which obviously does not affect the leading order term in v . Therefore, we arrive at the familiar condition

$$v|_{y=0} = -(\gamma + 1) \varkappa x + \dots,$$

derived at the very start of the inviscid analysis in section 2.1.1 in the assumption that $|\varkappa x| \ll 1$.

Recall that the cartesian velocity perturbations in region 1 are expressed via the

self-similar function $F(\xi)$, with $\xi = \frac{x}{y^\alpha}$ and $\alpha = \frac{3}{2}$:

$$u = yF'(\xi) = y\alpha^2\xi^2f(\xi),$$

$$v = y^\alpha[(3\alpha - 2)F - \alpha\xi F'] = y^\alpha\alpha^3\xi^3g(\xi),$$

$f(\xi)$ and $g(\xi)$ being the phase variables (see section 2.2.1). Since we are now working in region 3 with the local variables (s_*, y_*) defined according to

$$s = \sigma s_*, \quad r = \sigma\delta^{-1/3}y_*,$$

it is necessary to express the outer similarity variable ξ via them:

$$\xi = \frac{x}{y^{3/2}} = \varepsilon^{3/4}\xi_* \left[1 + \mathcal{O}(\delta^{2/3}/\varepsilon^{3/2})\right], \quad \xi_* = \frac{s_*}{y_*^{3/2}}. \quad (3.114)$$

Here ξ_* is the inner similarity variable of region 3; note that the estimate $\varepsilon \gg \text{Re}^{-1/6}$ yields $\delta^{2/3}/\varepsilon^{3/2} \ll \text{Re}^{-1/12} \ll 1$. Transformation (3.114) directly follows from (3.112), and only fails when $y_* \sim \delta^{4/3}/\varepsilon^{3/2} \equiv \sigma^{4/3}\varepsilon^{1/2} \ll 1$, because y becomes negative and ξ is not defined. However, the small areas next to the wall where the cartesian coordinate y is negative (see Fig. 3.6) prove to be insignificant for the inviscid analysis, unless we want to consider higher-order perturbations in the coordinate expansions.

Using the fact that $f(\xi)$ and $g(\xi)$ are invariant with respect to the transformation $\xi = \Lambda\xi_*$, $\Lambda = \varepsilon^{3/4}$, i.e. $f(\xi) = f(\xi_*)$ and $g(\xi) = g(\xi_*)$, we get the representation of the outer solution for u and v (region 1) in the inner variables of region 3:

$$u = \delta^{2/3} \left(\frac{\alpha s_*}{y_*}\right)^2 f(\xi_*), \quad v = \delta \left(\frac{\alpha s_*}{y_*}\right)^3 g(\xi_*). \quad (3.115)$$

The powers of δ in (3.115) coincide with the relevant powers in front of the u_1, v_1 terms in expansions (3.69), therefore allowing to match the inner and outer inviscid solutions. Plugging the inner representation (3.115) of the outer solution into (3.113), we obtain the corresponding curvilinear velocity components which provide the *far-field* matching conditions for the inner solution in region 3:

$$\begin{cases} u_1(s_*, y_*, \varepsilon) \rightarrow \left(\frac{\alpha s_*}{y_*}\right)^2 f(\xi_*), \\ v_1(s_*, y_*, \varepsilon) \rightarrow \left(\frac{\alpha s_*}{y_*}\right)^3 g(\xi_*) + \frac{(\gamma + 1)\varkappa s_*}{\varepsilon^{3/2}}, \end{cases} \quad y_* \rightarrow \infty, \quad \xi_* = \text{const}. \quad (3.116)$$

These are the exact expressions with no further asymptotic terms on the right-hand side;¹⁴⁾ they should hold for any fixed $\xi_* \in (-\infty, \infty)$, implying that $|s_*| \rightarrow \infty$ along the $\xi_* = \text{const}$ curves when $y_* \rightarrow \infty$. The $(\gamma + 1)$ term in the second matching condition is due to the coordinate transformation. The fact that it contains small parameter ε does not affect expansions (3.69) in region 3, as the functions (u_1, v_1) , (u_2, v_2) , etc. in front of the successive powers of δ depend on ε and can be further expanded based on this small parameter. As mentioned before, all the expansions introduced in section 3.2.1 for different tiers of the triple deck are effectively double, simply because of the presence of the two independent small parameters, ε and Re^{-1} , or their combinations σ and δ .

Functions u_1, v_1 satisfy the nonlinear Karman equations (3.72)–(3.73), and are related to $F_*(s_*)$ and $G_*(s_*)$ via boundary conditions (3.74)–(3.75) (matching with region 4). Solving the problem in region 3 will provide second relationship between F_* and G_* needed for deriving the interaction equation. It turns out that the required relationship can be obtained in a closed form due to the presence of small parameter ε in equation (3.72) and in the far-field boundary conditions (3.116).¹⁵⁾ To demonstrate that, let us start with introducing new functions $u_0(s_*, y_*, \varepsilon)$, $v_0(s_*, y_*, \varepsilon)$, which satisfy homogeneous conditions when $y_* \rightarrow \infty$ for fixed ξ_* :

$$\begin{aligned} u_0 &= u_1 - \left(\frac{\alpha s_*}{y_*} \right)^2 f(\xi_*), \\ v_0 &= v_1 - \left[\left(\frac{\alpha s_*}{y_*} \right)^3 g(\xi_*) + \frac{(\gamma + 1)\varkappa s_*}{\varepsilon^{3/2}} \right]. \end{aligned} \tag{3.117}$$

Indeed, applying matching conditions (3.116) to (3.117) yields

$$\begin{cases} u_0 \rightarrow 0, \\ v_0 \rightarrow 0, \end{cases} \quad y \rightarrow \infty, \quad \xi_* = \text{const}. \tag{3.118}$$

To derive the equations for u_0, v_0 , we need to recall that the phase variables $f(\xi_*)$,

¹⁴⁾ Higher-order corrections to the inviscid solutions in region 1, not considered in Chapter 2, match with the higher-order terms from expansions (3.69) in region 3, i.e. with (u_2, v_2) , etc.

¹⁵⁾ The latter also contain ε implicitly through functions $f(\xi_*)$ and $g(\xi_*)$ describing the inviscid flow in region 1 generated by an order- ε break in wall curvature.

$g(\xi_*)$ are described by the system

$$\begin{cases} \frac{df}{d\chi} = 2f + 3(\alpha - 1)g - 2\alpha f^2, \\ \frac{dg}{d\chi} = 3g + 2(\alpha - 1)f^2 - 3\alpha fg, \end{cases} \quad d\chi = \frac{d\xi_*}{(f - 1)\alpha\xi_*}.$$

(see section 2.2.1). With this in mind, one can express u_1, v_1 via u_0, v_0 using (3.117) and substitute into governing equations (3.72)–(3.73). After a number of simplifications we arrive at the required equations for u_0, v_0 in region 3:

$$\begin{cases} u_0 \frac{\partial u_0}{\partial s_*} - \frac{\partial v_0}{\partial y_*} + \frac{\partial}{\partial s_*} [y_* \alpha^2 \xi_*^2 f(\xi_*) u_0] = 0, \\ \frac{\partial v_0}{\partial s_*} - \frac{\partial u_0}{\partial y_*} = 0. \end{cases} \quad (3.119)$$

Therefore, although the transformation did not remove the nonlinearity, it made the second equation homogeneous. Note that the outer solution $f(\xi_*)$ is extended into region 3 and directly affects the triple deck ‘corrections’ u_0, v_0 through the first equation; these corrections take into the account the viscous-inviscid interaction, and are expected to provide regular solutions for u_1 and v_1 (with no singularity in the relevant pressure gradient).

Now we only need to derive the boundary conditions for u_0, v_0 when $y_* \rightarrow 0$, i.e. in the overlapping region between tiers 3 and 4. To do this, one has to recall that the outer solution in terms of $F(\xi)$ has the asymptotic forms

$$F(\xi \rightarrow \pm\infty) = \delta_{\pm} (\pm\xi)^{\lambda} - (\gamma + 1) \varkappa_{\pm} \xi + \mathcal{O}((\pm\xi)^{1/3}),$$

where $\lambda = 3 - \frac{2}{\alpha} = \frac{5}{3}$, and

$$\delta_{\pm} = \mp \frac{3\varepsilon G}{2\lambda}$$

(see (3.34) for the definition of G). Since $F(\xi) \equiv F(\Lambda\xi_*) = \Lambda^3 F(\xi_*)$ due to the basic property of the outer solution discussed in section 2.2.1 ($\Lambda = \varepsilon^{3/4}$ in this case), we get the following asymptotic form for $F(\xi_*)$:

$$F(\xi_* \rightarrow \pm\infty) = \frac{\delta_{\pm}}{\varepsilon} (\pm\xi_*)^{\lambda} - \frac{(\gamma + 1) \varkappa_{\pm} \xi_*}{\varepsilon^{3/2}} + \mathcal{O}((\pm\xi_*)^{1/3}), \quad \frac{\delta_{\pm}}{\varepsilon} = \mathcal{O}(1).$$

Thus,

$$\lim_{y_* \rightarrow 0} \left\{ y_* \alpha^2 \xi_*^2 f(\xi_*) \right\} = \mp \frac{3G}{2} (\pm s_*)^{2/3},$$

$$\lim_{y_* \rightarrow 0} \left\{ y_*^\alpha \alpha^3 \xi_*^3 g(\xi_*) \right\} = -\frac{(\gamma + 1) \varkappa_{\pm} s_*}{\varepsilon^{3/2}},$$

with \pm corresponding to $s_* \gtrless 0$. Taking this into the account, we apply the same limit to (3.117) to obtain the required boundary conditions:

$$u_0|_{y_*=0} = u_1|_{y_*=0} \pm \frac{3G}{2} (\pm s_*)^{2/3}, \quad (3.120)$$

$$v_0|_{y_*=0} = v_1|_{y_*=0},$$

where $u_1|_{y_*=0}$ and $v_1|_{y_*=0}$ are given by (3.74)–(3.75) and are expressed via F_* , G_* .

Problem (3.118), (3.119), (3.120) can be solved analytically due to the fact that the outer solution for $f(\xi_*)$ simplifies a lot when the break of curvatures is small (order- ε). Indeed, in section 2.4.6 it was shown that the relevant solution for $F(\xi)$ can be expressed by a sum of two main terms, and therefore

$$y_* \alpha^2 \xi_*^2 f(\xi_*) \equiv F'(\xi_*) = \mp \frac{3G}{2} (\pm \xi_*)^{2/3} - \frac{(\gamma + 1) \varkappa_{\pm}}{\varepsilon^{3/2}} (1 + \mathcal{O}(\varepsilon)), \quad \xi_* \gtrless 0. \quad (3.121)$$

This is valid for all ξ_* , and not just when $\xi_* \rightarrow \pm\infty$. The second term corresponds to the nearly unperturbed potential vortex flow which takes place when there is no curvature break, and the first term only comes to play when $|\xi_*| \gtrsim \varepsilon^{-9/4}$, i.e. in thin inviscid regions close to the wall (see section 2.4.6). The $\varepsilon^{-3/2}$ multiple in the second term is the key to dealing with the nonlinearity in equations (3.119).¹⁶⁾ Note that it is also possible to use \varkappa_- instead of \varkappa_{\pm} in (3.121), since $\varkappa_+ = \varkappa_- (1 + \mathcal{O}(\varepsilon))$, and the swap between the two curvatures preserves the accuracy with which the second term is written. Although the $\mathcal{O}(\varepsilon)$ correction gives an order $\varepsilon^{-1/2}$ contribution to $F'(\xi_*)$, it proves to have the same order of magnitude for all ξ_* , whereas the very first term in (3.121) grows with ξ_* and starts to dominate over the correction as soon as $|\xi_*| \gtrsim \varepsilon^{-3/4}$.

¹⁶⁾ $\varepsilon^{-3/2}$ itself appeared after the re-scaling, due to the fact that region 3 is stretched vertically in the original physical variables.

Based on the above observations, let us rewrite the entire problem in region 3:

$$\begin{aligned} \frac{\partial}{\partial s_*} \left\{ u_0 \left[\frac{u_0}{2} \mp \frac{3G}{2} (\pm s_*)^{2/3} - \frac{(\gamma+1)\varkappa_- y_*}{\varepsilon^{3/2}} (1 + \mathcal{O}(\varepsilon)) \right] \right\} &= \frac{\partial v_0}{\partial y_*}, \\ \frac{\partial v_0}{\partial s_*} - \frac{\partial u_0}{\partial y_*} &= 0, \\ u_0 \Big|_{y_*=0} &= -\frac{\tau_w}{R_w} G_*(s_*) \pm \frac{3G}{2} (\pm s_*)^{2/3}, \\ v_0 \Big|_{y_*=0} &= -\frac{1}{\tau_w} \frac{dF_*(s_*)}{ds_*}, \\ \lim_{y_* \rightarrow \infty} (u_0^2 + v_0^2) &= 0, \quad -\infty < \xi_* < \infty. \end{aligned} \tag{3.122}$$

The amplitude of the pressure gradient is assumed to be small in the current analysis, suggesting that finite-distance singularities are unlikely to occur. Therefore, u_0 , v_0 should be order one quantities in region 3 when $|s_*| \sim 1$, $y_* \sim 1$. From this it follows that the $\varepsilon^{-3/2}$ term dominates the left-hand side of the first equation, so that the latter is reduced to

$$\frac{(\gamma+1)\varkappa_- y_*}{\varepsilon^{3/2}} \frac{\partial u_0}{\partial s_*} + \frac{\partial v_0}{\partial y_*} = 0$$

in the leading order. Differentiating this with respect to s_* and substituting v_0 from the second equation of (3.122) yields:

$$\frac{\partial^2 u_0}{\partial y_*^2} + \frac{(\gamma+1)\varkappa_- y_*}{\varepsilon^{3/2}} \frac{\partial^2 u_0}{\partial s_*^2} = 0.$$

The general solution is given by the Fourier integral with respect to s_* :

$$u_0 = \frac{1}{2\pi} \int_{-\infty}^{\infty} E_\omega \text{Ai}(\Omega(\omega)y_*) e^{i\omega s_*} d\omega, \quad \Omega(\omega) = \frac{\omega^{2/3} ((\gamma+1)\varkappa_-)^{1/3}}{\varepsilon^{1/2}},$$

where E_ω is a function of ω only. This form suggests that the solution develops on the scale $y_* \sim \sqrt{\varepsilon} \ll 1$, $|s_*| \sim 1$, as the Airy function exponentially decays with y_* . Even at this small scale the $y_* \varepsilon^{-3/2}$ term in the first equation of (3.122) is of order of ε^{-1} and dominates the rest of the terms on the left-hand side, therefore linearizing the equation and validating the above asymptotic solution. However, this does not work when $y_* \sim \varepsilon^{3/2}$, which means there is some inner scale in tier 3 close to the wall where other terms in the nonlinear equation also come to play. We are going to call this region 3a.

It is worth clarifying at this stage that the Airy-function representation of the solution in the main part of region 3 follows from the Karman–Guderley equations for an inviscid transonic flow, the latter being of a mixed elliptic/hyperbolic type. On the other hand, the Airy equation solved in region 5 resulted from the parabolic boundary layer equations for a viscous flow near the wall. Thus, the two solutions with the Airy function arise from two completely different physical mechanisms, and consequently exhibit a fundamental difference in the way the argument of $\text{Ai}(z)$ depends on ω .

Moving to region 3a, we introduce the inner variable $\hat{y} = \varepsilon^{-3/2} y_* \sim 1$. The relevant boundary-value problem for u_0 follows from (3.122) after re-scaling and excluding v_0 :

$$\begin{aligned} \frac{\partial^2 u_0}{\partial \hat{y}^2} &= \varepsilon^3 \frac{\partial^2}{\partial s_*^2} \left\{ u_0 \left[\frac{u_0}{2} \mp \frac{3G}{2} (\pm s_*)^{2/3} - (\gamma + 1) \kappa_- \hat{y} (1 + \mathcal{O}(\varepsilon)) \right] \right\}, \\ u_0 \Big|_{\hat{y}=0} &= -\frac{\tau_w}{R_w} G_*(s_*) \pm \frac{3G}{2} (\pm s_*)^{2/3}, \\ \frac{\partial u_0}{\partial \hat{y}} \Big|_{\hat{y}=0} &= -\frac{\varepsilon^{3/2}}{\tau_w} \frac{d^2 F_*(s_*)}{ds_*^2}. \end{aligned} \quad (3.123)$$

One can easily spot that the nonlinear term in the equation once again has a small parameter in front of it, this time due to the re-scaling of $\partial^2 u_0 / \partial y_*^2$ when entering region 3a. The structure of the equation and the boundary conditions suggest u_0 can be sought in terms of an expansion based on powers of $\varepsilon^{1/2}$; however, the first three terms are only represented by the powers of $\varepsilon^{3/2}$:

$$u_0(s_*, y_*, \varepsilon) = u^{(0)}(s_*, \hat{y}) + \varepsilon^{3/2} u^{(1)}(s_*, \hat{y}) + \varepsilon^3 u^{(2)}(s_*, \hat{y}) + \dots \quad (3.124)$$

Plugging this into (3.123) yields the following equations for $u^{(0)}$, $u^{(1)}$ and $u^{(2)}$:

$$\frac{\partial^2 u^{(0)}}{\partial \hat{y}^2} = 0, \quad \frac{\partial^2 u^{(1)}}{\partial \hat{y}^2} = 0, \quad \frac{\partial^2 u^{(2)}}{\partial \hat{y}^2} = \frac{\partial^2}{\partial s_*^2} \left\{ u_0 \left[\frac{u_0}{2} \mp \frac{3G}{2} (\pm s_*)^{2/3} - (\gamma + 1) \kappa_- \hat{y} \right] \right\}.$$

Integrating with respect to \hat{y} and applying the boundary conditions, we get the exact solutions:

$$\begin{aligned} u^{(0)}(s_*) &= -\frac{\tau_w}{R_w} G_*(s_*) \pm \frac{3G}{2} (\pm s_*)^{2/3}, \\ u^{(1)}(s_*, \hat{y}) &= -\frac{\hat{y}}{\tau_w} \frac{d^2 F_*(s_*)}{ds_*^2}, \\ u^{(2)}(s_*, \hat{y}) &= C(s_*) \hat{y}^2 + D(s_*) \hat{y}^3, \end{aligned} \quad (3.125)$$

where

$$C(s_*) = \frac{1}{2} \frac{d^2}{ds_*^2} \left\{ u^{(0)} \left[\frac{u^{(0)}}{2} \mp \frac{3G}{2} (\pm s_*)^{2/3} \right] \right\},$$

$$D(s_*) = -\frac{(\gamma + 1)\kappa_-}{6} \frac{d^2 u^{(0)}}{ds_*^2}.$$

It can easily be spotted from (3.125) that the functions in the higher-order approximations with respect to $\varepsilon^{3/2}$ contain higher powers of \hat{y} . Therefore, when matching with the main part of region 3 is performed, i.e. when $\hat{y} \rightarrow \infty$, expansion (3.124) fails. Let us find out what determines the *maximum* power of \hat{y} in $u^{(n)}$ for all $n \in \mathbb{N}$ (for example, the maximum power of \hat{y} in $u^{(2)}$ is \hat{y}^3 ; it dominates the expression for $u^{(2)}$ when $\hat{y} \rightarrow \infty$, while \hat{y}^2 only provides a small correction). By writing

$$u_0(s_*, y_*, \varepsilon) = \sum_{n=0}^{\infty} u^{(n)}(s_*, \hat{y}) \varepsilon^{\frac{3n}{2}},$$

we obtain the series for $(u_0)^2$:

$$(u_0)^2 = \sum_{n=0}^{\infty} \varepsilon^{\frac{3n}{2}} \left[\sum_{k=0}^n u^{(k)} u^{(n-k)} \right].$$

Hence, according to (3.123) the recurring relationship for $u^{(n)}$ has the form

$$\frac{\partial^2 u^{(n+2)}}{\partial \hat{y}^2} = \frac{\partial^2}{\partial s_*^2} \left\{ \frac{1}{2} \left[\sum_{k=0}^n u^{(k)} u^{(n-k)} \right] - u^{(n)} \left[\pm \frac{3G}{2} (\pm s_*)^{2/3} + (\gamma + 1)\kappa_- \hat{y} \right] \right\}, \quad (3.126)$$

$n \in \mathbb{N}$. Using solutions (3.125), one can obtain the highest powers of \hat{y} in the nonlinear term and compare them to the relevant powers in $u^{(n)}\hat{y}$:

n	0	1	2	3	4	5	
nonlinear term	1	\hat{y}	\hat{y}^3	\hat{y}^4	\hat{y}^6	\hat{y}^7	etc.
$u^{(n)}\hat{y}$	\hat{y}	\hat{y}^2	\hat{y}^4	\hat{y}^5	\hat{y}^7	\hat{y}^8	

We see that the highest power of \hat{y} in the nonlinear term is always the same as in $u^{(n)}$ for any $n \in \mathbb{N}$, which may be easily proved by induction. However, due to the presence of \hat{y} in the linear multiples of $u^{(n)}$ on the right-hand side of (3.126), the highest power of \hat{y} in $u^{(n+2)}$ always comes from the linear term $u^{(n)}\hat{y}$. Indeed, the above table suggests the following pattern for the leading-order powers of \hat{y} in $u^{(n)}$

when $\hat{y} \rightarrow \infty$:

$$u^{(n)} = c_n \hat{y}^{3k} (1 + \mathcal{O}(\hat{y}^{-1})), \quad n = 2k,$$

$$u^{(n)} = c_n \hat{y}^{3k+1} (1 + \mathcal{O}(\hat{y}^{-1})), \quad n = 2k + 1,$$

$k \in \mathbb{N}$. The coefficients c_n are functions of s_* , the first three of them being

$$\begin{aligned} c_0(s_*) &= -\frac{\tau_w}{R_w} G_*(s_*) \pm \frac{3G}{2} (\pm s_*)^{2/3}, \\ c_1(s_*) &= -\frac{1}{\tau_w} \frac{d^2 F_*(s_*)}{ds_*^2}, \\ c_2(s_*) &= -\frac{(\gamma + 1)\chi_-}{6} \frac{d^2 c_0(s_*)}{ds_*^2} \end{aligned} \quad (3.127)$$

according to (3.125). Using this, we can write the corresponding solution for u_0 based only on the highest powers of \hat{y} in $u^{(n)}$ in order to perform the matching with the main part of region 3:

$$u_0 = \sum_{n=0}^{\infty} \varepsilon^{\frac{3n}{2}} u^{(n)} \sim \sum_{k=0}^{\infty} \varepsilon^{3k} \left[c_{2k} \hat{y}^{3k} + \varepsilon^{\frac{3}{2}} c_{2k+1} \hat{y}^{3k+1} \right], \quad \hat{y} \rightarrow \infty. \quad (3.128)$$

Thus, the powers of \hat{y} are combined in pairs, with a jump of 1 inside each pair and a jump of 2 between two adjacent pairs. As $\hat{y} \rightarrow \infty$, at some point the first term of any given pair will become of the same order as the second term of the previous pair. This will obviously happen before the two terms in every single pair become of the same order, simply because of the bigger jump between the pairs. It may be easily shown that $\varepsilon^{3k} u^{(2k)}$ catches the previous term $\varepsilon^{3k-\frac{3}{2}} u^{(2k-1)}$ in (3.124) when $\hat{y} \sim \varepsilon^{-3/4} \gg 1$. Therefore, introducing the intermediate region 3b with the variable $\tilde{y} = \varepsilon^{3/4} \hat{y}$, we transform (3.128) to

$$u_0 \sim c_0 + \sum_{k=1}^{\infty} (\varepsilon^{3/4} \tilde{y}^3)^k \left[c_{2k} + \frac{c_{2k-1}}{\tilde{y}^2} + \dots \right], \quad \tilde{y} \gtrsim 1, \quad (3.129)$$

which illustrates the effect described above. The dots stand for higher-order terms corresponding to smaller powers of \hat{y} in $u^{(n)}$; these terms take into the account the nonlinear effects in region 3a (see expression for $C(s_*)$ in (3.125)), but vanish in the limit $\tilde{y} \rightarrow \infty$, when we move into the main part of region 3 with $y_* \sim 1$.¹⁷⁾

¹⁷⁾ Note that when $\tilde{y} \sim 1$, we have $\hat{y} \sim \varepsilon^{-3/4}$ and $y_* \sim \varepsilon^{3/4}$.

Let us now reconsider the equation for u_0 in the newly introduced region 3b:

$$\frac{\partial^2 u_0}{\partial \tilde{y}^2} = \varepsilon^{3/4} \frac{\partial^2}{\partial s_*^2} \left\{ u_0 \left[\varepsilon^{3/4} \left(\frac{u_0}{2} \mp \frac{3G}{2} (\pm s_*)^{2/3} \right) - (\gamma + 1) \kappa_- \tilde{y} \right] \right\}. \quad (3.130)$$

The solution is sought in the form of an asymptotic expansion

$$u_0(s_*, y_*, \varepsilon) = \sum_{n=0}^{\infty} \varepsilon^{\frac{3n}{4}} \tilde{u}^{(n)}(s_*, \tilde{y}),$$

where functions $\tilde{u}^{(n)}$ replace $u^{(n)}$ from region 3a. Plugging this into (3.130) yields:

$$\frac{\partial^2 \tilde{u}^{(0)}}{\partial \tilde{y}^2} = 0, \quad \frac{\partial^2 \tilde{u}^{(1)}}{\partial \tilde{y}^2} = -(\gamma + 1) \kappa_- \tilde{y} \frac{\partial^2 \tilde{u}^{(0)}}{\partial s_*^2}, \quad \text{etc.}$$

The general solution for $\tilde{u}^{(0)}$ is

$$\tilde{u}^{(0)} = C^{(0)}(s_*) + D^{(0)}(s_*) \tilde{y},$$

and it has to match with the order ε^0 term in (3.129), thus giving $C^{(0)} \equiv c_0(s_*)$, $D^{(0)} \equiv 0$, so that

$$\tilde{u}^{(0)} = c_0(s_*).$$

The general solution for $\tilde{u}^{(1)}$ is

$$\tilde{u}^{(1)} = C^{(1)}(s_*) + D^{(1)}(s_*) \tilde{y} - \frac{(\gamma + 1) \kappa_- \tilde{y}^3}{6} \frac{d^2 c_0}{ds_*^2};$$

matching this with the $\varepsilon^{3/4}$ term in (3.129) and recalling the expression for c_2 , we get $C^{(1)} \equiv 0$, $D^{(1)} \equiv c_1(s_*)$, so that

$$\tilde{u}^{(1)} = c_2 \tilde{y}^3 + c_1 \tilde{y}.$$

Continuing the procedure, it can be shown that the entire solution in region 3b has exactly the same structure as (3.129):

$$u_0(s_*, y_*, \varepsilon) = c_0 + \sum_{n=1}^{\infty} (\varepsilon^{3/4} \tilde{y}^3)^n \left[c_{2n} + \frac{c_{2n-1}}{\tilde{y}^2} + \mathcal{O}(\tilde{y}^{-4}) \right], \quad (3.131)$$

where $\mathcal{O}(\tilde{y}^{-4})$ represents the contribution of the nonlinear terms in (3.130). The latter becomes clear when looking at the equation for $\tilde{u}^{(2)}$ along with the previously obtained solutions for $\tilde{u}^{(0)}$, $\tilde{u}^{(1)}$:

$$\frac{\partial^2 \tilde{u}^{(2)}}{\partial \tilde{y}^2} = \frac{\partial^2}{\partial s_*^2} \left\{ \tilde{u}^{(0)} \left[\frac{\tilde{u}^{(0)}}{2} \mp \frac{3G}{2} (\pm s_*)^{2/3} \right] \right\} - (\gamma + 1) \kappa_- \tilde{y} \frac{\partial^2 \tilde{u}^{(1)}}{\partial s_*^2},$$

and may be proved for all $\tilde{u}^{(n)}$, $n \in \mathbb{N}$, by induction.

It can easily be spotted from (3.131) that on the scale $\tilde{y} \sim \varepsilon^{-1/4}$, i.e. $y_* \sim \varepsilon^{1/2}$, all the $(\varepsilon^{1/4} \tilde{y})^{3n}$ terms are order one quantities. Therefore, if $\bar{y} = \varepsilon^{1/4} \tilde{y} \equiv \varepsilon^{-1/2} y_* \sim 1$ is the variable corresponding to this scale (subsequently referred to as region 3c), then

$$u_0(s_*, y_*, \varepsilon) = \sum_{n=0}^{\infty} c_{2n}(s_*) \bar{y}^{3n} + \sqrt{\varepsilon} \sum_{n=0}^{\infty} c_{2n+1}(s_*) \bar{y}^{3n+1} + \mathcal{O}(\varepsilon), \quad (3.132)$$

with the $\mathcal{O}(\varepsilon)$ term being due to the nonlinearity of the main equation.¹⁸⁾ Now recall that the original estimate at the start of this section gave an asymptotic solution for u_0 in terms of the Airy function of $y_*/\sqrt{\varepsilon} \equiv \bar{y}$. The latter obviously has a nontrivial behaviour when the argument is an order one quantity: $\bar{y} \sim 1$. It remains to prove that both of the leading-order series in (3.132) can be expressed via the Airy function, and to make sure that u_0 tends to zero when $\bar{y} \rightarrow \infty$.

Functions $c_n(s_*)$ are defined as the coefficients in front of the highest powers of \hat{y} in the respective solutions $u^{(n)}(s_*, \hat{y})$ from asymptotic expansion (3.128) in region 3a. The first three of them are given in (3.127) explicitly. Although in region 3a itself the terms containing c_n have the same order as the rest of the terms with smaller powers of \hat{y} (within each given approximation based on the powers of ε), they dominate the solution for u_0 in regions 3b and 3c, ultimately yielding (3.132) in region 3c. It has already been discussed above that the highest powers of \hat{y} in $u^{(n+2)}$ are due to the linear term on the right-hand side of (3.126), namely $u^{(n)}\hat{y}$. This leads to the following recurring relationships for $c_n(s_*)$:

$$\begin{aligned} c_{2n}(s_*) &= -\frac{(\gamma+1)\varkappa_-}{3n(3n-1)} \frac{d^2 c_{2n-2}}{ds_*^2}, \\ c_{2n+1}(s_*) &= -\frac{(\gamma+1)\varkappa_-}{3n(3n+1)} \frac{d^2 c_{2n-1}}{ds_*^2}. \end{aligned}$$

Assuming that $c_n(s_*)$ are differentiable enough, these equations can be traced back to c_0 and c_1 :

$$\begin{aligned} c_{2n}(s_*) &= (-1)^n \left(\frac{(\gamma+1)\varkappa_-}{9} \right)^n \frac{\Gamma(2/3)}{n! \Gamma(n + \frac{2}{3})} \frac{d^{2n}}{ds_*^{2n}} [c_0(s_*)], \\ c_{2n+1}(s_*) &= (-1)^n \left(\frac{(\gamma+1)\varkappa_-}{9} \right)^n \frac{\Gamma(4/3)}{n! \Gamma(n + \frac{4}{3})} \frac{d^{2n}}{ds_*^{2n}} [c_1(s_*)]. \end{aligned} \quad (3.133)$$

¹⁸⁾ The series in (3.132) are expected to converge due to a rapid diminishing of the coefficients c_n with n .

Plugging (3.133) into (3.132) yields:

$$\begin{aligned}
 u_0(s_*, y_*, \varepsilon) &= \Gamma(2/3) \left(\frac{z}{2}\right)^{\frac{1}{3}} J_{-\frac{1}{3}}(z) [c_0(s_*)] + \\
 &+ \sqrt{\varepsilon} \Gamma(4/3) \bar{y} \left(\frac{z}{2}\right)^{-\frac{1}{3}} J_{\frac{1}{3}}(z) [c_1(s_*)] + \mathcal{O}(\varepsilon),
 \end{aligned} \tag{3.134}$$

where the operator z contains differentiation with respect to s_* :

$$z = \frac{2}{3} \sqrt{(\gamma+1)\varkappa_-} \bar{y}^{3/2} \frac{\partial}{\partial s_*}, \tag{3.135}$$

and

$$J_\nu(z) = \left(\frac{z}{2}\right)^\nu \sum_{n=0}^{\infty} \frac{\left(-\frac{z}{2}\right)^{2n}}{n! \Gamma(\nu+n+1)}$$

is the Bessel function of the first kind. If $\nu = \pm 1/3$, as it is in our case, the Bessel function may be expressed via the Airy functions (Abramovitz & Stegun 1972):

$$J_{\pm\frac{1}{3}}(z) = \frac{1}{2} \left(\frac{3}{\zeta}\right)^{\frac{1}{2}} \left[\sqrt{3} \text{Ai}(-\zeta) \mp \text{Bi}(-\zeta) \right];$$

here

$$\zeta = \left(\frac{3z}{2}\right)^{\frac{2}{3}} = ((\gamma+1)\varkappa_-)^{1/3} \bar{y} \left(\frac{\partial}{\partial s_*}\right)^{\frac{2}{3}}$$

is also a differential operator, with the fractional derivative defined as follows:

$$\frac{d^\alpha f(x)}{dx^\alpha} = \frac{1}{\Gamma(1-\alpha)} \frac{d}{dx} \int_0^x \frac{f(t) dt}{(x-t)^\alpha}, \quad \Re(\alpha) < 1.$$

Using the Airy function representation, (3.134) may be written as

$$\begin{aligned}
 u_0 &= \frac{\Gamma(2/3) 3^{\frac{1}{6}}}{2} \left(\sqrt{3} \text{Ai}(-\zeta) + \text{Bi}(-\zeta) \right) [c_0(s_*)] + \\
 &+ \sqrt{\varepsilon} \frac{\Gamma(1/3) 3^{-\frac{1}{6}}}{2((\gamma+1)\varkappa_-)^{\frac{1}{3}}} \left(\sqrt{3} \text{Ai}(-\zeta) - \text{Bi}(-\zeta) \right) \left(\frac{\partial}{\partial s_*}\right)^{-\frac{2}{3}} [c_1(s_*)] + \mathcal{O}(\varepsilon).
 \end{aligned}$$

A Fourier transform of this with respect to s_* replaces $\partial/\partial s_*$ with $i\omega$:

$$\begin{aligned}
 u_\omega &= \int_{-\infty}^{\infty} u_0(s_*, y_*, \varepsilon) e^{i\omega s_*} ds_* = \frac{\Gamma(2/3) 3^{\frac{1}{6}}}{2} \left(\sqrt{3} \text{Ai}(-\Omega\bar{y}) + \text{Bi}(-\Omega\bar{y}) \right) c_0(\omega) + \\
 &+ \sqrt{\varepsilon} \frac{\Gamma(1/3) 3^{-\frac{1}{6}}}{2\Omega} \left(\sqrt{3} \text{Ai}(-\Omega\bar{y}) - \text{Bi}(-\Omega\bar{y}) \right) c_1(\omega) + \mathcal{O}(\varepsilon),
 \end{aligned} \tag{3.136}$$

where

$$\Omega(\omega) = (i\omega)^{2/3} ((\gamma+1)\varkappa_-)^{1/3},$$

and $c_0(\omega)$, $c_1(\omega)$ are the Fourier transforms of $c_0(s_*)$, $c_1(s_*)$. Again, the $\mathcal{O}(\varepsilon)$ terms (not written explicitly) are due to the nonlinearity.

When working out the inverse transform of (3.136), one has to make a branch-cut in the plane of complex ω connecting 0 and ∞ . If the branch-cut is made in the upper half-plane, for example along the imaginary axis, then $\arg \omega = -\pi$ for real negative ω , and $\arg \omega = 0$ for real positive ω . Therefore, for the regular branch of $(i\omega)^{2/3}$ defined according to the rule

$$\arg [(i\omega)^{2/3}] = \frac{\pi}{3} + \frac{2}{3} \arg \omega$$

we have:

$$\arg(-\Omega(\omega) \bar{y}) = \begin{cases} \frac{2\pi}{3}, & \omega < 0, \\ \frac{4\pi}{3}, & \omega > 0, \end{cases}$$

suggesting that at least one of the Airy functions in (3.136) will grow exponentially with \bar{y} . Rewriting (3.136) as

$$u_\omega = \hat{A}(\omega) \text{Ai}(-\Omega(\omega) \bar{y}) + \hat{B}(\omega) \text{Bi}(-\Omega(\omega) \bar{y}) + \mathcal{O}(\varepsilon),$$

where

$$\begin{aligned} \hat{A}(\omega) &= \frac{\sqrt{3}}{2} \left[\Gamma(2/3) 3^{1/6} c_0(\omega) + \Gamma(1/3) \frac{\sqrt{\varepsilon}}{3^{1/6} \Omega} c_1(\omega) \right], \\ \hat{B}(\omega) &= \frac{1}{2} \left[\Gamma(2/3) 3^{1/6} c_0(\omega) - \Gamma(1/3) \frac{\sqrt{\varepsilon}}{3^{1/6} \Omega} c_1(\omega) \right], \end{aligned} \quad (3.137)$$

and using the well-known formulae for the analytical continuation of Airy functions (Abramovitz & Stegun 1972), we get:

$$u_\omega = \begin{cases} [\hat{B} + i\hat{A}] e^{-i\pi/6} \text{Ai}(|\Omega| \bar{y}) + [\hat{B} - i\hat{A}] e^{i\pi/6} \text{Ai}(|\Omega| \bar{y} e^{-2\pi i/3}), & \omega < 0, \\ 2\hat{B} e^{i\pi/6} \text{Ai}(|\Omega| \bar{y}) + [\hat{A} - i\hat{B}] \text{Ai}(|\Omega| \bar{y} e^{-2\pi i/3}), & \omega > 0, \end{cases} \quad (3.138)$$

$$|\Omega(\omega)| = |\omega|^{2/3} ((\gamma + 1)\varkappa_-)^{1/3}.$$

Now, since due to the last matching condition in (3.122) $u_0(s_*, y_*, \varepsilon)$ has to tend to zero when $\bar{y} \rightarrow \infty$, the same should hold for u_ω , i.e.

$$\lim_{\bar{y} \rightarrow \infty} u_\omega = 0. \quad (3.139)$$

The asymptotic form of $\text{Ai}(|\Omega|\bar{y})$ contains

$$\exp\left\{-\frac{2}{3}(|\Omega|\bar{y})^{\frac{3}{2}}\right\}, \quad \bar{y} \rightarrow \infty,$$

which means it exponentially decays with \bar{y} and satisfies the required condition. However, $\text{Ai}(|\Omega|\bar{y}e^{-2\pi i/3})$ contains the same exponential with plus, leading to an unbounded growth when $\bar{y} \rightarrow \infty$. The only way to satisfy the matching condition for u_ω is to set the coefficient in front of $\text{Ai}(|\Omega|\bar{y}e^{-2\pi i/3})$ to be zero (3.138), yielding:

$$\hat{B} = i\hat{A}, \quad \omega < 0,$$

$$\hat{A} = i\hat{B}, \quad \omega > 0.$$

The two solutions can be combined together to give:

$$\hat{A}(\omega) = \frac{i\omega}{|\omega|} \hat{B}(\omega), \quad \omega \in \mathbb{R}.$$

Using the definition of \hat{A} , \hat{B} in (3.137), we get the required link between $c_0(\omega)$ and $c_1(\omega)$:

$$c_0(\omega) = -\frac{\Gamma(1/3)}{\Gamma(2/3)} \frac{\sqrt{\varepsilon}}{(3(\gamma+1)\varkappa_-)^{\frac{1}{3}}} \frac{c_1(\omega)}{|\omega|^{\frac{2}{3}}}, \quad \omega \in \mathbb{R}. \quad (3.140)$$

The same result can be obtained if the branch-cut is drawn in the lower half-plane ω , and therefore is independent on the choice of regular branches in (3.136).

To see how (3.140) works, we are going to assume, subject to subsequent confirmation in section 3.3.1, that $c_1(s_*) \sim 1$ when $|s_*| \sim 1$. Thus, equation (3.140) implies $c_0 \sim \sqrt{\varepsilon}$ on the same scale; according to (3.127), this results in

$$\frac{\tau_w}{R_w} G_*(s_*) = \pm \frac{3G}{2} (\pm s_*)^{2/3} + \mathcal{O}(\sqrt{\varepsilon}), \quad (3.141)$$

and the main asymptotic expansion for the triple deck correction u_0 in region 3c actually starts from the $\sqrt{\varepsilon}$ term:

$$u_0(s_*, y_*, \varepsilon) = \sqrt{\varepsilon} \bar{u}^{(1/2)}(s_*, \bar{y}) + \varepsilon \bar{u}^{(1)}(s_*, \bar{y}) + \dots \quad (3.142)$$

The $\bar{u}^{(1/2)}$ term here combines the first two terms in expression (3.136) for u_ω , leading to an order ε^2 estimate for the leading-order contributions from the nonlinearity. The

latter is clearly seen from the structure of the main equation for u_0 written in the internal variables of region 3c:¹⁹⁾

$$\frac{\partial^2 u_0}{\partial \bar{y}^2} + \frac{\partial^2}{\partial s_*^2} \left\{ u_0 \left[(\gamma + 1) \kappa_- \bar{y} + \varepsilon \left(\pm \frac{3G}{2} (\pm s_*)^{2/3} - \frac{u_0}{2} + \mathcal{O}(1) \right) \right] \right\} = 0.$$

In section 3.3.1 we are going to show that the $\mathcal{O}(\sqrt{\varepsilon})$ correction in (3.141) to the outer inviscid solution is crucial for the viscous-inviscid interaction.

The higher-order terms in expansion (3.142) for u_0 satisfy the outer matching condition (3.139) as long as their homogeneous solutions contain only exponentially decaying Airy functions, providing condition (3.140) holds. Thus, equation (3.140) obtained after imposing (3.139) on the first two terms in (3.142) is the necessary condition for the entire function u_0 to satisfy (3.139). It turns out to be sufficient for the analysis of the leading-order viscous-inviscid interaction (see section 3.3.1).

Applying the inverse Fourier transform to (3.140) gives:

$$c_0(s_*) = \frac{1}{2\pi} \int_{-\infty}^{\infty} c_0(\omega) e^{i\omega s_*} d\omega = \frac{Q}{2\pi} \int_{-\infty}^{\infty} \frac{e^{i\omega s_*}}{|\omega|^{2/3}} \left[\int_{-\infty}^{\infty} c_1(x) e^{-i\omega x} dx \right] d\omega,$$

where

$$Q = \frac{\sqrt{\varepsilon} \Gamma(1/3)}{\Gamma(2/3) (3(\gamma + 1) \kappa_-)^{1/3}}. \quad (3.143)$$

Splitting the integral with respect to ω into two parts, and swapping the integration order yields:

$$c_0(s_*) = \frac{Q}{2\pi} \int_{-\infty}^{\infty} c_1(x) \left[\int_0^{\infty} \frac{e^{i\omega(s_*-x)} d\omega}{\omega^{2/3}} + \int_0^{\infty} \frac{e^{-i\omega(s_*-x)} d\omega}{\omega^{2/3}} \right] dx.$$

A general formula for the Gamma function-like integrals reads:

$$\int_0^{\infty} \frac{e^{izt} dt}{t^\nu} = \Gamma(1-\nu) \left(\frac{e^{i\frac{\pi}{2} - i \arg z}}{|z|} \right)^{1-\nu}, \quad \nu < 1, \quad \arg z \in [0, \pi]. \quad (3.144)$$

Thus,

$$\int_0^{\infty} \frac{e^{\pm i\omega(s_*-x)} d\omega}{\omega^{2/3}} = \frac{\Gamma(1/3)}{|s_* - x|^{1/3}} e^{\pm i\frac{\pi}{6} \text{sign}(s_*-x)},$$

and

$$c_0(s_*) = \frac{\sqrt{3} \Gamma(1/3) Q}{2\pi} \int_{-\infty}^{\infty} \frac{c_1(x) dx}{|s_* - x|^{1/3}}. \quad (3.145)$$

¹⁹⁾ The $\mathcal{O}(1)$ term is directly related to $\mathcal{O}(\varepsilon)$ in the first equation of (3.122).

Equation (3.145), along with the definition of functions $c_0(s_*)$ and $c_1(s_*)$ in (3.127), provides the required second relationship between $F_*(s_*)$ and $G_*(s_*)$ generated in the inviscid region 3:

$$\frac{\tau_w}{R_w} G_*(s_*) - \frac{3G}{2} \frac{s_*}{|s_*|^{\frac{1}{3}}} = \frac{\sqrt{3} \Gamma(1/3) Q}{2\pi\tau_w} \int_{-\infty}^{\infty} \frac{d^2 F_*(x)}{dx^2} \frac{dx}{|s_* - x|^{\frac{1}{3}}}, \quad (3.146)$$

Q is defined in (3.143) and contains $\sqrt{\varepsilon}$. It shows that due to the predominantly subsonic nature of the flow in tier 3 the pressure at a given point s_* is influenced by the boundary layer displacement over the entire interaction region, both upstream and downstream of s_* . Equation (3.146) is in agreement with the leading-order terms in the asymptotic forms (3.64) of F_* and G_* when $|s_*| \rightarrow \infty$.

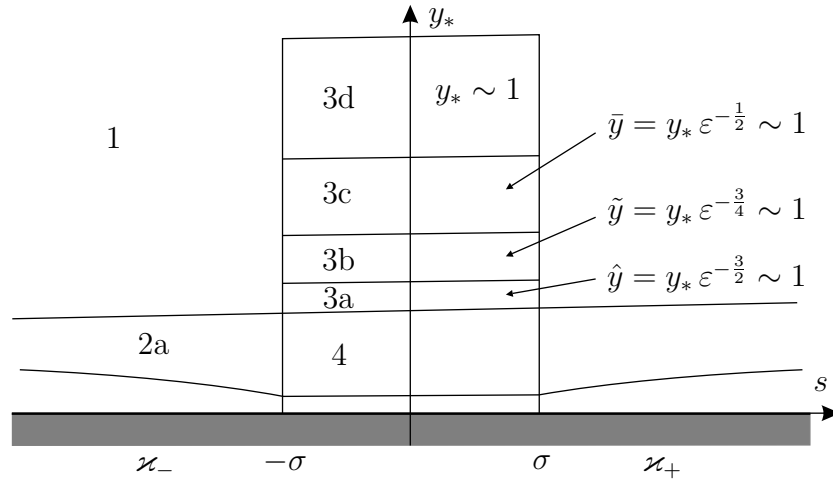


Figure 3.7: Regions that had to be considered in order to derive the two integral equations linking F_* and G_* .

Finally, the remaining part of region 3 where $y_* \sim 1$, referred to as 3d, turns out to be passive and only has an exponentially small solution for u_0 in it. As a result, the leading order functions u_1, v_1 in expressions (3.69) for the velocity components are very close to the solutions for u and v coming from the outer region 1. The entire structure of tier 3 with all the subregions and the corresponding inner variables is demonstrated in Fig. 3.7.

3.3 Solution of the Interaction Problem

3.3.1 Interaction equation

Now we have all the necessary components to derive the *interaction equation* for our problem. Equation (3.111) represents the displacement generated by the viscous sublayer 5 for a given pressure distribution, whereas equation (3.146) describes the pressure generated by the inviscid flow in region 3 in response to a given displacement distribution. Combining the two together and using expression (3.143) for Q yields:

$$\frac{\tau_w}{R_w} G_*(s_*) - \frac{3G}{2} \frac{s_*}{|s_*|^{\frac{1}{3}}} = \frac{\sqrt{3}}{2\pi} \frac{(\Gamma(1/3))^3}{(\Gamma(2/3))^2} \left[\frac{\alpha_w}{3(\gamma+1)\kappa_-} \right]^{1/3} \frac{\sqrt{\varepsilon}}{\tau_w} J(s_*),$$

$$J(s_*) = \int_{-\infty}^{\infty} \frac{dx}{|s_* - x|^{\frac{1}{3}}} \frac{d}{dx} \int_{-\infty}^x \frac{d^2 G_*(\xi)}{d\xi^2} \frac{d\xi}{(x - \xi)^{\frac{1}{3}}}.$$

The double integral in $J(s_*)$ can be reduced to the following expression with a single integral:

$$J(s_*) = \frac{(\Gamma(2/3))^2}{\Gamma(1/3)} \int_{s_*}^{\infty} \frac{d^2 G_*(\xi)}{d\xi^2} \frac{d\xi}{(\xi - s_*)^{\frac{2}{3}}}.$$

Therefore, we get a linear integral equation for the pressure distribution function $G_*(s_*)$ which describes the viscous-inviscid interaction:

$$\frac{\tau_w}{R_w} G_*(s_*) - \frac{3G}{2} \frac{s_*}{|s_*|^{\frac{1}{3}}} = \frac{\sqrt{3}}{2\pi} \frac{(\Gamma(1/3))^2}{(\Gamma(2/3))^2} \left[\frac{\alpha_w}{3(\gamma+1)\kappa_-} \right]^{1/3} \frac{\sqrt{\varepsilon}}{\tau_w} \int_{s_*}^{\infty} \frac{d^2 G_*(\xi)}{d\xi^2} \frac{d\xi}{(\xi - s_*)^{\frac{2}{3}}}.$$

Introducing the coefficients

$$g_1 = \frac{R_w}{\tau_w} G, \quad g_2 = \frac{\sqrt{3}}{2\pi} \frac{(\Gamma(1/3))^2}{(\Gamma(2/3))^2} \left[\frac{\alpha_w}{3(\gamma+1)\kappa_-} \right]^{1/3} \frac{R_w}{\tau_w^2}, \quad (3.147)$$

the interaction equation takes the form

$$G_*(s_*) - \frac{3g_1}{2} \frac{s_*}{|s_*|^{\frac{1}{3}}} = g_2 \sqrt{\varepsilon} \int_{s_*}^{\infty} \frac{d^2 G_*(\xi)}{d\xi^2} \frac{d\xi}{(\xi - s_*)^{\frac{2}{3}}}. \quad (3.148)$$

Note that both g_1 and g_2 are order one quantities, and that there is a small parameter $\varepsilon^{1/2}$ in front of the integral in (3.148). This suggests G_* is actually a function of ε with the asymptotic expansion

$$G_*(s_*, \varepsilon) = G_0(s_*) + \sqrt{\varepsilon} G_1(s_*) + \mathcal{O}(\varepsilon). \quad (3.149)$$

Expansion (3.149) may be used to investigate the basic properties of (3.148). Since the $\mathcal{O}(\varepsilon)$ terms in G_* coincide with the accuracy of (3.148) (swapping \varkappa_- for \varkappa_+ in g_2 gives the same order correction in the downstream region $s_* > 0$), and also have the same order as the neglected $\mathcal{O}(\varepsilon^2)$ terms in the original expansion (3.59) for sublayer 5, the main focus should be made on the G_0 and G_1 terms for which equation (3.148) appears to be exact. Plugging (3.149) into (3.148) gives:

$$G_0(s_*) = \frac{3g_1}{2} \frac{s_*}{|s_*|^{\frac{1}{3}}}$$

$$G_1(s_*) = g_2 \int_{s_*}^{\infty} \frac{d^2 G_0(\xi)}{d\xi^2} \frac{d\xi}{(\xi - s_*)^{\frac{2}{3}}} = -\frac{g_1 g_2}{3} \int_{s_*}^{\infty} \frac{d\xi}{\xi |\xi|^{\frac{1}{3}} (\xi - s_*)^{\frac{2}{3}}}.$$

It means that G_0 simply stands for the outer pressure distribution generated in region 1 resulting in the singular pressure gradient

$$\frac{\partial P_*}{\partial s_*} = G(\pm s_*)^{-1/3}$$

in the inner triple deck variables, while G_1 provides the leading-order correction due to the interaction. However, evaluating the integral in the expression for G_1 yields

$$G_1(s_*) = -\frac{g_1 g_2}{s_*}, \quad s_* > 0;$$

for $s_* < 0$ the integral diverges, and G_1 is not defined.

The key to understanding this situation is to look at what happens to expansion (3.149) when $s_* \rightarrow 0^+$. Since $G_0 \sim s_*^{2/3}$ and $\sqrt{\varepsilon} G_1 \sim \frac{\sqrt{\varepsilon}}{s_*}$, the second term becomes of the same order as the first one when $s_* \sim \varepsilon^{3/10}$, making expression (3.149) invalid in the $\mathcal{O}(\varepsilon^{3/10})$ vicinity of $s_* = 0$. Therefore, another inner scale exists in the interaction region on which the asymptotic solution of equation (3.148) has to be reconsidered. If we denote the relevant inner variable as X , then

$$s_* = \varepsilon^{3/10} X, \quad |X| \sim 1;$$

recalling that the outer physical coordinate $s = \sigma s_*$, $\sigma = (\varepsilon \text{Re})^{-3/10} \ll 1$, we get:

$$s = \text{Re}^{-3/10} X.$$

Thus, the inner interaction scale in physical variables is determined only by the Reynolds number and does not depend on ε .

A simple estimate suggests that $G_* \sim G_0 \sim \varepsilon^{1/5}$ when $s_* \sim \varepsilon^{3/10}$. Introducing the scaled inner pressure distribution

$$A(X) = \varepsilon^{-1/5} G_*(s_*, \varepsilon)$$

and the corresponding inner pressure gradient

$$B(X) = \frac{dA(X)}{dX} \equiv \varepsilon^{1/10} \frac{dG_*}{ds_*} \sim 1,$$

equation (3.148) may be transformed to

$$B(X) - \frac{g_1}{|X|^{1/3}} = g_2 \int_X^\infty \frac{d^2 B(\xi)}{d\xi^2} \frac{d\xi}{(\xi - X)^{2/3}}. \quad (3.150)$$

This equation describes the interaction taking place in the innermost part of the triple deck (see Fig. 3.8).

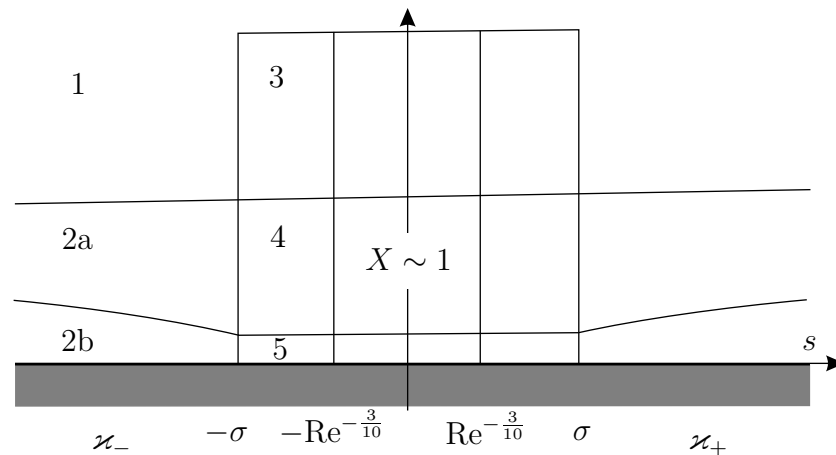


Figure 3.8: Viscous-inviscid interaction is taking place on the scale $X \sim 1$ ($s \sim \text{Re}^{-3/10}$) in the innermost part of the interaction region.

3.3.2 Analytical solution of the interaction equation

Equation (3.150) is solved using a Fourier transform with respect to X . The transform of $|X|^{-1/3}$ is given by

$$\left(|X|^{-1/3}\right)_\omega = \int_0^\infty \left[e^{i\omega X} + e^{-i\omega X}\right] \frac{dX}{X^{1/3}}.$$

Here the first integral converges when $2\pi n \leq \arg \omega \leq \pi + 2\pi n$, $n \in \mathbb{Z}$, and is equal to

$$\Gamma(2/3) \left[\frac{e^{\frac{i\pi}{2} + 2\pi in}}{\omega} \right]^{2/3},$$

while the second one converges when $2\pi n - \pi \leq \arg \omega \leq 2\pi n$, $n \in \mathbb{Z}$, and is reduced to

$$\Gamma(2/3) \left[\frac{e^{-\frac{i\pi}{2} + 2\pi in}}{\omega} \right]^{2/3}.$$

Therefore, the transform of $|X|^{-1/3}$ exists only for real ω ($\arg \omega = \pi k$, $k \in \mathbb{Z}$):

$$\left(|X|^{-1/3} \right)_\omega = \frac{\Gamma(2/3)}{|\omega|^{2/3}} \left[e^{\frac{i\pi}{3}} + e^{-\frac{i\pi}{3}} \right] = \frac{\Gamma(2/3)}{|\omega|^{2/3}}, \quad \omega \in \mathbb{R}.$$

This function, however, may be continued analytically to the complex plane when calculating the inverse Fourier transform.

The Fourier transform of the integral in the right-hand side of (3.150) exists for $2\pi n \leq \arg \omega \leq \pi + 2\pi n$, $n \in \mathbb{Z}$, and is equal to

$$-\omega^2 B_\omega \Gamma(1/3) \left[\frac{e^{\frac{i\pi}{2} + 2\pi in}}{\omega} \right]^{1/3},$$

where

$$B_\omega = \int_{-\infty}^{\infty} B(X) e^{-i\omega X} dX.$$

Combining these results together, we obtain the following solution for B_ω :

$$B_\omega = \frac{g_1 \Gamma(2/3)}{|\omega|^{2/3} \left[1 + g_2 \Gamma(1/3) |\omega|^{5/3} e^{\frac{i\pi}{6} \operatorname{sign} \omega} \right]}, \quad \omega \in \mathbb{R}. \quad (3.151)$$

In order to obtain the pressure gradient distribution $B(X)$, one needs to find the inverse transform of (3.151):

$$B(X) = \frac{1}{2\pi} \int_{-\infty}^{\infty} B_\omega e^{i\omega X} d\omega.$$

For the sake of convenience, we are going to apply the affine transform

$$X \longleftrightarrow (g_2 \Gamma(1/3))^{3/5} X, \quad \omega \longleftrightarrow \frac{\omega}{(g_2 \Gamma(1/3))^{3/5}},$$

which preserves $e^{i\omega X}$ and leaves only numerical coefficients in the integrand with respect to ω :

$$B(X) = \frac{g_1 \Gamma(2/3)}{2\pi (g_2 \Gamma(1/3))^{1/5}} \int_{-\infty}^{\infty} \frac{e^{i\omega X} d\omega}{|\omega|^{2/3} \left[1 + |\omega|^{5/3} e^{\frac{i\pi}{6} \operatorname{sign} \omega} \right]}. \quad (3.152)$$

This function asymptotically tends to

$$B_*(X) = \frac{g_1}{(g_2 \Gamma(1/3))^{1/5}} \frac{1}{|X|^{1/3}}$$

when $|X| \rightarrow \infty$, where $B_*(X)$ stands for the singular solution coming from region 1.

The inner variable X in (3.152) is related to s_* and s according to

$$s_* = \varepsilon^{3/10} (g_2 \Gamma(1/3))^{3/5} X, \quad s = \sigma s_* = \text{Re} e^{-3/10} (g_2 \Gamma(1/3))^{3/5} X; \quad (3.153)$$

this definition is going to be used henceforth. Note that parameter g_2 (defined in (3.147)) is a positive order-one quantity, and the $g_2 \Gamma(1/3)$ multiple has been introduced into (3.153) only to make the integral in (3.152) independent on any external parameters.

Solution (3.152) can be further simplified using analytical continuation of the integrand into the complex plane and applying Cauchy's theorem for contour integrals of analytical functions. This procedure is obviously different for positive and negative X due to the presence of $e^{i\omega X}$ in the integral. Let us consider these two cases separately.

1: $X > 0$. In this case the contour can be closed using an infinite arc in the upper half-plane. However, the non-analytical functions $|\omega|$ and $\text{sign } \omega$ require a branch-cut to be made from the origin through the upper half-plane (in this particular case), in order to separate different regular branches. On the left of the branch-cut $|\omega| = -\omega$, $\text{sign } \omega = -1$, while on the right $|\omega| = \omega$, $\text{sign } \omega = 1$, thus providing the required analytical continuation. It will be convenient to draw the branch-cut along the positive imaginary axis (see Fig. 3.9), and to consider two separate contours in the shape of a quarter of a circle.

The continuation of function $q(\omega) = 1 + |\omega|^{5/3} e^{\frac{i\pi}{6} \text{sign } \omega}$ has a single zero at $\omega = \omega_0 = i$. Indeed, when $0 \leq \arg \omega < \pi/2$, we have:

$$q(\omega) = 1 + \omega^{5/3} e^{\frac{i\pi}{6}}, \quad q(e^{\frac{i\pi}{2}-i0}) = 0;$$

on the other hand, if $\pi/2 < \arg \omega \leq \pi$,²⁰⁾ then

$$q(\omega) = 1 + (\omega e^{-i\pi})^{5/3} e^{-\frac{i\pi}{6}}, \quad q(e^{\frac{i\pi}{2}+i0}) = 0.$$

²⁰⁾ These values of the argument are chosen for convenience and imply that $|\omega| = \omega e^{-i\pi}$ on the left of the branch-cut.

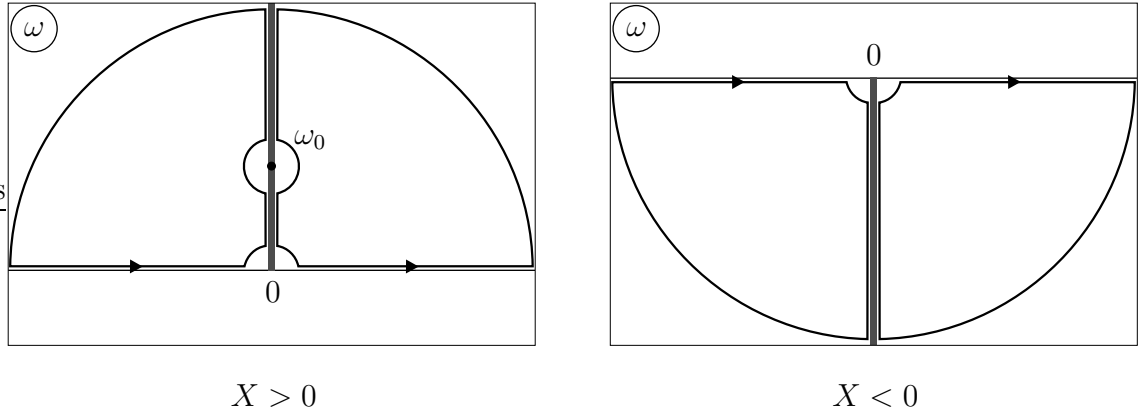


Figure 3.9: Integration contours in the plane of complex ω depending on the sign of X in the inverse Fourier transform.

The singular point ω_0 is a simple pole for the integrand in (3.152), because $\frac{dq(\omega)}{d\omega}\big|_{\omega=\omega_0} \neq 0$. Its presence on the imaginary axis suggests that both integrals along the sides of the branch-cuts will have infinitely-small arcs around ω_0 (see Fig. 3.9), contributing half a residue each. As the radius of the arcs tends to zero, the remaining integrals over the sides of the branch-cut become principle-value integrals, eventually leading to the following real solution for $B(X)$ when $X > 0$:

$$B(X) = \frac{g_1 \Gamma(2/3)}{(g_2 \Gamma(1/3))^{1/5}} \left[\frac{\sqrt{3}}{2\pi} \int_0^\infty \frac{e^{-tX} dt}{t^{2/3} [1 - t^{5/3}]} + \frac{3}{10} e^{-X} \right], \quad X > 0. \quad (3.154)$$

The separate exponential term is due to the residue in the simple pole ω_0 . According to (3.154),

$$B(0^+) = \frac{3g_1 \Gamma(2/3)}{10(g_2 \Gamma(1/3))^{1/5}} \left[1 + \sqrt{3 \left(1 + \frac{2}{\sqrt{5}} \right)} \right], \quad (3.155)$$

and $B(X)$ is finite on the right of $X = 0$.²¹⁾

2: $X < 0$. In this case the continuation is performed into the lower half-plane ($\Im(\omega) < 0$), which needs to have a branch-cut; it is convenient to draw the latter along the negative imaginary axis as shown in Fig. 3.9, and consider two separate contour in the shape of a quarter of a circle. As it is the case with the upper half-plane, $|\omega| = \omega$, $\text{sign } \omega = 1$ on the right of the branch-cut, and $|\omega| = -\omega$, $\text{sign } \omega = -1$ on the left, thus providing the required analytical continuations. Applying Cauchy's

²¹⁾ Recall that the original inviscid pressure gradient developed a singularity of $|s|^{-1/3}$ as $s \rightarrow 0$.

integral theorem to the contours in Fig. 3.9, (3.152) can be transformed to following real solution for $B(X)$ when $X < 0$:

$$B(X) = \frac{2\sqrt{3} g_1 \Gamma(2/3)}{\pi (g_2 \Gamma(1/3))^{1/5}} \int_0^\infty \frac{e^{tX} dt}{t^{2/3} [3 + (1 - 2t^{5/3})^2]}, \quad X < 0. \quad (3.156)$$

According to (3.156),

$$B(0^-) = \frac{\sqrt{3} g_1 \Gamma(2/3)}{10 (g_2 \Gamma(1/3))^{1/5}} \left[\frac{1}{\sin(\frac{\pi}{15})} + \frac{1}{\cos(\frac{\pi}{10})} \right]. \quad (3.157)$$

Since

$$\cos(\frac{\pi}{10}) = \frac{\sqrt{5 + \sqrt{5}}}{2\sqrt{2}}, \quad \sin(\frac{\pi}{15}) = \frac{1}{8} \left[\sqrt{2(5 + \sqrt{5})} - \sqrt{6(3 - \sqrt{5})} \right],$$

one can show from (3.157), (3.155) that $B(0^-) = B(0^+)$, i.e. the triple deck correction to the pressure gradient is continuous at $X = 0$.

Scaling solution (3.152) in such a way that the right-hand side does not depend on any external parameters and tends to $|X|^{-1/3}$ when $|X| \rightarrow \infty$, we get:

$$\hat{B}(X) = \frac{B(X)(g_2 \Gamma(1/3))^{1/5}}{g_1} = \frac{\Gamma(2/3)}{\pi} \int_0^\infty \left[\frac{\cos(\omega X) + \omega^{5/3} \cos(\omega X - \pi/6)}{1 + \sqrt{3} \omega^{5/3} + \omega^{10/3}} \right] \frac{d\omega}{\omega^{2/3}}.$$

This definition provides a *similarity criterion* for the pressure distribution. The scaled pressure gradient is plotted in Fig. 3.10, with the dashed lines corresponding to the scaled singular solution

$$\hat{B}_*(X) = \frac{B_*(X)(g_2 \Gamma(1/3))^{1/5}}{g_1} \equiv \frac{1}{|X|^{1/3}}$$

predicted by the classical boundary layer theory.

The triple deck solution for $B(X)$ is continuous thanks to the viscous-inviscid interaction taking place on the scale $|X| \sim 1$ ($|s| \sim \text{Re}^{-3/10}$). However, dB/dX appears to have a discontinuity at $X = 0$; the latter follows directly from (3.154) and (3.156). This higher-order discontinuity may be eliminated by introducing a further inner region where the flow is governed by the full Navier–Stokes equations. Also note that $\hat{B}(X)$ is positive for all X , so that the entire pressure gradient distribution is adverse when $G = +1$ and favorable when $G = -1$.

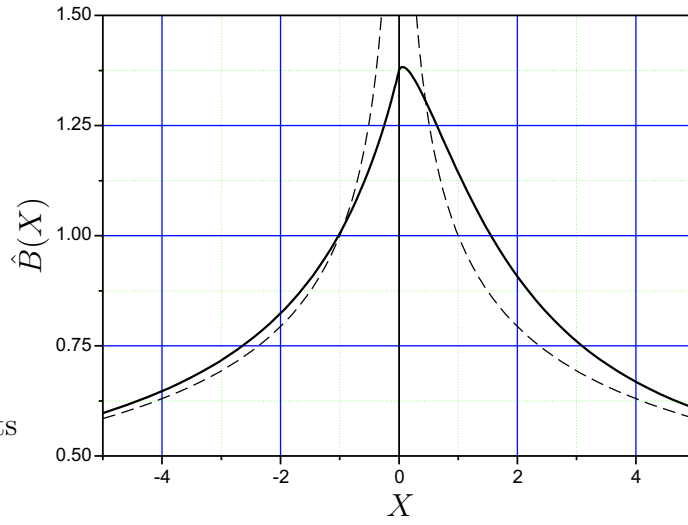


Figure 3.10: Pressure gradient distribution across the inner part of the interaction region (solid line). The dashed curves correspond to the singular pressure gradients predicted by the classical boundary layer theory.

With the known pressure distribution in the interaction region we can now obtain the functions $\varkappa(\omega)$ and $\theta(\omega)$ from the Fourier integral representation of the solution in region 5. Re-denoting the original functions \varkappa and θ from (3.104) as $\varkappa_\varepsilon(\omega)$ and $\theta_\varepsilon(\omega)$, we write the integral solution for dG_*/ds_* in the following way:

$$\frac{dG_*}{ds_*} = -\frac{a \Gamma(2/3)}{3\alpha_w^{2/3} \Gamma(1/3)} \int_0^\infty \frac{\varkappa_\varepsilon(\omega_*) \sin(\theta_\varepsilon(\omega_*) + \omega_* s_* - \pi/3)}{\omega_*^{2/3}} d\omega_*. \quad (3.158)$$

In order to relate this to the known solution (3.152) for $B(X)$, one has to perform the re-scaling:

$$s_* = \varepsilon^{3/10} (g_2 \Gamma(1/3))^{3/5} X, \quad \omega_* = \varepsilon^{-3/10} (g_2 \Gamma(1/3))^{-3/5} \omega.$$

Since by definition $B(X) = \varepsilon^{1/10} dG_*/ds_*$, the re-scaling of (3.158) yields:

$$B(X) = -\frac{a \Gamma(2/3)}{3\alpha_w^{2/3} \Gamma(1/3) (g_2 \Gamma(1/3))^{1/5}} \int_0^\infty \frac{\varkappa(\omega) \sin(\theta(\omega) + \omega X - \pi/3)}{\omega^{2/3}} d\omega, \quad (3.159)$$

where

$$\begin{aligned} \varkappa(\omega) &= \varkappa_\varepsilon \left(\varepsilon^{-3/10} (g_2 \Gamma(1/3))^{-3/5} \omega \right), \\ \theta(\omega) &= \theta_\varepsilon \left(\varepsilon^{-3/10} (g_2 \Gamma(1/3))^{-3/5} \omega \right) \end{aligned} \quad (3.160)$$

are the new re-scaled functions. The latter obviously retain the basic properties of the original functions \varkappa_ε and θ_ε :

$$\varkappa(-\omega) = \varkappa(\omega), \quad \theta(-\omega) = -\theta(\omega), \quad \omega \in \mathbb{R},$$

plus

$$\varkappa(0) = 1, \quad \theta(0) = 0.$$

The first two properties allow to rewrite (3.159) as

$$B(X) = \frac{a \Gamma(2/3)}{6\alpha_w^{2/3} \Gamma(1/3) (g_2 \Gamma(1/3))^{1/5}} \int_{-\infty}^{\infty} \frac{\varkappa(\omega) e^{i\theta(\omega) + i\omega X + \frac{i\pi}{6} \text{sign } \omega}}{|\omega|^{2/3}} d\omega.$$

Comparing this with (3.152) and recalling the definitions of a and g_1 (see (3.40), (3.147)), we get:

$$\varkappa(\omega) e^{i\theta(\omega)} = \frac{2}{\sqrt{3}} \frac{e^{-\frac{i\pi}{6} \text{sign } \omega}}{\left[1 + |\omega|^{5/3} e^{\frac{i\pi}{6} \text{sign } \omega}\right]}, \quad \omega \in \mathbb{R}. \quad (3.161)$$

It is clear from (3.161) that both $\varkappa(\omega)$ and $\theta(\omega)$ are not analytical functions, although they can be continued to the complex plane if necessary. Moreover, the limiting values of (3.161) are different when $\omega \rightarrow 0^+$ and $\omega \rightarrow 0^-$:

$$(\varkappa e^{i\theta})|_{\omega=0^+} = \frac{2 e^{-\frac{i\pi}{6}}}{\sqrt{3}}, \quad (\varkappa e^{i\theta})|_{\omega=0^-} = \frac{2 e^{\frac{i\pi}{6}}}{\sqrt{3}}. \quad (3.162)$$

The value of $\varkappa e^{i\theta}$ at $\omega = 0$ should be interpolated as an average of the above limiting values on the left and on the right of the discontinuity:

$$\varkappa(0) e^{i\theta(0)} = \frac{(\varkappa e^{i\theta})|_{\omega=0^-} + (\varkappa e^{i\theta})|_{\omega=0^+}}{2} = 1,$$

yielding $\varkappa(0) = 1$ and $\theta(0) = 0$, as required. This property follows from a well-known result for the values of a Fourier integral at its points of discontinuity, and from the fact that $\varkappa(\omega) e^{i\theta(\omega)}$ is actually expressed via a Fourier transform of the known function $B(X)$. To illustrate the property, it is helpful to plot $\varkappa \sin \theta$ versus $\varkappa \cos \theta$ as ω runs from $-\infty$ to ∞ , $\omega \in \mathbb{R}$ (see Fig. 3.11). Both parts of the plot are symmetric with respect to the real axis, resulting in the real solution for $B(X)$. The curves leave the origin when $\omega \rightarrow \pm\infty$ tangent to the lines with the direction vectors $e^{\mp \frac{i\pi}{3}}$, and enter the points $\frac{2}{\sqrt{3}} e^{\mp \frac{i\pi}{6}}$ when $\omega \rightarrow 0^\pm$.

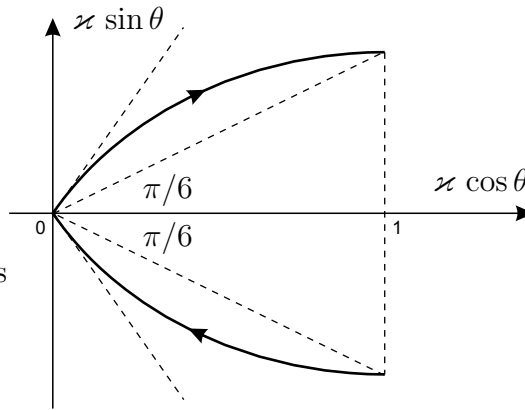


Figure 3.11: Real and imaginary parts of the complex function $K_\omega = \varkappa(\omega) e^{i\theta(\omega)}$ plotted for all real values of ω .

Since functions $\varkappa(\omega)$ and $\theta(\omega)$ are known, one could reconstruct the stream function in region 5 using (3.101).²²⁾ The ultimate goal, however, is to obtain the skin friction distribution throughout the interaction region, demonstrating how the boundary layer separation develops.

3.3.3 Skin friction distribution in the interaction region

The skin friction distribution is given by

$$t_w(s_*) = \mu_w \left. \frac{\partial U}{\partial Y} \right|_{Y=0} \equiv \frac{\mu_w}{R_w} \left. \frac{\partial^2 \psi_*}{\partial Y_*^2} \right|_{Y_*=0},$$

where s_* , Y_* are the local coordinates in region 5, and ψ_* is the relevant stream function. The latter can be represented in terms of an expansion based on ε (see (3.59)):

$$\psi_* = \psi_*^{(0)}(s_*, Y_*) + \varepsilon \psi_*^{(1)}(s_*, Y_*) + \dots$$

Since by definition

$$\left. \frac{\partial^2 \psi_*^{(0)}}{\partial Y_*^2} \right|_{Y_*=0} = \tau_w,$$

with τ_w being proportional to the known skin friction of an unperturbed flow, we get:

$$t_w(s_*) = \frac{\mu_w}{R_w} \left[\tau_w + \varepsilon \left. \frac{\partial^2 \psi_*^{(1)}}{\partial Y_*^2} \right|_{Y_*=0} + \mathcal{O}(\varepsilon^2) \right]. \quad (3.163)$$

²²⁾ Note that according to re-definitions of \varkappa and θ in (3.160) function K_ω from (3.101) is now equal to $\varkappa_\varepsilon(\omega) e^{i\theta_\varepsilon(\omega)}$.

In section 3.2.2 we introduced the function $\Phi(s_*, Y_*)$ directly related to the $\psi_*^{(1)}$ term in (3.163):

$$\frac{\partial^2 \psi_*^{(1)}}{\partial Y_*^2} = \Phi + \tilde{a} \ln Y_* + \tilde{c}, \quad (3.164)$$

where

$$\tilde{a} = 3a, \quad \tilde{c} = \frac{9a}{2} + 2c, \quad c = \frac{a}{2} \ln \sigma + (b + a_1).$$

Constant a is given in (3.40), a_1 is defined in (3.44), and b is a free controlling parameter which comes from the global solution and affects the structure of the pre-separated boundary layer. The dependence of $\partial^2 \psi_*^{(1)} / \partial Y_*^2$ on X (or s_*) is due to $\Phi(s_*, Y_*)$ only. The latter can be represented by Fourier integral (3.90) based on the Airy function. A formal differentiation of (3.90) with respect to Y_* , along with (3.93), yields:

$$\begin{aligned} \frac{\partial \Phi}{\partial Y_*} = & \frac{3a}{2\text{Ai}(0) Y_*} \left[\int_{0^-}^{-\infty} \text{Ai}(\lambda(\omega) Y_*) \frac{d}{d\omega} [K_\omega e^{i\omega s_*}] d\omega + \right. \\ & \left. + \int_{0^+}^{\infty} \text{Ai}(\lambda(\omega) Y_*) \frac{d}{d\omega} [K_\omega e^{i\omega s_*}] d\omega \right]. \end{aligned} \quad (3.165)$$

Here $\lambda(\omega) = \left(\frac{i\omega \tau_w}{\mu_w} \right)^{\frac{1}{3}}$, $K_\omega = \varkappa_\varepsilon(\omega) e^{i\theta_\varepsilon(\omega)}$, with $\varkappa_\varepsilon(\omega)$ and $\theta_\varepsilon(\omega)$ being related to the known functions $\varkappa(\omega)$ and $\theta(\omega)$ via (3.160), and the lower limits restrict the integration domains to the regions where K_ω is continuous. It can be easily shown that these integrals converge even in the case $Y_* = 0$ when the Airy function becomes a constant, while the original integral (3.90) diverges in the same limit. Our aim is to find the skin-friction distribution, and in order to do this we have to make a correction to (3.90) using (3.165), so that Φ may be evaluated at $Y_* = 0$.

Since $\Phi \sim Y_*^{-3}$ when $Y_* \rightarrow \infty$ (see (3.83)), expression (3.165) can be integrated with respect to Y_* from infinity, thus giving:

$$\Phi(s_*, Y_*) = \int_{\infty}^{Y_*} \frac{\partial \Phi(s_*, t)}{\partial t} dt.$$

Plugging (3.165) for $\partial \Phi / \partial t$, and swapping the integration order, we get:

$$\begin{aligned} \Phi(s_*, Y_*) = & \frac{3a}{2\text{Ai}(0)} \left[\int_{0^-}^{-\infty} \left(\int_{\infty}^{Y_*} \frac{\text{Ai}(\lambda(\omega)t)}{t} dt \right) \frac{d}{d\omega} [K_\omega e^{i\omega s_*}] d\omega + \right. \\ & \left. + \int_{0^+}^{\infty} \left(\int_{\infty}^{Y_*} \frac{\text{Ai}(\lambda(\omega)t)}{t} dt \right) \frac{d}{d\omega} [K_\omega e^{i\omega s_*}] d\omega \right]. \end{aligned}$$

If one integrates this by parts with respect to ω and uses the known limiting values of $\varkappa(\omega)$ and $\theta(\omega)$ when $\omega \rightarrow 0^\pm$ (see (3.162)), it will ultimately lead to a cancellation of the integration with respect to t , so that Φ may be expressed as follows:

$$\Phi(s_*, Y_*) = \frac{a}{2\text{Ai}(0)} \int_{-\infty}^{\infty} \left[\frac{2}{\sqrt{3}} e^{-\frac{i\pi}{6} \text{sign } \omega} - K_\omega e^{i\omega s_*} \right] \frac{\text{Ai}(\lambda(\omega)Y_*) d\omega}{|\omega|}. \quad (3.166)$$

The principal-value integral over $\omega \in \mathbb{R}$ excludes the singular point $\omega = 0$; its two fragments (for negative and positive ω) converge at $\omega = 0$ independently because

$$K_\omega e^{i\omega s_*} \equiv \varkappa_\varepsilon(\omega) e^{i\theta_\varepsilon(\omega) + i\omega s_*} = \frac{2}{\sqrt{3}} e^{-\frac{i\pi}{6} \text{sign } \omega} [1 + \mathcal{O}(\omega)], \quad |\omega| \rightarrow 0.$$

Note that changing ω to $-\omega$ in the integrand in (3.166) is equivalent to taking complex-conjugate of it (recall that $\lambda(\omega) = |\lambda(\omega)| e^{\frac{i\pi}{6} \text{sign } \omega}$, $\omega \in \mathbb{R}$). Therefore,

$$\Phi(s_*, Y_*) = \frac{a}{\text{Ai}(0)} \Re \left\{ \int_{0^+}^{\infty} \left[\frac{2}{\sqrt{3}} e^{-\frac{i\pi}{6}} - K_\omega e^{i\omega s_*} \right] \frac{\text{Ai}(\lambda(\omega)Y_*) d\omega}{\omega} \right\}. \quad (3.167)$$

This form allows to study the asymptotic behaviour of Φ when $Y_* \rightarrow 0$, ultimately leading to the required expression for the skin friction.

Although the integral in (3.167) does converge at 0^+ regardless of the Airy function, the latter becomes crucial for the convergence of the first term at infinity, and we cannot just set $Y_* = 0$ in the expression. For any fixed $\omega_0 \in (0, \infty)$ the integral may be split into two fragments with different types of convergence:

$$J_1 = \int_{0^+}^{\omega_0} \left[\frac{2}{\sqrt{3}} e^{-\frac{i\pi}{6}} - K_\omega e^{i\omega s_*} \right] \frac{\text{Ai}(\lambda(\omega)Y_*) d\omega}{\omega},$$

$$J_2 = \int_{\omega_0}^{\infty} \left[\frac{2}{\sqrt{3}} e^{-\frac{i\pi}{6}} - K_\omega e^{i\omega s_*} \right] \frac{\text{Ai}(\lambda(\omega)Y_*) d\omega}{\omega}.$$

The first of them has a simple asymptotic form when $Y_* \rightarrow 0$:

$$J_1 = \text{Ai}(0) \int_{0^+}^{\omega_0} \left[\frac{2}{\sqrt{3}} e^{-\frac{i\pi}{6}} - K_\omega e^{i\omega s_*} \right] \frac{d\omega}{\omega} + \mathcal{O}(Y_*).$$

However, the second integral is more subtle and requires a sequence of transformations to be performed in order to obtain that

$$J_2 = -\text{Ai}(0) \int_{\omega_0}^{\infty} \frac{K_\omega e^{i\omega s_*} d\omega}{\omega} - 2\sqrt{3} \left[\text{Ai}(0) e^{-\frac{i\pi}{6}} \ln(Y_* \omega_0^{1/3}) + \Lambda \int_0^\infty \ln t \text{Ai}'(\Lambda t e^{\frac{i\pi}{6}}) dt \right] + \mathcal{O}(Y_*), \quad Y_* \rightarrow 0,$$

where

$$\Lambda = \left(\frac{\tau_w}{\mu_w} \right)^{\frac{1}{3}}, \quad \text{Ai}'(z) = \frac{d\text{Ai}(z)}{dz}.$$

Combining the above results, we get:

$$\begin{aligned} \lim_{Y_* \rightarrow 0} \{ \Phi(s_*, Y_*) + 3a \ln Y_* \} &= -3a \ln(\omega_0^{1/3}) - \\ &- a \Re \left\{ \int_0^{\omega_0} \left[K_\omega e^{i\omega s_*} - \frac{2}{\sqrt{3}} e^{-\frac{i\pi}{6}} \right] \frac{d\omega}{\omega} + \int_{\omega_0}^{\infty} \frac{K_\omega e^{i\omega s_*} d\omega}{\omega} \right\} - \\ &- \frac{2a\Lambda\sqrt{3}}{\text{Ai}(0)} \Re \left\{ \int_0^{\infty} \ln t \text{Ai}'(\Lambda t e^{\frac{i\pi}{6}}) dt \right\}. \end{aligned} \quad (3.168)$$

The right-hand side of (3.168) is independent on the choice of ω_0 (this may simply be checked by differentiation), and so we are going to consider the limit $\omega_0 \rightarrow 0^+$. Due to Cauchy's integral theorem,

$$J = \int_0^{\infty} \ln t \text{Ai}'(\Lambda t e^{\frac{i\pi}{6}}) dt = \frac{1}{\Lambda e^{\frac{i\pi}{6}}} \left[\int_0^{\infty} \ln t \text{Ai}'(t) dt + \text{Ai}(0) \ln(\Lambda t e^{\frac{i\pi}{6}}) \right],$$

providing that $\ln z = \ln |z| + i \arg z$, i.e. the main branch of the logarithmic function is used. Since

$$\int_0^{\infty} \ln t \text{Ai}'(t) dt = \frac{\text{Ai}(0)}{6} \left[\frac{\pi}{\sqrt{3}} + 4\gamma_e - \ln 3 \right],$$

where

$$\gamma_e = - \int_0^{\infty} \ln t e^{-t} dt \approx 0.56$$

is Euler's constant, we have:

$$\Re\{J\} = \frac{\text{Ai}(0)}{2\sqrt{3}\Lambda} \left[\frac{\pi}{\sqrt{3}} + 2\gamma_e + \frac{3}{2} \ln 3 + \ln \alpha_w \right], \quad \alpha_w = \frac{\tau_w}{9\mu_w}.$$

As for the two integrals in (3.168) containing K_ω , they yield the following asymptotic form when $\omega_0 \rightarrow 0^+$:

$$\begin{aligned} \int_0^{\omega_0} \left[K_\omega e^{i\omega s_*} - \frac{2}{\sqrt{3}} e^{-\frac{i\pi}{6}} \right] \frac{d\omega}{\omega} &= \mathcal{O}(\omega_0), \\ \int_{\omega_0}^{\infty} \frac{K_\omega e^{i\omega s_*} d\omega}{\omega} &= -\frac{2e^{-\frac{i\pi}{6}}}{\sqrt{3}} \ln \omega_0 (1 + \mathcal{O}(\omega_0)) - \int_{0^+}^{\infty} \ln \omega \frac{d}{d\omega} [K_\omega e^{i\omega s_*}] d\omega. \end{aligned}$$

Plugging the above results into (3.168) gives the required asymptotic behaviour of $\Phi(s_*, Y_*)$ when $Y_* \rightarrow 0$:

$$\begin{aligned} \lim_{Y_* \rightarrow 0} \{ \Phi(s_*, Y_*) + 3a \ln Y_* \} &= a \int_{0^+}^{\infty} \ln \omega \frac{d}{d\omega} \left[\varkappa_\varepsilon(\omega) \cos(\theta_\varepsilon(\omega) + \omega s_*) \right] d\omega - \\ &- a \left[\frac{\pi}{\sqrt{3}} + 2\gamma_e + \frac{3}{2} \ln 3 + \ln \alpha_w \right]. \end{aligned}$$

It remains to substitute this into (3.164) to obtain the order- ε correction to the skin friction distribution:

$$\begin{aligned} \left. \frac{\partial^2 \psi_*^{(1)}}{\partial Y_*^2} \right|_{Y_*=0} &= a \left[\frac{9}{2} - \frac{\pi}{\sqrt{3}} - 2\gamma_e - \frac{3}{2} \ln 3 - \ln \alpha_w \right] + a \ln \sigma + 2(b + a_1) + \\ &+ a \int_{0^+}^{\infty} \ln \omega_* \frac{d}{d\omega_*} \left[\varkappa_\varepsilon(\omega_*) \cos(\theta_\varepsilon(\omega_*) + \omega_* s_*) \right] d\omega_*, \quad \sigma = (\varepsilon \operatorname{Re})^{-\frac{3}{10}}. \end{aligned}$$

If we apply the transformation

$$s_* = \varepsilon^{3/10} (g_2 \Gamma(1/3))^{3/5} X, \quad \omega_* = \varepsilon^{-3/10} (g_2 \Gamma(1/3))^{-3/5} \omega$$

to the integrand in the above expression, functions $\varkappa_\varepsilon(\omega_*)$, $\theta_\varepsilon(\omega_*)$ will be converted into $\varkappa(\omega)$, $\theta(\omega)$, and a $\ln \varepsilon$ term will be produced. Remarkably, the latter happens to cancel the $\ln \varepsilon$ term contained in $\ln \sigma$, eventually leading to the following skin friction distribution throughout the innermost part of the interaction region ($|X| \sim 1$):

$$\begin{aligned} t_w(X) &= \frac{\mu_w \tau_w}{R_w} + \\ &+ \varepsilon \frac{\mu_w a}{R_w} \left[-\frac{3}{10} \ln \operatorname{Re} + q + \int_{0^+}^{\infty} \ln \omega \frac{d}{d\omega} \left(\varkappa(\omega) \cos(\theta(\omega) + \omega X) \right) d\omega \right] + \quad (3.169) \\ &+ \mathcal{O}(\varepsilon^2), \end{aligned}$$

where

$$q = \frac{2(b + a_1)}{a} + \frac{9}{2} - \frac{\pi}{\sqrt{3}} - 2\gamma_e + \frac{3}{5} \ln(g_2 \Gamma(1/3)) - \frac{3}{2} \ln 3 - \ln \alpha_w = \mathcal{O}(1),$$

$\varkappa(\omega)$, $\theta(\omega)$ are given by (3.161), and the main parameter a is defined in (3.40).²³⁾

From (3.169) it can easily be spotted that the first three terms are constants which provide a background for the function of X described by the Fourier integral

$$J(X) = \int_{0^+}^{\infty} \ln \omega \frac{d}{d\omega} \left[\varkappa(\omega) \cos(\theta(\omega) + \omega X) \right] d\omega. \quad (3.170)$$

This function, plotted in Fig. 3.12 along with its derivative

$$J'(X) = \int_{0^+}^{\infty} \varkappa(\omega) \sin(\theta(\omega) + \omega X) d\omega,$$

²³⁾ Parameters a_1 and b are less important since they only appear as additive constants to the Fourier integral in (3.169), while parameter a multiplies the integral.

does not depend on any parameters of the flow. It has a unique minimum when $X = X_* \approx 0.6$, and is equivalent to $\ln |X|$ when $|X| \rightarrow \infty$; the latter enables matching with solution (3.42) in the upstream sublayer 2b, and also provides an additional boundary condition for the downstream sublayer. Note that $J''(X)$ develops a discontinuity at $X = 0$, revealing the limitations of the classical triple deck model. To resolve the singularity in $J''(X)$, one normally needs to consider a further inner region where the flow is described by the full Navier–Stokes equations. However, these further corrections to the triple deck theory are clearly beyond the scope of the current study which was aimed to provide a smooth solution for the pressure gradient and skin friction in the vicinity of the curvature break.

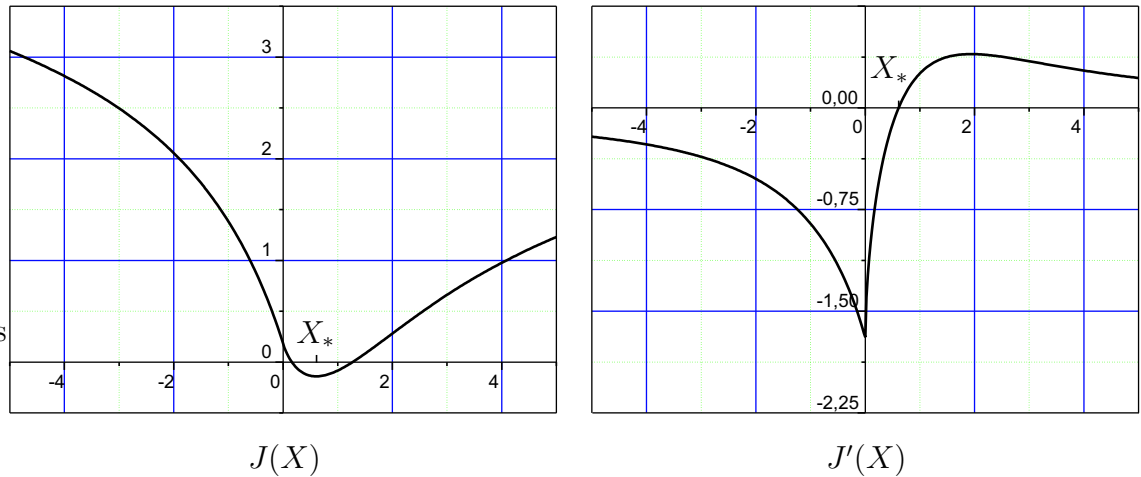


Figure 3.12: Function $J(X)$ describing the skin friction distribution across the innermost part of the interaction region, left, and its first derivative, right.

The shape of $J(X)$ with the distinct minimum suggests there is a possibility for a confined area with negative skin friction to exist, indicating the presence of a small *recirculation zone* around the break in wall curvature usually referred to as a *separation bubble* (see Fig. 3.13). If the upstream pressure gradient is adverse, i.e. $G = +1$ and consequently $a > 0$, then the first two terms in (3.169) may cancel each other in the leading order:

$$\tau_w - \frac{3}{10} \varepsilon a \ln \text{Re} = \mathcal{O}(\varepsilon). \quad (3.171)$$

In this case the boundary layer enters the interaction region in a pre-separated state,

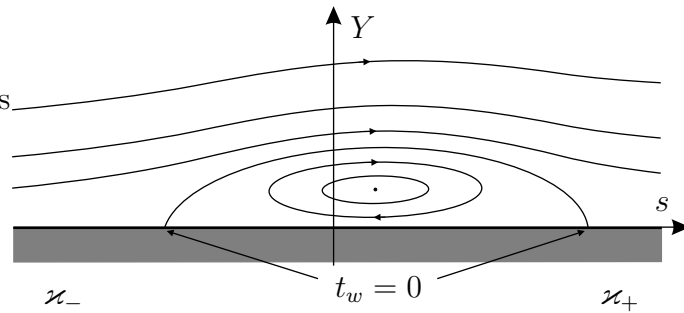


Figure 3.13: A typical confined recirculation zone (separation bubble) formed due to an adverse pressure gradient.

and negative skin friction can occur in the order- ε approximation in (3.169). The estimate (3.171) is equivalent to the following asymptotic expansion of ε based on negative integer powers of $\ln \text{Re}$:

$$\varepsilon(\text{Re}) = \frac{k_0}{\ln \text{Re}} \left[1 + \frac{k_1}{\ln \text{Re}} + \dots \right], \quad k_0 = \frac{10 \Gamma(2/3) \tau_w^2}{9 \alpha_w^{2/3} R_w}, \quad (3.172)$$

with k_1 being a controlling parameter which affects the size of the separation bubble. However, one should bear in mind that all of the above solutions, including the skin friction distribution (3.169), were obtained in the assumption that $\varepsilon \ll \frac{1}{\ln \text{Re}}$ needed for the expansion (3.36) in region 5 to be valid. Therefore, (3.169) does not hold when ε is estimated according to (3.172), and the very onset of the separation needs to be explained by a different theory.

It is worth mentioning that the case of $\varepsilon \sim \frac{1}{\ln \text{Re}}$ was studied numerically by Buldakov & Ruban (2002) who discovered a local recirculation zone (confined in the interaction region) formed due to the singular pressure gradient $\partial p / \partial s = \varepsilon (-s)^{-1/3}$. The relevant theory of the incipient separation caused by this pressure gradient is yet to be developed.

Chapter 4

Conclusions

Looking back on a century long development in the asymptotic theory of separated flows, it is clear that, despite a very good progress, certain problems remain unresolved. In particular, very little is still known about the nature of separation at transonic speeds, and the present work was aimed to address one of the important questions in this area. It was previously demonstrated by Messiter & Hu (1975) that a discontinuity in wall curvature is not capable of causing boundary layer separation both at subsonic and supersonic speeds. However, one might expect a different behaviour at transonic speeds. The main goal of this work, therefore, was to investigate whether boundary layer separation takes place due to a curvature break when the flow around it is transonic.

Firstly, guided by the well-known hierarchical structure of Prandtl's classical boundary layer theory, we considered an inviscid transonic flow in the vicinity of a curvature break assuming the separation is local (Chapter 2). This study revealed a complicated physical picture of the flow depending on the ratio of the curvatures. In particular, we discovered a certain type of supersonic flows which decelerate to subsonic speeds without a shock wave, transonic Prandtl–Meyer flow and supersonic flows with a weak shock. It was also shown that extending the flow beyond the *limiting characteristic* is both the necessary and the sufficient condition of a shock formation. As a consequence, a fundamental link between the local and the global flow patterns is observed in our problem. Eventually, from an asymptotic analysis of

the Karman–Guderley equation it was demonstrated that the curvature discontinuity leads to the singular pressure gradients $\partial p/\partial s \sim G_{\mp} (\mp s)^{-1/3}$ upstream and downstream of the break point respectively. In order to find the amplitude coefficients G_{\mp} , we performed computations and employed the *hodograph method* along with the so-called *phase portrait* of the flow.

With the known pressure distribution generated by the inviscid flow near the curvature break, we turned the focus on analyzing how this distribution affects the boundary layer (Chapter 3). It was discovered that the singular pressure gradient proportional to $(-s)^{-1/3}$ evokes a kind of a ‘resonance’ in the boundary layer upstream of the singularity, significantly changing its displacement effect as compared to other known cases. The relevant solution for the viscous sublayer, a region at the bottom of the boundary layer mostly affected by the outer pressure distribution, appears to exist only for a favourable pressure gradient upstream, i.e. for the case of $G_- < 0$, and becomes complex when G_- changes sign to positive.

This information suggested that the adverse pressure gradient actually causes separation well ahead of the curvature discontinuity. However, since there should always be a smooth transition between different physical regimes, we expected the real solution to exist at least for small positive values of G_- when the curvature break is also small. This allowed to develop an asymptotic theory of the *incipient viscous-inviscid interaction* in our particular problem. Our analysis of the interaction between the boundary layer and the inviscid transonic flow which takes place near the weak curvature break lead to a typical three-tier structure of the flow (triple deck). It appeared to be possible to construct analytical solutions in all the tiers of the triple deck when

$$\text{Re}^{-1/6} \ll |G_-| \ll \frac{1}{\ln \text{Re}},$$

where Re is the flow’s Reynolds number, assumed to be large. As a result, the *interaction equation*, describing how the pressure perturbations are converted into the displacement and vice versa, was derived in a closed form. Remarkably, in this case the displacement was found to be generated mainly in the overlapping region between the viscous sublayer and the main inviscid part of the boundary layer. At

the same time the flow in all three tiers of the triple deck has predominantly subsonic features, and the transonic nature of the viscous-inviscid interaction is largely due to the cumulative effects in the boundary layer upstream of the singularity. As it was the case in the work by Ruban & Turkyilmaz (2000), the structure of the boundary layer ahead of the interaction region is largely affected by the singular pressure gradient generated in the inviscid transonic flow. Consequently, the background on which the interaction develops appears to be different.

The analytical solution of the interaction equation revealed a local minimum in the skin friction distribution near the curvature break, indicating that a *local recirculation zone* (also called a *separation bubble*) may develop for stronger discontinuities in wall curvature. In fact, the recirculation zone is formed when the ratio of the curvatures is estimated as

$$\frac{\varkappa_+}{\varkappa_-} = 1 - \frac{\hat{k}_0}{\ln \text{Re}} + \frac{\hat{k}_1}{(\ln \text{Re})^2} + \dots,$$

where \hat{k}_0 is a fixed positive order one quantity depending on certain physical parameters of the flow, and \hat{k}_1 is an order one *controlling parameter* which affects the size of the separation bubble.¹⁾ These results suggest that boundary layer separation does take place due to a curvature break at transonic speeds. Nevertheless, the relevant theory of the incipient separation caused by the pressure gradient

$$\frac{\partial p}{\partial s} \sim \frac{1}{\ln \text{Re}} (-s)^{-1/3}$$

is yet to be developed.

Our theoretical prediction may be helpful in improving aerodynamic characteristics of airplanes by suggesting to avoid curvature breaks on the aerodynamic surfaces. The study also leaves few open questions.

First of all, both the incipient and the large-scale separation still need to be studied theoretically. The incipient separation is characterized by a transition between two different asymptotic solutions for the boundary layer upstream of the singularity, posing certain difficulties for a correct mathematical description of the flow in the viscous sublayer. The large-scale separation implies introducing a free streamline

¹⁾ Parameters \hat{k}_0 , \hat{k}_1 are related to the constants k_0 and k_1 from expansion (3.172).

into the model of the inviscid transonic flow, and is likely to involve solving nonlinear equations in at least two tiers of the triple deck numerically. The free streamline scenario would explain why the boundary layer equations yield complex solutions in the case of strong adverse pressure gradients upstream of the singularity (section 3.1.2).

It may also be possible to obtain some analytical solutions for the second special case leading to a small upstream pressure gradient (section 3.1.3). However, this would require to deal with a complicated inviscid flow pattern including the limiting characteristic and a weak shock, and solution of the interaction problem is likely to rely on the success of numerical methods. Since this particular inviscid flow regime is close to the transonic Prandtl–Meyer flow, we expect a *finite distance singularity* to develop in this case (Ruban et al. 2006).

Finally, it might be worth considering the effect of small displacements of the sonic point with respect to a curvature break on the separation phenomenon. The shift is going to create local subsonic/supersonic zones surrounding the curvature discontinuity; this is likely to diminish the size of the separation bubble since no separation should exist due to a curvature break at essentially subsonic or supersonic speeds (Messiter & Hu 1975). It might be possible to establish a criterion for the degree of the sonic point shift required to completely suppress the bubble formation in the incipient separation regime.

Bibliography

- Abramovitz, M. & Stegun, I. A. (1972). *Handbook Of Mathematical Functions With Formulas, Graphs, And Mathematical Tables*, 9 edn, Wiley-Interscience.
- Ackerberg, R. C. (1970). Boundary layer separation at a free streamline. part i. two-dimensional flow, *J. Fluid Mech.* **44**(2): 211–225.
- Bodonyi, R. J. & Kluwick, A. (1977). Freely interacting transonic boundary layers., *Phys. Fluids* **20**: 1432–1437.
- Bodonyi, R. J. & Kluwick, A. (1998). Transonic trailing-edge flow., *Q. J. Mech. Appl. Maths* **51**: 297–310.
- Buldakov, E. V. & Ruban, A. I. (2002). On transonic viscous-inviscid interaction., *J. Fluid Mech.* **470**: 291–317.
- Chaplygin, S. (1902). Gas Jets, *Scientific Memoirs, Moscow University* .
- Cole, J. D. & Cook, L. P. (1986). *Transonic Aerodynamics*, Elsevier Science Publishers B.V.
- Frankl, F. I. (1947). Studies in the theory of infinite aspect ratio wing moving with the speed of sound., *Dokl. Akad. Nauk SSSR* **57**(7): 1561–1564.
- Goldstein, S. (1930). Concerning some solutions of the boundary layer equations in hydrodynamics, *Mathematical Proceedings of the Cambridge Philosophical Society*, Vol. 26.
- Goldstein, S. (1948). On laminar boundary-layer flow near a position of separation., *Q. J. Mech. Appl. Math.* **1**(1): 43–69.

- Guderley, G. (1957). *Theorie Schallnahe Stromungen.*, Springer-Verlag Berlin. English translation: Addison-Wesley 1962.
- Landau, L. D. & Lifshitz, E. M. (1944). *Mechanics of Continuous Media*, Gostekhizdat, Moscow.
- Landau, L. D. & Lifshitz, E. M. (1959). *Fluid Mechanics.*, Pergamon Press.
- Liepmann, H. W. & Roshko, A. (1957). *Elements of Gasdynamics.*, John Wiley & sons, New York.
- Messiter, A. F. (1970). Boundary layer flow near the trailing edge of a flat plate., *SIAM J. Appl. Math.* **18**(1): 241–257.
- Messiter, A. F. & Hu, J. J. (1975). Laminar boundary layer at a discontinuity in wall curvature., *Q. Appl. Math.* **33**(3): 175–181.
- Neiland, V. Y. (1969). Theory of laminar boundary layer separation in supersonic flow., *Mekh. Zhid. Gaza.* **4**: 53–57.
- Neiland, V. Y. (1974). *Asymptotic problems in the theory of viscous supersonic flows.*, Tr. TsAGI.
- Prandtl, L. (1904). Uber flussigkeitbewegung bei sehr kleiner reibung., *Verh. III Intern. Math. Kongr., Heidelberg, 1904* .
- Ruban, A. I. (1974). On laminar separation at a corner point on a solid surface., *Uch. zap. TsAGI* **5**(2): 44–54.
- Ruban, A. I. & Turkyilmaz, I. (2000). On laminar separation at a corner point in transonic flow., *J. Fluid Mech.* **423**: 345–380.
- Ruban, A. I., Wu, X. & Pereira, R. M. S. (2006). Viscous-inviscid interaction in transonic prandtl-meyer flow., *J. Fluid Mech.* **568**: 387–424.
- Smith, F. T. (1973). Laminar flow over a small hump on a flat plate., *J. Fluid Mech.* **57**(4): 803–824.

- Stewartson, K. (1969). On the flow near the trailing edge of a flat plate., *Mathematika* **16**(1): 106–121.
- Stewartson, K. (1970). On laminar boundary layers near corners., *Q. J. Mech. Appl. Math.* **23**(2): 137–152.
- Stewartson, K. & Williams, P. G. (1969). Self-induced separation., *Proc. Roy. Soc.* **312**: 181–206.
- Sychev, V. V. (1972). Laminar separation., *Mekh. Zhid. Gaza* **3**: 47–59.
- Sychev, V. V., Ruban, A. I., Sychev, V. V. & Korolev, G. L. (1998). *Asymptotic Theory Of Separated Flows*, Cambridge University Press.

Appendix

Navier–Stokes Equations in The Curvilinear Coordinates

The general vector form of the steady Navier–Stokes equations for the scaled parameters of a compressible Newtonian fluid reads:

$$\begin{aligned}\operatorname{div}(\rho \mathbf{v}) &= 0, \\ \rho(\mathbf{v}\nabla)\mathbf{v} &= -\nabla p + \frac{1}{\operatorname{Re}} \left[2\operatorname{Div}(\mu \mathbb{D}) - \frac{2}{3} \nabla(\mu \operatorname{div} \mathbf{v}) \right], \\ \rho(\mathbf{v}\nabla)h &= (\mathbf{v}\nabla)p + \frac{1}{\operatorname{Re}} \left[2\mu \mathbb{D}^2 - \frac{2}{3} \mu(\operatorname{div} \mathbf{v})^2 + \frac{1}{\operatorname{Pr}} \operatorname{div}(\mu \nabla h) \right].\end{aligned}$$

Here \mathbf{v} stands for the velocity vector, ρ for density, p for pressure, μ for dynamic viscosity, h for enthalpy, Re for Reynolds number, Pr for Prandtl number, and \mathbb{D} is the rate-of-strain tensor:

$$\mathbb{D} = \left\| \begin{array}{cc} D_{11} & D_{12} \\ D_{21} & D_{22} \end{array} \right\| = \left\| \begin{array}{cc} \frac{\partial u}{\partial x} & \frac{1}{2} \left(\frac{\partial u}{\partial y} + \frac{\partial v}{\partial x} \right) \\ \frac{1}{2} \left(\frac{\partial v}{\partial x} + \frac{\partial u}{\partial y} \right) & \frac{\partial v}{\partial y} \end{array} \right\|,$$

with x, y being the Cartesian coordinates and u, v – the relevant velocity components.¹⁾ Finally,

$$\mathbb{D}^2 = D_{11}^2 + D_{22}^2 + 2D_{12}^2,$$

and Div denotes the divergence of a tensor. The above system needs to be closed by specifying the function $\mu(h)$, as well as the equation of state.

¹⁾ We restrict our attention to the two-dimensional case for the sake of simplicity.

In our analysis of the boundary layer and the interaction region (Chapter 3) the curvilinear coordinates (s, r) related to the surface of a rigid body are used (Fig. 3.1). This affects the form of the Navier–Stokes equations through addition of extra ‘centrifugal’ terms. There is no need to list the complete set of the Navier–Stokes equations written in the curvilinear coordinate system because of the degeneration which takes place in different regions of the flow. For example, in the viscous sublayer 2b (Fig. 3.4) and consequently in the lower tier 5 of the triple deck the flow is slow and behaves like incompressible, therefore excluding the thermodynamics from the system. On the other hand, the flow in regions 2a, 3 and 4 is predominantly inviscid, effectively cancelling the groups of terms with the Reynolds number. However, the continuity equation and the inertial terms in the momentum equation are always present, and their structure in the curvilinear coordinates is obviously crucial for the correct description of the flow in the interaction region. Thus, we are going to write only these terms explicitly, leaving all the other terms of the Navier–Stokes equations in the vector form as given above.

Let s, r be the curvilinear coordinates and v_τ, v_n – the relevant velocity components. In the new coordinates the continuity equation has the form

$$\frac{1}{H} \frac{\partial(\rho v_\tau)}{\partial s} + \frac{\partial(\rho v_n)}{\partial r} + \frac{\varkappa \rho v_n}{H} = 0,$$

where $\varkappa(s)$ stands for the local curvature of the surface and $H(s, r) = 1 + \varkappa(s)r$.

The convective terms are converted to

$$(\mathbf{v}\nabla)\mathbf{v} = \frac{v_\tau}{H} \frac{\partial}{\partial s} \begin{vmatrix} v_\tau \\ v_n \end{vmatrix} + v_n \frac{\partial}{\partial r} \begin{vmatrix} v_\tau \\ v_n \end{vmatrix} + \frac{\varkappa v_\tau}{H} \begin{vmatrix} v_n \\ -v_\tau \end{vmatrix}.$$

Therefore, the source terms have been added to all of the expressions as a result of the transformation.